ISMRM German CHAPTER

23RD ANNUAL MEETING OF THE GERMAN CHAPTER OF THE ISMRM

PROGRAMME & PROCEEDINGS

Zurich, 9th-10th September 2021

ETH zürich
University of Zurich[UZH]
Institute for Biomedical Engineering

Liebe Kolleginnen und Kollegen,

Willkommen zur 23. Jahrestagung der Deutschen Sektion der International Society for Magnetic Resonance in Medicine! Im Namen der Organisatoren vor Ort möchte ich meine grosse Freude darüber ausdrücken, dass dieser Event nach einem Jahr durch die COVID-19 Pandemie verursachten Unterbruchs endlich stattfindet und besonders, dass wir die meisten von Ihnen persönlich treffen können. Dies ist möglich geworden, weil Sie willens sind die momentanen Unannehmlichkeiten des Reisens auf sich zu nehmen und die restriktiven Sicherheitsbestimmungen akzeptieren. Dafür möchten wir uns herzlich bedanken!

Unsere Dankbarkeit gilt auch den aktuellen und ehemaligen Mitgliedern des Sektionsvorstandes, im Besonderen der ehemaligen Präsidentin Susann Boretius für ihren Vorschlag, dieses Meeting an der ETH Zürich durchzuführen. Mit Stolz und Freude übernehmen wir diese Aufgabe und sind überzeugt, dass Sie diese wunderschöne Stadt für die zwei Tage Meeting und, idealerweise, ein erholsames Wochenende schätzen werden. Zürich ist berühmt für seine Beiträge zur Wissenschaft, unter anderem Magnetresonanz, seine kulturelle Reichhaltigkeit – Kunstsammlungen, Architektur, Musik, Küche und Nachtleben, wie auch für seine einzigartige Lage am See mit einer atemberaubenden Aussicht auf die Alpen. Wir hoffen, dass ein bisschen von all dem bei Ihnen hängen bleibt.

Mit den vielen ausgezeichneten Beiträgen konnten wir ein umfangreiches Programm erstellen. Zusätzlich zu den Gastvorträgen der bekannten Wissenschaftler Professor Paul Unschuld aus Genf und Professor Maxim Zaitsev aus Wien, präsentieren wir 24 Kurzvorträge, aufgeteilt in drei Sessionen zu den Themen «Herz, Körper und Seele», welche das breite Spektrum der MR-bezogenen Forschung in den deutschsprachigen Ländern zeigen, sowie 14 Poster. Traditionsgemäss führen wir auch zwei Spezialsessionen mit längeren Vorträgen der Gorter-Preis-Finalisten (diesmal sind es sechs) sowie eine Panel-Diskussion über aktuelle Karriereoptionen für MR-Wissenschaftler durch. Letztere beinhaltet neu, zusätzlich zu Wissenschaftlern und etablierten Teilnehmern im MRI-Markt, einen Gast von SKOPE, einem erfolgreichen Startup mit Wurzeln in unserem Institut für Biomedizinische Technik. Wir hoffen, dass Ihnen dies eine breitere Sicht auf die beruflichen Möglichkeiten nach der Verteidigung Ihrer Doktorarbeit bietet.

Dieses Meeting wird aufgrund seiner Kombination von physischer Anwesenheit und Fernteilnahme besonders sein. Diese anspruchsvolle technische Herausforderung, wie auch andere organisatorische Aufgaben, wurde mit viel Enthusiasmus und Perfektion von meinen Kollegen im lokalen Organisationsteam, das unten aufgelistet ist, gemeistert, was uns alle zu Dank verpflichtet. Vielen Dank auch an das Programmkomitee, weiter unten aufgelistet, für die Evaluation aller Beiträge und die Zusammenstellung der Sessionen.

Wir wünschen Ihnen allen ein interessantes und inspirierendes Meeting und eine grossartige Zeit in Zürich!

Dr. Franciszek (Franek) Hennel

Institut für Biomedizinische Technik, ETH Zürich and Universität Zürich, Schweiz

Dear Colleagues,

Welcome to the 23rd Annual Meeting of the German Chapter of the International Society for Magnetic Resonance in Medicine! On behalf of the Local Organizers, I would like to express our great joy that this event is finally taking place after a yearlong break caused by the COVID-19 pandemic and, above all, that we can meet most of you in person. This is due to your willingness to travel despite burdens caused by the pandemic and to accept restrictive safety measures. Many thanks for that!

Our gratitude also goes to present and former Boards of the Chapter – in particular, the former President Susann Boretius – for proposing to organize this meeting at ETH Zurich. We are proud and happy to take on this task and believe you all will appreciate being in this beautiful city for the two days of work and, hopefully, a relaxing weekend. Zurich is famous for its contributions to science (magnetic resonance, in particular), for its cultural wealth – art collections, architecture, music, cuisine and nightlife – as well as for its unique lakeside location with a breathtaking view of the Alps. We hope that, after this Meeting, a little bit of all of these offerings will be yours (in a spiritual sense, of course).

With so many excellent submissions, we were able to build quite a rich programme. In addition to the invited talks by two prominent scientists, Professor Paul Unschuld of Geneva and Professor Maxim Zaitsev of Vienna, we have 24 short oral presentations grouped into three sessions around the themes “heart, body and soul”, illustrating how broad the scope of MR-related research is in German-speaking countries, and 14 posters. As tradition requires, we also have two special sessions with longer presentations by the Gorter Prize Finalists (six, this time) and a panel discussion of present career options for MR scientists. The latter now includes more industrial players in the MRI market than usual. We hope that this discussion will provide a broader view of some professional opportunities after doctoral studies.

This Meeting will be special because of the combination of physical and remote participation modes. This tricky technical challenge, as well as all other tasks related to the meeting organization, were accomplished with enthusiasm and perfection by my Colleagues from the Local Organizing Team, listed below, who deserve great thanks from all of us. Many thanks as well to the Programme Committee, listed further, for evaluating all contributions and composing the sessions.

We wish you all an interesting and inspiring Meeting and a great time in Zurich!

Dr. Franciszek (Franek) Hennel

Institute for Biomedical Engineering, ETH Zurich and University of Zurich, Switzerland

Local Organizing Team

General matters	Franek Hennel, Klaas Pruessmann
Sekretariat	Isabel Spiess
Teleconference	Samuel Bianchi, Hannes Dillinger, Christian Günthner
Webpage	Thomas Ulrich
Programmbuch	Emily Baadsvik, Eric Michael
Career Session	Franz Patzig
Polls, Presenations	Julia Trächtler

Programme Committee & Reviewing

Alexander Gotschy, University Hospital Zurich
Christian Günthner, IBT Zurich
Jakob Heinzle, TNU/IBT Zurich
Franek Hennel, IBT Zurich
Jan Klohs, Bruker BioSpin
Roger Luechinger, IBT Zurich
Daniel Nanz, University of Zurich
Klaas Pruessmann, IBT Zurich
Philip Staempfli, University of Zurich
Ruth Tuura, Children Hospital Zurich
Valery Vishnevskiy, IBT Zurich
Markus Weiger, IBT Zurich
Niklaus Zoelch, University of Zurich

Vielen Dank an unsere Sponsoren für die wertvolle Unterstützung!

Many thanks to our Sponsors for their valuable support!

skope

RAPID Biomedical

MR Coils - Made to Measure

PHILIPS Healthcare

BRUKER

ETH zürich

University of Zurich[UZH]

Institute for Biomedical Engineering

23rd Annual Meeting of the German Chapter of ISMRM

September 9-10, 2021

ETH Zurich, ETZ-Building, Gloriastrasse 35, Zurich, Switzerland

Lectures: Paul Scherrer Auditorium, Floor F

Posters: Foyer, Floor E

PROGRAMME

Thursday, September 9, 2021

09:30 – 11:00 **Welcome and Invited Talks**

Chair: Franek Hennel

Zoom: https://ethz.zoom.us/s/68740728140

Imaging the aging brain: on track for preconditions of sustained mental health

Prof. Paul Unschuld, University of Geneva, Switzerland

MRI Together

Prof. Maxim Zaitsev, Medical University of Vienna, Austria

11:00 – 11:30 Coffee break

11:30 – 13:15 **Session 1: Heart and Motion**

Chair: Thomas Kampf

Zoom: https://ethz.zoom.us/s/63602894937

V1* A novel phantom for realistic dynamic flow and wall shear stress measurements in an aneurysm model, Patrick Winter *et al*.

V2 Über die Messung der Porenverteilungsfunktion und das Erscheinen von Signal-Peaks bei Verwendung langer Diffusionsgradienten, Christoph Martin Stuprich *et al.*

V3 4D-flow background phase correction using M-estimate SAmple Consensus (MSAC), Carola Fischer *et al.*

V4 Concomitant field compensation in a double diffusion encoding sequence using oscillating gradients: Feasibility and efficiency, Julian Rauch *et al.*

V5 Magnetic Particle Imaging goes Human-sized, Patrick Vogel *et al.*

V6 Vergleichende MRT-Untersuchungen der kardialen Funktion nicht-humaner Primaten, Ina Barnekow *et al.*

V7 Neurometabolic changes in neonates with congenital heart disease and the relation to developmental outcome, Céline Steger *et al.*

V8 Estimation of Head Motion using a Linear Signal Model and Orbital K-space Navigators, Thomas Ulrich *et al.*

13:15 – 14:15 Lunch

14:15 – 15:30 Gorter Prize Finalists 1

Chair: Amir Moussavi

Zoom: https://ethz.zoom.us/s/67806224180

G1 Measuring the iron content of dopaminergic neurons in substantia nigra with MRI relaxometry, **Malte Brammerloh** *et al*.

G2 Hirngewebe besitzen Einzel-Voxel-Signaturen in multispektra-ler MR-Bildgebung, **Alexander German** *et al*.

G3 Schnelle online-Optimierung von parallelen Sendepulsen für die Anwendung in der klinischen Praxis, **Jürgen Herrler** *et al*.

15:30 – 16:00 Coffee break

16:00 – 17:15 Gorter Prize Finalists 2

Chair: Markus Weiger

Zoom: https://ethz.zoom.us/s/68266580580

G4 3D Sodium (^{23}Na) Magnetic Resonance Fingerprinting for time-efficient relaxometric mapping, **Fabian J. Kratzer** *et al*.

G5 Concepts for Wearable Technology in MR: Lightweight Flexible Radio Frequency Coils and Optical Wireless Communication, **Lena Nohava**

G6 Acquisition and Reconstruction Algorithms for Highly Efficient Magnetic Resonance Imaging, **Daniel Polak**

17:30 – 18:45 **Career Options – Panel Discussion from Academia to Industry**

Zoom: https://ethz.zoom.us/s/68813935326

19:00 – 20:00 **Poster Session (Floor E)**

Chair: Julia Trächtler

Zoom: https://ethz.zoom.us/s/66584955748

The classic poster session (at the boards) will take place simultaneously with the virtual one (Zoom meeting, link above). All poster files will be available for viewing on the webpage. Authors present in Zurich are also requested to place their posters on the boards in the lobby and be available there from time to time after 19:00 on Thursday for questions. At the same time (19:00), a Zoom meeting will be started to allow all authors (present and remote) to answer questions. Physically present participants will use their laptops or smartphones for that purpose (eduroam WiFi available). Please ask your questions in the Zoom chat when the given author is not there. Remember to indicate the abstract number in your question. Authors, please rename yourself in the Zoom session so that the poster number (P01, P02 etc.) comes before your name and check the chat history to find questions for you.

19:00-21:00 **Apéro (Floor E – Terrace)**

Friday, September 10, 2021

09:30 – 11:15 **Session 2: Body**

Chair: Daniel Nanz

Zoom: https://ethz.zoom.us/s/64866436463

V9* Kurtosis versus D(b50,b750) und D(b750,b1500) zur Differenzierung maligner und benigner Brustläsionen in der diffusionsgewichteten Brust-MRT, Mona Pistel *et al.*

V10* T2-Mapping zur Evaluation einer Chondromalazie des posterolateralen Tibiaplateaus, Mirjam Gerwing *et al.*

V11 Improved UTE AFI spoiling scheme for faster B_1 correction, Marta Brigit Maggioni *et al.*

V12 Einfluss von Messtechniken und Rekonstruktionsverfahren auf die Klassifizierbarkeit von Läsionen in der ^{23}Na-MRT, Laurent Ruck *et al.*

V13 Layered graph-cuts for water–fat–silicone separation in chemical shift encoding-based breast MRI, Jonathan Stelter *et al.*

V14* SPIRAL ^{7}Li MRI for in vivo neuroimaging of lithium in mice: a feasibility study, Tor Rasmus Memhave *et al.*

V15 Bestimmung von ultrakurzen T_2^* Relaxationszeiten, Nico Egger *et al.*

V16* Assessment of Whole-Body Fat Using Magnetic Resonance Imaging: Pilot Study and Validation in a Population-based Cohort, Marie-Luise Kromrey *et al.*

11:15 – 11:45 Coffee break

11:45 – 13:30 Session 3: Brain

Chair: Roger Lüchinger

Zoom: https://ethz.zoom.us/s/63984205691

V17 Mapping myelin content in ex-vivo MS brain tissue using short-T2 MRI of the lipid-protein bilayer, Emily Louise Baadsvik *et al.*

V18 Partial Simultaneous Multi-Slice Acquisition of Combined T2*-Weighted Imaging of the Human Brain and Cervical Spinal Cord, Ying Chu *et al.*

V19 Evaluating diffusion dispersion across an extended range of b-values and frequencies using advanced OGSE methodology, Eric Michael *et al.*

V20 Synchronous-nonmonotonic-changes-in-functional-connectivity-and-white-matter-integrity-in-a-rat-model-of-sporadic-Alzheimers-disease, Yujian Diao *et al.*

V21 Optimierte Hintergrundunterdrückung für Arterial Spin Labeling bei 3 Tesla, Christian Eisen *et al.*

V22 NN-driven mapping of multiple diffusion metrics at high to ultra-high resolution using the bSSFP frequency profile, Florian Birk *et al.*

V23 Fusion of ultra-high-field DTI and 3D mesoSPIM microsco-py for white matter tractography in mice, Maria Karatsoli *et al.*

V24 Removing T2 blurring in RARE sequences by using a DenseNet, Hoai Nam Dang *et al.*

13:30 – 14:30 Lunch

14:30 – 15:30 Business Meeting (Mitgliederversammlung)

Zoom: https://ethz.zoom.us/s/62638303803

15:30 – 16:00 Awards and Farewell

Zoom: https://ethz.zoom.us/s/63055204648

List of Posters

P1 fMRI comparison of optogenetic and electrical stimulation in the mouse hippocampus, Nikolaos Molochidis *et al.*

P2 The next snapshot CEST for fast 3D APTw imaging at 3T, Patrick Liebig *et al.*

P3 Entwicklung und in-vitro-Evaluation einer GlucoCEST-Sequenz an klinischen 3 T MR-Scannern, Tobias Krähling *et al.*

P4* ^{7}Li-/ ^{1}H-Messaufbau für tierexperimentelle Anwendungen, Marco Deckers *et al.*

P5 Optimierte IR-DWI Aufnahmeparameter für ein 2-Kompartimentmodell der Prostata, Felix Gloger *et al.*

P6 Dependence of Biexponential IVIM Parameters on the Number of Slices in the Liver, Martin Loh *et al.*

P7 Orientierungsverteilung der Faserrichtungen in weißer Hirnsubstanz, Lucian Spitzner

P8 Investigation of changes in flow velocity due to wall motion on 3D printed tubes using 2D PC MRI, Isil Unal *et al.*

P9* Flow quantification with MRI in the presence of flow diverter stents, Eva Peschke *et al.*

P10 Automatische Segmentierung des fibroglandulären Gewebes mittels U-Nets in der diffusionsgewichteten Bildgebung, Astrid Müller *et al.*

P11* Super-selective pseudocontinuous arterial spin labeling MRI and angiography in Moyamoya disease, Patricia Ulloa *et al.*

P12 Schnellere MR-Bildgebung des Kniegelenkes mit Compressed SENSE und künstlicher Intelligenz, Andra-Iza Iuga *et al.*

P13 Simultaneous mapping of B_0, B_1 and T_1 for the correction of CEST-MRI contrast, Kerstin Heinecke

P14* Merging T1w and QSM provides a unique Tissue Contrast, Rakshit Dadarwal *et al.*

(*) Remote presentation

Best Talk and Best Poster Poll

It is a tradition of the German Chapter Meetings to distinguish best papers in both categories by a public poll. Please cast your votes until Friday 15:00 via these links using the tokens each of you will receive individually per email:

Best talk: http://etc.ch/Brhv

Best poster: http://etc.ch/eE8s

Gorter Prize Finalists (G1-G6)

Measuring the iron content of dopaminergic neurons in substantia nigra with MRI relaxometry

Malte Brammerloh,[1,2,3*] Markus Morawski,[4] Isabel Friedrich,[4] Tilo Reinert,[1] Charlotte Lange,[1,3] Primož Pelicon,[5] Primož Vavpetič,[5] Steffen Jankuhn,[3] Carsten Jäger,[1] Anneke Alkemade,[6] Rawien Balesar,[6] Kerrin Pine,[1] Filippos Gavriilidis,[1] Robert Trampel,[1] Enrico Reimer,[1] Thomas Arendt,[4] Nikolaus Weiskopf,[1,3†], and Evgeniya Kirilina[1,7†]

[1] Department of Neurophysics, Max Planck Institute for Human Cognitive and Brain Sciences, Leipzig, Germany.

[2] International Max Planck Research School on Neuroscience of Communication: Function, Structure, and Plasticity.

[3] Felix Bloch Institute for Solid State Physics, Faculty of Physics and Earth Sciences, Leipzig University, Leipzig, Germany.

[4]Paul Flechsig Institute of Brain Research, Leipzig University, Leipzig, Germany.

[5]Jožef Stefan Institute, Ljubljana, Slovenia.

[6]Integrative Model-based Cognitive Neuroscience Research Unit, University of Amsterdam, Amsterdam, The Netherlands.

[7]Center for Cognitive Neuroscience Berlin, Free University Berlin, Berlin, Germany.
*mbrammerloh@cbs.mpg.de †NW and EK contributed equally to this work.

Adapted from Brammerloh M, et al. Measuring the Iron Content of Dopaminergic Neurons in Substantia Nigra with MRI Relaxometry. NeuroImage 2021;239:118255.

Synopsis: While MRI promises to detect the loss of iron-rich dopaminergic neurons in nigrosome 1 of Parkinson's disease patients, the contrast mechanisms remain poorly understood. Here, we devise and validate a generative model that explains iron's impact on quantitative MRI parameters in nigrosome 1, combining quantitative 3D iron histology with quantitative MRI on *post mortem* brain tissue. We show that R2* measures iron in dopaminergic neurons. We extrapolate that *in vivo* MRI may monitor dopaminergic neurons for early diagnosis of Parkinson's.

Zusammenfassung: Zwar verspricht MRT den Verlust von eisenreichen dopaminergen Neuronen im Nigrosom 1 von Parkinson-Patienten zu messen, allerdings sind die Kontrastmechanismen nur unzureichend verstanden. Hier entwerfen und validieren wir ein generatives Modell, das den Einfluss von Eisen auf quantitative MRT-Parameter im Nigrosom 1 erklärt, indem wir quantitative 3D-Eisenhistologie mit quantitativer MRT an postmortalem Hirngewebe kombinieren. Wir zeigen, dass R2* das Eisen in dopaminergen Neuronen misst und extrapolieren, dass MRT in vivo dopaminerge Neuronen für die Frühdiagnose von Parkinson überwachen kann.

Motivation

In Parkinson's disease (PD), iron overload in *substantia nigra* dopaminergic neurons (DN) is followed by their depletion, starting in neuron-rich nigrosome 1 (1). The majority of DN are irreversibly lost before PD diagnosis (2), making curative treatment for PD impossible so far. Hence, *in vivo* methods capable of monitoring iron content and loss of DN are highly desirable for early diagnosis and treatment monitoring.

Recent advances in magnetic resonance imaging (MRI) promise to provide such information, since transverse (R2) and effective transverse (R2*) relaxation rates are highly sensitive to tissue iron (3). Moreover, the MRI contrast in SN of PD patients is altered (4).

Despite promising results and a wide-spread use of MRI for imaging SN, it is not well understood which tissue components contribute to the MRI contrast in SN. While iron was suggested to induce most contrast (6), it is unclear which chemical form iron is responsible: Does iron in neuromelanin, the iron storage molecule in DN, or iron in ferritin, the iron storage protein in other brain tissue, contribute predominantly? Moreover, quantitative histological data on iron in the *substantia nigra* is largely lacking (7). A strong quantitative link between MRI parameters and the cellular iron distribution is needed to enhance the specificity and interpretability of MRI as a biomarker.

Herein, we build and validate a quantitative biophysical model of iron-induced MR relaxation in the nigrosomes of SN. This model was informed with 3D quantitative microscopic iron maps obtained from histochemistry and Proton-Induced X-ray Emission (PIXE). Combining ul-

tra-high resolution, quantitative MRI, and chemical iron extraction from tissue with biophysical modeling of the MRI signal, we demonstrate that the iron content in DN induces most iron-induced effective transverse relaxation rate (R2*) in N1. We show that biomarkers of the iron content in DN are within reach of state-of-the-art *in vivo* MRI. We therefore provide the crucial quantitative link between MRI parameters and cellular iron distribution, which is an important step toward *in vivo* characterization of DN to enable PD diagnosis at an earlier stage of the disease.

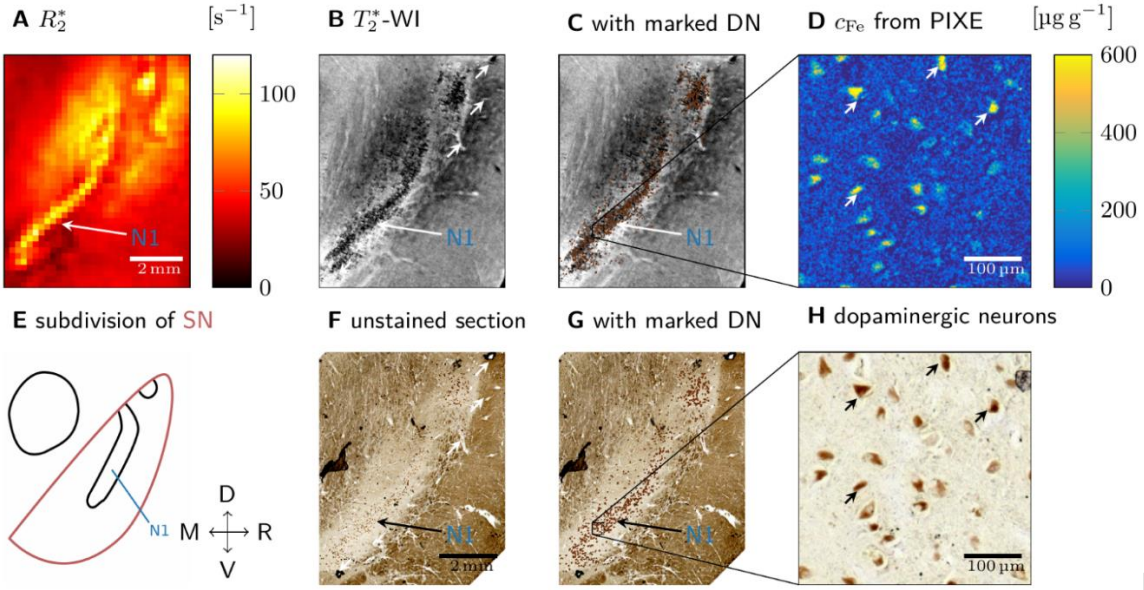

Fig. 1: Quantitative histology and MRI. A: On a quantitative R2* map of SN, nigrosome N1 is visible as hyperintense stripe. B: On ultra-high resolution T2*-WI of SN, granular hypointensities are visible in N1. C: Clusters of DN marked on unstained sections (G) correspond to regions with granular hypointensities on T2*-WI. D: Quantitative PIXE iron map in N1 shows iron hot spots in the neuromelanin domains within DN. E: Subdivision of SN along medial (M), right (R), ventral (V), and dorsal (D), showing N1 (1). F: Unstained tissue section shows N1 as stripe with increased density of brown neuromelanin pigment. G: On F, DN were marked with brown dots to improve visibility. H: PIXE measurement area on unstained section. Corresponding DN indicated with arrows in D and in H.

Theoretical considerations

The iron in tissue contributes to the transverse (R2) and effective transverse (R2*) relaxation rates through processes that can be categorized as molecular interactions on the nanoscale and dephasing due to a heterogeneous cellular iron distribution on the microscale (8, 9). Nanoscale processes impact R2 and R2* equally, as water diffusion fully averages out this length scale. Microscale processes impact R2* stronger than R2, up to an exclusive contribution to R2* in the static dephasing regime of large or well separated iron-rich cells. In this case, R2* is a highly informative biomarker: It is proportional to the susceptibility difference between the cells and their surrounding (10).

Importantly, iron stored in ferritin and neuromelanin contributes differently to relaxation rates both for nanoscale and microscale relaxation mechanisms (9).

We estimated the dominating relaxation mechanism in the nigrosomes and quantified the contribution of DN to R2* and R2 based on quantitative 3D microscopic iron distribution maps in both chemical forms (9). Such maps predicted Larmor frequency perturbation induced by the microscopic iron distributions within a voxel. Gradient echo (GE) and spin echo (SE) decays were simulated using Monte Carlo simulations for the general case and static dephasing theory in case of negligible water diffusion, both informed by the 3D Larmor frequency perturbation maps (9).

Materials and Methods

Three human *post mortem* specimen containing SN were immersion-fixed in 4 % paraformaldehyde in phosphate buffered saline.

Quantitative MRI measurements were performed at 7 T (Magnetom 7 T, Siemens Healthineers, Erlangen) (9). R2* was estimated using a 3D multi-echo FLASH (isotropic resolution of 0.22 mm, TE1...12=4...40 ms, TR=60 ms); R2 maps were obtained from a 2D SE sequence (0.22 mm in-plane resolution, 0 .6mm slice thickness, TE1...6 =11, ..., 83 ms). Ultra-high resolution T2*-weighted images (T2*-WI) were acquired using 3D FLASH (isotropic resolution of 50 µm, TE=20 ms, TR=180 ms) to achieve precise co-registration to histology. Diffusion tensor imaging (isotropic resolution of 1 mm, 6 diffusion directions, b=4000 s/mm²) was per-

formed to estimate the apparent diffusion coefficient in fixed *post mortem* tissue used in the biophysical model.

To quantify the impact of iron on R2 and R2* relaxation rates, one SN specimen was imaged before and after chemical iron extraction (9).

After MRI scanning, the *post mortem* specimens were embedded in paraffin and cut into 10 µm sections, on which histochemistry and PIXE quantitative elemental mapping were performed (9).

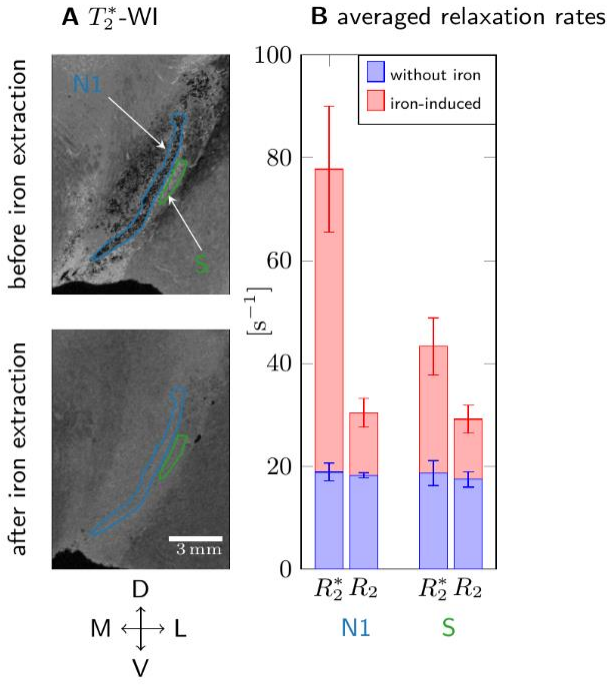

Fig. 2: MRI contrast before and after chemical iron extraction. A: On ultra-high resolution T2*-WI, granular hypointensities in N1 (top) disappeared after iron removal (bottom). B: R2 and R2* averaged over N1 and surrounding tissue (S) before iron extraction (red plus blue bar) and after (blue bar). In N1, iron-induced R2* was five times higher than the iron-induced R2 (red bars), indicating that static dephasing causes relaxation. After iron extraction, R2* and R2 were similar in N1 and S. The error bars indicate the standard deviation in the ROI. Anatomical directions as in Fig. 1.

Nigrosomes were delineated using the established method based on calbindin immunohistochemistry (1).

3D quantitative microscopic maps of iron in neuromelanin and ferritin, used for informing the biophysical model, were obtained combining Perls' stain for iron and PIXE (9). Iron in neuromelanin was assumed to be exclusively bound to neuromelanin.

Microscopy and MRI data were affinely registered using vessels on stained sections and ultra-high resolution T2*-WI as landmarks (Fig. 1B, F).

Section-sized maps of iron in the neuromelanin of DN were estimated from histology using a linear relation between PIXE iron concentrations and optical density of neuromelanin on unstained sections (9).

Results

To examine the origin of effective transverse relaxation in the nigrosomes, we compared quantitative MRI acquired at 7 T to histology and quantitative iron mapping on tissue blocks containing SN (Fig. 1). N1 in SN showed increased R2* and granular hypointensities on ultra-high-resolution T2*-WI in all investigated samples (Figs. 1A, B; 2A, B). DN were visible as regions of increased iron concentration in maps acquired with PIXE (Fig. 1D), suggesting that they induce the contrast.

Tissue iron extraction strongly decreased R2* in N1, supporting this hypothesis (Fig. 2). Iron-induced R2* in N1 was much higher than iron-induced R2, indicating that static dephasing causes the signal decay (Fig. 2B).

Since we found iron to cause nigrosome contrast, we quantified the 3D microscopic iron distribution in N1 to inform our biophysical model (Fig. 3). Iron quantification in N1 using PIXE (Fig. 3B) revealed that the iron concentration in DN neuromelanin was three to seven times higher than in ferritin outside of DN (9). Nevertheless, the majority of about 80 % of tissue iron was outside of the sparse DN.

In order to obtain 3D quantitative iron maps, we co-registered ten consecutive sections stained with Perls' for iron. Next, we calibrated those maps with PIXE iron concentrations in neuromelanin and ferritin, generating quantitative iron maps spanning over several voxels (Fig. 3D).

We predicted MRI signal decays by informing our biophysical model with these maps (Fig. 4). The GE decays in static dephasing regime showed an excellent agreement with the Monte Carlo simulation prediction and experimentally observed linear exponential signal decay (Fig. 4A). As microscale relaxation caused by iron in DN contributes predominantly to R2* in N1, R2* can be used to estimate the iron load of DN (10).

Based on these results, we proposed two biomarkers of DN iron in N1 (9) (Fig. 5). The first is given by $c_{Fe,NM,1}=(R2^*-R2)/r2^*_{NM}$, where $r2^*_{NM}$ is the microscale relaxivity of iron in DN neuromelanin predicted by our model. This biomarker is proportional to the reversible relaxation rate (10), *i. e.* the difference R2*-R2, within N1 (Fig. 5A). The second is given by $c_{Fe,NM,2}=(R2^*|_{N1}-R2^*|_S)/(r2^*_{NM}+r2_{NM})$, where $r2_{NM}$ is the nanoscale relaxivity of iron in neuromelanin. This biomarker is driven by the difference between R2* in N1 and R2* in the

directly surrounding, DN-poor tissue (e.g. S in Fig. 2) (Fig. 5B). Both biomarkers predict a qualitatively and quantitatively similar iron distribution in dopaminergic neurons as estimated from histology.

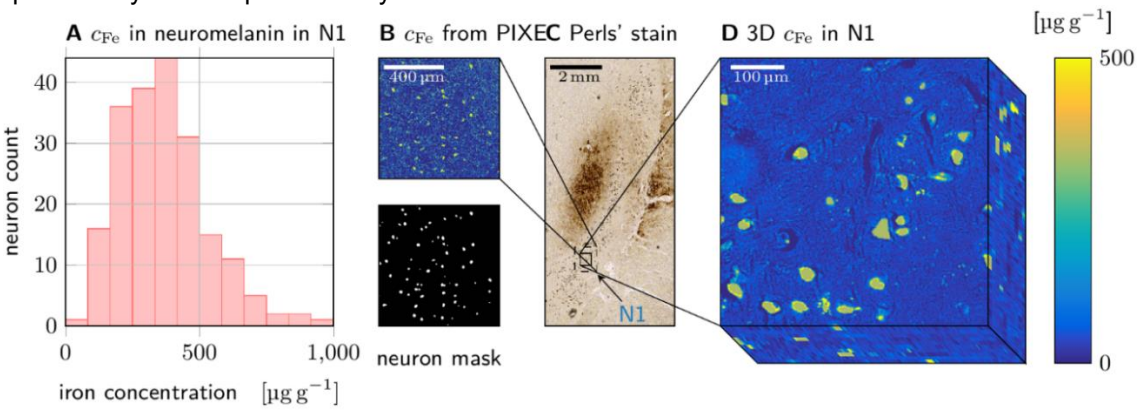

Fig. 3: Quantitative iron histology in N1. A: Histogram of iron concentrations found in DN neuromelanin in N1. B: Quantitative iron concentration maps obtained with PIXE (top) were masked using neuromelanin maps from an unstained section (bottom) to obtain the concentration of ferritin-bound iron (outside neuromelanin masks) and neuromelanin-bound iron. C: N1 is visible as a stripe of high DN density on a Perls'-stained section. D: A microscopic 3D quantitative iron map of N1 within several voxels was generated by calibrating and co-registering 10 adjacent sections stained with Perls' for iron. This volume was used for biophysical modeling.

Eventually, we estimated whether our proposed biomarkers are within reach of *in vivo* MRI. The increased body temperature *in vivo* leads to decreased magnetic susceptibility of iron and a higher diffusivity. Both effects decrease iron's impact on R2*, but our model predicted that both effects decrease the R2* induced by iron in DN by merely 7.8 %. Importantly, thus also *in vivo*, R2* is a parameter sensitive to the iron concentration in DN. A multi-echo GE acquisition with a resolution of 500 µm resulting in R2* maps with an averaged SNR of about 20 was demonstrated at 7T *in vivo* (13), opening the path for *in vivo* assessment of *substantia nigra*'s substructure.

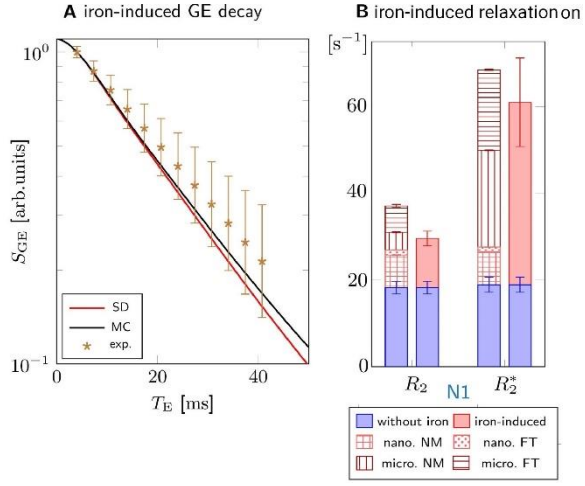

Fig. 4: Modeling iron-induced relaxation in N1. A: The GE signal decay predicted using static dephasing theory (SD) is in good agreement with Monte Carlo simulations (MC) and experimental data. B: Comparison of predicted R2* (patterned) to experimental R2* (solid color) in N1. The sum of the predictions of R2* agrees with the experimental iron-induced R2* within the error bar. The contribution of neuromelanin-bound iron to microscale R2* (micro. NM, vertical stripes) dominates.

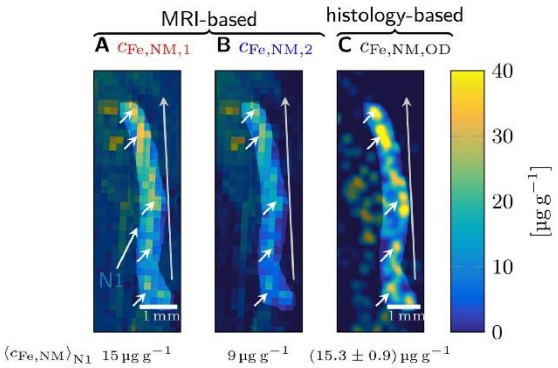

Fig. 5: Validating MRI-based biomarkers of the iron concentration in DN neuromelanin in N1. Both biomarkers (A, B) show similar iron hot spots (small white arrows) and concentration gradient (gray arrow) as the histological estimate (C). Quantitatively, the biomarkers are within 60 % of the value of the histological estimate.

Discussion

This work establishes a comprehensive biophysical model of iron-induced transverse and effective transverse relaxation rates in the nigrosomes of human substantia nigra. Our model has fundamental implications for the understanding of relaxation mechanisms in the human brain. It demonstrates that knowledge about the cellular iron distribution and iron's chemical form are indispensable for interpreting GE and SE signal decays in iron-rich brain regions. Current models (12) oversimplify this relation, leading to a 50 % underestimation of the R2* rate in N1. This stresses the importance of precise and specific models, as developed and presented here.

Our approach can be extended to study other iron-rich structures in the human brain. It predicts that iron impacts quantitative MRI parameters R2*, R2, and susceptibility differently, which may be combined to enable a separate quantification of different iron pools.

Our proposed biomarkers of DN iron in N1 are driven by the volume averaged iron concentration in DN, i.e. by the product of local iron concentration in DN and DN density (9). These biomarkers are likely informative because the density of DN and their iron load strongly varies across the SN and also between individuals (7). The biomarkers are expected to be sensitive to age-related iron accumulation in DN (11) and to DN depletion in Parkinson's disease (1).

This work encompasses several experimental limitations and biophysical modeling assumptions (9). The biophysical model developed in this study was derived from first principles, but relies on light microscopy to assess the cellular distribution of iron, disregarding the iron distribution on smaller length scales. Moreover, literature-derived magnetic and MR-properties of ferritin- and neuromelanin-bound iron obtained from *in situ* experiments were used. The model was informed and validated with histology and MRI on *post mortem* tissue, which differs from *in vivo* with regard to temperature and fixation effects.

Conclusion

In this work, we have introduced a generative model of iron-induced transverse relaxation in nigrosome 1, informed by 3D quantitative iron histology. Our biophysical model constitutes an important step on the road toward a unified, quantitative understanding of iron-induced MRI relaxation in the human brain. We demonstrate that and explain why dopaminergic neurons contribute predominantly to iron-induced R2* in N1, although their neuromelanin contains only a minority of tissue iron. By linking R2* to the tissue iron concentration in dopaminergic neurons, this study lays the groundwork for developing a biomarker of nigral integrity. Such a biomarker would help in understanding the relationship between iron accumulation and neuronal depletion in healthy aging and Parkinson's disease.

References

1. Damier P, et al. The Substantia Nigra of the Human Brain. II. Patterns of Loss of Dopamine-Containing Neurons in Parkinson's Disease. Brain. 1999;122(8):1437-48.

2. Kalia, LV, and Lang AE. Parkinson's Disease. Lancet 2015;9996:896–912.

3. Weiskopf, et al. Quantitative magnetic resonance imaging of brain anatomy and in-vivo histology. Nature Reviews Physics. (accepted)

4. Cosottini, M, et al. MR Imaging of the Substantia Nigra at 7 T Enables Diagnosis of Parkinson Disease. Radiology. 2014;3:831–38.

5. Kim EY, et al. Nigrosome 1 Imaging: Technical Considerations and Clinical Applications. Brit J Radiol. 2019;92:1101.

6. Lee H, et al. Specific Visualization of Neuromelanin-Iron Complex and Ferric Iron in the Human Post-Mortem Substantia Nigra Using MR Relaxometry at 7T. NeuroImage. 2018;172:87485.

7. Friedrich I, et al. Cell Specific Quantitative Iron Mapping on Brain Slices by Immuno-MPIXE in Healthy Elderly and Parkinson's Disease. Acta Neuropath Commun. 2021;9(1):47.

8. Kiselev VG and Novikov DS. Transverse NMR Relaxation in Biological Tissues. NeuroImage 2018;182:149–68.

9. Brammerloh M, et al. Measuring the Iron Content of Dopaminergic Neurons in Substantia Nigra with MRI Relaxometry. NeuroImage 2021;239:118255.

10. Yablonskiy DA and Haacke EM. Theory of NMR Signal Behavior in Magnetically Inhomogeneous Tissues: The Static Dephasing Regime. Magn Reson Med. 1994;32(6):749–63.

11. Zecca L, et al. The Role of Iron and Copper Molecules in the Neuronal Vulnerability of Locus Coeruleus and Substantia Nigra during Aging. PNAS. 2004;101(26):9843–48.

12. Stüber C, et al. Myelin and Iron Concentration in the Human Brain: A Quantitative Study of MRI Contrast. NeuroImage 2014;93(1):95–106.

13. Tardif CL, et al. Multi-contrast multi-scale surface registration for improved alignment of cortical areas. NeuroImage. 2015;111:107-22.

Hirngewebe besitzen Einzel-Voxel-Signaturen in multispektraler MR-Bildgebung

Alexander German[1,2,3]*, Angelika Mennecke[1], Jan Martin[2,4], Jannis Hanspach[2], Andrzej Liebert[2], Jürgen Herrler[1,2], Tristan Anselm Kuder[5], Manuel Schmidt[1], Armin Nagel[2], Michael Uder[2], Arnd Doerfler[1], Jürgen Winkler[3], Moritz Zaiss[1,6], Frederik Bernd Laun[2]

[1] Neuroradiologische Abteilung, Universitätsklinikum Erlangen, Friedrich-Alexander-Universität Erlangen-Nürnberg (FAU), Erlangen, Deutschland

[2] Radiologisches Institut, Universitätsklinikum Erlangen, Friedrich-Alexander-Universität Erlangen-Nürnberg (FAU), Erlangen, Deutschland

[3] Molekulare Neurologie, University Hospital Erlangen, Friedrich-Alexander-Universität Erlangen-Nürnberg (FAU), Erlangen, Deutschland

[4] Physical Chemistry, Lund University, Lund, Schweden

[5] Medizinische Physik in der Radiologie, Deutsches Krebsforschungszentrum (DKFZ), Heidelberg, Deutschland

[6] Abteilung für Hochfrequenz-Magnetresonanz, Max-Planck-Institut für Biologische Kybernetik, Tübingen, Deutschland

* Alexander German, Universitätsklinikum Erlangen, Schwabachanlage 6 (Kopfklinikum), 91054 Erlangen, Deutschland, alex.german@fau.de

Synopsis: Seit den Arbeiten von Brodmann und seinen Zeitgenossen ist bekannt, dass verschiedene Hirnregionen aufgrund ihrer einzigartigen zyto- und myeloarchitektonischen Merkmale unterscheidbar und klassifizierbar sind. Hier habe ich in Kooperation mit einem interdisziplinären Team die Machbarkeit der Übertragung dieses klassischen Klassifizierungsansatz auf die MRT untersucht und dabei mehrere technologische Fortschritte genutzt: Ultrahochfeld-MRT, q-Raum-Trajektorienbildgebung, chemische Austausch-Sättigungs-MRT, sowie aktuelle neuronale Netzwerkarchitekturen. Es zeigte sich, dass eine globale Hirnklassifikation von 97 Hirnregionen mit einer Klassifikationsgenauigkeit von 60% möglich ist.

Motivation

Im Nachfolgenden ist die in (1) veröffentlichte Originalarbeit zusammengefasst, mit der ich mich um den Gorter-Preis 2021 bewerbe.

Seit den bahnbrechenden Arbeiten von Brodmann (2) und Vogt und Vogt (3) ist bekannt, dass verschiedene Gehirnregionen einzigartige zyto- und myeloarchitektonische Merkmale aufweisen. Die Übertragung des Ansatzes, Hirngewebe - und andere Gewebe - auf der Grundlage ihrer intrinsischen Merkmale zu klassifizieren auf den Bereich der Magnetresonanz (MR) ist ein langjähriges Bestreben. Die Idee, Gewebe anhand ihrer T_1- und T_2-Relaxationszeiten zu klassifizieren, lässt sich bis in die Zeit vor dem Aufkommen der Magnetresonanztomographie (MRT) zurückverfolgen (4). Tatsächlich motivierte Lauterbur damit die MRT (5), und das zu Recht; der hohe Weichteilkontrast, der sich aus den T_1- und T_2-Zeiten im menschlichen Körper ergibt, ist ein Eckpfeiler der heutigen Radiologie, die häufig relaxationszeitgewichtete MR-Bilder verwendet.

Die ersten automatisierten Ansätze zur Klassifizierung von Geweben auf der Basis intrinsischer MR-Merkmale wurden in den 1980er Jahren vorgestellt (6). Auch die heute so erfolgreichen neuronalen Netzwerke kamen bereits in den frühen 1990ern zum Einsatz (7). Meist wurden T_1- und T_2-Karten oder T_1- und T_2-gewichtete Bilder verwendet. Obwohl erfolgreiche Klassifizierungen beispielsweise für bis zu 10 Gewebeklassen berichtet wurden (8), schränkte die limitierte Menge an Eingangsmerkmalen die Möglichkeit ein, Klassifizierungen für eine höhere Anzahl an Gewebeklassen zu erreichen.

Aus diesem Grund wurden atlasbasierte Ansätze mit großem Erfolg eingeführt, die räumliche Informationen nutzen, um die Anzahl potenzieller Gewebeklassen an einer bestimmten Position zu reduzieren (9). Ich möchte an dieser Stelle aus der wegweisenden Arbeit von Fischl et al. (9) aus dem Jahr 2002 zitieren, um die Situation zu beschreiben: "...es ist offensichtlich, warum kein globales Klassifikationsschema erfolgreich Strukturen voneinander unterscheiden kann, die nur auf der Intensitätsinformation basieren - es gibt einen viel zu großen Überlapp zwischen den Klassenverteilungen (sogar kortikale graue Substanz und weiße Substanz überlappen sich um mehr als 12%). Während das Hinzufügen zusätzlicher MRT-Sequenzen mit unterschiedlichen Kontrasteigenschaften oder unterschiedlichen Bildgebungsmodalitäten helfen kann, die Klassenverteilungen zu trennen,

sind immer noch räumliche Informationen erforderlich, um das Klassifikationsproblem zu lösen.".

Nichtsdestotrotz wurde der Ansatz nach 2002 weiterverfolgt, Gewebe auf der Basis intrinsischer MR-Eigenschaften zu klassifizieren. Der Fokus lag dabei auf Klassifizierungsproblemen mit nur wenigen Klassen und auf der Verwendung zusätzlicher Kontraste wie der diffusionsgewichteten MRT, z.B. in der Diagnostik des Prostatakarzinoms (10).

In der vorliegenden Studie untersuchte ich die Realisierbarkeit einer globalen Hirnklassifikation auf der Basis intrinsischer MR-Merkmale. Zu diesem Zweck nutzte ich mehrere technologische Fortschritte. Erstens verwendete ich einen 7-Tesla-Scanner der neuesten Generation, der ein erhöhtes Kontrast-Rausch-Verhältnis für viele MR-Kontraste bietet (11). Zweitens verwendete ich eine neuartige Diffusions-MR-Technik, die q-Raum-Trajektorienbildgebung (12). Mit dieser können nicht nur die voxelgemittelten Diffusionsmetriken gemessen werden, sondern auch die Varianz der Diffusionstensoren innerhalb eines Voxels, was in vielen Regionen der kortikalen grauen Substanz mit mehr als einer dominanten Faserorientierung relevant ist. Drittens verwendete ich eine chemische Austausch-Sättigungs-Transfer-Sequenz (CEST). Den daraus resultierenden Magnetisierungstransfer (MT)-Kontrast halte ich für einen geeigneten Marker der Myelinisierung, der zur Unterscheidung und Segmentierung verschiedener kortikaler Regionen verwendet werden kann (13). Darüber hinaus ist die Ultrahochfeld-CEST-Bildgebung reich an Informationen über verschiedene chemisch relevante Gewebekomponenten- und Eigenschaften, wie pH, Glutamat, Phosphokreatin, Proteingehalt und Lipide. In dieser Arbeit zeige ich, dass eine globale Klassifizierung des Gehirns somit möglich wird.

Material und Methoden

Probanden. Ich rekrutierte 38 Probanden: acht junge Männer (24,9±1,6 Jahre) und 18 gesunde ältere Probanden (58,6±6,5 Jahre, 14 Männer) sowie 12 Probanden mit idiopathischer Parkinson-Krankheit (PD) (58,4±8,2 Jahre, 10 Männer). Mögliche krankheitsbedingte Hirnveränderungen wurden als nicht relevant erachtet, da sich die Patienten im frühesten Krankheitsstadium befanden. Alle Teilnehmer gaben eine schriftliche Einverständniserklärung zur Teilnahme an der Studie ab, die von der lokalen Ethikkommission genehmigt wurde.

MRT. Die MRT-Aufnahmen wurden mit einem 7T-MRT-Scanner (Magnetom Terra, Siemens Healthineers AG, Erlangen), einer 32-Kanal-Empfangs-Kopfspule und einer 8-Kanal-Parallel-Sendespule (ptx) aufgenommen.

Zwei hochaufgelöste Datensätze wurden für die Goldstandard-Klassifizierung aufgenommen: ein 3D ptx T_1-gewichteter MPRAGE-Datensatz (0.65×0.65×0.65 mm³) und ein QSM-Datensatz (Quantitative Susceptibility Mapping, 0.6×0.6×0.6 mm³) (14,15).

Die **CEST-MRT** wurde mit einer Snapshot-Sequenz (1.8×1.8×3 mm³) durchgeführt (16) mit zwei verschiedenen Sättigungs-B_1-Niveaus von 0,7 und 1,0 µT, vorgesättigt bei jeweils 56 verschiedenen Offsets. Für den Vorsättigungspulszug wurde die Multiple Interleaved Mode Sättigungstechnik (MIMOSA) verwendet (17). Nach Korrekturen für Bewegung, B_1- und B_0-Inhomogenitäten wurden die CEST-Peaks mit einen 5-Lorentz-Pool-Modell voxelweise gefittet.

QTI. Diffusionsgewichtete Bilder wurden mit einer echoplanaren Spinecho-Sequenz (18) mit linearen, planaren und sphärischen b-Tensoren und b-Werten 0, 100, 500, 1000, 1500 und 2000 s/mm² aufgenommen (1,5×1,5×3 mm³). Ich führte Korrekturen für Bewegungen, Wirbelstrom-Effekte und Bildverzerrungen durch. Diffusions- und Kovarianztensoren wurden voxelweise angepasst und die in (12) beschriebenen Diffusionsmetriken bestimmt (AD, Cc, CM, CMD, Cµ, FA, K_{bulk}, K_{shear}, MD, MK, µFA, Kµ, V_{iso}, V_{MD}, V_{shear}).

Koregistrierung. Die Daten wurden mittels des FSL-Registrierungstools FLIRT koregistriert (Zieldatensatz: MPRAGE).

Goldstandard-Segmentierung. Eine Segmentierung der Gehirne in 102 anatomische Regionen wurde durchgeführt (Details siehe (1)).

Klassifizierung. Der Klassifikationsansatz ist in Abb. 1 visualisiert. Es wurde ein Datensatz von allen Probanden außer einem jungen Mann (Testdatensatz) erstellt. Für jeden einzelnen Teilnehmer wurden 10% der Voxel jeder anatomischen Region aus dem MP-RAGE-Raum zufällig ausgewählt. Für jedes ausgewählte Voxel wurden die lokalen 15 QTI-Parameter, 210 diffusionsgewichteten Signale, vier Lorentz-CEST-Amplituden-Parameter und 112 z-Spektrumswerte aus den Bildern extrahiert, koregistert und auf den MPRAGE-Raum interpoliert und in einem 2D-Array mit $6 \cdot 10^6$ Zeilen und 341 Spalten gespeichert. Die entsprechende anatomische Region wurde in einem one-hot-kodierten 2D-Array mit $6 \cdot 10^6$ Zeilen und 102 Spalten gespeichert. Die beiden Datensätze wurden dann gemischt, gesplittet und auf einen Mittelwert von Null und eine Einheitsvarianz normalisiert und enthielten keine räumlichen Informationen mehr. Ich definierte ein dichtes neuronales

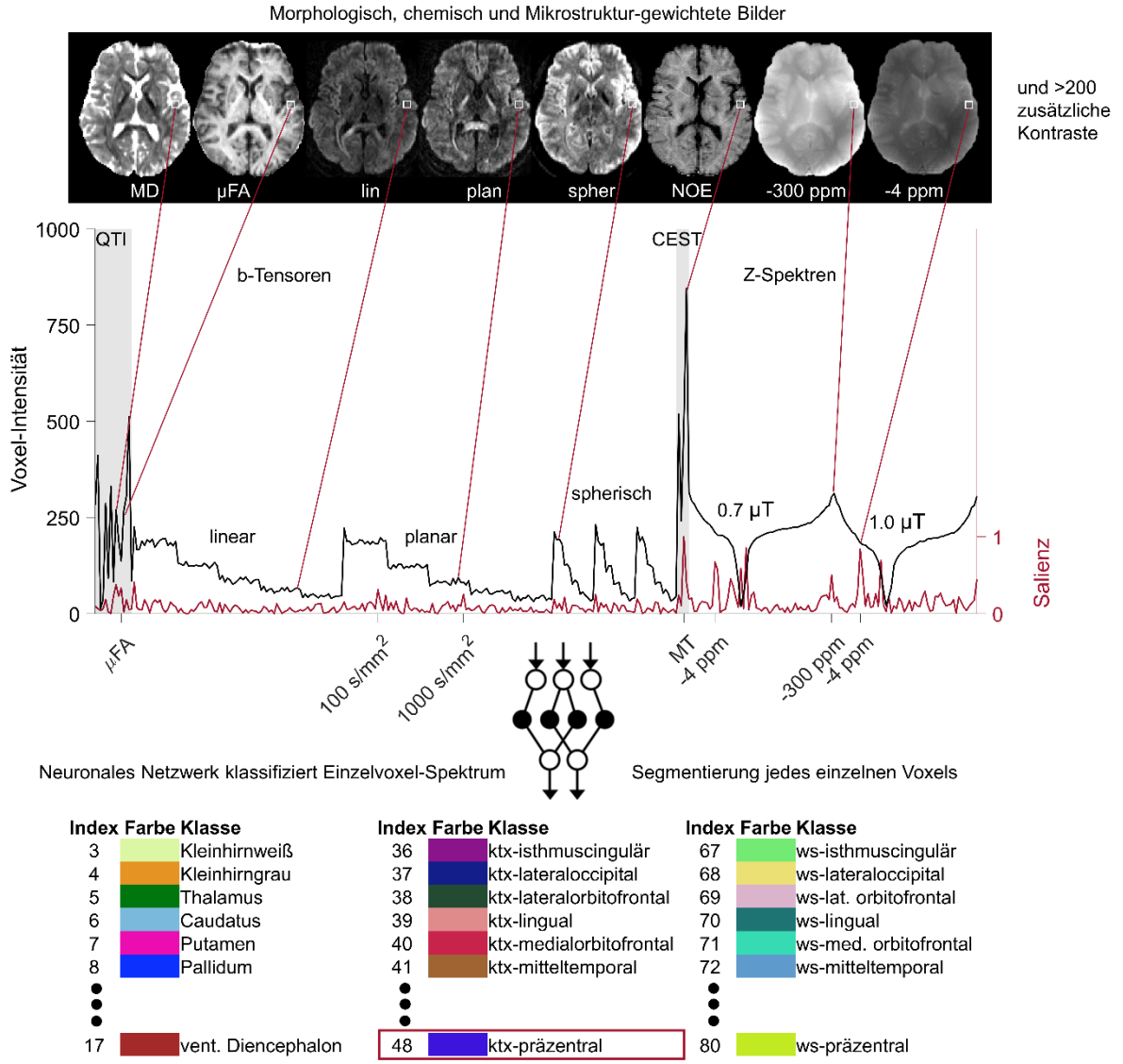

Abb. 1. Visualisierung des Klassifikationsansatzes. Als Beispiel sind acht von 341 Bildern einer Schicht mit unterschiedlichen Kontrasten dargestellt (oben). Jedes Voxel ergibt einen 341-dimensionalen Vektor, das Spektrum, das einem neuronalen Netz zugeführt wird, um die Gewebeklasse zu bestimmen (unten). Zusätzlich wird die Salienz des Netzes für dieses Voxel angezeigt. Modifiziert aus (1).

Netzwerk (DNN) in TensorFlow Keras (19) mit vier vollständig verbundenen, vorwärtsgerichteten versteckten Schichten mit jeweils 4096 Neuronen, um eine der 102 anatomischen Gehirnregionen vorherzusagen. Das Modell hatte etwa 52 Millionen trainierbare Parameter und einen Dropout von 50% nach jeder versteckten Schicht während des Trainings. Die Aktivierungsfunktionen waren *rectified linear unit* (ReLU) für die versteckten Schichten und softmax für die Ausgabeschicht, das Verlustmaß war die kategoriale Kreuzentropie plus ein L2-Regularisierungsterm für jede Schicht ($\lambda=10^{-5}$), ein Optimierungsalgorithmus mit adaptiven Momenten wurde verwendet mit einer auf 10^{-5} beschränkten Lernrate, Stapelgröße 128, Anzahl der Epochen 30.

Nach dem Training wurde das DNN verwendet, um eine voxelweise Vorhersage für den Testteilnehmer durchzuführen. Die Genauigkeit, definiert als Anzahl der korrekt klassifizierten Voxel geteilt durch die Gesamtzahl der Voxel, wurde berechnet.

Zudem wurde eine Kreuzvalidierung durchgeführt (Details siehe (1)).

Funktionsweise des DNN. Um das Funktionsprinzip der DNN-Klassifikation zu untersuchen, berechnete ich u.a. die Salienz-Vektoren (20) gemittelt über die jeweiligen Regionen des Testteilnehmers (vereinfacht, Salienz = ∂Ausgang/∂Eingang). Für eine Darstellung dieser Analyseergebnisse möchte ich auf (1) verweisen.

Ergebnisse

Abbildung 2 zeigt die Segmentierungsergebnisse für den Testdatensatz (Abb. 2a,b,c). Die Genauigkeit aus der 38-fachen Kreuzvalidierung ist in Abb. 2d als Graustufenintensität dargestellt. Die Grenzen des Thalamus, der Capsula interna und der Basalganglien sind in der voxelweisen Segmentierung noch glatter sind als in der Goldstandard-Segmentierung; allerdings sind die kortikalen Grenzen stärker gestreut. Die Klassifizierungs-Genauigkeit war 60%.

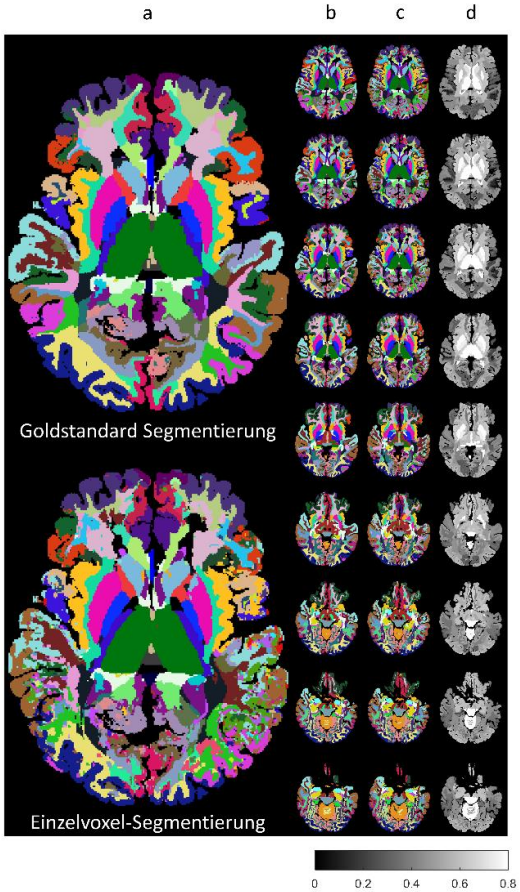

Abb. 2. Visualisierung der Segmentierung. a) Eine Schicht des Testdatensatzes nur mit Einzel-Voxel-Informationen klassifiziert (unten) und mit der Goldstandard-Segmentierung (oben). b) Goldstandard-Segmentierung. c) Einzel-Voxel-Segmentierung. d) Genauigkeit berechnet mit 38-facher Kreuzvalidierung gemittelt über alle Probanden. Modifiziert aus (1).

Diskussion

In Erweiterung früherer Arbeiten zur globalen Gehirnklassifikation habe ich neuartige hochdimensionale Kontraste in den Eingabedatenraum aufgenommen. Beim Ansatz der Einzel-Voxel-Klassifikation dient die räumliche Kohärenz der Vorhersageergebnisse in benachbarten Voxeln als inhärente Metrik der Zuverlässigkeit (wie in Abb. 2). Aktuelle atlasbasierte Klassifizierungsansätze übertreffen die von mir beobachtete Genauigkeit (21). Es ist jedoch verlockend, die MR-basierten Muster als analog zu histologischen Gewebefingerabdrücken zu betrachten (2,3). Mögliche Störfaktoren können B_0- oder B_1-Inhomogenitäten sein, die bei 7 T im Vergleich zu niedrigeren Feldstärken zunehmen, und welche das Netzwerk zur Klassifizierung mit verwenden könnte (erweiterte Diskussion siehe (1)). In der CEST-Präparation habe ich die B_1-Inhomogenität mit Hilfe des MIMOSA-Ansatzes adressiert. Darüber hinaus wurde eine B_0- und B_1-Korrektur unter Verwendung der erfassten Feldkarten durchgeführt.

Der hier vorgestellte Ansatz als solcher ist allgemein und stellt ein Beispiel für das Bestreben dar, die ständig wachsende Vielfalt an MR-Kontrasten in „MR-Biosignaturen“ zu verwandeln.

Schlussfolgerung

Die Einzel-Voxel-Klassifikation von Hirngewebe basierend auf Hochfeld-Diffusions- und CEST-Merkmalen erreicht eine hohe Genauigkeit. Dies deutet darauf hin, dass einzigartige Merkmale von Hirnregionen nicht nur durch die Histologie, sondern auch durch Einzel-Voxel-MR-Signaturen erkennbar sind.

Acknowledgement und eigener Beitrag

Diese Arbeit ist im Rahmen meiner medizinischen Doktorarbeit entstanden. Sie wäre ohne eine enge interdisziplinäre Zusammenarbeit nicht möglich gewesen. Für den Beitrag meiner Koautoren bin ich sehr dankbar. Er war wie folgt: Entwicklung und Optimierung von Sequenzen und Nachverarbeitungs-Techniken (qti: JM, TAK, FBL; CEST: AL, AMN, MZ; QSM: JH, FBL; ptx: JH, AL, AMN; fs, FSL: AM), Einlernen in die MRT-Benutzung, Supervision und Unterstützung bei der Protokoll-Optimierung, Unterstützung bei den Messungen (AM), klinische Supervision und Unterstützung bei der Patienten-Rekrutierung und -messung (MS, AD, JW), technische Supervision (FBL, MZ). Für die Bereitstellung der ASPIRE-Sequenz danke ich Simon Robinson und Korbinian Eckstein.

Ziel der Datenaufnahme war die Unterscheidung zwischen frühen Formen der Parkinson-Krankheit und gesunden Probanden. Die gesunden Probanden habe ich selbstständig rekrutiert und zunehmend selbstständig gemessen, die PD-Probanden mit Unterstützung durch die Kliniker. Zuerst optimierte ich ein MR-Protokoll für dieses Vorhaben (15 Probanden-Voruntersuchungen) und adaptierte die vorhandenen Auswerte-Routinen für die qti- und CEST-Rekonstruktionen. Dabei führte ich die vorhandenen Auswertungs-Skripte zusammen und entwickelte sie in verschiedenen Aspekten weiter (z.B. CEST-Bewegungskorrektur, geeignete Koregistrierung).

Die abschließende Untersuchung zur Unterscheidung PD/gesund steht noch aus. Bei einem umfangreichen Data-Mining fiel mir auf, dass gewisse Cluster-Algorithmen unterschiedliche Hirnregionen sehr gut trennten. Dies trieb mich zur Entwicklung des beschriebenen Klassifizierungs-Ansatzes an, den ich selbstständig erdacht, implementiert und evaluiert habe.

Referenzen

1. German A, Mennecke A, Martin J, Hanspach J, Liebert A, Herrler J, Kuder TA, Schmidt M, Nagel A, Uder M, Doerfler A, Winkler J, Zaiss M, Laun FB. Brain tissues have single-voxel signatures in multi-spectral MRI. Neuroimage 2021;234:117986.
2. Brodmann K. Vergleichende Lokalisationslehre der Großhirnrinde: Barth, Leipzig; 1909.
3. Vogt C, Vogt O. Allgemeine Ergebnisse unserer Hirnforschung. J Psychol Neurol 1919;25:275-462.
4. Damadian R. Tumor Detection by Nuclear Magnetic Resonance. Science 1971;171(3976):1151-1153.
5. Lauterbur PC. Image Formation by Induced Local Interactions - Examples Employing Nuclear Magnetic-Resonance. Nature 1973;242(5394):190-191.
6. Vannier MW, Butterfield RL, Jordan D, Murphy WA, Levitt RG, Gado M. Multispectral Analysis of Magnetic-Resonance Images. Radiology 1985;154(1):221-224.
7. Amartur SC, Piraino D, Takefuji Y. Optimization Neural Networks for the Segmentation of Magnetic-Resonance Images. Ieee Transactions on Medical Imaging 1992;11(2):215-220.
8. Taxt T, Lundervold A. Multispectral Analysis of the Brain Using Magnetic-Resonance-Imaging. Ieee Transactions on Medical Imaging 1994;13(3):470-481.
9. Fischl B, Salat DH, Busa E, Albert M, Dieterich M, Haselgrove C, van der Kouwe A, Killiany R, Kennedy D, Klaveness S, Montillo A, Makris N, Rosen B, Dale AM. Whole brain segmentation: Automated labeling of neuroanatomical structures in the human brain. Neuron 2002;33(3):341-355.
10. Chan I, Wells W, Mulkern RV, Haker S, Zhang JQ, Zou KH, Maier SE, Tempany CMC. Detection of prostate cancer by integration of line-scan diffusion, T2-mapping and T2-weighted magnetic resonance imaging; a multichannel statistical classifier. Medical Physics 2003;30(9):2390-2398.
11. Ladd ME, Bachert P, Meyerspeer M, Moser E, Nagel AM, Norris DG, Schmitter S, Speck O, Straub S, Zaiss M. Pros and cons of ultra-high-field MRI/MRS for human application. Progress in Nuclear Magnetic Resonance Spectroscopy 2018;109:1-50.
12. Westin CF, Knutsson H, Pasternak O, Szczepankiewicz F, Ozarslan E, van Westen D, Mattisson C, Bogren M, O'Donnell LJ, Kubicki M, Topgaard D, Nilsson M. Q-space trajectory imaging for multidimensional diffusion MRI of the human brain. NeuroImage 2016;135:345-362.
13. Glasser MF, Coalson TS, Robinson EC, Hacker CD, Harwell J, Yacoub E, Ugurbil K, Andersson J, Beckmann CF, Jenkinson M, Smith SM, Van Essen DC. A multi-modal parcellation of human cerebral cortex. Nature 2016;536(7615):171-178.
14. Eckstein K, Dymerska B, Bachrata B, Bogner W, Poljanc K, Trattnig S, Robinson SD. Computationally Efficient Combination of Multi-channel Phase Data From Multi-echo Acquisitions (ASPIRE). Magnetic resonance in medicine 2018;79(6):2996-3006.
15. Wei H, Dibb R, Zhou Y, Sun Y, Xu J, Wang N, Liu C. Streaking artifact reduction for quantitative susceptibility mapping of sources with large dynamic range. NMR Biomed 2015;28(10):1294-1303.
16. Zaiss M, Ehses P, Scheffler K. Snapshot-CEST: Optimizing spiral-centric-reordered gradient echo acquisition for fast and robust 3D CEST MRI at 9.4 T. NMR in Biomedicine 2018;31(4):e3879.
17. Liebert A, Zaiss M, Gumbrecht R, Tkotz K, Linz P, Schmitt B, Laun FB, Doerfler A, Uder M, Nagel AM. Multiple interleaved mode saturation (MIMOSA) for B1+ inhomogeneity mitigation in chemical exchange saturation transfer. Magnetic resonance in medicine 2019;82(2):693-705.
18. Martin J, Endt S, Wetscherek A, Kuder TA, Doerfler A, Uder M, Hensel B, Laun FB. Contrast-to-noise ratio analysis of microscopic diffusion anisotropy indices in q-space trajectory imaging. Z Med Phys 2020;30(1):4-16.
19. Abadi M, Agarwal A, Barham P, Brevdo E, Chen Z, Citro C, Corrado GS, Davis A, Zheng X. TensorFlow: Large-scale machine learning on heterogeneous systems. 2015.
20. Simonyan K, Vedaldi A, Zisserman A. Deep Inside Convolutional Networks: VisualisingImage Classification Models and Saliency Maps. arXiv:13126034v2 2014.
21. Greve DN, Fischl B. Accurate and robust brain image alignment using boundary-based registration. NeuroImage 2009;48(1):63-72.

Schnelle online-Optimierung von parallelen Sendepulsen für die Anwendung in der klinischen Praxis

Jürgen Herrler[1*], Patrick Liebig[2], Rene Gumbrecht[2], Dieter Ritter[2], Sebastian Schmitter[3], Andreas Maier[4], Manuel Schmidt[1], Michael Uder[5], Arnd Doerfler[1], Armin M. Nagel[5,6,7]

[1]Institut für Neuroradiologie, Universitätsklinikum Erlangen, Universität Erlangen-Nürnberg (FAU), Deutschland

[2]Siemens Healthineers AG, Erlangen, Deutschland

[3]Physikalisch-Technische Bundesanstalt (PTB), Braunschweig und Berlin, Deutschland

[4]Lehrstuhl für Mustererkennung, Universität Erlangen-Nürnberg (FAU), Deutschland

[5]Radiologisches Institut, Universitätsklinikum Erlangen, Universität Erlangen-Nürnberg (FAU), Deutschland

[6]Institut für medizinische Physik, Universitätsklinikum Erlangen, Universität Erlangen-Nürnberg (FAU), Deutschland

[7]Abteilung für Medizinische Physik in der Radiologie, Deutsches Krebsforschungszentrum (DKFZ), Heidelberg, Deutschland

Zusammenfassung: MRT bei 7 Tesla geht mit einer starken Inhomogenität des Anregungsfeldes einher, was zu räumlichen Inhomogenitäten der Signalintensität und des Kontrastes führt. In dieser Arbeit wird eine Methode beschrieben, die mit Hilfe von parallelen Sendepulsen trotzdem eine homogene Verteilung der Flipwinkel erzeugt. Die Pulse werden voroptimiert, sodass sie während der Untersuchung in etwa einer Minute individuell angepasst werden können. In 72 ausgewerteten Datensätzen zeigen diese Pulse homogenere Flipwinkelverteilungen, auch bei Pathologien. Damit sind individuell optimierte parallele Sendepulse erstmals klinisch anwendbar.

Motivation

Die MRT bei hohen Magnetfeldstärken ($B_0 \geq 7\mathrm{T}$) bietet großes Potential für die Bildgebung des menschlichen Kopfes [1].

Eine klinische Nutzung dieser sogenannten Ultra-Hochfeld (UHF)-MRT ist jedoch noch nicht verbreitet, obwohl ein 7T-MR System 2017 erstmals klinisch zugelassen wurde. Ein Grund dafür besteht in der damit einhergehenden räumlichen Inhomogenität des Anregungsfeldes (B_1). Diese B_1-Inhomogenität wird im Wesentlichen durch die generell kleinere Wellenlänge (etwa 12 cm in biologischem Gewebe), die Geometrie der Anregungskanäle sowie die Anatomie der Patienten beeinflusst. Sie führt bei standardmäßig verwendeten Hochfrequenz (HF)-Pulsen, die das B_1-Feld erzeugen, zu ebenso inhomogenen Verteilungen der Flipwinkel. Jene können wiederum an einigen Stellen den Bildkontrast nachteilig beeinflussen oder gar Signalauslöschungen verursachen. Auch die spezifische Absorptionsrate (SAR), die zur Erwärmung des Gewebes führt, weist stärkere lokale Feldvariationen auf und muss daher ortsaufgelöst (lokal) und generell konservativer überwacht werden [1, 2].

Eine vielversprechende Technik, um homogenere Flipwinkelverteilungen zu erreichen, ist die Methode des ‚parallelen Sendens' (engl. *parallel transmission*, pTx). Hierbei werden mehrere (z.B. 8) Sendekanäle gleichzeitig angesteuert. Das B_1-Feld ergibt sich durch Überlagerung, also Interferenz derjenigen Felder, die durch einzelne Sendekanäle erzeugt werden.

Bei sogenanntem ‚statischem pTx' werden die Sendekanäle mit derselben Pulsform (z.B. ‚sinc'- oder rechteckförmig), jedoch mit kanalspezifischer Magnitude und Phase angesteuert. Dadurch kann eine bessere Homogenität als bei sonst üblichen, von Einkanalsystemen erzeugten zirkular polarisierten Anregungsfeldern (engl.: *circularly polarized,* CP) erreicht werden [3]. Das Potential von statischem pTx ist jedoch begrenzt und gerade in Regionen mit sehr inhomogenem B_1-Feld reicht es nicht aus, um eine klinisch akzeptable Bildqualität zu erreichen [4].

Deshalb wurde das Konzept von ‚dynamischen' pTx-Pulsen entwickelt [4]. Hierbei werden sämtliche Sendespulen mit individuellen Pulsformen angesteuert und währenddessen B_0-Feldgradienten angelegt, welche sonst üblicherweise zur Ortskodierung verwendet werden. Während eines dynamischen pTx-Pulses werden bewusst inhomogene B_1-Feldverteilungen zugelassen und zusätzlich Gradientenfelder angelegt, welche die räumliche Phasenverteilung der während des Pulses erzeugten Magnetisierung ortsabhängig manipuliert. Lediglich am Ende des Pulses soll die dann entstandene Flipwinkelverteilung möglichst homogen sein. Die dadurch deutlich größere Zahl an Freiheits-

graden führt jedoch zu komplexen Optimierungsprozeduren für die Pulsberechnung, was bislang noch 15 Minuten oder länger dauert [5] und damit klinisch nicht einsetzbar ist.

Einen ersten Schritt zur klinischen Nutzung von dynamischen pTx-pulsen bietet das Konzept der ‚Universalpulse' (UP) von Gras et al. [5]. Hierbei werden die B_1- und B_0-Feldverteilungen von mehreren Probanden verwendet, um einen pTx-Puls zu optimieren, der dann ohne weitere Kalibrierung für alle Patienten eingesetzt wird. Dadurch wird generell eine zuverlässig bessere Homogenität erreicht als etwa bei standardmäßig verwendeten zirkular polarisierten Pulsen (CP-Pulse) und auch statischem pTx. Insbesondere bei Pathologien und besonderen anatomischen Gegebenheiten, die in den Trainingsdaten nicht enthalten sind, ist die durch UP erreichbare Homogenität unklar, da die individuellen B_1- und B_0-Feldverteilungen nicht berücksichtigt werden [5].

Wir führen daher das Konzept der ‚schnell online-angepassten (engl. *Fast Online-Customized*, FOCUS) Pulse ein [6]. Diese Pulse werden, dem Konzept der Universalpulse folgend, vorkalibriert und während der Messung nach schneller Kartierung des B_1- und B_0-Feldes individuell optimiert.

Material und Methoden

Datenaufnahme

Alle Messungen wurden an einem 7T MR-System (MAGNETOM Terra, Siemens Healthcare GmbH, Erlangen, Deutschland) und mit einer 8Tx/32Rx Kopfspule durchgeführt (Nova Medical, Wilmington, MA). Die B_0-Kartierung wurde mit einer Gradientenecho-Sequenz mit einer Akquisitionszeit (TA) von 12s durchgeführt, die B_1-Kartierung erfolgte in TA = 40s mit einer Saturation-Recovery-Sequenz. Die pTx-Pulse wurden als Anregungspulse neben adiabatischen Inversionspulsen in einer 3D MPRAGE-Sequenz mit TA = 7min 11s und einer isotropen Auflösung von 0,65 mm³ verwendet. B_1- und B_0-Karten wurden von insgesamt 72 Probanden aufgenommen, von denen 12 für die Pulsoptimierung verwendet wurden, und weitere 12 Pathologien (Tumore, MS-Plaques, OP, etc.) oder Anomalien (Zysten) aufwiesen. Die restlichen Probanden wurden in zwei Gruppen unterteilt, nämlich 36 (gesunde) Europäer und 12 (gesunde) Asiaten. Sieben zusätzliche Probanden wurden anschließend mit der beschriebenen MPRAGE-Sequenz untersucht.

Trajektorie und HF-Pulsoptimierung

Dynamische pTx-Pulse bestehen im Wesentlichen aus einer Sende-k-Raum Trajektorie und kanalspezifischen Pulsformen. Üblicherweise wird für nichtselektive Pulse eine k_T-Punkte Trajektorie verwendet [7]. Dabei wird der pTx-Puls in mehrere (z.B. 5) rechteckförmige HF-Subpulse unterteilt, die sich mit zwischengeschaltenen Gradientenfeldern abwechseln. Man ‚fährt' also im Sende-k-Raum für jeden Subpuls an eine bestimmte Stelle. Wir verwenden hier jedoch eine ‚spiral nonselective' (SPINS)-Trajektorie, welche ursprünglich von Malik et al. für ein Einkanal-System bei 3T vorgestellt wurde [8] und zuvor als spezielle Auslesetrajektorie zum Einsatz kam. Hierbei werden über die gesamte pTx-Pulsdauer komplizierter geformte HF-Pulse mit allen Sendekanälen gesendet und gleichzeitig Gradienten angelegt. Wir haben diese Trajektorie aufgrund der größeren Zahl an Freiheitsgraden für die zugehörigen HF-Pulse gewählt und zusätzliche Terme (0. und 2. Ordnung) hinzugefügt, um außerdem noch mehr potentielle Trajektorien zu ermöglichen. In Kugelkoordinaten wird diese erweiterte SPINS-Trajektorie wie folgt beschrieben:

$$k_r(t) = \frac{k_{\max}}{1 + e^{\alpha\left(\frac{t}{T}-\beta\right)} + e^{\gamma\left(\left(\frac{t}{T}\right)^2-\delta\right)}}$$
$$k_\theta(t) = \theta_0 + \omega_\theta t + \upsilon_\theta t^2$$
$$k_\varphi(t) = \varphi_0 + \omega_\varphi t + \upsilon_\varphi t^2 \qquad [1]$$

Elf wählbare Parameter und eine festgelegte Pulsdauer T = 1 ms sind hierfür ausreichend. Da bei der verwendeten Spule sämtliche Anregungskanäle in einer transversalen Ebene liegen, was mit dementsprechend wenig Homogenisierungspotential in z-Richtung einhergeht, wird nach der Transformation in kartesische Koordinaten der Parameter c_z als Skalierungsfaktor in z-Richtung hinzugefügt. Ist eine Trajektorie festgelegt und wurden B_1- und B_0-Karten gemessen, kann mit Hilfe der Kleinwinkel-Näherung eine Systemmatrix **A** definiert werden, die beschreibt, welche HF-Pulsformen an den einzelnen Kanälen zu welchen räumlichen Flipwinkelverteilungen im Patienten führen. Um die HF-Pulsformen aller Sendekanäle **b** zu optimieren, sodass ein Zielflipwinkel $\alpha_t = 7°$ der Spinensembles in jedem Voxel erreicht wird, kann so das folgende Problem gelöst werden:

$$\min_{\mathbf{b}} \| |\mathbf{Ab}| - \alpha_t \|_2^2 + \lambda \|\mathbf{b}\|_2^2 \qquad [2]$$

Um die SAR-Belastung durch die pTx-Pulse kontrollierbar zu halten, wird dabei zusätzlich eine Energieregularisierung mit dem Wichtungsfaktor $\boldsymbol{\lambda}$ eingeführt. Dieses Optimierungsproblem kann relativ schnell mit dem etablierten ‚Variable Exchange' Algorithmus [9] gelöst werden.

Universelle Voroptimierung

Neben den B_1- und B_0-Karten muss also die Trajektorie und der Wichtungsfaktor bestimmt sein, um Gleichung (2) lösen zu können.

Jene werden, dem Konzept der Universalpulse folgend, mit Hilfe von B_1- und B_0-Karten von $N_p = 12$ Probanden voroptimiert. Da die optimale Wahl von λ von der Trajektorie abhängt, werden die zwölf Trajektorienparameter und λ zusammengefasst als ‚Combined Optimization Values' (COV) definiert und optimiert. Die folgende Kostenfunktion wird dafür minimiert:

$$\min_{\mathbf{COV}} \sum_{p=1}^{N_p} [w_{\mathrm{Hom}} \exp(NRMSE_p(\mathbf{COV})) + w_{\mathrm{SED}} \exp(SED_p(\mathbf{COV}))] \quad [3]$$

Um einen einzelnen Kostenwert, also für einen bestimmten Wertevektor **COV**, zu ermitteln, wird für alle Probanden p eine individuelle HF-Pulsoptimierung durchgeführt (s. Gleichung 2). Die resultierende Homogenität wird mit der normierten Standardabweichung der Flipwinkel von α_t ($NRMSE_p$) bewertet und der Beitrag dieses Pulses zur lokalen SAR-Belastung wird als spezifische Energiedosis (SED_p) bezeichnet und mit Hilfe von sog. virtuellen Beobachtungspunkten (*virtual observation points*, VOPs) berechnet. Um COV zu vermeiden, die für einzelne Probanden zu schwachen NRMSE- und SED-Werten führen, werden diese Werte exponentiell gewichtet. Homogenität und SAR-Belastung der Pulse können außerdem mit w_{Hom} und w_{SED} gegeneinander abgewogen werden. Universelle HF-Sendepulse, die als Startwerte für die schnelle individuelle Optimierung (2) verwendet, aber auch direkt appliziert werden können, werden auf analoge Weise optimiert. Im Gegensatz zu den originalen UP werden hier die universellen COV bzw. UP nicht bezüglich ihrer direkten Anwendung im Patienten bewertet, sondern danach, wie gut sie als Startwerte für eine individuelle Optimierung fungieren.

Individuelle Anpassung

Zu Beginn einer Sequenz werden individuelle Dämpfungsfaktoren an jedem Sendekanal gemessen, welche zu individuell etwas unterschiedlichen SAR-Werten führen. Eine Sequenz mit fest eingestelltem Protokoll kann also in Einzelfällen die vorberechneten SAR-Grenzwerte verletzen und daher nicht ausführbar sein.

Darum wurde eine zusätzliche (online-)SED-Regularisierung eingeführt. Bei festen COV bzw. UP wird dabei der Regularisierungsparameter λ variiert und für die daraus folgenden individuell optimierten Pulse die entsprechenden SED-Werte für jeden Trainingsdatensatz errechnet. Mit Hilfe dieser Werte wird eine Anpasskurve $SED(\lambda)$ optimiert, um den Einfluss der Änderung von λ auf die resultierende individuelle SED zu schätzen. Mit dieser Kurve kann ein speziell entwickelter Algorithmus im Falle einer Überschreitung der SAR-Grenzwerte λ entsprechend anpassen.

Zusammenfassend zeigt Abbildung 1 die Schritte zur Optimierung der vorgestellten FOCUS-Pulse.

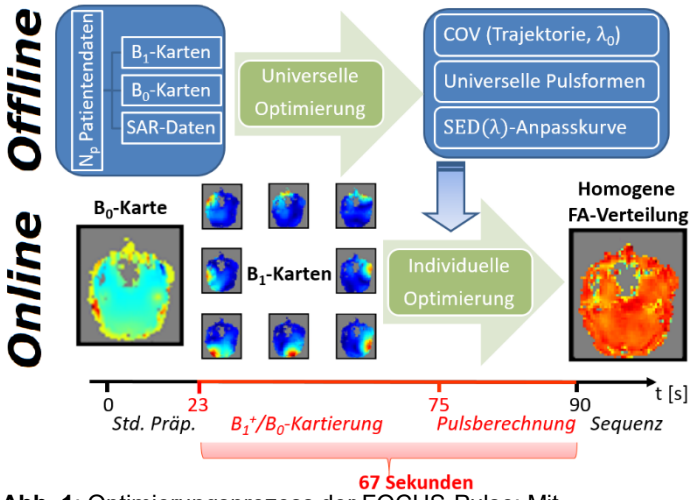

Abb. 1: Optimierungsprozess der FOCUS-Pulse: Mit Hilfe von B_1-/B_0-Karten, sowie individuellen Dämpfungsfaktoren von mehreren Probanden werden universelle COV, UPs und SED(λ)-Kurven errechnet. Während der Patientenmessung wird nach schneller B_1/B_0-Kartierung damit in maximal 15s ein individuell optimierter Puls berechnet.

Insgesamt wurden für die Studie vier pTx pulse optimiert, die mit jeweils zwei verschiedenen Wertepaaren $[w_{\mathrm{Hom}}, w_{\mathrm{SED}}] = [1{,}1]$ und $[5{,}1]$ optimiert wurden und anschließend entweder als Universalpulse (UP_{11}, UP_{51}) oder als individuell optimierte Pulse (IOP_{11}, IOP_{51}) appliziert wurden. Sieben weitere Probanden wurden mit der genannten MPRAGE-Sequenz untersucht und hinsichtlich der Homogenität und SAR-Belastung ausgewertet.

Ergebnisse

Die simulierten NRMSE- und SED-Werte der standardmäßig verwendeten CP-Pulse und aller generierten pTx-Pulse für 72 Datensätze, unterteilt in vier Gruppen, werden in Abbildung 2 gezeigt.

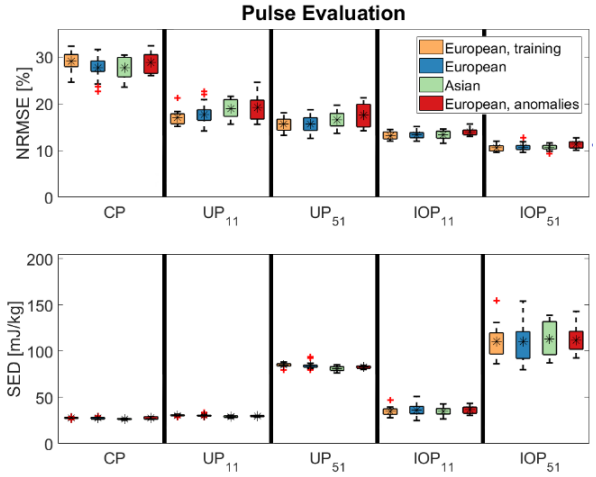

Abb. 2: NRMSE- und SED-Werte aller Pulse für alle Gruppen. Sämtliche UP zeigen niedrigere NRMSE-Werte für alle Gruppen als CP-Pulse. Individuell optimierte Pulse (IOP_{ij}) zeigen noch bessere NRMSE-Werte und höhere SED-Werte als die zugehörigen UP. IOP_{11} zeigt aber sowohl niedrigere NRMSE- als auch SED-Werte als UP_{51}.

Ein Vergleich von UP_{11} und IOP_{11} mit zirkular polarisierten Pulsen in Abbildung 3 verdeutlicht die deutlich homogenere Ausleuchtung der MPRAGE-Bilder, wenn pTx-Pulse verwendet werden.

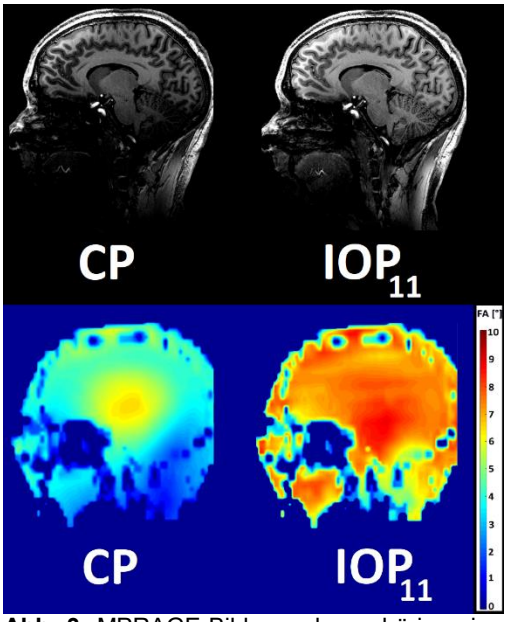

Abb. 3: MPRAGE-Bilder und zugehörige simulierte Flipwinkelverteilungen, akquiriert mit einem CP-Puls mit nominellem Flipwinkel von 7° (CP) und dem FOCUS-Puls IOP_{11}. Letzterer führt zu einer deutlich homogeneren Flipwinkelverteilung.

Die UP und FOCUS-Pulse werden genauer in Abbildung 4 verglichen. Letztere verhindern mögliche Signalauslöschungen (zu niedriger Flipwinkel) und Kontrastvariationen, was bei UP immer noch auftreten kann. Besonders deutlich sichtbar ist die Verbesserung bei einem Patienten, bei dem Teile des Gehirns operativ entfernt werden mussten (Proband 1).

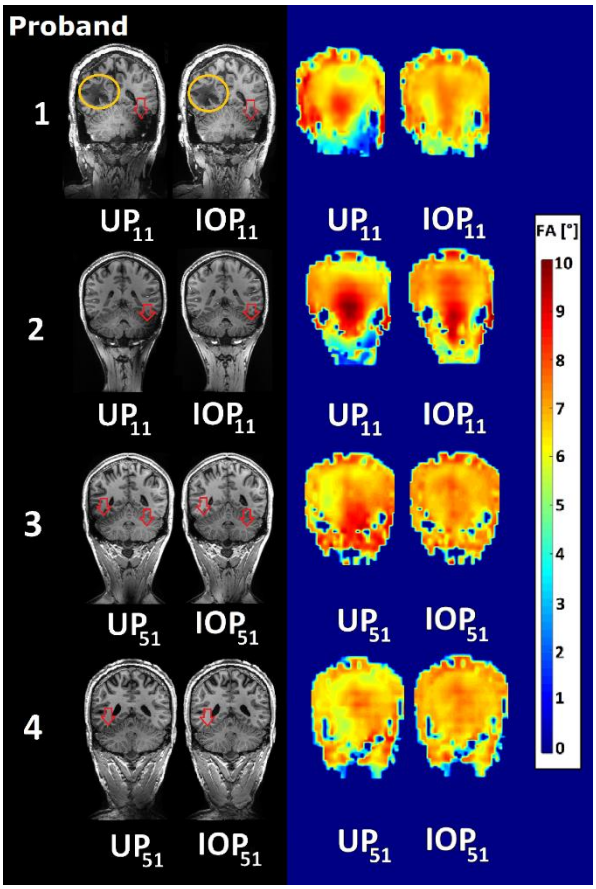

Abb. 4: MPRAGE-Bilder und zugehörige Flipwinkelkarten von beiden UPs und den zugehörigen IOPs. Die individuelle Optimierung führt zu sichtbaren Verbesserungen der Homogenität, besonders im Kleinhirn (rote Pfeile) und bei einem Hirn-OP Patienten (orangener Kreis).

Diskussion

Wir haben in dieser Arbeit eine Methode entwickelt, die mit Hilfe des Konzepts der UP und schneller individueller Optimierung eine verlässlich homogene Ausleuchtung unter strikten SAR-Grenzen erreicht werden kann. Die optimierten UP zeigen bessere Homogenität als die standardmäßig verwendeten zirkular polarisierten Pulse, wie auch von Gras et al. gezeigt. FOCUS-Pulse zeigen anhand von Simulationen mit 72 Probanden bessere Homogenität und bei entsprechender Einstellung von [w_{Hom}, w_{SED}] auch niedrigere SED-Werte als UP. Mit dieser kontrollierten SED-Belastung der entwickelten pTx-Pulse konnten sie in einer 0,65 mm^3 aufgelösten MPRAGE-Sequenz mit adiabatischer Inversion angewandt werden.

Im Gegensatz zu den originalen UP, welche auf k_T-Punkten basieren, haben wir eine SPINS-Trajektorie mit zusätzlich eingeführten Parametern verwendet, um möglichst viele Freiheitsgrade bei alleiniger, individueller HF-Pulsoptimierung zu erhalten. Dadurch wird eine vergleichbare Homogenität wie die individuell optimierten (*subject tailored*) Pulse von Gras et

al. erreicht. Aufgrund der geringen Unterschiede der untersuchten Gruppen erscheinen spezifische COV bzw. UP für ebenjene Gruppen für den Fall nichtselektiver kleinwinkliger Anregungspulse als nicht notwendig. Das Konzept der FOCUS-Pulse konnten wir auf Inversionspulse übertragen und deren Generalisierbarkeit anhand von zwei verschiedenen Spulen demonstrieren [10]. Hier werden aktuell jedoch, trotz der oben beschriebenen Nachteile, k_T-Punkte verwendet, um angesichts der aufwendigeren Optimierung ohne Kleinwinkelnäherung kurze online-Optimierungszeiten beizubehalten. Für schichtselektive Pulse kann eine dazu analoge Spokes-Trajektorie [4] verwendet werden, wobei hier aufgrund der stärkeren Unterschiede der B_1/B_0-Karten für verschiedene Probanden und Schichtpositionen nicht universelle COV/UP voroptimiert werden, sondern verschiedene Cluster eingeführt werden.

Andere Trajektorien könnten die Robustheit der FOCUS-Pulse gegenüber starken B_0-Variationen weiter verbessern [11]. Außerdem kann durch geeignete Parametrisierung und angepasste Algorithmen versucht werden, auch die Trajektorien individuell anzupassen. Des Weiteren können mit Hilfe von geeigneten VOP die lokalen SAR-Grenzwerte direkt in den Optimierungsprozess integriert werden. Speziell die vorgestellte SPINS-Trajektorie mit deutlich mehr verschiedenen Anregungsfeldern während des Pulses als eine k_T-Punkte-Trajektorie bietet dabei Potential, um die lokale SAR-Belastung besser auf verschiedene Regionen (bzw. VOP) zu verteilen [12].

Schlussfolgerung

Es wurde eine klinisch anwendbare Methode entwickelt, um pTx-Pulse zu berechnen, die in ca. 1 min (inkl. B_1- und B_0-Kartierung) individuell angepasst werden können. In Simulationen mit 72 Probanden konnte gezeigt werden, dass FOCUS-Pulse generell niedrigere NRMSE-Werte, je nach Einstellung auch bei gleichzeitig niedrigerer SAR-Belastung, erreichen. Die besseren Simulationswerte konnten anschließend anhand von sieben Probandenmessungen experimentell bestätigt werden. Die bessere Bildqualität bei Verwendung der FOCUS-Pulse wird gerade bei Patienten mit starken anatomischen Anomalien deutlich.

Referenzen

1. Ladd, M.E., et al., *Pros and cons of ultra-high-field MRI/MRS for human application.* Prog Nucl Magn Reson Spectrosc, 2018. **109**: p. 1-50.
2. Deniz, C.M., *Parallel Transmission for Ultrahigh Field MRI.* Top Magn Reson Imaging, 2019. **28**(3): p. 159-171.
3. Schmitter, S., et al., *Towards high-resolution 4D flow MRI in the human aorta using kt-GRAPPA and B1+ shimming at 7T.* J Magn Reson Imaging, 2016. **44**(2): p. 486-99.
4. Padormo, F., et al., *Parallel transmission for ultrahigh-field imaging.* Nmr in Biomedicine, 2016. **29**(9): p. 1145-1161.
5. Gras, V., et al., *Universal pulses: A new concept for calibration-free parallel transmission.* Magn Reson Med, 2017. **77**(2): p. 635-643.
6. Herrler, J., et al., *Fast online-customized (FOCUS) parallel transmission pulses: A combination of universal pulses and individual optimization.* Magn Reson Med, 2021. **85**(6): p. 3140-3153.
7. Cloos, M.A., et al., *kT -points: short three-dimensional tailored RF pulses for flip-angle homogenization over an extended volume.* Magn Reson Med, 2012. **67**(1): p. 72-80.
8. Malik, S.J., et al., *Tailored excitation in 3D with spiral nonselective (SPINS) RF pulses.* Magn Reson Med, 2012. **67**(5): p. 1303-15.
9. Setsompop, K., et al., *Magnitude least squares optimization for parallel radio frequency excitation design demonstrated at 7 Tesla with eight channels.* Magn Reson Med, 2008. **59**(4): p. 908-15.
10. Herrler, J., et al., *Evaluating Universal and Fast Online Customized Pulses for parallel transmission using two different RF coils*, in *ISMRM & SMRT Virtual Conference & Exhibition*. 2021.
11. Van Damme, L., et al., *Universal nonselective excitation and refocusing pulses with improved robustness to off-resonance for Magnetic Resonance Imaging at 7 Tesla with parallel transmission.* Magn Reson Med, 2021. **85**(2): p. 678-693.
12. Williams, S., et al., *SAR Management in pTx Sequence Design: The Impact of Electromagnetic-Field-Derived Virtual Observation Points*, in *ISMRM & SMRT Virtual Conference & Exhibition*. 2021.

3D Sodium (^{23}Na) Magnetic Resonance Fingerprinting for time-efficient relaxometric mapping

Fabian J. Kratzer[1,2,*] Sebastian Flassbeck[1,3,4], Sebastian Schmitter[1,5], Tobias Wilferth[6], Arthur W. Magill[1], Benjamin R. Knowles[1], Tanja Platt[1], Peter Bachert[1,2], Mark E. Ladd[1,2,7], Armin M. Nagel[1,6]

[1] Medizinische Physik in der Radiologie, Deutsches Krebsforschungszentrum (DKFZ), Heidelberg
[2] Fakultät für Physik und Astronomie, Ruprecht-Karls Universität, Heidelberg
[3] Center for Biomedical Imaging, New York University, New York
[4] Center for Advanced Imaging Innovation and Research, New York University, New York
[5] Physikalisch-Technische Bundesanstalt (PTB), Braunschweig und Berlin
[6] Universitätsklinikum Erlangen, Friedrich Alexander Universität Erlangen-Nürnberg (FAU), Erlangen
[7] Fakultät für Medizin, Ruprecht-Karls Universität, Heidelberg
* Corresponding author: f.kratzer@dkfz.de

Synopsis: The aim of this work was the development of a framework for 3D mapping of ^{23}Na-relaxation times, based on MRF. Here, ISTO simulations, a hybrid of single- and double-echo readouts and a CRLB-optimized FA pattern were exploited. In the human head we found $T_{1,brain}$=(35.0±3.2)ms, $T_{2l,brain}^{*}$=(29.3 ±3.8)ms, $T_{2s,brain}^{*}$=(5.5±1.3)ms, $T_{1,CSF}$=(61.9 ±2.8)ms and $T_{2,CSF}^{*}$=(46.3±4.5)ms, measured in 64min with a resolution of (5mm)^3. In further investigations, a reduction of the scan duration to 1/2h was possible, moving sodium relaxometry toward clinically feasible measurement times.

Zusammenfassung: Das Ziel dieser Arbeit war die Entwicklung einer auf MRF basierenden Methode zur Relaxometriebestimmung von ^{23}Na-Kernen. Hierzu wurden ISTO-Simulationen, ein Hybrid aus einer Einzel- und einer Doppel-Echo-Sequenz und ein CRLB-optimiertes Flipwinkelmuster verwendet. In einer in-vivo Studie im menschlichen Kopf wurden $T_{1,brain}$=(35.0±3.2)ms, $T_{2l,brain}^{*}$=(29.3 ±3.8)ms, $T_{2s,brain}^{*}$=(5.5±1.3)ms, $T_{1,CSF}$=(61.9 ±2.8)ms und $T_{2,CSF}^{*}$=(46.3±4.5)ms, bei einer Messzeit von 64min mit einer Auflösung (5mm)^3, quantifiziert. Weitere Untersuchungen ergaben, dass eine Messzeitreduzierung auf 1/2h möglich ist, was ein weiterer Schritt zur Natriumrelaxometrie innerhalb klinisch relevanter Messzeiten darstellt.

Motivation

(^{23}Na) ions yield the second highest signal in the human body and are involved in many physiological processes. Consequently, ^{23}Na-MRI has been exploited to investigate a variety of pathologies, such as neurodegenerative diseases or cancer. Here, often the tissue sodium concentration (TSC) was evaluated, which comprises a volume-weighted combination of intra- and extracellular sodium signal. Other studies focused on quantification of ^{23}Na relaxation times and found alteration of the latter in several diseases [1-4]. In clinical routine, however, sodium relaxometry only found limited application due to long scan times, which are often in the order of 1h for standard mapping of a single relaxation parameter. In recent years, techniques like 3D-MERINA [5] and the variable flip angle method [6] were developed to tackle these long measurement times. We recently proposed a different approach, where we used Magnetic Resonance Fingerprinting (MRF) for ^{23}Na relaxometry [7]. This was the first application of MRF in X-nuclei relaxometry, to the best of our knowledge. In MRF, the magnetization is driven in a transient state during which a time series of heavily undersampled images is acquired. In the reconstruction, the temporal evolution of each voxel is compared to the entries of a precalculated dictionary, containing the simulated signal evolutions for different parameter combinations of T_1, T_{2l}^{*}, T_{2s}^{*}, T_2^{*} and ΔB_0. The best match then determines the quantified parameters in each voxel. However, acquisition of the aforementioned parameters with 2D MRF still required 1h for a 2D slice.

In this work, we present an extension to the ^{23}Na -MRF framework with major improvements. First, a more accurate signal model, based on irreducible spherical tensor operators (ISTOs) [8], was implemented to allow simulation of the full spin dynamics of spin 3/2 nuclei. Second, the sequence was extended to a 3D version with increased readout efficiency. Last, the FA pattern was numerically optimized using the Cramér Rao Lower Bound (CRLB).

The conjunction of these improvements allowed 3D mapping of T_1, T_{2l}^{*}, T_{2s}^{*}, T_2^{*} and ΔB_0 with automatic differentiation between bi- and monoexponential transverse relaxation in the

human head in 32min, pushing ^{23}Na relaxometry towards clinically feasible measurement times.

Materials and Methods

Two 3D ^{23}Na-MRF sequences, termed MRF I and MRF II were developed in this work and their encoding capabilities compared. The sequences are based on a 3D center-out radial [9] SSFP sequence and our recently published 2D ^{23}Na-MRF technique [7]. Inspired by ^{1}H-MRF techniques [10], the transient state is generated by 1000 cycles of varying FAs and TRs. Furthermore, varying TEs were implemented to sensitize the sequence towards transverse relaxation, which is required due to the short transverse relaxation times of ^{23}Na nuclei with respect to TR. In the following one succession of 1000 cycles is referred to as a pulse train.

In the MRF I sequence, each cycle starts with a non-selective excitation pulse with varying amplitude according to the FA pattern. Subsequently, a variable TE is inserted, where the pattern is pseudo-randomly distributed between TE_{min} = 0.55ms and TE_{max} = TE_{min} + 20ms. Next, spatial encoding is achieved using a radial density-adapted readout gradient, followed by a rewinder and a spoiler gradient. The readouts are successively rotated by the 13th tiny golden angle [11] to ensure full k-space coverage over the entire measurement. The next cycle starts directly after the spoiler gradient, leading to a variable TR due to the varying TE. After the last cycle in one pulse train, full relaxation towards thermal equilibrium is enabled by insertion of a 1s pause. The next pulse train, consisting of the same 1000 cycles, consequently samples the signal in the same states as the previous one. Incrementing the readout direction between pulse trains consequently leads to 1000 time frames in k-space, each containing $N_{pulse\text{-}trains}$ equidistantly distributed spokes.

The MRF II sequence was derived from MRF I with two major modifications. First, an optimized FA pattern was constructed using the CRLB to improve the T_1-encoding. Secondly, the readout efficiency was increased by acquiring a second echo when the current TE was larger than the combined duration of a readout and a rewinder gradient.

To simulate the theoretical signal evolutions and construct a dictionary from the latter, a GPU-accelerated ISTO simulation was implemented [8], which allows simulation of the full spin dynamics of 3/2 particles. Here, two modifications regarding the relaxation times were implemented. First, in literature the longitudinal relaxation is commonly modeled with a single relaxation constant T_1, whereas the ISTO framework intrinsically yields a biexponential relaxation with the relaxation times T_{1s} and T_{1l}. Hence, a monoexponential estimate was constructed by a first order Taylor approximation, yielding

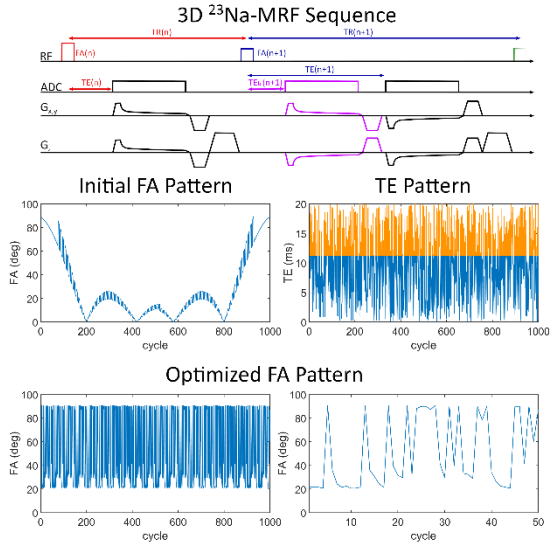

Figure 1: 3D ^{23}Na-MRF sequence diagram, where the purple readout is inserted in the MRF II sequence if TE is larger than the time required for acquisition of a spoke. TEs for which this holds true are marked in orange in the TE pattern. The initial (MRF I) and the optimized (MRF II) FA pattern are shown.

$$T_1 \approx \frac{1}{\frac{0.8}{T_{1l}} + \frac{0.2}{T_{1s}}}.$$

Second, T_2^* (rather than T_2) relaxation was enabled by intravoxel dephasing of the magnetization, constructed using a Lorentzian-shaped distribution of off-resonances.

The dictionary was compressed up to rank 12 using an SVD. The reconstruction was performed using a low-rank alternating direction method of multipliers [12]. Automatic distinction between voxels experiencing a bi- and voxels relaxing with a monoexponential transverse relaxation was enabled as the dictionary contained both models. In the following, monoexponential voxels are masked in pink in T_{2l}^* and T_{2s}^* maps. In T_2^* maps, biexponential areas are masked, respectively.

All measurements were performed on a 7T scanner using a double resonant ^{23}Na/^{1}H coil. To validate the MRF sequences, measurements with both MRF (TA = 64min) and reference sequences were conducted in a phantom containing 0.9% Na and compartments with Agarose concentration ranging from 2% to 7%. To determine the reference values for the transverse relaxation times, data measured with a multi-echo GRE sequence (TA = 56min) were fitted with both a bi- and a monoexponential relaxation model in each voxel. Differentiation which model described the data better was based on

the goodness of the fit. Reference T_1 maps were determined using an inversion (IR) recovery sequence (TA = 5h 48min). All phantom measurements were acquired with a nominal resolution of $(3mm)^3$.

Finally, the relaxation times in brain tissue and CSF were determined in an in vivo study, conducted in four healthy volunteers using MRF II (TA = 64min, $(5mm)^3$). Different undersampling factors were retrospectively applied onto the data to investigate the effects on virtually reduced measurement times. Based on these investigations, one volunteer was measured a second time with reduced scan duration (TA = 32min).

Results

Quantitative T_1 and ΔB_0 maps acquired with MRF I, MRF II and the references are shown in Figure 2. In the T_1 maps, a substantial improvement by the use of MRF II over MRF I was found, which is mostly due to the optimized FA pattern. Good agreement between all ΔB_0 maps is found.

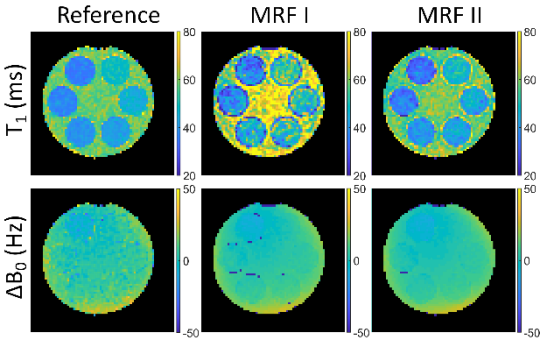

Figure 2: T_1 and ΔB_0 maps of the central slice are shown, acquired with the references, MRF I and MRF II. Images were masked based on magnitude images. A quantitative comparison is illustrated in Figure 4.

The transverse relaxation times T_{2l}^*, T_{2s}^* and T_2^* are illustrated in Figure 3, where good agreement between MRF II and the reference is found.

The reconstruction consistently classified voxels in aqueous sodium solution to relax monoexponentially, whereas the Agarose compartments were found to decay biexponentially.

A quantitative comparison is shown in Figure 4, where the mean and SD of all relaxation times in each phantom compartment are displayed. The mean deviation between relaxometric parameters obtained with MRF I and the reference methods was 10.8%, whereas MRF II only deviated by 1.0%.

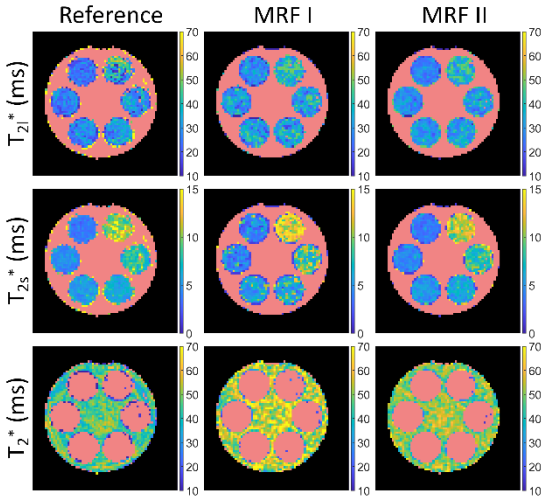

Figure 3: The transverse relaxation times T_{2l}^*, T_{2s}^* and T_2^* are shown. In the T_{2l}^* and T_{2s}^* maps voxels where monoexponential relaxation was detected are masked in pink. In the T_2^* map biexponential voxels are masked. All maps are masked on magnitude images. A quantitative comparison is illustrated in Figure 4.

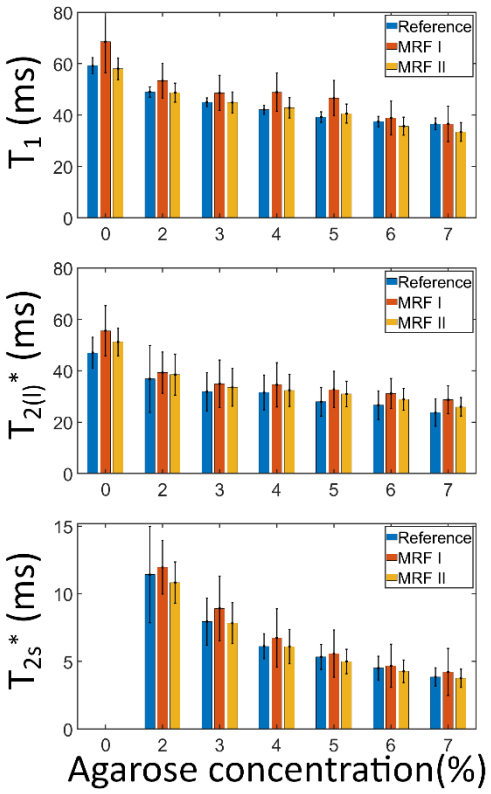

Figure 4: Mean and SD of all relaxation parameters in each phantom compartment are shown, evaluated over the 10 central slices. The mean deviation between MRF I and the references was 10.8%, whereas MRF II only differed 1.0% on average.

Relaxation times in the human head were quantified in four healthy volunteers. Retrospective undersampling (not shown) revealed a good compromise between scan duration and image quality for a virtual measurement time of

32min, which was subsequently confirmed in a new in vivo measurement. Relaxation maps of an exemplary volunteer are shown in Figure 5, acquired with MRF II within the two different scan durations (64min and 32min). Here, a sodium image (labeled as "Nav") was constructed by summation of all MRF time frames. The T_1 maps show a good distinguishability between CSF and brain tissue. In the T_{2l}^* and T_{2s}^* maps monoexponential areas are masked in pink, which is found in areas dominated by CSF. In areas with high off-resonances, such as tissue near the ear canals and the frontal cortex show, erroneous values are quantified. In the T_2^* maps monoexponential tissue is masked. In brain tissue a mean longitudinal relaxation constant of $T_{1,brain}$ = (35.0±3.2)ms was found, averaged over all four volunteers (TA = 64min). The transverse relaxation parameters were $T_{2l,brain}^*$ = (29.3±3.8)ms and $T_{2s,brain}^*$ = (5.5±1.3)ms. In CSF $T_{1,CSF}$ was (61.9±2.8)ms and $T_{2,CSF}^*$ = (46.3±4.5)ms.

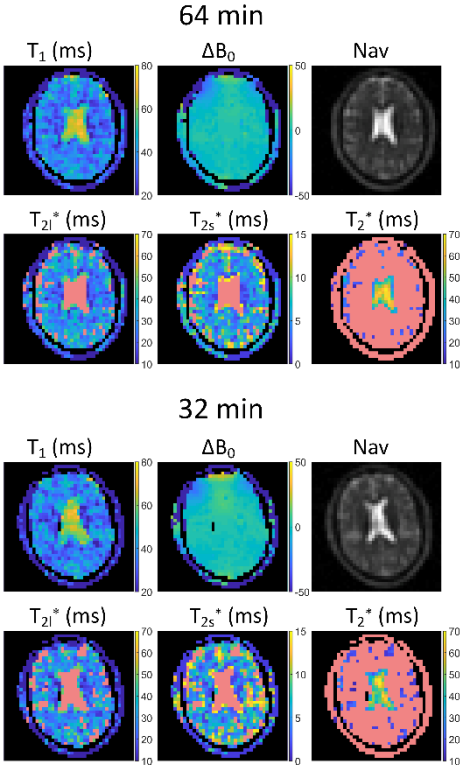

Figure 5: Relaxation times in a slice of a human head are shown, measured with MRF II in 64min and 32min. The Nav-image corresponds to a ^{23}Na image, constructed by summation of all MRF time frames. All images were masked on magnitude images.

Discussion

In this work, an MRF framework for quantification of sodium relaxation times was presented. Both MRF sequences were tested in a phantom and results were compared to results obtained with reference methods. The MRF I sequence resulted in a mean difference of 10.8% with respect to the references. The optimized sequence MRF II only showed an average deviation of 1.0%. Successful relaxometric quantification in the human head was possible within 32min. Measurement of the relaxation parameters in brain tissue and CSF in four healthy volunteers yielded good agreement with literature, where $T_1 \approx 37$ms, $T_{2l}^* \approx$ 20-40ms and T_{2s}^* = 2.0-6.5ms were reported in brain tissue and $T_1 \approx 37$ms and $T_2^* \approx$ 42-56ms in CSF, respectively [3,5,7,13,14]. The transverse relaxation times in CSF might be biased by partial volume (PV) effects, which could be tackled by multicompartment MRF [15] or PV corrections if the point spread function (PSF) is known. Further, increased resolution could reduce PV effects, which might be achieved with more sensitive coils and higher static fields. In areas with high off-resonances the borders of the dictionary were reached in the dictionary matching, resulting in erroneous quantification of relaxation parameters. This could be improved by extending the parameter range of the dictionary at the expense of increased computational burden.

In future, the sequence could be further improved by also optimizing the TE pattern. Further, a homogenous B_1^+ field was assumed in this work which could be considered by implementing the latter as an additional dictionary parameter.

Conclusion

In conclusion, relaxometric mapping of the human head in 32min was possible. Hence, MRF appears to be a promising candidate to push sodium relaxation relaxometry towards scan times feasible in clinical routine.

This abstract is based on:

Kratzer F.J., Flassbeck S., Schmitter S., Wilferth T., Magill A.W., Knowles B.R., Platt T., Bachert P., Ladd M.E., Nagel A.M. (2021). 3D Sodium (23Na) Magnetic Resonance Fingerprinting for time-efficient relaxometric mapping. *Magnetic resonance in medicine*. doi: 10.1002/mrm.28873

References

1. Kline RP, Wu EX, Petrylak DP, Szabolcs M, Alderson PO, Weisfeldt ML, Cannon P, Katz J. Clin Cancer Res 2000;6(6):2146-2156.
2. Stobbe R, Beaulieu C. Magn Reson Med 2005;54(5):1305-1310.
3. Nagel AM, Bock M, Hartmann C, Gerigk L, Neumann JO, Weber MA, Bendszus M, Radbruch A, Wick W, Schlemmer HP, Semmler W, Biller A. Invest Radiol 2011;46(9):539-547.
4. Nagel AM, Amarteifio E, Lehmann-Horn F, Jurkat-Rott K, Semmler W, Schad LR, Weber MA. Invest Radiol 2011;46(12):759-766.

5. Blunck Y, Josan S, Taqdees SW, Moffat BA, Ordidge RJ, Cleary JO, Johnston LA. Magn Reson Med 2018;79(4):1950-1961.
6. Coste A, Boumezbeur F, Vignaud A, Madelin G, Reetz K, Le Bihan D, Rabrait-Lerman C, Romanzetti S. Magn Reson Imaging 2019;58:116-124.
7. Kratzer FJ, Flassbeck S, Nagel AM, Behl NGR, Knowles BR, Bachert P, Ladd ME, Schmitter S. Magn Reson Med 2020;84(5):2577-2591.
8. Hancu I, Van der Maarel J, Boada F. Journal of Magnetic Resonance 2000; 147(2):179-191.
9. Nagel AM, Laun FB, Weber MA, Matthies C, Semmler W, Schad LR. Magn Reson Med 2009;62(6):1565-1573.
10. Ma D, Gulani V, Seiberlich N, Liu K, Sunshine JL, Duerk JL, Griswold MA. Nature 2013;495(7440):187-192.
11. Frydahl A, Holst K, Caidahl K, Ugander M, Sigfridsson A. MAGMA. 2020. doi: 10.1007/s10334-020-00859-z.
12. Asslander J, Cloos MA, Knoll F, Sodickson DK, Hennig J, Lattanzi R. Magn Reson Med 2018;79(1):83-96.
13. Lommen JM, Flassbeck S, Behl NGR, Niesporek S, Bachert P, Ladd ME, Nagel AM. Magn Reson Med 2018;80(2):571-584.
14. Ridley B, Nagel AM, Bydder M, Maarouf A, Stellmann JP, Gherib S, Verneuil J, Viout P, Guye M, Ranjeva JP, Zaaraoui W. Sci Rep 2018;8(1):4357.
15. Tang S, Fernandez-Granda C, Lannuzel S, Bernstein B, Lattanzi R, Cloos M, Knoll F, Asslaender J. Inverse Probl. 2018; 34:094005. doi: 10.1088/1361-6420/aad1c3.

Concepts for Wearable Technology in MR: Lightweight Flexible Radio Frequency Coils and Optical Wireless Communication

Lena Nohava[1,2*]

[1] High Field MR Center, Center for Medical Physics and Biomedical Imaging, Medical University of Vienna, Vienna, Austria.
[2] Laboratoire d'Imagerie Biomédicale Multimodale Paris Saclay (BioMaps), Université Paris-Saclay, CEA, CNRS, Inserm, Orsay, France.

* lena.nohava@meduniwien.ac.at

Synopsis: In this PhD thesis work, concepts for the development of wearable MR technology were studied: flexible size-adapted coaxial radio frequency coils for 3 T and 7 T MRI, and the perspectives in wireless MRI, with a focus on the development of a custom optical wireless communication module.

Zusammenfassung: In dieser Dissertationsarbeit wurden Konzepte für die Entwicklung von Wearable-Technologie für die MR untersucht: flexible, größenadaptierte koaxiale Hochfrequenzspulen für 3 T und 7 T MRT und die Perspektiven in der drahtlosen MRT, mit einem Schwerpunkt auf der Entwicklung eines optischen drahtlosen Kommunikationsmoduls.

Motivation

Magnetic resonance imaging (MRI) has become a largely accessible non-invasive medical imaging modality in clinical diagnostics and is subject to lively research in various medical and technological fields.

The MR image quality depends on the achievable signal-to-noise ratio (SNR). Therefore, several development strategies related to hardware, aiming for signal enhancement have been pursued: The increase in static magnetic B_0 field strength (e.g. 7 T, (1,2)) is motivated by the fact that it creates higher net tissue magnetization and, therefore, higher detectable signal amplitudes. The benchmark for standard clinical imaging is 3 T while a first certified clinical ultra-high field (UHF) 7 T MR scanner is already on the market. Gradient hardware development is focused on improving linearity, gradient strength, and slew rate. Another main aspect is the optimization of transmit and receive characteristics of RF coils and the development of coil arrays (3). At 3 T, it is common to use a large body coil integrated in the scanner bore for homogeneous RF transmit field creation in combination with small receive-only surface coils with high sensitivity close to the body region to be imaged. At 7 T, due to the difficulties in producing a homogeneous RF transmit field related to wavelength effects, no such body coil is integrated and, therefore, typically surface coils are used in transmit/receive (Tx/Rx) mode. Higher coil channel counts allow for parallel imaging (4–6) and parallel transmission techniques (7), resulting in drastically shorter examination times and more homogeneous RF excitation which is especially required at UHF.

In addition, the development of form-fitting and flexible or even stretchable RF coils has been emphasized. This is motivated by signal gain, less variation in coil loading and, therefore, more stable inter-subject performance, increased patient comfort and efficient workflow due to improved usability with close-fitting lightweight coil design as well as the adaptability to different anatomies and subject sizes.

Consequently, a trend towards construction of fully wearable MR devices has been noticeable within the research community in recent years. A wearable MR device is not only characterized by flexibility and lightweight material but also by the removal of cabling. This implies wireless MR data transmission, wireless power supply, and transmission of control signals in the MR environment.

Further, the integration of additional sensors or on-coil components during the MRI process, e.g., for motion correction or localized shimming, have gained interest as they can improve image quality and robustness of the acquisition.

In this context, in this PhD thesis, two main technological aspects were identified and studied, which are indispensable for the emergence of wearable technology in MR:

- The development of flexible lightweight RF coils and coil arrays.
- Strategies for wireless signal and power transmission in the MR environment.

Flexible Coaxial RF Coils

The first part of this work was focused on the investigation of flexible self-resonant coaxial transmission line resonators (TLRs) made from commercially available non-magnetic coaxial cable with multiple cable turns and/or conductor gaps. This conformal coil design principle was studied in silico by analytical calculations and

3D electromagnetic simulations. Numerous prototypes were fabricated, and their performance was experimentally tested both on the bench and in MRI at 3 T and 7 T.

Design Principle of Multi-Turn Multi-Gap (MTMG) Coaxial Coils

The published concept of single turn and single-gap (1T1G) coaxial ("high impedance") coils (8) is limited in terms of possible coil diameters by the target resonant frequency (f_0) and by the properties of the coaxial cable used, i.e. the outer diameter (d_1), permittivity (ε_r) and impedance (Z_0). The combination of coaxial coils with the MTMG TLR principle (9) increases the degrees of freedom in flexible coil design and enables the choice of almost arbitrary coil size. The resulting form-fitting, ideally dimensioned coil yields optimal SNR and penetration depth (10) depending on the target anatomical application.

Fig.1 shows the design concept of MTMG coaxial coils studied in this work. Examples of gap positioning with 1-3 turns and 1-3 gaps are shown (Fig.1a) together with the coaxial cable parameters (Fig.1b) and the equivalent circuit diagram (Fig.1c) which was used to analytically determine the self-resonance frequency (f_0) of MTMG coaxial coils (11).

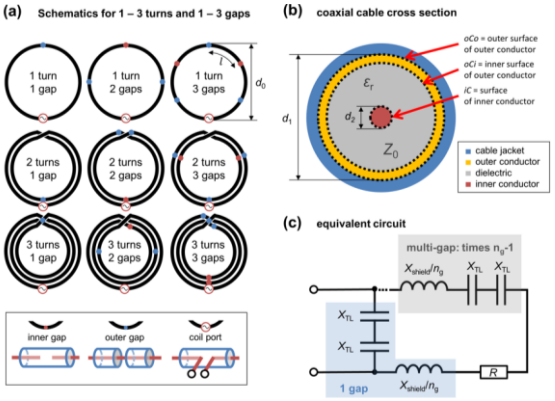

Fig. 1: **(a)** Design concept of coaxial coils with 1-3 gaps and 1-3 turns, **(b)** coaxial cable parameters, **(c)** equivalent circuit model for an arbitrary number of turns, n_g...number of gaps, d_0...coil diameter, l...length of one coaxial stub, d_1...outer diameter of outer conductor of coaxial cable, d_2...diameter of inner conductor, ε_r...relative permittivity, Z_0...characteristic cable impedance (Ω), X_{shield}...inductive reactance of the outer surface of the coax shield, X_{TL}...reactance of one coaxial stub (capacitive at resonance), R...resistance (ohmic coil losses).

Fig.2 illustrates the extension of the achievable coil diameters using the MTMG concept (blue boxes) compared to 1T1G coils (yellow boxes) based on calculations with realistic values for all coil and cable parameters. Due to the discrete nature of some of the parameters, small voids in the diameter ranges at 9.4 and 10.5 T can be observed.

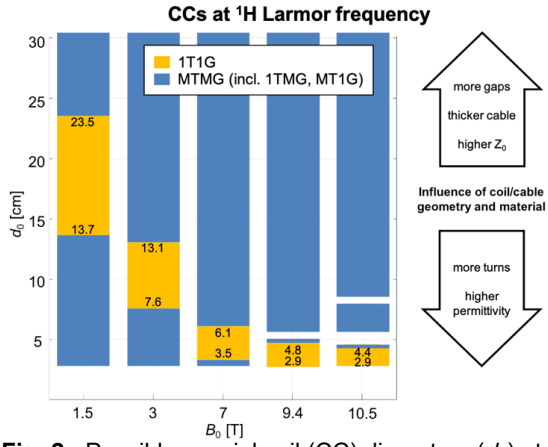

Fig. 2: Possible coaxial coil (CC) diameters (d_0) at the ^{1}H Larmor frequency for 5 different common field strengths using realistic coil and cable parameters.

Coil Fabrication

Coaxial coils of different diameters were fabricated along with standard copper wire coils of the same size for comparison (possible biomedical applications are given in parenthesis): 4 cm (skin, hand, wrist), 7 cm (elbow, ankle, breast, head), 10 cm (breast, head, knee) and 15 cm (heart, abdomen).

In this study, coils were fabricated for operation in Rx-only mode for 3 T MRI (Fig. 3a) and Tx/Rx mode for 7 T MRI (Fig. 3b).

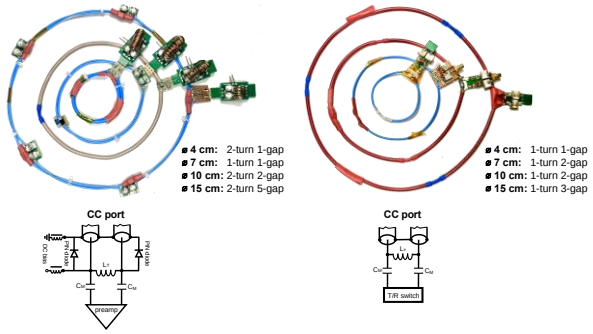

Fig. 3: Coaxial coils fabricated for Rx-only use at 3 T (left) and Tx/Rx use at 7 T MRI (right).

Electromagnetic Simulations

In CST Studio Suite 2020 (Dassault Systèmes, Paris, France), electromagnetic (EM) simulations of all coils - unloaded and loaded with a box-shaped phantom (σ=0.6 S/m, ε_r=80) - were carried out.

Fig. 4 shows the simulation results of the surface current density K=dI/dl and the surface current $|I|$ of a 1T1G coil (Fig. 4a) and a 2T5G coil (Fig. 4b) at their respective self-resonances f_0. The typical transmission line behavior can be observed for the inner conductor *iC* and the inner surface of the outer conductor *oCi*: the current on *iC* is the mirror current of the current on *oCi*, with a maximum at each outer gap and a zero at each inner gap. However, the current on *oCo*, which corresponds to the effective current

seen at a distance from the coil, is constant along the conductor.

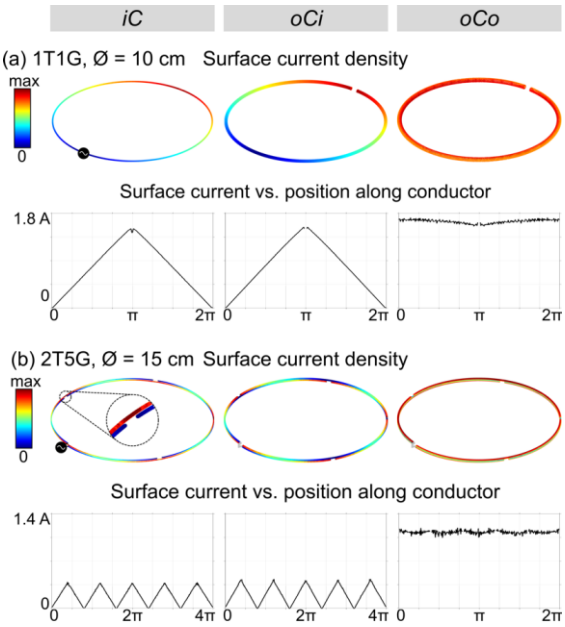

Fig. 4: Surface current density and surface current simulation results. Two representative simulation results are shown to depict the coaxial coils' behavior for **(a)** a single-turn single-gap (1T1G) and **(b)** a multi-turn multi-gap (2T5G) coil at their respective self-resonances f_0.

SAR simulations revealed that 7 T coaxial coils have comparable point SAR and SAR efficiency ($B_1^+/\sqrt{(}$max.10g SAR)) performance to standard coils but offer the advantage of flexibility. Fig. 5 shows the comparison of a 10 cm coaxial and standard coil which is representative for all simulations.

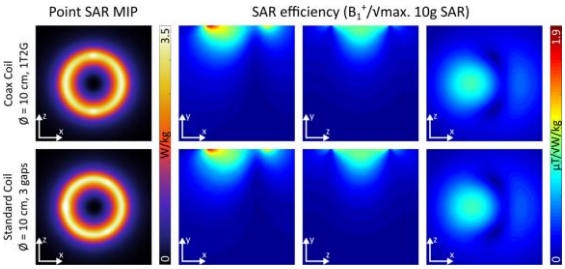

Fig. 5: Point SAR MIPS (maximum intensity projections) in the coronal plane and SAR efficiency maps (all planes) of a 10 cm coaxial and standard coil.

Experimental validation

Bench measurements of the coaxial coils' self-resonance frequency revealed a maximum deviation between the measured and calculated values of ±13.9 % which validates the equivalent circuit model for MTMG coaxial coils. *Q* factor measurements showed that the Q_u/Q_l ratio is generally lower for coaxial than for standard coils. At 3 T and 7 T, for both coil types, for different coil positioning (flat, bent) and different phantom volumes, the Q_u/Q_l ratios were always greater than 2, demonstrating coil operation in a sample noise dominated regime. Although mechanically robust against bending, power matching levels at the Larmor frequency of some coaxial coils had to be slightly readjusted in the bent position.

MRI experiments at 3 T revealed that sufficient decoupling between the whole-body Tx coil and Rx-only multi-gap coaxial coils was only achievable with an active decoupling circuit consisting of a set of PIN diodes placed at each inner gap and an RF choke connecting the outer gaps. At 3 T, the average SNR in a circular region of interest (ROI) is lower for coaxial coils than for standard coils in flat position. The use of a bent coaxial coil on a phantom compared to a flat standard coil results in a moderate SNR gain or slightly lower SNR in the same ROI. 2D Gradient echo MR images shown in Fig. 6 demonstrate the imaging performance of the coaxial coils bent to different types of fruit.

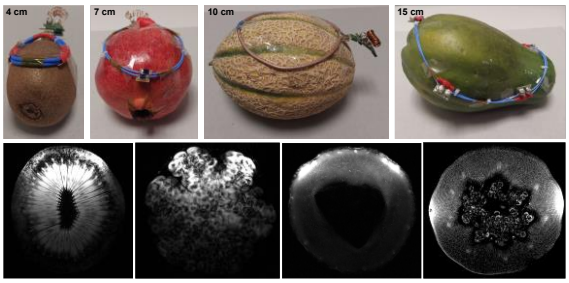

Fig. 6: MR images acquired at 3 T with coaxial coils of four sizes positioned on different fruit.

At 7 T, the transmit efficiency ($B_1^+/\sqrt{P}$) maps shown in Fig. 7a prove good comparability of coaxial and standard coils. Bent coaxial coils yield higher transmit efficiency than the flat standard coils. Calculated SNR maps (Fig. 7b) show a significant gain in average SNR in a circular ROI with a bent coaxial coil.

It was demonstrated that the proposed MTMG coaxial coil design presents a reliable flexible alternative to rigid standard copper wire coils. This coil design is especially suitable for applications where inter-patient variability of anatomy size is large and a conformal "one-size-fits-all" coil yields optimum SNR for most patients.

Wireless Data Transmission in MR

The sparse available literature reviewing the topic of wireless communication in MR was the initial motivation for the second part of this work (12): a comprehensive summary and analysis of the status quo of MR hardware develop

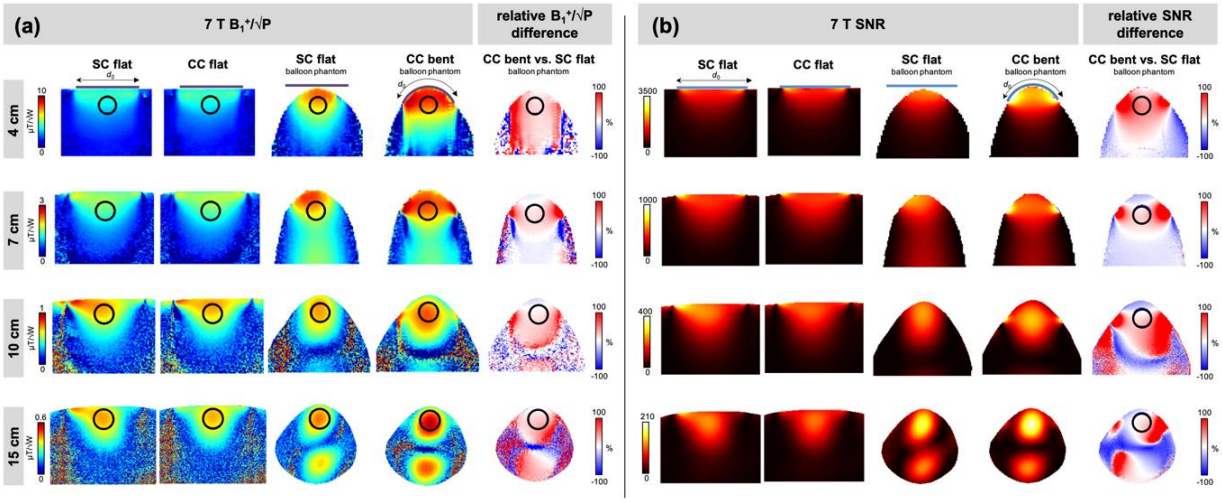

Fig.7: 7 T MRI results, **(a)** B1+/√P maps and **(b)** SNR maps in the central sagittal slice for the 4, 7, 10 and 15 cm SC and CC in flat position and the SC in flat and the CC in bent position, relative B1+/√P and SNR difference maps (CC vs. SC on balloon phantom).

ments related to wireless RF coils. This provides an overview of efficient strategies and an outlook on the feasibility of wireless RF coils in the future.

The focus was further put on the exploration of optical wireless communication (OWC) for use in MR. The implementation for motion sensor data transmission was the aim of preliminary tests with a custom-built OWC module prototype which is a first step towards future optical wireless signal transmission in the MR.

Perspectives in Wireless RF Coil Development

Several technological challenges are related to the development of wireless RF coils. The requirements for implementing a wireless system concern three important subsystems in the MR receive chain as depicted in Fig. 8a: wireless data (MR signals), control signals and power supply.

For RF signals of modern MRI setups (e.g., 3 T, 64 RF receive channels), with on-coil digitization and advanced methods for dynamic range (DR ≥ 16-bit) and data rate compression, still data rates > 500 Mbps are likely to be required. For wireless high-speed MR data transmission, e.g., 60 GHz technologies and OWC appear to be suitable strategies; however, on-coil functionality during MRI scans remains to be verified. Some wireless transceiver positioning variants are sketched in Fig. 8b. Besides RF signals, control signals for on-coil components, e.g., active detuning, synchronization to the MR system, and B_0 shimming for some applications, must be managed. Wireless power supply becomes an important issue, especially with a large amount of additional on-coil components. Wireless power transfer systems (>10 W) seem to be an attractive solution compared to bulky MR-compatible batteries and energy harvesting with low power output. In our opinion, completely wireless RF coils will ultimately become feasible in the future by combining efficient available strategies from recent scientific advances and novel research. Besides ongoing improvement of all three subsystems, innovations are specifically required regarding wireless technologies, MR compatibility, and wireless power supply.

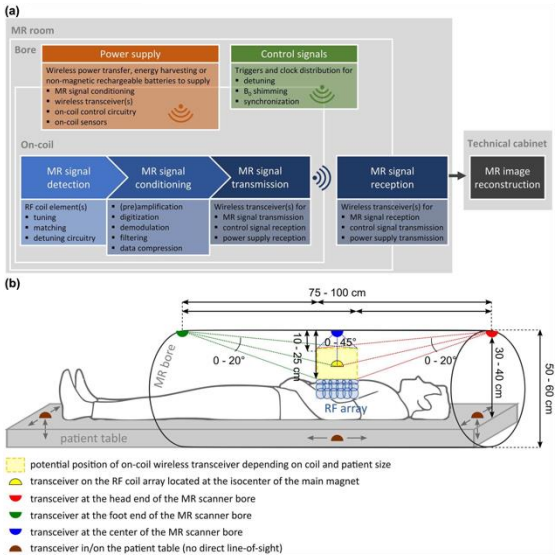

Fig.8: (a) Functional block diagram of a wireless MR receive chain consisting of three main subsystems: wireless MR signals (blue), control signals (green), and power supply (orange). **(b)** Side view of wireless transceiver positioning variants.

Development of an OWC module

Experimentally, an optical wireless communication module prototype was designed and fabricated using off-the-shelf optical components operating in the near infrared range together with a dedicated Tx and Rx circuitry, as schematically shown in Fig. 9. Preliminary tests revealed that the prototype modules can realize both short (0.3 m) and long (1.5 m) range optical

wireless communication. The maximum achievable data rate for reliable transmission over this range is 2 Mbps. The prototype performance accommodates different module positioning scenarios in the MR as shown in Fig. 8b. The achievable data rate covers the requirements for Manchester-encoded motion sensor signals, as developed by a collaborator in Nancy, France (13).

Fig. 9: Schematic of bidirectional communication between two optical wireless module prototypes, PD(s)…photodiode(s), LED(s)…light emitting diodes, RasPi…Raspberry Pi single board computer.

Conclusion

In conclusion, this thesis work presents the development and implementation of flexible RF coils based on coaxial transmission line resonator technology for 3 T MRI in Rx-only and 7 T MRI in Tx/Rx mode. The design concept relies on the extension to multiple coaxial cable turns and/or gaps enabling the construction of form-fitting coils of optimal size for a target penetration depth depending on the anatomical application. The flexible design yields optimal coil sensitivity and transmit efficiency when conformed to a bent shape and can be exploited in array configuration in the future. Together with their low weight and flexibility, and in combination with wireless motion sensors, coaxial coils could be an ideal building block for wearable coil arrays with increased diagnostic value in breast, knee, or cardiac MRI.

This work also includes a comprehensive review of the perspectives in wireless radio frequency coil development for MRI and gives an outlook on the future implementation of a custom-built optical wireless communication system in the MR environment.

References

1. Moser E, Meyerspeer M, Fischmeister FPS, Grabner G, Bauer H, Trattnig S. Windows on the Human body - in Vivo High-Field Magnetic Resonance Research and Applications in Medicine and Psychology. Sensors 2010;10:5724–5757 doi: 10.3390/s100605724.

2. Moser E, Stahlberg F, Ladd ME, Trattnig S. 7-T MR-from research to clinical applications? NMR Biomed. 2012;25:695–716 doi: 10.1002/nbm.1794.

3. Roemer PB, Edelstein WA, Hayes CE, Souza SP, Mueller OM. The NMR Phased Array. Magn. Reson. Med. 1990;16:192–225 doi: 10.1109/ICCOMM.2010.5509053.

4. Pruessmann KP, Weiger M, Scheidegger MB, Boesiger P. SENSE: sensitivity encoding for fast MRI. Magn. Reson. Med. 1999;42:952–962 doi: 10.1002/(SICI)1522-2594(199911)42:5<952::AID-MRM16>3.0.CO;2-S.

5. Pruessmann KP. Encoding and reconstruction in parallel MRI. NMR Biomed. 2006;19:288–299 doi: 10.1002/nbm.1042.

6. Sodickson DK, Manning WJ. Simultaneous acquisition of spatial harmonics (SMASH): Fast imaging with radiofrequency coil arrays. Magn. Reson. Med. 1997;38:591–603 doi: 10.1002/mrm.1910380414.

7. Katscher U, Börnert P, Leussler C, van den Brink JS. Transmit SENSE. Magn. Reson. Med. 2003;49:144–150 doi: 10.1002/mrm.10353.

8. Zhang B, Sodickson DK, Cloos MA. A high-impedance detector-array glove for magnetic resonance imaging of the hand. Nat. Biomed. Eng. 2018;2:570–577 doi: 10.1038/s41551-018-0233-y.

9. Frass-Kriegl R, Laistler E, Hosseinnezhadian S, et al. Multi-turn multi-gap transmission line resonators - Concept, design and first implementation at 4.7T and 7T. J. Magn. Reson. 2016;273:65–72 doi: 10.1016/j.jmr.2016.10.008.

10. Kumar A, Edelstein WA, Bottomley PA. Noise figure limits for circular loop MR coils. Magn. Reson. Med. 2009;61:1201–1209 doi: 10.1002/mrm.21948.

11. Nohava L, Czerny R, Roat S, et al. Flexible multi-turn multi-gap coaxial RF coils: design concept and implementation for Magnetic Resonance Imaging at 3 and 7 Tesla. IEEE Trans. Med. Imaging 2021;40:1267–1278 doi: 10.1109/TMI.2021.3051390.

12. Nohava L, Ginefri J-C, Willoquet G, Laistler E, Frass-Kriegl R. Perspectives in Wireless Radio Frequency Coil Development for Magnetic Resonance Imaging. Front. Phys. 2020;8:11 doi: 10.3389/fphy.2020.00011.

13. Chen B, Weber N, Odille F, et al. Design and validation of a novel MR-compatible sensor for respiratory motion modeling and correction. IEEE Trans. Biomed. Eng. 2017;64:123–133 doi: 10.1109/TBME.2016.2549272.

Acquisition and Reconstruction Algorithms for Highly Efficient Magnetic Resonance Imaging

Daniel Polak [1,2,3]

[1] Department of Physics and Astronomy, University of Heidelberg, Heidelberg, Germany
[2] Siemens Healthcare GmbH, Erlangen, Germany
[3] Department of Radiology, Martinos Center for Biomedical Imaging, Charlestown, MA, USA
* Daniel Polak. Email: daniel.m.polak@gmail.com

Synopsis: Wave CAIPI was implemented and optimized for its use across multiple clinical imaging contrasts which enabled the development of a 9-fold accelerated high-resolution 3D volumetric brain protocol A joint multi-contrast reconstruction framework was introduced which enables higher acceleration by leveraging shared anatomical information across multiple jointly reconstructed tissue contrasts. When combined with advanced acquisition techniques, this approach enables up to 16-fold acceleration for volumetric brain imaging which should help pave way to more routine usage of high-resolution volumetric brain protocols.

Motivation

In clinical brain imaging, typically multiple contrast preparations from the same region of interest are acquired, as these provide complementary diagnostic information. However, due to the slow encoding of MRI, the acquisition of several imaging sequences often leads to long exam durations. Shortening the acquisition time of MRI is an important field of research as it increases patient throughput, improves patient experience and compliance and reduces the chance of involuntary patient motion [1].

Parallel imaging techniques increase the acquisition speed and have been widely adopted into clinical imaging. However, in standard clinical 2D slice-by-slice imaging, these techniques are limited to 2-3-fold acceleration to avoid image artifacts and noise amplification. For 3D volumetric imaging, higher acceleration has been demonstrated using controlled aliasing techniques [2]. The Wave-CAIPI method [3] extends this concept to the full extent which at 3T has enabled up to R=9-fold acceleration for structural brain imaging using standard clinical scanner hardware. Recently, also the use of deep learning for inverse problem solving has found wide-spread attention. These techniques have outperformed state-of-the art parallel imaging and constrained reconstruction approaches thereby allowing higher accelerations for conventional 2D imaging [4].

In the light of these recent developments, the dissertation D. Polak *"Acquisition and Reconstruction Algorithms for Highly Efficient Magnetic Resonance Imaging"* introduces novel acquisition and reconstruction algorithms that dramatically reduce the acquisition time of 3D brain scans. Very rapid volumetric imaging was facilitated by optimizing the Wave-CAIPI acquisition strategy, along with a novel deep learning reconstruction approach that leverages shared anatomical information across multiple clinical imaging contrasts.

Materials and Methods

Wave-CAIPI plays sinusoidal gradients during the readout to create a corkscrew trajectory in k-space (Fig. 1a). This causes a voxel spreading effect along the readout (x) direction in image space which varies linearly as a function of the spatial y and z coordinates. In an accelerated acquisition, this voxel spreading adds controlled aliasing along the readout and hence supplements the controlled aliasing from 2D-CAIPIRINHA (Fig. 1b).

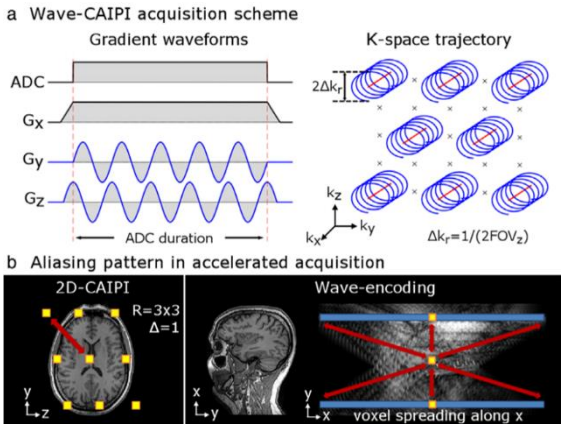

Fig. 1: a) In Wave-CAIPI two sinusoidal gradients played during the readout create a corkscrew trajectory in k-space. This introduces a voxel spreading (controlled aliasing) effect along the readout (x) which varies linearly as a function of the spatial y and z coordinates. b) The combined controlled aliasing effect form 2D CAIPI and Wave-encoding increases the distance between collapsing voxels along all three spatial dimensions (red arrows) which allows full use of the 3D sensitivity profile.

In this work, the Wave-CAIPI acquisition strategy was optimized to ensure robust, high quality imaging across multiple clinical imaging sequences. For this purpose, a framework to design and optimize the Wave k-space trajectory was created. In particular, the Wave corkscrew design parameters (gradient amplitude and number of sinusoidal cycles) and their effect on the voxel spreading/coupling along the readout were characterized. Moreover, interactions between the Wave corkscrew and potential signal modulation along the echo train due to T1 and T2 relaxation was analyzed as this can introduce ringing/blurring artifacts in Wave-CAIPI reconstructions. The Wave-CAIPI acquisition strategy was implemented into MPRAGE, SPACE and GRE/SWI to provide the principal clinical contrasts T1, T2, T2-FLAIR and T2*/SWI. Based on the findings from Fig. 4, each acquisition was optimized for rapid imaging at R=9-fold acceleration which resulted in a total acquisition time of 6 min for whole brain coverage at 1 mm³ isotropic resolution.

For highly time sensitive and/or motion prone clinical situations even faster brain exams may be needed. This can be achieved through higher acceleration however, this will likely cause unacceptable noise amplification due to the intrinsic √R noise penalty. For this purpose, a new reconstruction method was developed in this work which utilizes prior information and exploits shared anatomical structures across multiple clinical tissue contrasts that are commonly acquired in clinical brain exams. Based on the variational network architecture [4], a framework for multi-contrast reconstructions is introduced. As demonstrated in Fig. 2, the variational network (VN) employs an unrolled gradient descent optimization to perform the parallel imaging reconstruction. Each descent step (GD) contains a data fidelity term and a learnt regularizer which is composed of convolutional filters k and learnt activation functions ϕ. In the proposed joint variational network (jVN) data from multiple clinical contrasts are reconstructed jointly. This is achieved by mixing the different input contrasts $\vec{u}$ in the convolutional filters k thus allowing shared anatomical information to be exchanged. Moreover, the proposed network architecture was synergistically combined with advanced acquisition techniques (Wave-CAIPI and complementary k-space sampling) to support the reconstruction at very high acceleration. Supervised training was performed across T1, T2 and T2-FLAIR weighted data from nine healthy subjects using R=4x4 acceleration (retrospective undersampling). For testing, data with prospective acceleration (R=16) was obtained from separate subjects and jVN was compared against VN and standard SENSE.

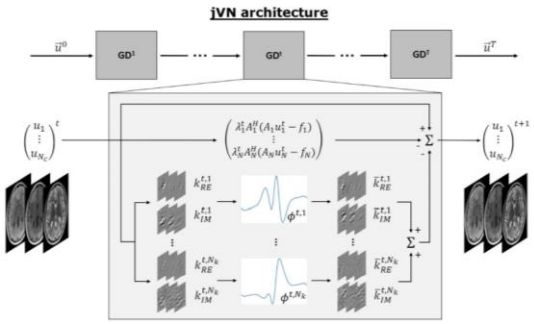

Fig. 2: jVN is based on the variational network architecture [4] and employs unrolled gradient descent (GD) optimization that includes learnt regularizers and data fidelity. The multi-contrast regularizer contains convolutional filters k that mix the different input contrasts $\vec{u}$. This allows shared anatomical information to be exchanged. Non-linear activation ϕ and transposed filter kernels $\bar{k}$ transform the generated feature channels to the original input contrasts. Data-fidelity is computed for each input contrast individually and is weighted by a learnt regularization parameter λ.

Results

In Fig. 4a the voxel spreading/coupling effect is demonstrated for various Wave corkscrew parameters. As can be seen, the extent of voxel spreading is governed by the amplitude of the sinusoidal Wave gradients. In contrast, the number of cycles dictates the spacing between coupled readout voxels. However, as evidenced by the roughly constant g-factor as a function of the number of cycles (Fig. 4b), the spacing between coupled voxels does not seem to impact controlled aliasing as much as the extent of voxel spreading.

Figure 5 shows example reconstructions of the developed 6-minute Wave-CAIPI whole-brain exam. The isotropic resolution (1x1x1 mm³) allows each scan to be reformatted and viewed in arbitrary orientations. Despite 9-fold acceleration, all scans provided good SNR and high image quality as reflected by the negligible average g-factor (g_{avg} ≤ 1.04).

The joint variational network was introduced to achieve beyond R=9-fold acceleration where standard parallel imaging typically exhibits large noise amplification and artifacts due to insufficient encoding capability (c.f. SENSE in Fig. 6). In contrast, the variational network reconstructions achieved much better image quality at R=16-fold acceleration, however, the proposed multi-contrast approach (jVN+Wave) better preserved fine anatomical details (red arrows) and resulted in fewer parallel imaging artifacts than the standard single-contrast network (VN). Moreover, the example reconstructions in Fig. 6 show that the scan-specific contrast is retained in jVN despite the mixing of tissue contrasts.

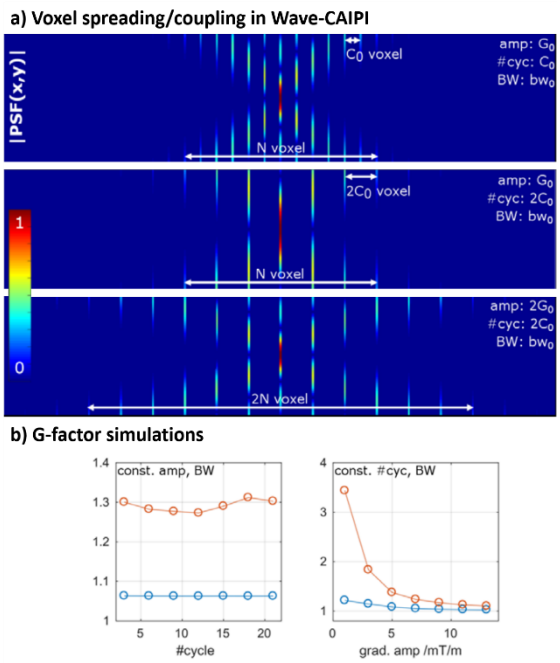

Fig. 3: (a) The Wave point spread function |PSF(x,y)| demonstrates the discrete voxel spreading/coupling along the readout direction that is caused by the sinusoidal Wave gradients. The number of cycles determines the spacing between coupled voxels while the Wave's gradient amplitude controls the extent of spreading (b) To a good approximation, the g-factor is independent of the voxel coupling (#cycles) but mainly controlled by the extent of voxel spreading (gradient amplitude).

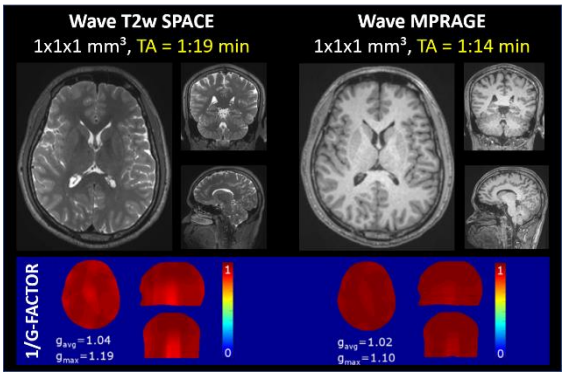

Fig. 4: Example Wave reconstructions for T2w SPACE and MPRAGE at R=9-fold acceleration. Inverse g-factor maps are reported in the bottom of the figure. Example reconstructions for SPACE-FLAIR and SWI are available in [5].

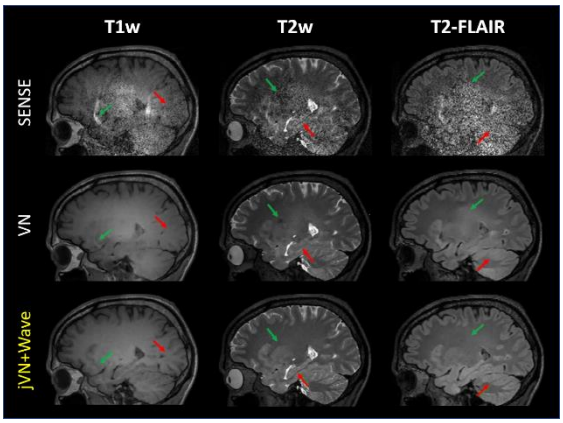

Fig. 5: At R=16, SENSE results in unacceptable SNR due to the intrinsic √R and g-factor noise penalty. Both deep learning reconstructions prevented large noise enhancement however, the proposed jVN+Wave better preserved fine anatomical details (red arrows) and resulted in fewer artifacts (green arrows) than the single-contrast VN.

Discussion

In this work, novel acquisition and reconstruction algorithms were developed which dramatically reduced the acquisition time for high-resolution 3D volumetric brain imaging.

The recently proposed Wave-CAIPI encoding extends controlled aliasing to the full extent which increases the encoding capability at high acceleration. However, sequence specific optimization of the corkscrew k-space trajectory is required to ensure high quality imaging. For this reason, an intuitive framework to optimally choose the Wave acquisition parameters was developed in this work. Extensive simulations have shown that the amount of controlled aliasing (~g-factor) is mainly given by the extent of voxel spreading (Wave gradient amplitude) and to a good approximation is independent of the spacing between coupled voxels (#cycles). This can be explained intuitively as the gradient amplitude determines the slope of the sinusoidal phase modulation along k_x which in turn controls the extent of voxel spreading along the readout (x). This controlled aliasing/ voxel spreading effect is directly correlated to the g-factor performance as evidenced by extensive simulations in this work. In contrast, increasing the number of cycles (at fixed gradient amplitude) only changes the radius of the k-space corkscrew, and since the slope of phase modulation remains unchanged in this situation, there is no associated g-factor improvement.

Wave-CAIPI was implemented into three clinical imaging sequences and each acquisition protocol was optimized individually to minimize g-factor noise amplification and blurring artifacts that can arise from the coupling of the Wave corkscrew and signal modulations due to T1/T2 relaxation (c.f. [5] for details). In a small clinical

study, the resulting six-minute whole-brain exam was then evaluated on healthy volunteers and patients and compared against a conventional roughly 3x slower GRAPPA accelerated exam where comparable diagnostic image quality was obtained [5]. It is thus expected that the rapid 3D brain exam developed in this work will provide several advantages over previous accelerated brain exams that rely on conventional 2D imaging. The highly efficient Wave encoding allows high resolution scans with mostly isotropic resolution to be acquired within short scan time. Moreover, the high-through plane resolution should help increase the diagnostic information as thick-slices and slice gaps can be avoided. Ultimately, the isotropic resolution eliminates the need for reacquisition in different planes, as the Wave-CAIPI scans can be reformatted and viewed in arbitrary orientations.

Achieving beyond R=9-fold acceleration is challenging due to the intrinsic $\sqrt{R}$ SNR penalty from k-space under-sampling. To overcome large noise amplification, additional regularization needs to be included into the Wave-CAIPI reconstruction which has been previously achieved using Compressed Sensing (CS) [6] and LORAKS [7]. In this work, a highly efficient regularizer was obtained by combining deep learning with a multi-contrast reconstruction approach that exploits shared/redundant anatomical information across multiple tissue contrasts. This approach helped to overcome large SNR loss and parallel imaging artifacts at high acceleration. Moreover, it achieved better image quality than previous multi-contrast implementations using CS [8] as these methods relied on handcrafted regularizes that did not sufficiently capture the complex contrast differences across the jointly reconstructed scans (cf. [9]).

To further improve the conditioning of the multi-contrast parallel imaging reconstruction, jVN was also combined with advanced acquisition techniques. The synergistic combination enabled up to 16-fold acceleration for whole brain 3D volumetric imaging at 1 mm³ isotropic resolution thus allowing T1, T2 and T2-FLAIR weighted data to be obtained in under three minutes of scan time. These developments should help pave the way for more routine usage and deployment of very rapid high resolution 3D brain exams.

Conclusion

By enabling an order of magnitude acceleration for clinical brain exams the developed technologies are anticipated to benefit patient diagnosis and prognosis.

References

[1] M. Zaitsev, J. Maclaren, and M. Herbst, “Motion artifacts in MRI: A complex problem with many partial solutions,” *J. Magn. Reson. Imaging*, vol. 42, no. 4, pp. 887–901, 2015, doi: 10.1002/jmri.24850.

[2] F. A. Breuer *et al.*, “Controlled aliasing in volumetric parallel imaging (2D CAIPIRINHA),” *Magn. Reson. Med.*, vol. 55, no. 3, pp. 549–556, 2006, doi: 10.1002/mrm.20787.

[3] B. Bilgic *et al.*, “Wave-CAIPI for highly accelerated 3D imaging,” *Magn. Reson. Med.*, vol. 73, no. 6, pp. 2152–2162, 2015, doi: 10.1002/mrm.25347.

[4] K. Hammernik *et al.*, “Learning a variational network for reconstruction of accelerated MRI data,” *Magn. Reson. Med.*, vol. 79, no. 6, pp. 3055–3071, 2018, doi: 10.1002/mrm.26977.

[5] D. Polak *et al.*, “Highly-accelerated volumetric brain examination using optimized wave-CAIPI encoding,” *J. Magn. Reson. Imaging*, vol. 50, no. 3, pp. 961–974, 2019, doi: 10.1002/jmri.26678.

[6] B. Bilgic, H. Ye, L. L. Wald, and K. Setsompop, “Optimized CS-Wave imaging with tailored sampling and efficient reconstruction,” in *Proceedings of ISMRM 24th Annual Meeting*, 2016, p. 0612, [Online]. Available: https://cds.ismrm.org/protected/16MPresentations/abstracts/0612.html.

[7] T. H. Kim, B. Bilgic, D. Polak, K. Setsompop, and J. P. Haldar, “Wave-LORAKS: Combining wave encoding with structured low-rank matrix modeling for more highly accelerated 3D imaging,” *Magn. Reson. Med.*, vol. 81, no. 3, pp. 1620–1633, 2019, doi: 10.1002/mrm.27511.

[8] B. Bilgic, V. K. Goyal, and E. Adalsteinsson, “Multi-contrast reconstruction with Bayesian compressed sensing,” *Magn. Reson. Med.*, vol. 66, no. 6, pp. 1601–1615, 2011, doi: 10.1002/mrm.22956.

[9] D. Polak *et al.*, “Joint multi-contrast variational network reconstruction (jVN) with application to rapid 2D and 3D imaging,” *Magn. Reson. Med.*, vol. 84, no. 3, pp. 1456–1469, 2020, doi: 10.1002/mrm.28219.

Talks
(V1-V24)

A novel phantom for realistic dynamic flow and wall shear stress measurements in a human aneurysm model

Patrick Winter[1, 2*], Michael Seeg [1], Teresa Reichl[1], Thomas Kampf[1, 3], Stefan Herz[4], Kristina Andelovic[2, 5], Wolfgang Rudolf Bauer[2], Peter Michael Jakob[1], Volker Herold[1] and Patrick Vogel[1]

[1] Experimental Physics V, University of Wuerzburg, Wuerzburg, Germany.
[2] Medical Clinic and Policlinic I, University Clinics Wuerzburg, Wuerzburg, Germany.
[3] Diagnostic and Interventional Neuroradiology, University Clinics Wuerzburg, Wuerzburg, Germany.
[4] Diagnostic and Interventional Radiology, University Clinics Wuerzburg, Wuerzburg, Germany.
[5] Institute for Experimental Biomedicine, University Clinics Wuerzburg, Wuerzburg, Germany.
* Corresponding author

Synopsis: 4D flow MRI is useful to examine the fluid dynamics in complex vessel geometries. In particular measurements in 3D printed vascular phantoms are beneficial since they allow studies of the complicated flow-related interrelations causing the development of pathologies and also provide a quality control for the development of more realistic vascular phantoms. Self-navigated phase contrast techniques are especially beneficial since they allow retrospective measurements of the flow velocity fields and wall shear stress without the need of additional triggering hardware.

Zusammenfassung: 4D-Flow-MRT ist nützlich, um die Strömungsdynamik in komplexen Gefäßgeometrien zu untersuchen. Insbesondere Messungen an 3D-gedruckten Gefäßphantomen sind von Vorteil, da sie die Untersuchung der komplizierten strömungsbezogenen Zusammenhänge, die die Entstehung von Krankheiten bedingen, ermöglichen und auch eine Qualitätskontrolle für die Entwicklung realistischerer Gefäßphantome bieten. Selbstnavigierte Phasenkontrasttechniken eignen sich besonders, da sie retrospektive Messungen der Geschwindigkeitsfelder und der Wandschubspannung ohne zusätzliche Trigger-Hardware ermöglichen.

Motivation

Flow measurements using 4D phase contrast (PC) magnetic resonance imaging (MRI) are a versatile tool to examine the hemodynamics of complex vessel geometries such as the aortic arch or aneurysms. In addition, the use of realistic vessel phantoms in combination with pulsatile flow has great potential to study the complicated fluid dynamics and the mechanisms leading to pathological changes under controlled conditions. In particular self-gated radial PC MRI offers some advantages since the MRI signal can also be used for synchronization of the measurement with the flow pump. Recently a radial sequence for high-resolution 4D flow measurements in the murine aortic arch was presented. This method enabled the calculation of wall shear stress (WSS) maps without the need of ECG probes [1]. In this abstract, we demonstrate the use of this technique in a completely different environment, i.e. a 3D printed vessel phantom and a flow pump providing pulsatile flow.

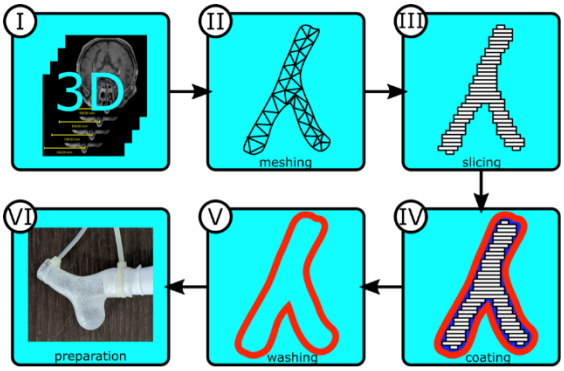

Fig. 1: From 3D data to flow phantom: the 3D data (I) are used for extraction of desired vessel region (II – meshing). The STL file is printed with a water-solvable filament (PVA) (III – slicing) and coated with xylitol and silicone (IV – coating). After washing out the PVA and xylitol (V – washing), the phantom can be prepared for experiment (VI – preparation).

Materials and Methods

Vessel phantom

The fabrication of the vascular phantoms was performed in several steps as indicated in Fig. 1 [2]. After data acquisition (Fig.1.I), the desired vessel structure is extracted from a high-resolution isotropic 3D CT/MRI dataset using a dedicated framework for vessel wall extraction (Fig.1.II) [3]. The converted STL file of the desired vessel was printed as a solid model using polyvinyl alcohol (PVA) filament (Fig.1.III) printed with desktop 3D printer. In a next step, the phantom was coated with small layer of xylitol and finally casted with two layers of silicone (~2mm thickness, shore hardness A32) (Fig.1.IV). The vascular phantom was immersed in water after silicone coating became

completely hardened. The PVA model and xylitol coating should melt into water (Fig.1.V). Finally, the phantom was prepared for flow experiments (Fig.1.VI).

Flow pump

For the flow measurements a flow pump is used, which provides either constant or pulsatile flow. For the pulsatile flow measurements, the pumping cycle is adjusted to a period of 1s (0.5s pumping, 0.5s waiting period) with a peak flow value of 3000 ml/minutes. For the constant flow setting, the flow is set to 1500ml/minutes. $CuSo_4$-doped water (concentration: 0.5%) is used as medium.

MRI measurements

All experiments are conducted in a 7T small animal MRI system with a 470mT/m gradient system, a 72mm quadrature transmit birdcage and a custom self-gated radial 4D phase contrast cine MRI sequence using a balanced 4-point flow-encoding scheme. The scan parameters are: TR/TE: 10.0/1.8ms, flip angle 20°, $5.9x10^3$ radial projections, encoding velocity: 125cm/s. The total scan time is 39 minutes. Self-navigation signals are extracted from the center k-space signal and trigger time stamps are calculated with thresholds for the subsequent retrospective reconstructions (see Fig.2). For each flow-encoding step, a 3D-cine with 20 movie frames and an isotropic resolution of 167µm, respectively, is reconstructed.

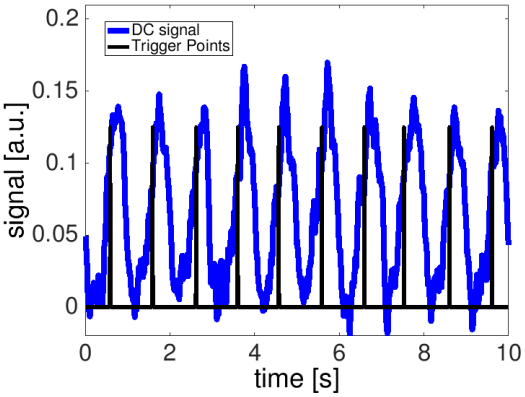

Fig. 2: Radial DC signal used for self-navigation (blue) and the trigger time stamps used for the retrospective cine reconstruction (black).

Wall shear stress

The phantom is segmented using the magnitude data and a threshold-based segmentation. The velocity components are calculated from the phase differences of the 4 flow-encoded cines and the wall shear stress is derived from the spatial gradients of the velocity fields at the vessel wall, as described in [1]. A viscosity value of 0.001Pas is used for the WSS calculations.

Results

Flow Measurements

Flow was measured in vascular phantoms using the constant flow mode of the flow pump. Fig.3 displays a streamline representation of the flow through the vessel, indicating the direction and magnitude of the velocities. Near the bottleneck of the phantom an increase of the flow values is observable. In the bulge, large eddy currents are prominent.

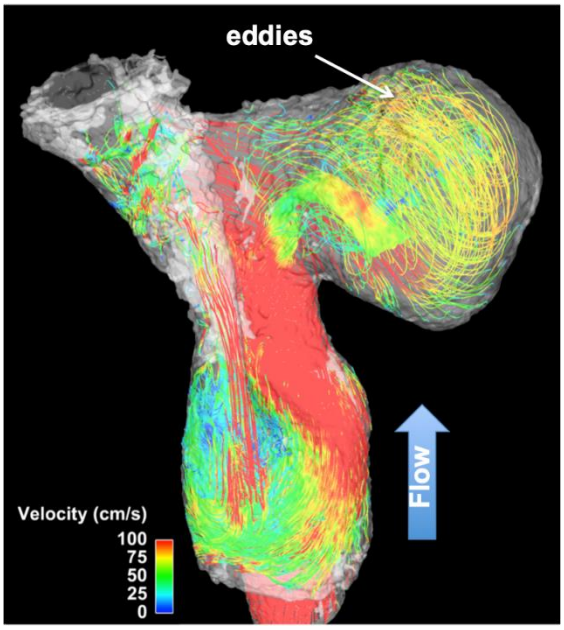

Fig. 3: Streamline visualization of the flow through the aneurysm phantom (constant flow mode: 1500ml/min).

Fig.4 shows volume renderings of the peak flow through the vascular phantom during the pulsatile pumping mode. Two different connection directions were examined. The results indicate significant differences in the flow characteristics inside the bulge depending on the orientation of the vascular phantom.

Wall shear stress

WSS values were determined from the time-dependent velocity fields. Fig.5 displays mean WSS maps averaged over the pumping cycle. The results show distinct differences in the WSS distribution depending on the orientation of the connections.

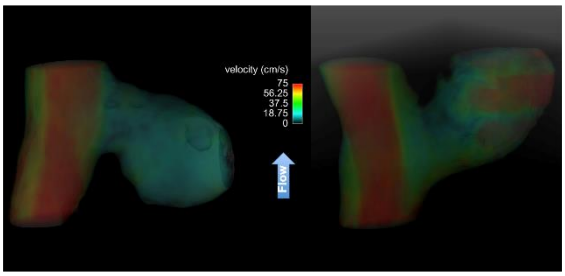

Fig. 4: Volume rendering of the peak flow through the vessel phantom (pulsatile mode). Two different connection directions were examined.

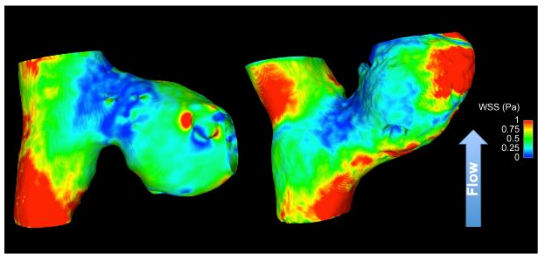

Fig. 5: Temporally averaged wall shear stress maps obtained from the cine reconstructions. Two different orientations of the aneurysm phantom were examined.

Discussion and Conclusion

This abstract demonstrates the feasibility of self-navigated flow and WSS measurements in 3D printed aneurysm phantoms. This technique can be used to study the complex fluid dynamics under controlled environments. It has great potential for preclinical studies of the formation mechanics of arterial aneurysms and can be used to study the influence of parameters such as geometry and elasticity on the WSS distribution. Furthermore this *in vitro* platform provides a potential tool to optimize the flow-encoding sequence for subsequent *in vivo* measurements and for a quality control for the development of more realistic vascular phantoms.

Acknowledgements

This work was funded by the Deutsche Forschungsgemeinschaft (SFB1158 A10, ZE827/15–1, BA 1069/14–1, HA 7152/8–1, HE 7108/3–1), the Bundesministerium für Bildung und Forschung (BMBF01, E01004), the University of Wuerzburg in the funding program Open Access Publishing and the Comprehensive Heart Failure Center (Deutsches Zentrum für Herzinsuffizienz).

References

1. Winter, Andelovic et al., Fast self-navigated wall shear stress measurements in the murine aortic arch using radial 4D phase contrast cardiovascular magnetic resonance imaging at 17.6T, JCMR, 2019

2. Guggenberger et al., High-resolution Compressed-sensing T_1 Black-blood MRI, Clin Neuroradiol, 2019.

3. Liu et al., Fabrication of cerebral aneurysm simulator with a desktop 3D printer, Sci Rep, 7:44301, 2016.

Über die Messung der Porenverteilungsfunktion und das Erscheinen von Signal-Peaks bei Verwendung langer Diffusionsgradienten

C.M. Stuprich[1*], T.A. Kuder[2], B. Hensel[3], M. Uder[1], F.B. Laun[1]

[1] Radiologisches Institut, Universitätsklinikum Erlangen, Friedrich-Alexander-Universität Erlangen-Nürnberg (FAU), Erlangen, Deutschland
[2] Medizinische Physik in der Radiologie, Deutsches Krebsforschungszentrum (DKFZ), Heidelberg, Deutschland.
[3] Zentrum für Medizinisches Physik und Technik, Friedrich-Alexander-Universität Erlangen-Nürnberg (FAU), Erlangen, Deutschland
* Christoph Stuprich, Universitätsklinikum Erlangen, Maximiliansplatz 3, 91054 Erlangen, Deutschland, christoph.stuprich@uk-erlangen.de

Zusammenfassung: In der Diffusions-MR sind für kurze Gradientenpulse oszillierende Signalkurven und Signal-Peaks in zahlreichen Arbeiten beschrieben worden. Diese charakteristischen Oszillationen oder „Peaks“ im Signal entstehen, wenn eine charakteristische Längenskala in der untersuchten Probe vorhanden ist. Mitra und Halperin erwähnen die Möglichkeit (2), dass „Bragg ähnliche“ Signal-Peaks auch bei langen Gradientenpulsen vorkommen können. In dieser Arbeit werden diese Signalpeaks bei Verwendung langer Diffusionsgradienten in Theorie und Simulation explizit aufgezeigt und interpretiert.

Motivation

In der diffusionsgewichteten Bildgebung werden üblicherweise „lange“ Diffusionsgradientenpulse verwendet, d.h. es gilt $D\delta \gg L^2$, wobei D der freie Diffusionskoeffizient, δ die Dauer der Diffusionsgradienten und L die typische Längenskala der Diffusionsrestriktionen ist (z.B. der Zelldurchmesser).

Die Verwendung kurzer Gradientenpulse (also $D\delta \ll L^2$) ist aufgrund der technisch limitierten Gradientenamplitude schwer erreichbar, da die Diffusionswichtungsstärke, d.h. der b-Wert, proportional zu $G^2\delta^2$ ist. Nichtsdestotrotz ist das Limit kurzer Gradientenpulse mit manchen Gerätekonfigurationen erreichbar und zeigt interessante Eigenschaften (2). Die Diffusionsbewegung während der kurzen Gradientenpulse kann vernachlässigt werden und dadurch kann der volumengemittelte Diffusionspropagator gemessen werden (1, 3).

Im Langzeitlimit, d.h. im Limit großer Zeitabstände Δ zwischen den diffusionswichtenden Gradientenpulsen, ist der Diffusionspropagator in vielen Fällen eng mit der Gewebestruktur verknüpft. Zusätzlich besteht eine Fourier-Relation zwischen dem Diffusionspropagator und dem gemessenen Signal (1). Falls daher eine wohldefinierte Längenskala L der Diffusionsrestriktionen in der Probe existiert, weist das gemessene Signal oft charakteristische Oszillationen oder „Peaks“ auf, die es ermöglichen Aussagen über die Diffusionsrestriktionen zu treffen.

Bei langen Diffusionsgradienten wurde nach Kenntnisstand der Autoren die Existenz solcher Charakteristika, insbesondere von Peaks, bisher nicht in Simulationen oder experimentell nachgewiesen. In dieser Arbeit wird theoretisch und in Simulationen anhand einer einfachen Modellgeometrie gezeigt, dass Peaks auch bei Verwendung langer Diffusionsgradientenpulse auftreten und Informationen über die vorhandenen Diffusionsrestriktionen liefern können.

Theorie

Bei langen Gradientenpulsen kann nach Mitra und Halperin das diffusionsgewichtete Signal durch

$$S(\boldsymbol{q}) = \langle exp\left(-i\boldsymbol{q}\cdot\left(\boldsymbol{x}_{cm,2}-\boldsymbol{x}_{cm,1}\right)\right)\rangle \qquad (1)$$

beschrieben werden mit $\boldsymbol{q} = \gamma G\delta$, wobei angenommen wird, dass bipolare Gradientenpulse der Amplitude G und der Dauer δ zur Diffusionswichtung verwendet werden (2). $\boldsymbol{x}_{\mathrm{cm},1}$ and $\boldsymbol{x}_{\mathrm{cm},2}$ sind die Schwerpunkte der Teilchentrajektorien während des ersten und zweiten Gradientenpulses und die spitzen Klammern zeigen die Mittelung über alle Teilchen an (vgl. Abb. 1).

Im Limit $\delta \to 0$ gilt $\boldsymbol{x}_{\mathrm{cm},1} \to \boldsymbol{x}_1$ und $\boldsymbol{x}_{\mathrm{cm},2} \to \boldsymbol{x}_2$, wobei $\boldsymbol{x}_1$ und $\boldsymbol{x}_2$ Anfangs- und Endpunkt der Teilchentrajektorien sind. Für $\Delta \gg L^2/D$ gilt bei geschlossenen Poren (bzw. Zellen)

$$S(\boldsymbol{q}) = |\tilde{\chi}(\boldsymbol{q})|^2, \qquad (2)$$

wobei $\tilde{\chi}(\boldsymbol{q})$ die Fourier-Transformierte der Porenfunktion $\chi(\boldsymbol{r})$ ist, welche innerhalb der Pore gleich 1 und außerhalb der Pore gleich 0 ist (1). $|\tilde{\chi}(\boldsymbol{q})|^2$ weist in diesem Fall Oszillationen im q-Raum auf, deren Länge mit L^{-1} skaliert.

Bei endlicher Membran-Permeabilität können die Teilchen die Poren verlassen und Gleichung (1) kann im Limit $\delta > L^2/D$ und $\delta \approx \tau \ll \Delta$ verallgemeinert werden, wobei τ die mittlere Aufenthaltsdauer in einer Pore ist:

$$S(\boldsymbol{q}) \approx \sum_{n,m} P_{n,m}(\Delta) \exp\left(i\boldsymbol{q} \cdot \left(\boldsymbol{x}_{\mathrm{cm,Pore},n} - \boldsymbol{x}_{\mathrm{cm,Pore},m}\right)\right)$$

mit dem Massenschwerpunkt $x_{\mathrm{cm,Pore},m}$ der m-ten Pore. $P_{n,m}(\Delta)$ ist die Wahrscheinlichkeit, dass ein Teilchen von der Pore n in die Pore m wandert. Da alle Poren äquivalent sein sollen und nur Translationen wichtig sind, kann $n = 0$ und $\boldsymbol{x}_{\mathrm{cm,pore},n} = 0$ gesetzt werden:

$$S_{n=0}(\boldsymbol{q}) \approx \textstyle\sum_m P_m(\Delta) \exp\left(-i\boldsymbol{q} \cdot \boldsymbol{x}_{\mathrm{cm,Pore},m}\right) \quad (3)$$

Somit, und das ist der wichtigste Punkt dieser Arbeit, kann die Fourier-Transformierte der Porenverteilungsfunktion gemessen werden.

Methoden

Das Signal bei Verwendung langer Diffusionsgradienten wurde durch „Random Walk" Simulationen in einer Modellgeometrie aus unendlich vielen unendlich ausgedehnten parallelen Platten untersucht (Abb. 1). Für diese Modellgeometrie ist $S_{n=0}(q)$ ein Dirac-Delta-Kamm, der mit $P_m(\Delta)$ moduliert wird. Die Dirac-Delta-Funktionen haben einen Abstand von $2\pi L^{-1}$. Folgende Simulationsparameter wurden verwendet: Abstand der Platten L = 10 µm, D = 2 µm²/ms, δ = 0.1 und 50 ms, Δ = 300 ms, Membranpermeabilität ρ = 0, 0.005 und 0.05 µm/ms, Zahl der Schritte = 1 000, Schrittweite = 0.04 µm, Zahl der Teilchen = 100 000.

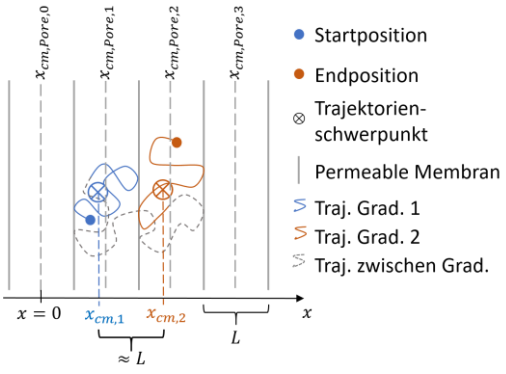

Abb. 1: Visualisierung der Trajektorien in der untersuchten Modellgeometrie.

Ergebnisse

Bei Verwendung der langen Diffusionsgradienten entstehen in der simulierten Modellgeometrie Signalpeaks bei Vielfachen von $q = 2\pi L^{-1}$, d.h. der Dirac-Delta-Kamm wird sichtbar (siehe Abb. 2). Es gibt einerseits eine Linienverbreiterung (weil die Näherung $x_{\mathrm{cm}} \rightarrow x_{\mathrm{cm,Pore}}$ nicht perfekt gilt) und eine Einhüllende (weil die Teilchen nicht das ganze Gitter abgetastet haben).

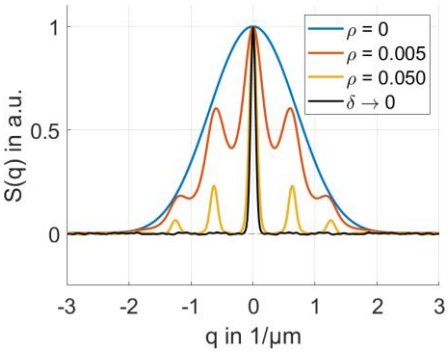

Abb. 2: Signalpeaks entstehen nur bei endlicher Permeabilität und nur für lange Gradientenpulse. Die schwarze Kurve zeigt zum Vergleich das normierte Signal bei ρ = 0.05 µm/ms für Gradientenpulse mit δ = 0.1 ms.

Diskussion

Das Auftreten von Signalpeaks für kurze Gradientenpulse ist wohlbekannt (1,2,3). Für lange Gradientenpulse erwähnen Mitra und Halperin, dass Bragg-Interferenz-ähnliche Peaks auftreten können (2). In unserer Arbeit wird explizit gezeigt, dass die Signalpeaks auch bei langen Gradienten auftreten können.

Sowohl bei kurzen als auch bei langen Gradientenpulsen treten Peaks nur bei periodischer Anordnung der Zellen auf, Gl. (3) gilt jedoch auch bei nicht-periodischer Anordnung.

Schlussfolgerung

Bei langen Gradientenpulsen liefert der Anteil der Teilchen, die sich während der beiden Gradientenpulse in (näherungsweise) geschlossenen Poren aufhalten in den Limits $\delta > L^2/D$ und $\delta \approx \tau \ll \Delta$ ein diffusionsgewichtetes Signal, das der Fourier-Transformierten der Zellenverteilungsfunktion entspricht.

Referenzen

1. Callaghan PT, Coy A, MacGowan D, Packer KJ, Zelaya FO. Diffraction-like effects in NMR diffusion studies of fluids in porous solids. *Nature*. 1991;351(6326):467-469

2. Mitra, PP, Halperin BI. Effects of finite gradient-pulse widths in pulsed-field-gradient diffusion measurements. *Journal of Magnetic Resonance, Series A*. 1995;*113*(1), 94-101

3. Grebenkov DS. NMR survey of reflected Brownian motion. *Reviews of Modern Physics*. 2007;*79*(3), 1077

4D-flow background phase correction using M-estimate SAmple Consensus (MSAC)

Carola Fischer,[1,2*] Jens Wetzl,[2] Tobias Schäffter[1,3,4] und Daniel Giese[2]

[1] Department of Medical Imaging, Technical University of Berlin, Berlin, Germany.
[2] Magnetic Resonance, Siemens Healthcare GmbH, Erlangen, Germany.
[3] Physikalisch-Technische Budensanstalt (PTB), Braunschweig and Berlin, Germany.
[4] School of Imaging Sciences and Biomedical Engineering, King's College London, London, United Kingdom
* carola.fischer@siemens-healthineers.com

Synopsis: In 4D-flow imaging, background phase correction is necessary to correctly quantify velocities. However, conventional stationary tissue correction suffers from wrap-around artifacts distorting correction fits. We propose the M-estimate SAmple Consensus (MSAC) algorithm to automatically reject outliers like wrap-around and correct efficiently for background phase errors. In this abstract, we show the feasibility of M-estimate sample consensus on 4D-flow data and its benefits when correcting images with wrap-around artefacts.

Zusammenfassung: Eine Hintergrundphasenkorrektur in der 4D-Flussbildgebung ist notwendig, um Geschwindigkeiten akkurat bestimmen zu können. Hierfür wird eine Funktion auf statisches Gewebe gefittet und von dem Bild abgezogen. Allerdings werden bei der Detektion statischen Gewebes auch Einfaltungen akzeptiert, was zu falschen Korrekturen führt. Wir schlagen daher vor, Ausreißer mit Hilfe von M-Estimate Sample Consensus zu ermitteln und vom Fit auszuschließen. In diesem Abstract zeigen wir, dass M-Estimate Sample Consensus auf 4D-Flussaufnahmen möglich ist, und dass die Korrektur auch bei Einfaltungen robust ist.

Motivation

Background phase correction is necessary to correctly quantify flow velocities and other inferred parameters. Commonly, it is corrected by polynomial regression to stationary tissue. However, this method is bound to fail in the presence of wrap around. Therefore, outlier rejection algorithms were proposed (1-2). In this work, we use M-estimate Sample Consensus (MSAC) (2-3) to reject outliers and prove its feasibility in 4D flow imaging. MSAC correction was compared to ground truth fits based on static phantom scans and fits based on stationary tissue masks.

Materialien und Methoden / Materials and Methods

Four in vivo 4D flow datasets were acquired on a 1.5T system (MAGNETOM Sola, Siemens Healthcare, Erlangen, Germany) and a 3T system (MAGNETOM Vida, Siemens Healthcare, Erlangen, Germany) respectively. In each case, a static phantom scan with identical protocols was additionally acquired to measure the ground truth background phases.

MSAC removes outlier starting with a magnitude mask (pixel pool M) to filter noise using a temporally averaged magnitude image. MSAC then randomly selects *m* samples from M and fits a first order polynomial to the data. Inliers are all pixels in M which have a distance $\varepsilon_i = |v_i - v_{fit,i}|$ to the volume below a threshold *t*. Together, they form a consensus set. The cost of the consensus set is defined as:

$$C = \sum_{i \in M} \begin{cases} \varepsilon_i, & \varepsilon_i < t \\ t, & \text{else} \end{cases}$$

This process is repeated N-times. Each velocity direction is handled individually. In the end, an n^{th}-polynomial order correction fit is generated from the consensus set with the lowest cost.

First, MSAC was applied to the phantom scan, to generate a ground truth fit without wrap-around. Second, MSAC was applied to the in vivo datasets and correction fits were generated based on the calculated masks., MSAC parameters were N=1000, *m*=10, *t*=0.75%*venc. For phantom scans, the threshold was set to *t*=0.5%*venc.

Additionally, a stationary tissue mask was created by thresholding the temporal variance image as described in Walker et al. (4).

The RMSE is defined as the distance between the ground truth fit and MSAC or stationary tissue correction as percentage of the venc within the phantom volume:

$$RMSE = \sqrt{\sum_{i \in Phantom} \left\| v_{i,fit} - v_{i,ground\ truth} \right\|^2}$$

All background phase correction was implemented offline in Matlab.

Ergebnisse / Results

Fig. 1 shows that MSAC successfully removes region of wrap-around from the tissue masks.

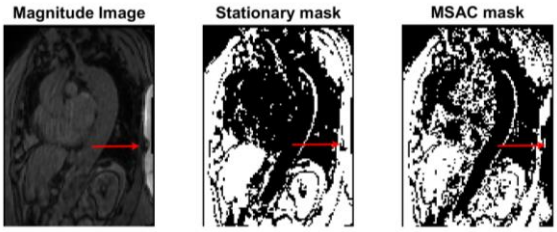

Fig. 1: Comparison of tissue masks. MSAC (right) removes wrap around from the right border compared to the stationary tissue mask (middle).

Table 1 summarizes the results for all four acquisitions using a 3rd-order correction fit. This shows that in presence of wrap-around, MSAC performs better than stationary tissue fit correction and similarly if no wrap-around is present.

		No wrap	Wrap-around
1.5T	Stationary	0.46 %	0.71 %
	MSAC	0.37 %	0.39 %
3T	Stationary	0.58 %	0.68 %
	MSAC	0.44 %	0.55 %

Table 1: Summary of 3rd- order fit correction for all 4 acquisitions as percentage of venc. MSAC performs better in wrap-around cases.

Averaging the values from Table 1, MSAC reduced background phases from (6.6 ± 0.1)% to (0.44 ± 0.05)%. Stationary tissue correction reduced the background phase to (0.60 ± 0.06)%. This is also displayed in Fig. 2 for other polynomial fit orders.

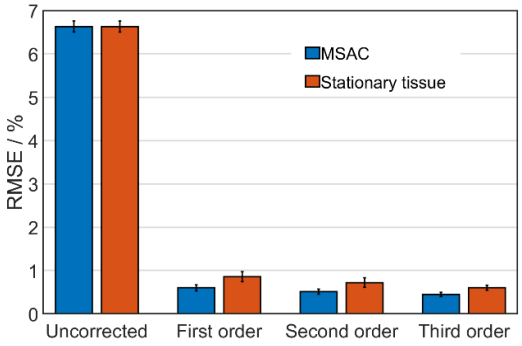

Fig. 2: On average over all four acquisitions, MSAC (blue) performed better than stationary tissue (orange) correction for varying polynomial orders.

Diskussion / Discussion

MSAC successfully removes wrap-around and flow regions from the magnitude mask. It could be observed, that even for these mild cases of wrap-around, an improvement, as compared to static tissue correction was achieved. The variation in fit order can be attributed to the eddy-current variations between systems.

Schlussfolgerung / Conclusion

We could prove that MSAC is also applicable to 4D flow imaging. The generated masks efficiently removed regions of wrap-around and improved background phase correction.

Further in-vivo analyses regarding fit order, degree of wrap-around, MSAC parameter settings and combination with acceleration techniques are warranted.

References

1. Pruitt AA, Jin N, Liu Y, Simonetti OP, Ahmad R. A method to correct background phase offset for phase-contrast MRI in the presence of steady flow and spatial wrap-around artifact. Magn Reson Med. 2019;81(4):2424-2438.

2. Fischer C, Wetzl J, Schäfer T, Giese D. Automatic and robust background phase correction on phase-contrast MRI using M-estimate SAmple Consensus (MSAC). In: International Society for Magnetic Resonance in Medicine (ISMRM) 29th Annual Meeting & Exhibition.; 2021.

3. Torr PHS, Zisserman A. MLESAC: A new robust estimator with application to estimating image geometry. *Comput Vis Image Underst*. 2000;78(1):138-156.

4. Walker PG, Cranney GB, Scheidegger MB, Waseleski G, Pohost GM, Yoganathan AP. Semiautomated method for noise reduction and background phase error correction in MR phase velocity data. *J Magn Reson Imaging*. 1993;3(3):521-530.

Concomitant field compensation in a double diffusion encoding sequence using oscillating gradients: Feasibility and efficiency

Julian Rauch[1,2,*], Frederik B. Laun[3], Theresa Palm[3], Jan Martin[3,4], Maxim Zaitsev[5,6], Mark E. Ladd[1,2,7], Peter Bachert[1,2], and Tristan A. Kuder[1]

[1]Division of Medical Physics in Radiology, German Cancer Research Center, Heidelberg, Germany

[2]Faculty of Physics and Astronomy, Heidelberg University, Heidelberg, Germany

[3]Institute of Radiology, University Hospital Erlangen, Friedrich-Alexander-Universität Erlangen-Nürnberg (FAU), Erlangen, Germany

[4]Division of Physical Chemistry, Lund University, Lund, Sweden

[5]Medical Physics, Department of Radiology, Faculty of Medicine, Medical Center University of Freiburg, Freiburg, Germany

[6]High Field Magnetic Resonance Center, Center for Medical Physics and Biomedical Engineering Medical University of Vienna, Vienna, Austria

[7]Faculty of Medicine, Heidelberg University, Heidelberg, Germany

*j.rauch@dkfz.de

Synopsis: In this study, we show the feasibility of reducing concomitant field-related artifacts with additional oscillating gradients in a double diffusion encoding sequence. An analysis of the efficiency of the proposed method when combining diffusion weighting and compensation in one gradient waveform was carried out with simulations, revealing a strong dependency between the compensation efficiency and the angle between two desired gradient directions.

Zusammenfassung: In dieser Studie zeigen wir die Möglichkeit, durch Begleitfelder erzeugte Artefakte mit zusätzlichen oszillierenden Gradienten in einer doppelt diffusionsgewichteten Sequenz zu reduzieren. Eine simulationsbasierte Effizienzanalyse der vorgeschlagenen Methode bei der Kombination von Diffusionswichtung und Kompensation in demselben Gradientenprofil ergab eine starke Abhängigkeit zwischen der Kompensationseffizienz und dem Winkel zwischen zwei gewünschten Gradientenrichtungen.

Motivation

In diffusion-weighted MRI, usually strong gradients are used. These gradients generate concomitant or Maxwell fields, which may cause severe artifacts (1,2). In this study, we present a proof-of-concept demonstration of Maxwell field compensation in the context of double diffusion encoding (DDE) using additional oscillating gradients that allow compensation theoretically without increase in echo time and significant change in b-value (3). Furthermore, simulations were carried out to analyze the compensation efficiency of the proposed method when combining diffusion weighting and compensation in one waveform while conserving the diffusion direction which becomes important when deriving orientationally invariant metrics such as microscopic anisotropy (4).

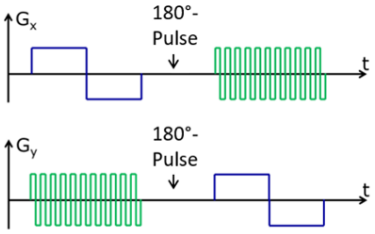

Fig. 1: Bipolar diffusion-weighting gradients (blue) are used for double diffusion encoding, while oscillating gradients (green) are implemented to null the induced Maxwell fields.

Materials and Methods

Imaging experiments were conducted using a DDE sequence adapted for concomitant field compensation (Figure 1) on a 3T MRI system (Magnetom Prisma, Siemens, Erlangen, Germany). The oscillating gradients were implemented to fulfill the compensation condition

$$\int_0^{\mathrm{TE}} s_n(t)\, G(t)^2 dt = 0 \qquad [1],$$

with TE being the echo time, G the gradient amplitude and $s_n(t) = (-1)^{n_{rf}(t)}$, where $n_{rf}(t)$ is the number of refocusing pulses within time interval t to TE. An elongated water phantom was used in all measurements. The decrease of the signal magnitude due to concomitant fields was assessed for a gradient amplitude of 70 mT/m.

For the simulations, two bipolar diffusion gradients introducing a diffusion weighting of b = 500 s/mm^2 with gradient pulse duration δ = 12 ms on perpendicular gradient axes were

considered. The maximum amplitude of all gradients was limited to 76 mT/m at a slew rate of 200 mT/m/ms. The angle between the two waveforms was decreased stepwise to zero. In every step, oscillating gradients introducing a b-value of at most 100 s/mm² were added on the twisted second diffusion waveform. The best parameter combinations for the oscillations, i.e. number of applied oscillations, flat top time of one oscillating lobe and the oscillation strength, were determined for every angle with respect to the highest compensation efficiency defined as the percental decrease of $\int_0^{TE} s_n(t)\, G(t)^2 dt$ over the whole gradient profile including the first bipolar gradient. To yield a better compensation, the effect of prolonging the duration of the gradient waveform by 5, 10 and 20 ms was evaluated.

Results

As shown in the magnitude images in Figure 2, concomitant field-induced artifacts worsen with distance from the isocenter (a). These artifacts are reduced with the usage of additional oscillating gradients (b).

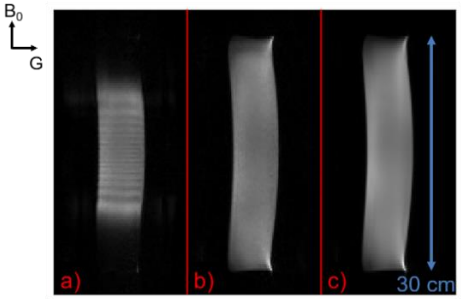

Fig. 2: Acquired magnitude images without concomitant field compensation (a), with compensation (b), and without diffusion weighting as reference (c).

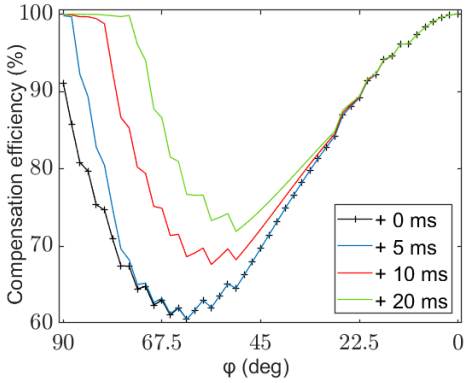

Fig. 3: Compensation efficiencies for the angle interval φ = $[90, 0]$° between the two waveforms for an increase of the waveform duration between 0 and 20 ms.

The simulation results in Figure 3 reveal a sharp drop in the compensation efficiency when the angle between the waveforms initially decreases. For smaller angles, the efficiency rises again and almost no differences in the efficiencies are present. Prolonging the gradient waveforms results in better compensation as expected, since more oscillations can be included for the compensation, reaching compensation efficiencies always higher than 67 % in the case of 10 ms temporal extension.

Discussion

Concomitant field-induced artifacts can be reduced by additional oscillating gradients. To null the effect of the Maxwell fields, a sufficient number of oscillations with adequate strength and duration is needed, whose application might exceed the stimulation limit and could lead to a temporal extension of the compensating waveform. While the efficiency is high for perpendicular and parallel double diffusion encodings without increase in TE, increasing TE might be justified depending on the exact sequence parameters and the desired degree of artifact reduction for angles of e.g. 45° between the directions. Limitations of this study include the disregard of possible stimulation exceedance and sampling the parameter space for discrete values only resulting in artifacts in Figure 3.

Conclusion

The usage of oscillating gradients is an efficient tool for the reduction of concomitant field-induced artifacts in the context of DDE. When combining diffusion weighting with simultaneous Maxwell compensation, optimal settings have to be found to ensure adequate compensation without inadequate increase in echo time and additional b-value.

References

1. Bernstein MA et al. Concomitant gradient terms in phase contrast MR: analysis and correction. Magn Reson Med. 1998;39:300–8.
2. Szczepankiewicz F et al. Maxwell-compensated design of asymmetric gradient waveforms for tensor-valued diffusion encoding. Magn Reson Med. 2019;82:1424-37
3. Rauch et al. Concomitant field compensation using additional oscillating gradients in a double diffusion encoding imaging sequence. Ann. Meet. Int. Soc. Magn. Reson. Med. 2021
4. Jespersen SN et al. Orientationally invariant metrics of apparent compartment eccentricity from double pulsed field gradient diffusion experiments. NMR Biomed. 2013;26:1647-6

Magnetic Particle Imaging goes Human-sized

P. Vogel,[1*] M.A. Rückert,[1*] C. Greiner,[3] T. Reichl, [1] J. Günther, [1] A. von Böhn, [1] L. Mirzojan, [1] T. Kampf, [1,3] T.A. Bley, [2] S. Herz[2] and V.C. Behr [1]

[1] Department of Experimental Physics 5 (Biophysics), University of Würzburg, Würzburg, Germany.
[2] Department of Diagnostic and Experimental Radiology, University Hospital Würzburg, Würzburg, Germany.
[3] Department of Diagnostic and Experimental Neuroradiology, University Hospital Würzburg, Würzburg, Germany
* Patrick.Vogel@physik.uni-wuerzburg.de.

Motivation and Introduction

Over the past decade, Magnetic Particle Imaging (MPI) has become a promising tomographic method for multiple applications in biology, chemistry, medicine and physics [1]. For cardiovascular medicine in particular, MPI could become an applicable radiation-free technique for endovascular interventions supporting the common x-ray gold-standard (digital subtraction angiography – DSA) [2, 3].

As next step on the path of MPI into clinical practice, MPI hardware needs to be scaled up for human-sized applications [4, 5]. This comes with several challenges when keeping the flexibility and speediness of MPI. Furthermore, additional issues related to SAR (specific absorption rate) and PNS (peripheral nerve stimulation) limitations [6] due to strong magnetic field gradients required for high spatial resolution have to keep in mind.

In this abstract, a first dedicated concept for a human-sized MPI scanner based on the Traveling Wave approach is presented [7], which is specifically designed to meet the requirements for real-time cardiovascular interventions such as percutaneous transluminal angioplasty (PTA) and stenting.

Materials and Methods

The aim of the interventional MPI scanner (iMPI) is to provide a radiation-free system comparable to the clinical gold-standard DSA (digital subtraction angiography). This requires spatial resolution in the range of millimeters, high temporal resolution below 100 ms per image, near real-time visualization with low latency, and an open design that provides a comfortable and flexible environment for patients and medical staff, as well as sufficient space for interventional instrumentation and its operation. Additionally, the open design allows for simultaneous conventional DSA, which is especially important in the trial and testing phase [8].

To provide a sufficient magnetic field gradient, which is required for a high spatial resolution in MPI, a novel hardware approach is used to generate a FFL dynamically within a specific region of interest (ROI) (see Fig. 1 left). By rapidly moving the FFL along specific trajectories through the ROI using additional coils, the nonlinear response signal of the tracer (superparamagnetic iron-oxide nanoparticles – SPION) is used to determine their spatial distribution [9]. The result is projection display comparable to DSA, e.g., of vascular structures and stent positioning.

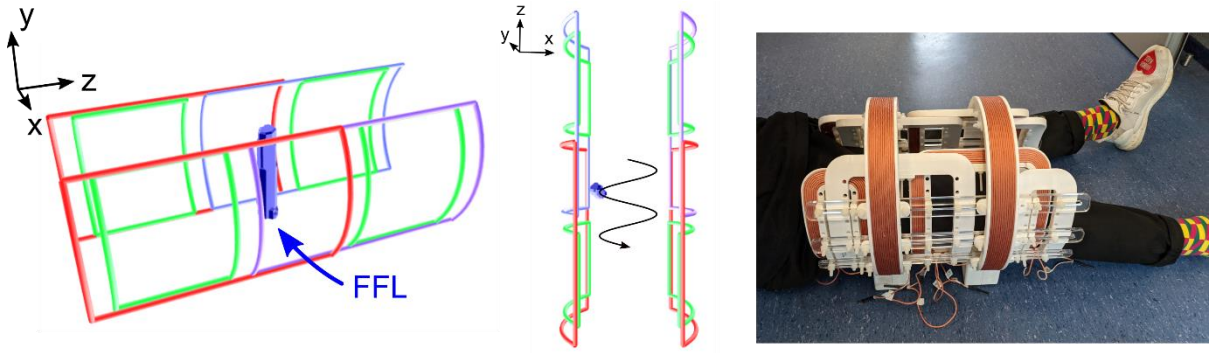

Fig. 1: left: basic hardware concept for the generation of the field free line (FFL) encoding scheme. Right: picture of the first iMPI prototype.

Results

To guarantee a strong magnetic field gradient of about 0.7 T/m, currents of about 200 Ampere driving the main electromagnets (number of windings *N*=32) are required. This results in a power dissipation of about 50-60 Kilowatts in continuous mode, which requires a sophisticated cooling management.

An alternative approach is a pulsed measurement mode, where a short sequence (<1 ms) is generated to scan the ROI sequentially.

Furthermore, to guarantee real-time imaging, the in combination with high spatial resolution, the acquisition sequence have to be modified.

In Fig. 2 the results of a simulated dataset of a femoral artery model with the proposed scanner design is indicated.

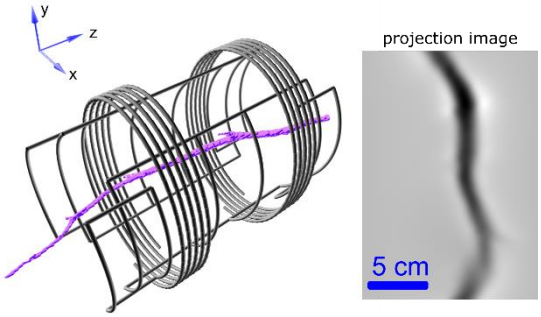

Fig. 2: Simulation example of a projection image of a femoral artery.

Conclusion

A first human-sized projection MPI scanner for interventional treatment of human-sized legs has been designed and built providing promising results to pave the way to clinical routine..

References

1. Gleich B & Weizenecker J. Tomographic Imaging using the nonlinear response of magnetic particles. *Nature*. 2005; 435:1214-7.

2. Herz S et al. Magnetic Particle Imaging Guided Real-Time Percutaneous Transluminal Angioplasty in a Phantom Model. *Cardiovasc Intervent Radiol*. 2018; 41(7):1100-5.

3. Herz S et al. Magnetic Particle Imaging-Guided Stenting. *J Endovasc Ther*. 2019; 26(4):512-9.

4. Graeser M et al. Human-sized magnetic particle imaging for brain applications. *Nature Comm*. 2019; 10:1936.

5. Mason E E et al. Design analysis of an MPI human functional brain scanner. *Int J Magn Part Imaging*. 2017; 3(1):1703008.

6. Saritas E U. Magnetostimulation Limits in Magnetic Particle Imaging. *IEEE TMI*. 2013; 32(9):1600-10.

7. Vogel P et al. Traveling Wave Magnetic Particle Imaging. *IEEE TMI*. 2014; 33(2):400-7.

8. Vogel P et al. Magnetic Particle Imaging meets Computed Tomography: first simultaneous imaging. *Nature Sci Rep*. 2019; 9:12627.

10. Vogel P et al. Flexible and Dynamic Patch Reconstruction for Traveling Wave Magnetic Particle Imaging. *Int J Magn Part Imaging*. 2016; 2(2):1611001.

Vergleichende MRT-Untersuchungen der kardialen Funktion nicht-humaner Primaten

Ina Barnekow,[1,2*] Susann Boretius,[1,3] Amir Moussavi[1]

[1] Abteilung Funktionelle Bildgebung, Deutsches Primatenzentrum GmbH, Leibniz-Institut für Primatenforschung, Göttingen, Deutschland
[2] Fakultät Ingenieurwissenschaften und Gesundheit, Hochschule für angewandte Wissenschaft und Kunst Hildesheim/Holzminden/Göttingen, Göttingen, Deutschland
[3] Johann-Friedrich-Blumenbach Institut für Zoologie und Anthropologie, Georg-August-Universität, Göttingen, Deutschland
* E-Mail: ibarnekow@dpz.eu

Synopsis: As our closest genetic relatives, the non-human primates (NHPs) have recently emerged as a most valuable model system for translational cardiovascular research. While in humans, diagnostics are routinely performed by MRI, only very few studies have been performed in NHPs thus far. The aim of this work was to investigate inter-species differences in the cardiac function of NHPs and humans. Preliminary results show a significantly higher normalized cardiac output in marmosets compared to other primates.

Zusammenfassung: Aufgrund ihrer genetischen Verwandtschaft zum Menschen sind nicht-humane Primaten (NHP) für die translationale Herz-Kreislauf-Forschung besonders wertvoll. Während die MRT am Menschen routinemäßig zur Herz-Kreislauf-Diagnostik verwendet wird, ist die Anwendung in Studien an NHPs bisher sehr begrenzt. Ziel dieser Arbeit war es, eine exakte Beschreibung der kardialen Funktion verschiedener NHPs im Vergleich zum Menschen zu erstellen. Erste Ergebnisse zeigen relativ zum Köpergewicht ein deutlich höheres Herzzeitvolumen in Weißbüschelaffen im Vergleich zu anderen Primaten.

Motivation

In den letzten 25 Jahren ist die Zahl der Menschen mit Herz-Kreislauf-Erkrankungen (HKE) stetig angestiegen [1]. Diese Erkrankungen gehören weltweit zu den häufigsten Todesursachen [2]. Dies verdeutlicht die hohe Relevanz der präklinischen Forschung zu HKE. Als dem Menschen sehr ähnlich, eignen sich NHPs besonders als Tiermodelle in der präklinischen Forschung. Für die Übertragbarkeit der Ergebnisse auf den Menschen ist eine umfassende Kenntnis der Gemeinsamkeiten aber auch der Unterschiede zwischen den einzelnen NHP-Spezies und dem Menschen essentiell.

In der kardiovaskulären Forschung hat sich die MRT mittlerweile zu einem Standardverfahren entwickelt. Sie besitzt den Vorteil, dass sowohl die Morphologie, als auch funktionelle Prozesse mit einer hohen zeitlichen Auflösung dargestellt werden können. Weltweit gibt es bisher jedoch nur eine geringe Zahl von kardialen MRT-Studien an NHPs [3]. Aus diesem Grund erscheint ein Speziesvergleich verschiedener NHPs und Menschen mittels quantitativer Analyse von MRT-Bilddaten lohnenswert. Durch die daraus resultierenden Erkenntnisse über Gemeinsamkeiten und Unterschiede könnte die Übertragbarkeit der präklinischen Forschung auf den Menschen zukünftig verbessert werden. Dies könnte sich langfristig auch auf die Prävention, Diagnostik und Therapie von HKE auswirken und so mithelfen der Morbidität und Mortalität dieser Erkrankungen entgegenzuwirken.

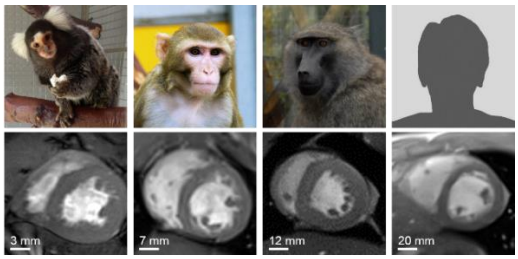

Abb. 1: Mittventrikuläre Kurzachsen-Schnitte des Herzens in der Phase der Diastole. Von links nach rechts: Weißbüschelaffen, Rhesusmakaken, Anubispaviane und Menschen im Speziesvergleich.

Material und Methoden

Es wurden 3 Menschen (*Homo sapiens*, mittleres Körpergewicht: 75 ± 3 kg, 2 Männer), 6 Anubispavianen (*Papio anubis*, mittleres Körpergewicht: 30 ± 3 kg, 6 Männchen), 32 Rhesusmakaken (*Macaca mulatta*, mittleres Körpergewicht: 9 ± 2 kg, 20 Männchen) und 2 Weißbüschelaffen (*Callithrix jacchus*, mittleres Körpergewicht: 0,4 ± 0,0 kg, 2 Männchen) untersucht. Die MRT-Daten der NHPs wurden im Rahmen unterschiedlicher tier-experimenteller Studien unter Narkose erhoben. Während der MR-Messungen wurden kontinuierlich physiologische Parameter wie Herzfrequenz und Atemfrequenz erhoben. Bei den Menschen wurde dauerhaft die Herzfrequenz überwacht.

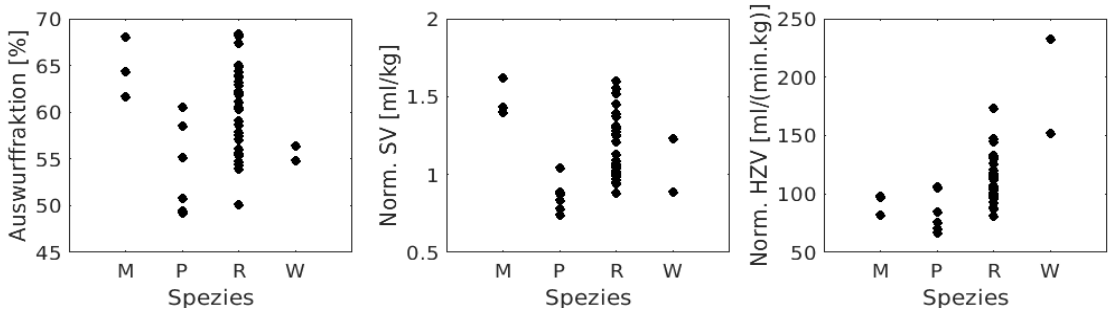

Abb. 2: Gegenüberstellung der Auswurffraktion (li.), des normierten SVs (Mitte) und des normierten HZVs (re.) der Spezies Mensch (M), Pavian (P), Rhesusmakaken (R) und Weißbüschelaffen (W).

Die Messungen der Menschen, Anubispaviane und Rhesusmakaken erfolgten an einem 3T Ganzkörper-MRT (Magnetom Prisma, Siemens Healthineers). Die der Weißbüschelaffen an einem 9,4T Kleintier-MRT (BioSpec 94/30, Bruker Biospin MRI GmbH). Zur Erstellung der Kurzachsen-Schnitte wurde entweder eine retrospektiv getriggerte FLASH-Sequenz in exspiratorischer Atemanhaltephase (Siemens), oder eine IntraGate-Sequenz in freier Atmung (Bruker) verwendet. Die räumliche Auflösung variiert je nach Größe der Spezies (Menschen: 1,77×1,77×6 mm³, Paviane: 1,25×1,25×3 mm³, Rhesusmakaken: 0,85×0,85×3 mm³ und Weißbüschelaffen: 0,2×0,2×1,2 mm³).

Die Bilddaten wurden mit der frei verfügbaren Software Segment (R8456, Medviso) ausgewertet. Endokardiale sowie epikardiale Konturen wurden zum Zeitpunkt der Diastole und Systole manuell von der Basis bis zur Herzspitze des linken Ventrikels markiert. Um eine Vergleichbarkeit der Werte zwischen den Spezies zu gewährleisten, wurde außerdem eine Normierung auf das Körpergewicht durchgeführt.

Ergebnisse

Kurzachsen-Schnitte (mittventrikulär, Diastole) der verschiedenen Spezies sind in Abb.1 dargestellt. Die Unterschiede in Struktur (Papillarmuskeln und Trabekularisierung) und Größe zwischen den Spezies sind deutlich zu erkennen. Obwohl es keine signifikanten Unterschiede in der Auswurffraktion gab (Abb. 2, li.), zeichneten sich deutliche Unterschiede in den auf das Körpergewicht normierten Volumina ab. Das normierte Schlagvolumen (SV) des Menschen war z.B. bis zu 50% höher als das des Pavians (Abb. 2, Mitte). Das normierte Herzzeitvolumen (HZV) des Weißbüschelaffen hingegen entsprach dem zweifachen HZV des Menschen. Des Weiteren zeigte sich eine Abhängigkeit des HZV von der Körpergröße bzw. der Herzfrequenz. Kleinere Tiere (höhere Herzfrequenz) wiesen tendenziell ein höheres HZV auf (Abb. 2, re.).

Diskussion

Es wurden keine signifikanten Unterschiede in der Auswurffraktion der untersuchten Spezies gefunden. Allerdings wurde ein bis zu 50% höheres normiertes SV im Menschen beobachtet. Dennoch stellt sich das HZV im Menschen am geringsten und in Weißbüschelaffen am höchsten dar. Möglicherweise ist dies auf eine Abhängigkeit des HZVs von der Herzfrequenz (HF) zurückzuführen. Die HF ist antiproportional zur Körpergröße, sodass die deutlich höhere HF der Weißbüschelaffen zu einem deutlich höheren normierten HZV führen könnte als z.B. beim Menschen.

Schlussfolgerung

Nach aktuellem Wissensstand ist diese Arbeit die erste Arbeit, die eine umfangreiche quantitative Analyse der Herzfunktion im Vergleich bei Primaten vornimmt und die erste MRT-Studie dieser Art überhaupt. Eine Vergrößerung der Gruppengröße der untersuchten Spezies sowie eine erweiterte Analyse (Quantifizierung der Herzform und Untersuchung des rechten Ventrikels) der bereits erhobenen Bilddaten ist in Vorbereitung.

References

1. Wilkins E, Wilson L, Wickramasinghe K et. al. European cardiovascular disease statistics 2017. Brussel: European Heart Network. 2017.
2. GBD 2017 Causes of death collaborators. Global, regional, and national age-sex-specific mortality for 282 causes of death in 195 countries and territories, 1980-2017: a systematic analysis for the Global Burden of Disease Study 2017. The Lancet. 2018; 392: 1736–1788.
3. Sampath S, Parimal AS, Feng D et. al. Quantitative MRI biomarkers to characterize regional left ventricular perfusion and function in nonhuman primates during dobutamine-induced stress: A reproducibility and reliability study. Journal of Magnetic Resonance Imaging. 2017; 45: 556–569.

Neurometabolic changes in neonates with congenital heart disease and the relation to developmental outcome

C. Steger[1,2], M. Feldmann[3,4], J. Borns[4,5,6], B. Latal[3,4], U. Held[7], A. Jakab[1,2,4], W. Knirsch[4,5], R. Tuura[1,4]

[1] Center for MR-Research, University Children's Hospital, Zurich, Switzerland.

[2] Neuroscience Center Zürich, Zürich, Switzerland.

[3] Child Development Centre, University Children's Hospital, Zurich, Switzerland.

[4] Children's Research Centre, University Children's Hospital, Zürich, Switzerland.

[5] Pediatric Cardiology, University Children's Hospital, Zürich, Switzerland.

[6] Pediatric Cardiology, Inselspital Bern, Bern, Switzerland.

[7] Department of Biostatistics at Epidemiology, Biostatistics and Prevention Institute, University of Zurich, Switzerland.

* celine.steger@kispi.uzh.ch, Steinwiessenstrasse 75, 8032 Zürich, Switzerland

Synopsis: Congenital heart defects (CHD) delays brain maturation and put patients at risk for developmental deficits. In this analysis, magnetic resonance spectroscopy (MRS) of CHD neonates and healthy controls was analysed to identify differences in neurometabolic profiles. Secondly, the relationship between altered metabolite ratios (NAA/Cho) and neurodevelopmental outcome of patients at one year of age was examined. While CHD neonates showed lower NAA/Cho and lower outcome scores, no correlation between the two measurements was found.

Zusammenfassung: Angeborene Herzfehler (CHD) verzögern die Hirnentwicklung und Patienten haben ein erhöhtes Risiko Defizite in der Entwicklung zu erleiden. In dieser Analyse wurden Magnetresonanz Spektroskopie (MRS) Daten von neugeborenen mit CHD und gesunden Kontollkindern untersucht, um Unterschiede in Neurometaboliten zu identifizieren. In einem zweiten Schritt wurde untersucht, in welcher Beziehung die veränderten Metaboliten (NAA/Cho) zu dem beobachteted Entwicklungsstand nach einem Jahr stehen.

Motivation

Congenital heart defects (CHD) are the most common birth defects, affecting 700 children in Switzerland per year (1). While survival has improved in recent decades, neurodevelopmental impairment remains a concern in many patients. Neuroimaging studies revealed that neonates with severe CHD show delayed myelination (2), reduced brain volume (3) and a risk for brain injuries (4). These findings have been associated with an adverse neurodevelopmental outcome. However, even in the absence of structural brain abnormalities, metabolic changes arising from the heart defect may also impact the neurodevelopment of CHD children. While the relationship between altered metabolites and neurodevelopment has not been described for CHD patients it has been reported in preterm children, a patient group also known to show a delay in brain maturation.

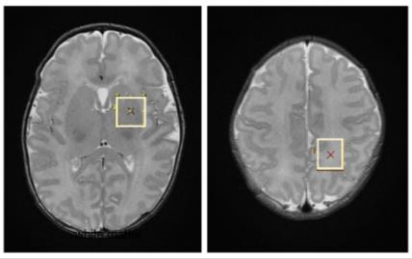

Fig. 1: Voxel location of MR Spectroscopy. Left: basal ganglia, right: white matter.

Materials and Methods

Data was collected at the University Children's Hospital Zurich. Magnetic resonance spectroscopy (MRS) was acquired on a 3.0 T GE MR750 scanner (GE Healthcare, Milwauke, WI, USA). CHD neonates were scanned twice, pre- and post-surgery, while the control group underwent one scan.

Short-TE single voxel point resolved (PRESS) sequences were acquired in two brain regions (basal ganglia and white matter). Spectra were then analysed using an automated spectral fitting method (LCModel) (7). The following metabolites were referenced to Creatine (Cre): N-acetyl aspartate (NAA), Choline (Cho), glutamate+glutamine (Glx), myo-inositol (mI), and Lactate (Lac). The ratio NAA/Cho, which serves as a brain maturation marker, was calculated in R.

First, linear mixed effects models with metabolite ratios as outcome, group (CHD or control), gestational age at MRI (GA), sex and scanner software update as independent variables and subject as random effect were used to identify the effect of CHD on the metabolite ratios. Multiple testing was corrected with false discovery

rate correction. Second, linear models with the Bayley-III Scales of Infant and Toddler Development composite scores (motor, cognition and language, BCS-III) of CHD patients as outcome variable and metabolite ratio (white matter NAA/Cho), socioeconomic status (SES), GA and diagnosis as independent variables were used to explore the correlation between altered metabolite (pre- and post- surgery) ratios and developmental outcome.

Results

For white matter NAA/Cho ratios we found a partial effect of -0.25 for being in the CHD group (beta estimate: -0.25, 95%CI: -0.39 - -0.10, corr. p-value=0.01). No significant differences were found for other ratios (Lac/Cre, Glx/Cre, Glu/Cre, Cho/Cre, mI/Cre). There was no evidence that white matter NAA/Cho ratios in CHD patients would correlate with any outcome score (BCS-III).

Discussion

The reduced NAA/Cho is consistent with existing literature (6,7). We found no evidence for a correlation between NAA/Cho and outcome in our cohort. However, it has to be considered, that the overall outcome in participants was good, which might have limited the ability to detect a correlation. Furthermore, neurodevelopment is not complete at one year of age and functional deficits might form at later stages.

Conclusion

We found reduced NAA/Cho ratios in our CHD patients in comparison to the healthy controls but no correlation between NAA/Cho and individual Bayley composite scores. Both, metabolite ratios and neurodevelopment are time sensitive, which makes their association complex.

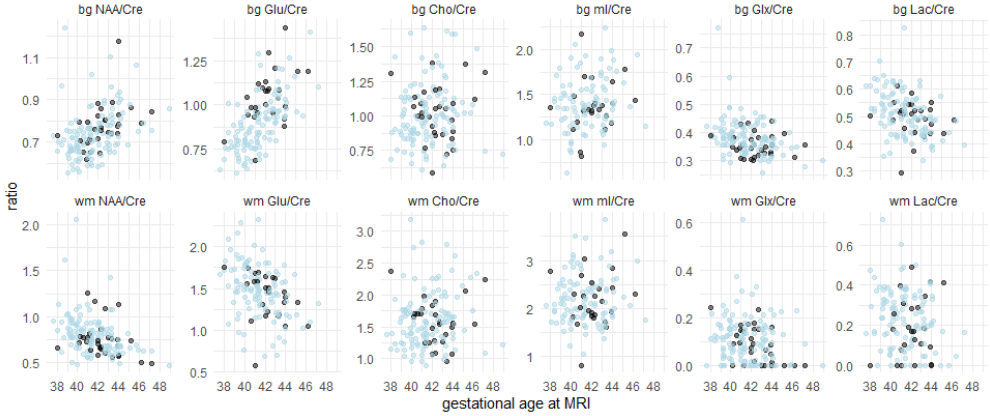

Fig. 2: Acquired metabolite ratios over gestational age at MRI. Top row: basal ganglia (bg), bottom row: white matter (wm), black: controls, lightblue: CHD patient

References

1. Schwerzmann M, Schwitz F, Thomet C, Kadner A, Pfammatter JP, Wustmann K. Challenges of congenital heart disease in grown-up patients. Swiss Med. Wkly. 2017;147:w14495 doi: 10.4414/smw.2017.14495.

2. Licht DJ, Shera DM, Clancy RR, et al. Brain maturation is delayed in infants with complex congenital heart defects. J. Thorac. Cardiovasc. Surg. 2009;137:529–537 doi: 10.1016/j.jtcvs.2008.10.025.

3. von Rhein M, Buchmann A, Hagmann C, et al. Severe Congenital Heart Defects Are Associated with Global Reduction of Neonatal Brain Volumes. J. Pediatr. 2015;167:1259-1263.e1 doi: 10.1016/j.jpeds.2015.07.006.

4. Bertholdt S, Latal B, Liamlahi R, et al. Cerebral lesions on magnetic resonance imaging correlate with preoperative neurological status in neonates undergoing cardiopulmonary bypass surgery. Eur. J. Cardio-Thoracic Surgery, 2014;45:625–632 doi: 10.5167/UZH-83548.

5. Meuwly E, Feldmann M, Knirsch W, et al. Postoperative brain volumes are associated with one-year neurodevelopmental outcome in children with severe congenital heart disease. Sci. Rep. 2019;9 doi: 10.1038/s41598-019-47328-9.

6. McQuillen PS, Miller SP. Congenital heart disease and brain development. Ann. N. Y. Acad. Sci. 2010;1184:68–86 doi: 10.1111/j.1749-6632.2009.05116.x.

7. Limperopoulos C, Tworetzky W, McElhinney DB, et al. Brain volume and metabolism in fetuses with congenital heart disease: Evaluation with quantitative magnetic resonance imaging and spectroscopy. Circulation 2010;121:26–33 doi: 10.1161/CIRCULATIONAHA.109.865568.

Estimation of Head Motion using a Linear Signal Model and Orbital K-space Navigators

Thomas Ulrich,[1*] Klaas Prüssmann,[1]

[1] Institute for Biomedical Engineering, ETH Zürich und Universität Zürich, Schweiz
* ulrich@biomed.ee.ethz.ch

Synopsis: We propose a novel algorithm for head motion estimation with k-space navigators. The algorithm estimates patient motion from the complex-valued navigator signal by means of linear least-squares parameter fitting. We propose a linear signal model, which describes how the navigator signal changes under patient motion.

Zusammenfassung: Wir schlagen einen neuartigen Algorithmus zur Schätzung der Kopfbewegung mit k-Raum-Navigatoren vor. Der Algorithmus schätzt die Patienten-bewegung aus dem komplexwertigen Navigatorsignal mit Hilfe einer linearen Least-Squares-Parameterschätzung. Wir schlagen ein lineares Signalmodell vor, das beschreibt, wie sich das Navigatorsignal bei Patientenbewegung ändert.

Motivation

Patient motion is a frequent problem in MR imaging practice, leading to image degradation and artifacts. Many different methods for motion estimation have been studied. K-space navigators are a promising approach, which does not require any additional hardware. Patient motion can be estimated from an additional signal readout, which needs to be repeated in regular intervals, i.e. before or after each imaging line readout. We propose a novel algorithm for navigator-based head motion estimation, which relies on a linear signal model that is derived from the complex-valued navigator signal. It estimates rotations and translations simultaneously by means of linear least-squares estimation.

Methods

When the subject rotates their head during an imaging scan, the corresponding k-space signal gets equally rotated. Translational shifts, however, lead to a linear phase shift on the k-space signal. Therefore, many k-space navigators have been proposed, which often include 2D circular segments or even spherical shells in their k-space trajectory. We suggest using a previously proposed variant of orbital navigators. This navigator k-space trajectory consists of three orthogonal circles in k-space, and can be acquired in one shot.(1)

In previous work, patient rotation and translation were usually estimated separately. Since translational displacements of the patient's head only change the signal phase, the signal magnitude is only affected by rotational motion. Therefore, it was often proposed to first estimate rotation from the signal magnitude, usually with some linear or non-linear parameter fitting approach. Afterwards, translation was often estimated by fitting the slope of the phase change to the phase difference of two navigator echoes.

In contrast, we propose to estimate rotations and translations simultaneously using one linear signal model, which models the relation between patient motion and changes to the complex-valued navigator signal.

Formally, if we denote by $s\big(k(t)\big)$ and $\tilde{s}\big(k(t)\big)$ the k-space signal before and after applying a 3x3 rotation matrix $R(\theta)$ and a 3D shift vector Δx, then:

$$\tilde{s}\big(k(t)\big) = s\big(R(\theta)k(t)\big)e^{i\Delta x^T k(t)}$$

If the rotation angles and translation vector are small, one can approximate the above non-linear expression by a first-order Taylor series. This requires the derivative of the expression with respect to θ and Δx. The latter is easy, since $e^{ix} \approx 1 + ix$.

The rotational derivative is more challenging. One possibility is to measure it with a two-point finite difference. This would require the acquisition of four reference navigator profiles: one in the reference orientation and three navigator profiles where the navigator trajectory has been rotated slightly around one of the three coordinate axes.

Alternatively, one can split the rotational derivative into two additive components – a directional derivative in the tangential direction of the navigator trajectory, and another directional derivative in the off-tangential direction.(2)

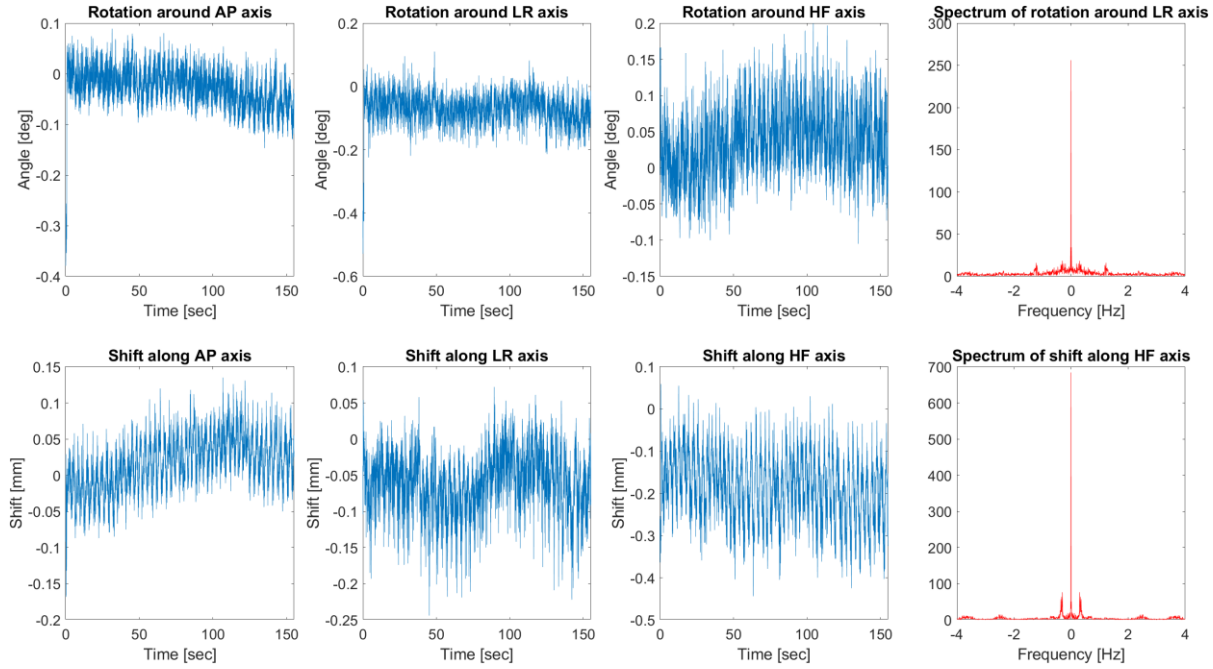

Fig 1. First three columns: Estimated motion parameters from an in-vivo experiment where the volunteer was instructed to hold still. Fourth column: Spectra of the motion time series of two selected axes. Rotations around the LR axis show a peak in the spectrum at 1.22 Hz, shifts along the HF axis at 0.30 Hz.

In either case, the derivatives of the signal with respect to rotation angles and translational shifts need to be stacked as columns into a matrix M, and one needs to solve the least-squares parameter estimation problem

$$\min_{\Delta x,\theta} \left\| M \begin{pmatrix} \Delta x \\ \theta \end{pmatrix} - (\tilde{s} - s) \right\|_2^2$$

We performed an in-vivo experiment to validate our method. During a 2.5 min. T2*-weighted gradient echo scan, the volunteer was instructed to hold still and the motion parameters were estimated using our proposed method.

Results

Figure 1 shows the estimated rotation angles and shifts from the in-vivo experiment. During the experiment without intentional motion, the rotation was estimated to be within the range of ±0.2 degrees and ±0.25mm, except for the HF axis, where the estimated shift values seem to drift and oscillate around -0.2mm. The spectrum showed distinct peaks at 0.30 Hz and 1.22 Hz.

Discussion

For this in-vivo experiment, no ground truth is available, unfortunately. However, the results indicate that our algorithm is sensitive to head motion. The peaks in the spectrum at 0.30 Hz and 1.22 Hz are likely due to respiration and heartbeat. Further investigation of the accuracy and precision for head motion estimation is to be conducted in the future.

Additional phantom and in-vivo experiments, which show that the method exhibits high accuracy and precision, have been presented in the past. (2)

Conclusion

We have proposed a novel algorithm for rigid-body motion estimation, which can estimate motion with high accuracy and precision at low computational cost.

References

1. Ulrich T, Patzig F, Wilm BJ, Pruessmann KP. Towards Optimal Design of Orbital K-Space Navigators for 3D Rigid-Body Motion Estimation. In: Online; 2020.

2. Ulrich T, Pruessmann KP. Detection of Head Motion using Navigators and a Linear Perturbation Model. In: Online; 2021.

Kurtosis versus $D(b50, b750)$ und $D(b750, b1500)$ zur Differenzierung maligner und benigner Brustläsionen in der diffusionsgewichteten Brust-MRT

Mona Pistel[1,2*], Frederik B. Laun[1], Sebastian Bickelhaupt[1], Astrid Müller[1], Anes Dada[1], Elisabeth Weiland[2], Torsten Niederdränk[2], Tristan Kuder[3], Michael Uder[1], Rolf Janka[1], Evelyn Wenkel[1], Sabine Ohlmeyer[1]

[1] Radiologisches Institut, Universitätsklinikum Erlangen, Friedrich-Alexander-Universität Erlangen-Nürnberg (FAU), Erlangen, Deutschland
[2] Siemens Healthcare, Erlangen, Deutschland
[3] Medizinische Physik in der Radiologie, Deutsches Krebsforschungszentrum (DKFZ), Heidelberg, Deutschland.
* Mona Pistel, Universitätsklinikum Erlangen, Maximiliansplatz 3, 91054 Erlangen, Deutschland, mona.pistel@extern.uk-erlangen.de

Zusammenfassung: Zur Differenzierung von gutartigen und bösartigen Brustläsionen in der diffusionsgewichteten Magnetresonanztomographie (MRT) wurden zwei Ansätze verglichen. Einerseits wurde der klassische Diffusions-Kurtosis-Ansatz zur Datenauswertung verwendet, andererseits eine Datenrepräsentation mit $D(b50, b750)$ und $D(b750, b1500)$. Die zugrundeliegenden Daten wurden mit den b-Werten 50, 750 und 1500 s/mm² gemessen. Beide Ansätze waren ähnlich gut in der Lage, zwischen den Läsionstypen zu differenzieren. Ein voxelweiser Kurtosis-Fit mit anschließender Mittelung der gefitteten Parameter sollte jedoch vermieden werden.

Motivation

In der Diagnostik des Mammakarzinoms kommt die diffusiongewichtete MRT (DWI) immer häufiger zum Einsatz [1]. Sie ermöglicht es im Gegensatz zur Biopsie, Läsionen nichtinvasiv zu charakterisieren. Die Differenzierung zwischen benignen und malignen Läsionen erfolgt auf der Basis von Diffusionsparametern.

Bei Diffusionswichtungsstärken (b-Werten) bis zu etwa der Größe $b = 3/(DK)$ kann das diffusionsgewichtete Signal $S(b)$ gut durch folgende Gleichung

$$S(b) = S_0 \cdot e^{\left(-b \cdot D + \frac{1}{6} b^2 D^2 K\right)} \qquad \text{(I)}$$

beschrieben werden, wobei S_0 das Signal ohne Diffusionsrichtung, D der scheinbare Diffusions-Koeffizient und K die Diffusions-Kurtosis sind [2]. Die Kurtosis ist dabei ein Maß für die Abweichung von Gaußscher Diffusion.

Sowohl D als auch K wurden in Studien bereits erfolgreich zur Differentialdiagnose benigner und maligner Läsionen der weiblichen Brust verwendet [2]. Das residuale Fettsignal kann die Bestimmung der Kurtosis jedoch erschweren [1]. Zudem ist der Fit der Kurtosis nicht-linear, wodurch er anfälliger für Instabilitäten ist.

Die Bestimmung von K erfordert eine Messung mit mindestens drei Diffusionswichtungsstärken. Um die Messdauer minimal zu halten, werden oft genau drei b-Werte gemessen, d.h. es stehen die Messsignale $S(b_1)$, $S(b_2)$ und $S(b_3)$ zur Verfügung.

Eine alternative Auswertungsmöglichkeit, die den nicht-linearen instabilen Kurtosis-Fit vermeidet, ist die Bestimmung der Größen

$$D(b1, b2) = -\frac{1}{b_2 - b_1} \ln \frac{S(b_2)}{S(b_1)} \qquad \text{(IIa)}$$

$$D(b2, b3) = -\frac{1}{b_3 - b_2} \ln \frac{S(b_3)}{S(b_2)}. \qquad \text{(IIb)}$$

Ziel dieser Arbeit war es zu evaluieren, ob es für die Differenzierung maligner und benigner Läsionen in der weiblichen Brust besser ist, D und K mittels Gleichung (I) zu bestimmen oder, alternativ, $D(b1, b2)$ und $D(b2, b3)$ aus (IIa) und (IIb) zu verwenden.

Material und Methoden

Im Zeitraum April 2017 bis Januar 2020 wurden 123 Patientinnen in die Studie eingeschlossen. Alle Patientinnen haben schriftlich der Studienauswertung ihrer MRT-Daten zugestimmt. Für die Studie lag ein positives Votum der Ethikkommission vor. Alle Patientinnen wurden an 3T-MRT-Geräten (MAGNETOM Skyra/Vida, Siemens Healthcare, Erlangen, Deutschland) gemessen. Mit einer prototypischen ssepi Sequenz wurden Bilder mit den b-Werten 50 (b50), 750 (b750) und 1500 s/mm² (b1500) aufgenommen (TE (ms): 66, TR (ms): 6290-8695, Voxelgröße (mm³): 7.48-11.29, Mittelungen pro b-Wert: 3/b50, 8/b750, 15 oder 20/b1500, Inversion-Recovery Fettsättigung). Die Läsionen wurden mit der MITK-Software auf der b1500-Aufnahme segmentiert (MITK, Version v2018.04.2, DKFZ, Heidelberg).

Die Parameter D und K wurden mittels Gleichung (I) gefittet, die Parameter

$D(b50, b750)$ und $D(b750, b1500)$ mittels Gleichung (IIa) und (IIb). Die Fits wurden einmal mit in Volume-of-interest (VOI) gemittelten Signalen durchgeführt und einmal voxelweise. Bei der voxelweisen Auswertung wurde anschließend der Mittelwert der Parameter berechnet.

Die Spezifität der einzelnen Parameter wurde für die Sensitivitäten 1, 0.99, 0.96 und 0.93 berechnet. Zudem wurde eine logistische Regression verwendet, welche einmal die einzelnen Parameter D und K kombinierte und einmal die Parameter $D(b50, b750)$ und $D(b750, b1500)$. Für die logistische Regression wurde eine Receiver-Operating-Curves (ROCs) Analyse durchgeführt.

Ergebnisse

Es wurden 114 Patientinnen mit insgesamt 155 Läsionen ausgewertet. Abb. 1 zeigt die ROC-Analyse für Kombinationen mittels logistischer Regression.

- Methode 1: Voxelweiser Fit, Kombination $D(b50, b750)$ und $D(b750, b1500)$
- Methode 2: Voxelweiser Fit, Kombination D und K
- Methode 3: VOI-gemitteltes Signal, $D(b50, b750)$ und $D(b750, b1500)$
- Methode 4: VOI-gemitteltes Signal, Kombination D und K

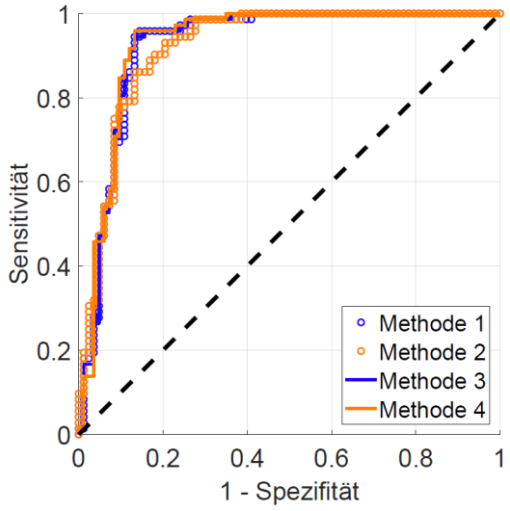

Abb. 1: ROC-Kurven verschiedener Methoden.

Alle Methoden haben ähnliche Area under the curves (AUC) (Meth.1: 0.925, Meth.2: 0.921, Meth.3: 0.927, Meth.4: 0.930). Der Verlauf der Kurven ist für alle Methoden bis auf Methode 2 sehr ähnlich. Methode 2 erreicht für Sensitivitäten im Bereich 0.79 bis 0.97 sichtlich geringere Spezifitäten. Bei einer Sensitivität von 0.93 erreicht Methode 2 lediglich eine Spezifität von 0.80, die anderen eine Spezifität von 0.87.

Die Ergebnisse für die voxelweise Bestimmung der einzelnen Parameter (d.h. nicht kombiniert) sind in Tab.1 zu sehen.

	Median	IQ-Abstand
$D(b50, b750)$	1.60/1.03	0.57/0.23
$D(b750, b1500)$	1.12/0.64	0.43/0.17
D	1.95/1.27	0.56/0.33
K	0.57/0.98	0.31/0.46

Tab. 1: Median und Interquartils-Abstand (IQ) für benigne/maligne Läsionen bei voxelweiser Bestimmung.

Diskussion

Sowohl der klassische Kurtosis-Ansatz (d.h. die Verwendung von D und K) als auch die alternative Datenrepräsentation mittels $D(b50, b750)$ und $D(b750, b1500)$ waren in der Lage, zwischen benignen und malignen Läsionen gut zu differenzieren. Bei Verwendung VOI-gemittelter Signalwerte schnitten beide Ansätze etwa gleich gut ab. Bei Verwendung voxelweise gefitteter Parameter spielte der Ansatz der Datenrepräsentation jedoch den Vorteil der stabileren Fit-Eigenschaften aus.

Schlussfolgerung

Ein voxelweiser Kurtosis-Fit mit anschließender Mittelung der gefitteten Parameter sollte vermieden werden. Bei Verwendung VOI-gemittelter Signale für den Fit scheint die Verwendung des klassischen Kurtosis-Fits dem Ansatz äquivalent zu sein, $D(b50, b750)$ und $D(b750, b1500)$ zu verwenden.

Referenzen:

1. Mlynarska-Bujny A, Bickelhaupt S, Laun FB, Konig F, Lederer W, Daniel H, Ladd ME, Schlemmer HP, Delorme S, Kuder TA. Influence of residual fat signal on diffusion kurtosis MRI of suspicious mammography findings. Sci Rep 2020;10(1):13286.
2. Palm T, Wenkel E, Ohlmeyer S, Janka R, Uder M, Weiland E, Bickelhaupt S, Ladd ME, Zaitsev M, Hensel B, Laun FB. Diffusion kurtosis imaging does not improve differentiation performance of breast lesions in a short clinical protocol. Magn Reson Imaging 2019;63:205-216.

T2-Mapping zur Evaluation einer Chondromalazie des posterolateralen Tibiaplateaus

Mirjam Gerwing,[1*] Moritz Wildgruber,[1,2] Josef Stolberg-Stolberg[3] und Tobias Krähling[4]

[1] AG Translationale Radiologie, Klinik für Radiologie, UK Münster, Münster, Deutschland.
[2] Klinik und Poliklinik für Radiologie, LMU Klinikum, München, Deutschland.
[3] Klinik für Unfall-, Hand- und Wiederherstellungschirurgie, UK Münster, Münster, Deutschland.
[4] AG Hybrid MRI Physics, Klinik für Radiologie, UK Münster, Münster, Deutschland.
* Mirjam.Gerwing@ukmuenster.de.

Synopsis: Posttraumatic chondromalacia after anterior cruciate ligament rupture at the posterolateral tibial plateau was evaluated by T2 mapping, for which patients with arthroscopically diagnosed chondromalacia were first examined in comparison to the contralateral side. Here, a shortening of the T2 time is observed compared to the contralateral control, with a decrease from the ventral to the dorsal portion of the dorsal tibial plateau. Similarly, there is a significant difference at the interfaces of the superficial and deep layers. T2 mapping is thus suitable to detect posttraumatic posterolateral chondromalacia.

Zusammenfassung: Es wurde eine posttraumatische Chondromalazie nach vorderer Kreuzbandruptur am posterolateralen Tibiaplateau mittels T2-Mapping evaluiert, wofür zunächst Patienten mit arthroskopisch diagnostizierter Chondromalazie im Vergleich zur kontralateralen Seite untersucht wurden. Hier zeigt sich eine Verkürzung der T2 Zeit im Vergleich zur kontralateralen Kontrolle, mit einem Abfall vom ventralen zum dorsalen Anteil des dorsalen Tibiaplateaus. Ebenso zeigt sich ein signifikanter Unterschied an den Grenzflächen der oberflächlichen und tiefen Schicht. T2-Mapping ist somit geeignet um eine posttraumatische posterolaterale Chondromalazie zu detektieren.

Motivation

Bei etwa 5% der Patienten mit traumatischer Ruptur des vorderen Kreuzbandes findet sich außerdem eine Chondromalazie des posterolateralen Tibiaplateaus. Dies ist mit der Subluxation, zu der es im Rahmen des Traumas kommt und die zu der Ruptur des Kreuzbandes führt, zu erklären. Diese Chondromalazie ist assoziiert mit einem erhöhten Risiko für eine posttraumatische Arthrose, wobei eine arthroskopische bzw. operative Versorgung das Outcome der Patienten verbessern kann.

Um Patienten mit einer solchen Verletzung zu identifizieren, ist eine MRT-Untersuchung notwendig, die neben den etablierten Sequenzen dezidiert den Knorpel evaluiert.

Material und Methoden

Im Rahmen dieses Projekts wurde daher eine multiparametrische MRT-Untersuchung des Knies etabliert, die neben Verletzungen von Ligamenten und Menisken auch eine posttraumatische Chondromalazie am posterolateralen Tibiaplateau mittels T2-Mapping evaluiert.

Untersucht wurden 5 Patienten (2 weiblich, 3 männlich; Alter 22 – 41) nach Ruptur des vorderen Kreuzbandes und bei denen während der operativen Versorgung mittels Kreuzbandplastik eine Chondromalazie festgestellt wurde. Bei allen Patienten war das kontralaterale Knie intakt.

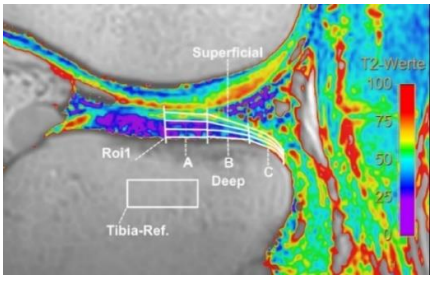

Abb.1: Schema der Auswertung mit IntelliSpace Portal. Der dorsale Knorpel des lateralen Tibiaplateaus wurde in drei Abschnitte unterteilt (A-C, wobei A am weitesten ventral liegt) und diese wiederum in eine oberflächliche, mittlere und tiefe Schicht.

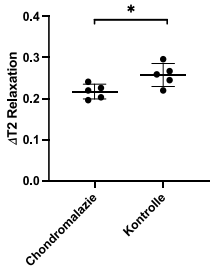

Abb. 2: Übersicht über die T2 Relaxationszeiten der Patienten, normiert auf das Signal des Tibiaplateaus.

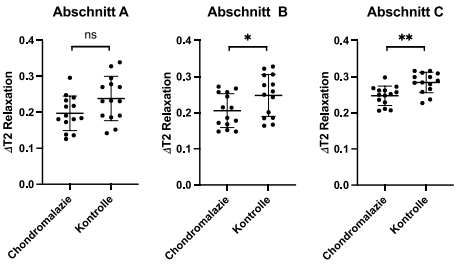

Abb. 3: Unterschiede zwischen Chondromalazie und gesundem Knorpel je nach Abschnitt, vor allem im dorsalen Anteil zeigt sich eine deutliche Diskrepanz (A: 0.2 ± 0.05 vs. 0.24 ± 0.06, p=0.06; B: 0.21 ± 0.05 vs. 0.25 ±0.06 p=0.04; C: 0.25 ± 0.03 vs. 0.28 ± 0.03, p=0.002); Werte normiert auf Tibiaplateau.

Die MR-Messungen erfolgten an einem 3T Scanner (Ingenia, Philips Medical Systems, Best, Niederlande) mit einer dStream 16-Kanal Knie Sende-/Empfangsspule. Untersucht wurde zunächst das Knie mit Chondromalazie, anschließend das kontralaterale Knie, mit Routinesequenzen und einer zusätzlichen T2-Mappingsequenz, wobei diese jeweils zu Beginn der Untersuchung als zweite Sequenz eingefügt wurde. Für das T2-Mapping wurde eine sagittale 2D Multi-Echo Spin-Echo-Sequenz mit 7 Echozeiten TE = 32, 77, 122, 167, 212, 257 und 302 ms verwendet (TR: 2600 ms; akquirierte Voxelgröße: 0,65mm x 0,64 mm x 3 mm; rekonstruierte Voxelgröße: 0,44 mm x 0,44 mm x 3 mm). Die T2-Maps wurden direkt durch die MR-Konsole erstellt.

Jeweils in einer repräsentativen, sagittalen Schicht erfolgte die Bestimmung der T2-Zeiten mit IntelliSpace Portal (Philips Medical Systems, Best, Niederlande). Hierfür wurde das posterolaterale Tibiaplateau in 3x3-Bereich aufgeteilt (Abb. 1) und die mittleren T2-Relaxationszeiten und Standardabweichungen bestimmt und im Verhältnis zur T2-Relaxationszeit der Tibia gesetzt. Die statistische Auswertung erfolgte mit Prism 9 (GraphPad Software Inc., San Diego, USA).

Ergebnisse

Trotz des kleinen Patientenkollektivs zeigten sich signifikant unterschiedliche T2-Relaxationszeiten zwischen dem Knorpel mit Chondromalazie und der kontralateralen Kontrolle. Knie mit Chondromalazie am posterolateralen Tibiplateau zeigten eine verkürzte T2-Relaxationszeit (normiert auf das Signal vom Tibiaplateau 0.22 ± 0.02 vs. 0.26 ± 0.03, p=0.027) im Vergleich zu der Kontrolle auf der kontralateralen Seite (Abb. 2).

In der dezidierten Analyse der Abschnitte sowie der Schichten zeigt sich ein zunehmender Unterschied zwischen gesundem Knorpel und Chondromalazie nach dorsal (Abb. 3, 4). Wenn die einzelnen Schichten getrennt betrachtet werden (Abb. 4) zeigt sich ein Unterschied in der tiefen und oberflächlichen Schicht und lediglich ein Trend in der mittleren Schicht.

Diskussion

In dieser Studie zeigte sich eine verringerte T2-Zeit bei Chrondomalazie am posteolateralen Tibiaplateau im Vergleich zur kontralateralen

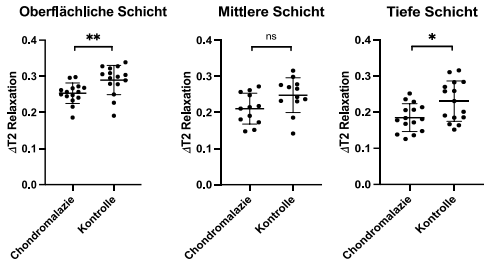

Abb. 4: Unterschiede zwischen Chondromalazie und gesundem Knorpel, mit einem Unterschied in der tiefen (0.19 ± 0.04 vs. 0.23 ± 0.06, p=0.01) und der oberflächlichen Schicht (0.24 ± 0.03 vs. 0.29 ± 0.04, p=0.008), in der mittleren Schicht ist lediglich ein Trend zu einer verkürzten T2 Zeit sichtbar (0.21 ± 0.04 vs. 0.25 ± 0.05, p=0.06); Werte normiert auf Tibiaplateau.

Seite. In einer anderen Studie konnte bei dem Großteil der Patienten einen Anstieg der T2-Zeit bei chondralen Läsionen detektiert werden, bei 1,3 % jedoch auch ein Abfall (1), ebenso konnte jedoch auch nach physikalischer Belastung des Kniegelenks mittels Laufen ein Abfall der T2-Zeit detektiert werden (2). Die Unterschiede zwischen den drei Abschnitten passt zu dem Unfallmechanismus, bei dem das größte Trauma auf den hinteren Abschnitt einwirkt, mit weniger Effekt auf den mittleren und vorderen Anteil. Eine mögliche Erklärung für den Unterschied zwischen den Schichten ist, dass es sich hierbei um die Grenzschichten handelt, wodurch die mittlere Schicht der wenigsten Belastung ausgesetzt ist. Die Effekte sind trotz des kleinen Kollektivs messbar, als nächster Schritt erfolgt nun die MRT Messung bei Patienten vor der Operation.

Schlussfolgerung

Mit zusätzlichen Akquisition einer T2-Map kann eine im Rahmen eines Knietraumas entstandene Chondromalazie des posterolateralen Tibiaplateaus als relevante Begleitdiagnose bei Patienten mit Kreuzbandruptur detektiert werden. Ob dieser Knorpelschaden prognostisch für eine posttraumatische Arthrose ist, bleibt Gegenstand zukünftiger Forschung.

Referenzen

1. Kijowski R,*et al*. 2013. Radiology. 267(2):503-13.
2. Mosher TJ, *et al*. 2010. Osteoarthritis Cartilage. 18(3):358-64.

Improved UTE AFI spoiling scheme for faster B_1 correction

Marta B. Maggioni,[1*] Martin Krämer,[1,2] Jürgen R. Reichenbach [1]

1 Medical Physics Group, Institute of Diagnostic and Interventional Radiology, Jena University Hospital - Friedrich Schiller University Jena, Germany.
2 Institute of Diagnostic and Interventional Radiology, Jena University Hospital - Friedrich Schiller University Jena, Germany
* marta.maggioni@uni-jena.de

Synopsis: This works proposes an improved spoiling scheme for UTE AFI based B_1 mapping that removes the dependency on the RF phase increment and reduces the acquisition time by half while still providing accurate B_1 correction.

Zusammenfassung: In dieser Arbeit schlagen wir ein verbessertes Spoilingschema für UTE AFI basiertes B_1 mapping vor. Diese Methode beseitigt die Abhängigkeit von RF Phasenfaktor und reduziert die Messzeit um die Hälfte ohne die Genauigkeit der B_1 Korrektur zu beeinträchtigen.

Motivation

T_1 estimation is a notoriously difficult topic in MRI because it often requires B_1 correction. This is especially true if a method like Variable Flip Angle (VFA) is used, where inhomogenities of the B_1 field are reflected in erroneous values of the flip angle thus leading to incorrect T_1 estimation. However most B_1 mapping methods are unable to provide a correction in short T_2^* tissues such as tendons and ligaments. Recently a B_1 mapping method that is compatible to an ultra-short echo-time (UTE) acquisition, and thus able to retrieve signal in short T_2^* species, called Actual Flip angle Imaging (AFI) has been introduced. This method, however, requires long acquisition times to achieve a sufficiently spoiled signal, which hinders its applicability in the clinical practice, and it is also highly dependent on the RF spoiling phase increment. This work presents an improved spoiling scheme for UTE AFI sequences that allows for a reduction of the acquisition time while still providing adequate B_1 correction and removing the dependency from the RF spoiling factor.

Materials and Methods

A 3D UTE sequence was modified to incorporate the two interleaved TR of the AFI sequence and to be able to modify different RF spoiling phase increment factors. The sequence was further modified to include gradient spoilers in all three spatial directions with different areas for TR_1 and TR_2. While the gradient along the z direction used alternatively the two different preselected areas for TR_1 and TR_2, the direction of the x and y gradients was additionally randomized with each repetition time. A comprehensive comparison with the different implementations of the AFI method from literature with the proposed sequence was performed in phantoms. The phantom was composed by two tubes (with 2 cm diameter) of a solution of agar and water doped with varying concentration of the contrast agent Gadovist.

Both experiments were performed on a 3T Siemens MRI scanner. The acquisition parameters for the VFA sequence were TR 10 ms, while the AFI measurements were acquired with TR_1/TR_2=10/50 and spoiling gradient areas 27/130 for both the phantom and in-vivo experiments. Additionally, during the phantom test, the original AFI implementation was acquired with TR_1/TR_2= 20/100 and a gradient areas of 450/2250 as per literature. In-vivo experiments were performed on three healthy volunteers in the knee (age 27-36 years old) with anisotropic resolution (1.8 × 1.8 × 3.8) mm^3. A 2D multi slice inversion recovery data were acquired as a reference of T_1 quantification to compare the results in the phantom.

Results

Figure 1 shows the results of B_1 corrected T_1 quantification on 1 tube of the phantom. The proposed method (last column) is shown compared to the original implementation of the AFI method[1] (I), and subsequent modifications that included the introduction of a randomized RF spoiling factor[2] (II), only randomization along the z direction[3] (III) and combination of randomization along the z direction and randomized RF spoiling factor[4] (IV).

In figure 1 it can be observed that the original AFI method still holds a dependency on the RF factor reflected both from the distributions of the measured data points and from the increased value of the standard variation (table 1), this dependency is effectively removed by the introduction of randomized spoiling along the x and y direction. It is important to notice that the original AFI implementation was acquired with a TR

combination of TR_1/TR_2=20/100 while our proposed method was acquired with 10/50,

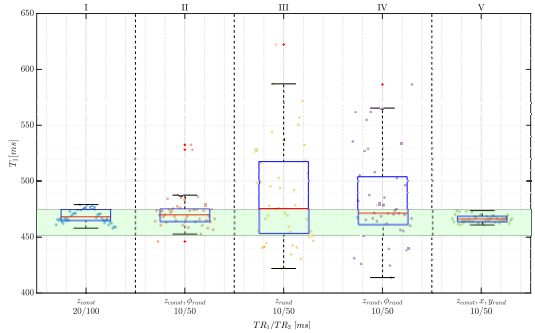

Fig. 1: Comparison of the proposed method with literature, reported are the T_1 results in phantom. The different values for the RF increment (from 0°to 180°in steps of 4) are shown as horizontal spread within each block

effectively cutting the acquisition time in half. Furthermore all the other methods presented in literature, lead to an erroneous T_1 estimation. As a ground truth the T_1 estimation from an inversion recovery sequence are reported on the graph as a green area.

Method	**I**	**II**	**III**	**IV**	**V**
T_1	468 ± 6	472 ± 15	488 ± 44	482 ± 40	465 ± 3

Tab. 1: T_1 results from the phantom experiment. All the results are in ms and provided as mean ± std

Figure 2 shows the results of the in vivo T_1 quantification before and after B_1 correction. The incorrect T_1 values towards the edge of the field of view are corrected by the application of the AFI B_1 map with the proposed method. Furthermore the results of the T_1 quantification for a few selected are reported in table 2 and are in line with current literature on the topic[5].

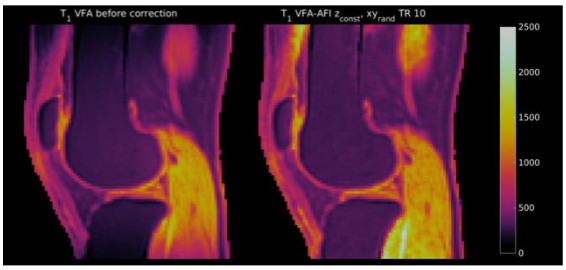

Fig. 2: In vivo T_1 maps for one volunteer before and after B_1 correction. The maps are scaled between 0 and 1500 ms.

Method	UTE T_1 VFA [ms]	UTE T_1 VFA-AFI [ms]
Patellar Tendon	600 ± 59	640 ± 56
Quadriceps Tendon	592 ± 30	768 ± 38
Bone Marrow	313 ± 5	337 ± 8

Tab. 2: Summary table of the T_1 results for selected Regions of Interest in the knee.

Discussion and Conclusion

The work of Lin and Song[4] shows that the center-out implementation of the 3D-UTE sequence contributes to the stability of the proposed method because the radial acquisition scheme effectively oversamples the center of k-space averaging small signal fluctuations.

In conclusion, we proposed an improved spoiling scheme of 3D UTE AFI B_1 mapping that is more stable than previously proposed methods due to the additional randomization of the x-y spoiling and the acquisition scheme used. The T_1 results obtained with this method were comparable with the original one and the acquisition time was reduced by 50%.

References

1. Yarnykh VL. Optimal radiofrequency and gradient spoiling for improved accuracy of T_1 and B_1 measurements using fast steady-state techniques. Magn Reson Med 2010;63:1610–26.
2. Zur Y, Wood ML, Neuringer LJ. Spoiling of transverse magnetization in steady-state sequences. Magn Reson Med 1991;21:251–63.
3. Darrasse H, Mao l.Steady-state management in fast low-angle imaging. In: Proceedings of the 5th Annual Meeting of ISMRM, Toronto, Montreal, Canada, 1986 (Abstract 234) n.d.:1.
4. Lin W, Song HK. Improved signal spoiling in fast radial gradient-echo imaging: Applied to accurate T_1 mapping and flip angle correction. Magn Reson Med 2009;62:1185–94.
5. Ma YJ et al. Whole knee joint T_1 values measured in vivo at 3T by combined 3D ultrashort echo time cones actual flip angle and variable flip angle methods. Magn Reson Med 2019;81:1634–44.

Einfluss von Messtechniken und Rekonstruktionsverfahren auf die Klassifizierbarkeit von Läsionen in der ^{23}Na-MRT

L. Ruck[1]*, A. Mennecke[2], B. Hensel[3], M. Uder[1] und A. M. Nagel[1]

[1] Radiologisches Institut, Friedrich-Alexander-Universität (FAU), Erlangen, Deutschland
[2] Neuroradiologie, Friedrich-Alexander-Universität (FAU), Erlangen, Deutschland
[3] MSBT, Friedrich-Alexander-Universität (FAU), Erlangen, Deutschland
* E-Mail-Adresse: Laurent.Ruck@uk-erlangen.de

Synopsis: Mininimum classifiable volumes (AUC > 0.9) were found to be 0.18 cm^3 (^{23}Na-MRI) and 1.2 cm^3 (^{23}Na-IR-MRI), respectively. When comparing different reconstructions (gridding, compressed sensing (CS) with and without anatomical prior information) in terms of classifiability, CS reconstruction with incorporation of anatomical ^{1}H prior information performed worst overall.

Zusammenfassung: Bei der Klassifizierung von MS-Läsionen wurden als minimal klassifizierbare Volumina (AUC > 0,9) 0,18 cm^3 (^{23}Na-MRT) bzw. 1,2 cm^3 (^{23}Na-IR-MRT) gefunden. Beim Vergleich verschiedener Rekonstruktionen (Gridding, Compressed Sensing (CS) mit und ohne anatomische Vorinformationen) hinsichtlich der Klassifizierbarkeit schnitt die CS-Rekonstruktion mit Einbezug von anatomischen ^{1}H-Vorinformationen insgesamt am schlechtesten ab.

Motivation

Eine erhöhte Na^+-Konzentration kann in vielen Fällen auf Pathologien hinweisen und wurde bei verschiedenen Erkrankungen, wie z. B. in Multiple Sklerose (MS)-Läsionen (1), beobachtet. Insbesondere wurde festgestellt, dass MS-Läsionen je nach Läsionstyp unterschiedliche Na^+-Konzentrationen aufweisen, wobei scheinbar der Grad der Gewebeschädigung in der Läsion eng mit dem Anstieg der Na^+-Konzentration verbunden ist (1). Dementsprechend wäre es für frühzeitige Therapiemaßnahmen zur Minimierung von Gewebeschäden wichtig, unterscheiden zu können, ob eine erhöhte Na^+-Konzentration in einer Läsion vorliegt oder nicht.

Material und Methoden

Um die Klassifizierbarkeit von MS-Läsionen in der ^{23}Na-MRT beurteilen zu können, wurden Simulationen nach dem Schema von Lommen (2) durchgeführt. Für die ^{23}Na-Simulation wurde eine dreidimensionale dichteangepasste Radialsequenz (3) (8000 Projektionen, (4 mm)^3, TA = 13:20 min) verwendet. Für die ^{23}Na-IR-Bilder wurde die gleiche Sequenz mit einem zusätzlichen Inversionspuls (TI = 32 ms) simuliert. Das SNR entsprach jeweils ungefähr dem SNR in Kopfmessungen bei 3 T.

Die Gridding-Rekonstruktion wurde sowohl ohne als auch mit zusätzlichem Hamming-Filter (siehe **Abb. 1 b**) durchgeführt. Für die CS-Rekonstruktionen wurde der in (4) vorgestellte iterative Algorithmus angewandt. In dieser Arbeit wurden als Regularisierungen sowohl eine Binärmaske als auch eine übliche totale Variation (CS BMTV2) bzw. eine mit ^{1}H-Wichtungsfaktoren gewichtete totale Variation (CS BMAnaWeTV2) (5) verwendet. Die CS-Wichtungsfaktoren wurden in Kopfsimulationen anhand des NRMSE optimiert.

Zur Bestimmung der Klassifizierbarkeit der Läsionen wurde ein Phantom aus weißer Hirnsubstanz (41 mmol/l, T_1 = 33 ms) sowohl ohne als auch mit zehn kugelförmigen Läsionen (86 mmol/l, T_1 = 50 ms) verschiedener Volumina (siehe **Abb. 1 a**) simuliert. Die Simulationen wurden jeweils 100-mal mit unterschiedlich verteiltem Rauschen durchgeführt. Basierend auf den Verteilungen beider Simulationen wurden sogenannte *receiver operating characteristics* (ROC-Kurven) berechnet und anhand der Fläche unter der ROC-Kurve (AUC) die Klassifizierbarkeit bewertet. Mit Hilfe von *bootstrapping* konnten zudem die 95 % - Konfidenzintervalle der AUC bestimmt werden.

Ergebnisse

Im Vergleich zur ^{23}Na-IR-MRT wird in der klassischen ^{23}Na-MRT bei gleichem Volumen ein höherer AUC-Wert und somit eine höhere Klassifizierbarkeit erreicht (siehe **Abb. 1 c**). Bei der kleinsten Läsion in der ^{23}Na-IR-MRT verläuft die ROC-Kurve diagonal (siehe **Abb. 1 d**), was auf eine vom Zufall abhängige Klassifizierung hinweist. Als minimal klassi-fizierbare Läsionsvolumina (AUC > 0,9) wurden V_{23Na} = 0,18 cm^3 und $V_{23Na\text{-}IR}$ = 1,2 cm^3 gefunden, sodass das minimal klassifizierbare Läsionsvolumen in der ^{23}Na-IR-MRT beinahe um einen Faktor 7 größer ist.

Im Vergleich der Rekonstruktionsmethoden (siehe **Abb. 1 c**) zeigte sich, dass die CS-Rekonstruktion mit anatomischen ^{1}H-Vorinformati-

onen (CS BMAnaWeTV2) am schlechtesten abschnitt. So lagen die AUC-Werte.für 8 von 10 Läsionen in der ^{23}Na-IR-MRT signifikant ($p < 0{,}05$) niedriger als für die Gridding-Rekonstruktion mit Hamming-Filter bzw. die CS BMTV2 ohne ^{1}H-Vorinformationen. Dieselbe Beobachtung trat in der ^{23}Na-MRT für die ersten drei Läsionen auf, bei denen noch keine optimale Klassifizierbarkeit (AUC = 1) erreicht wurde.

Diskussion

Der Anstieg der Klassifizierbarkeit mit dem Läsionsvolumen lässt sich einerseits durch reduzierte Partialvolumeneffekte bei größeren Läsionen begründen und andererseits verringert die höhere Voxelanzahl in größeren Volumina statistische Schwankungen des Läsionsmittelwerts.

Die verringerte Klassifizierbarkeit der ^{23}Na-IR-MRT im Vergleich zur ^{23}Na-MRT lässt sich über die zusätzliche T_1-Wichtung der IR-Sequenz erklären, welche zu einem niedrigeren Kontrast und SNR führt.

Grundsätzlich hängt die Klassifizierbarkeit stark von den für die Läsionen verwendeten Na^+-Konzentrationen und Relaxationszeiten ab, sodass die AUC-Werte in der Realität abweichen können.

Für die CS BMAnaWeTV2 wurden in der ^{1}H-Vorinformation immer Läsionen vorgegeben - auch für ^{23}Na-Simulationen ohne Läsionen. So könnte die CS BMAnaWeTV2 möglicherweise in diesen Fällen vermehrt zu falsch positiven Klassifizierungen geführt haben, wodurch insgesamt die AUC-Werte am niedrigsten waren. Im Gegensatz dazu wurden für die CS BMTV2 ohne ^{1}H-Vorinformationen höhere AUC-Werte erreicht.

Schlussfolgerung

Für die angenommenen Na^+-Konzentrationen und Relaxationszeiten ist eine Klassifizierung erst ab einem Läsionsdurchmesser von etwa 7 mm (^{23}Na-MRT) bzw. 13,2 mm (^{23}Na-IR-MRT) mit akzeptablen AUC-Werten (> 0,9) durchführbar. Hinsichtlich der Klassifzierbarkeit ergaben sich durch die Verwendung einer CS-Rekonstruktion mit Einbezug von anatomischen ^{1}H-Vorinformationen keine Vorteile, sondern eher Nachteile.

Literatur

1. Eisele P et al. Heterogeneity of acute multiple sclerosis lesions on sodium (23Na) MRI. Mult Scler 2016;22(8):1040-1047.
2. Lommen J et al. Realistic simulation of 23Na brain data: understanding the influence of acquisition parameters on the accuracy of 23Na concentration measurement. 2017.
3. Nagel AM et al. Sodium MRI using a density-adapted 3D radial acquisition technique. Magn Reson Med 2009;62(6):1565-1573.
4. Lachner S et al. Compressed sensing reconstruction of 7 Tesla (23)Na multi-channel breast data using (1)H MRI constraint. Magn Reson Imaging 2019;60:145-156.
5. Gnahm C, Nagel AM. Anatomically weighted second-order total variation reconstruction of 23Na MRI using prior information from 1H MRI. Neuroimage 2015;105:452-461.

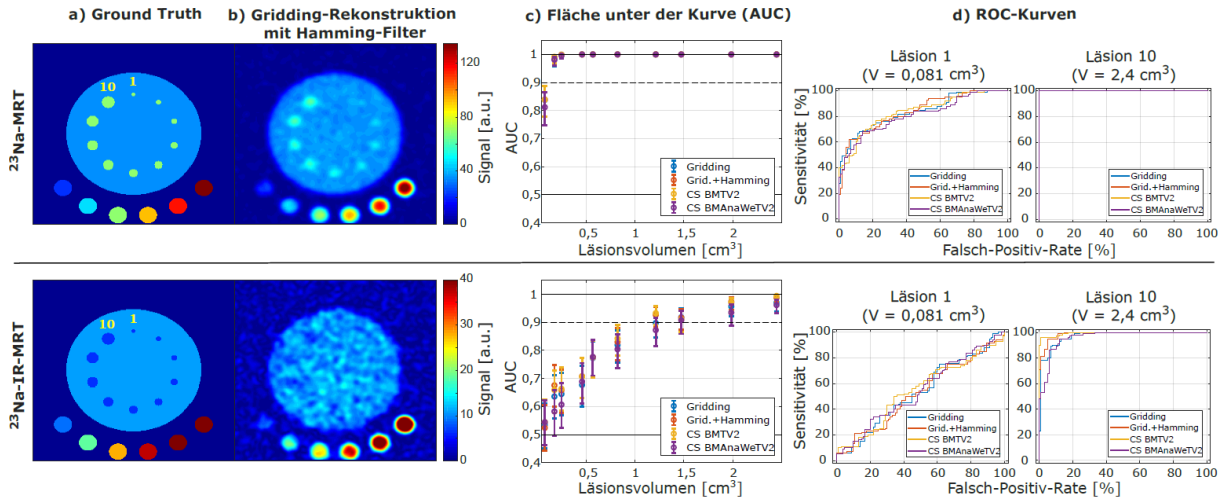

Abbildung 1: *Ground truth* (GT) der Simulation mit Läsionen (a) sowie eine beispielhafte Gridding-Rekonstruktion mit Hamming-Filter interpoliert auf die GT-Auflösung von 1 mm isotrop (b). AUC-Werte der vier Rekonstruktionsmethoden für jedes Läsionsvolumen (c) sowie ROC-Kurven der kleinsten und größten Läsion (d).

Layered graph-cuts for water–fat–silicone separation in chemical shift encoding-based breast MRI

Jonathan K. Stelter[1,2*], Christof Boehm[1], Kilian Weiss[3], Maximilian N. Diefenbach[1], Marcus R. Makowski[1], Dimitrios C. Karampinos[1]

[1] Department of Diagnostic and Interventional Radiology, School of Medicine, Technical University of Munich, Munich, Germany
[2] Physik-Department, Technical University of Munich, Garching, Germany
[3] Philips Healthcare, Hamburg, Germany
* jonathan.stelter@tum.de

Synopsis: Subjects with silicone breast implants are typically examined with a water- and fat-suppressed sequence to verify the implant's integrity. Chemical shift encoding-based water–fat separation (CSE-WFS) has been recently used to assess breast density and for extracting magnetic susceptibility maps to detect breast calcifications. However, up to now CSE-WFS cannot be applied in subjects with silicone implants. In this work, a layered graph-cut framework is presented for a joint and robust water–fat and water–fat–silicone separation.

Zusammenfassung: Bei Patienten mit Silikon-Brustimplantaten wird die Unversehrtheit des Implantats üblicherweise mithilfe einer wasser- und fettsignalunterdrückenden Sequenz festgestellt. Chemical-shift-basierte Wasser-Fett-Separierung (CSE-WFS) ermöglicht die Beurteilung der Brustdichte und die Erkennung von Kalzifikationen mithilfe der Darstellung magnetischer Suszeptibilität. Bei Patienten mit Brustimplantaten aus Silikon kann CSE-WFS jedoch nicht angewandt werden. In dieser Arbeit wird ein Framework aus geschichteten Graph-Cuts für die gemeinsame und robuste Wasser-Fett- und Wasser-Fett-Silikon-Separierung vorgestellt.

Motivation

Multi-echo gradient echo imaging has been recently combined with chemical shift encoding-based water–fat separation for quantifying water–fat composition[1,2] and for extracting magnetic susceptibility maps[3-5].

It has also been shown that CSE-WFS can be utilized for the robust separation of additional components such as silicone[6]. Silicone-separated images might allow the replacement of the water- and fat-suppressed silicone-only sequence, at a reduced examination time in combination with improved efficiency allowing for improved resolution.

However, a previously introduced method based on a single graph-cut needs a minimum of 6 echoes for the robust separation of water, fat and silicone and the regularization parameter might need to be adjusted for different subjects[6]. In this work, a graph-cut framework consisting of multiple layers is presented for the joint separation of water and fat or water, fat and silicone. Each layer allows for different signal models, spatial resolution (Fig. 1), regularization, and sampling ranges enabling a fast and more robust chemical species separation.

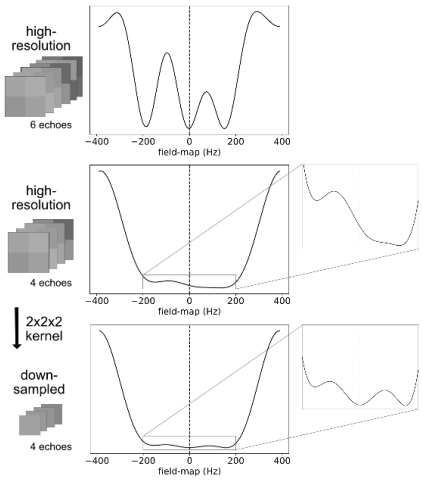

Fig. 1: Residual as function of field-map: minima are broadened and more noise-affected for 4 echoes than with 6 echoes. Signal averaging enables the minima estimation for the residual with a reduced number of echoes.

Materials and Methods

The water–fat voxel signal model was extended for silicone and its chemical shift[6]. A variable projection (VARPRO) method was applied to solve firstly for the field-map[7]. For each layer in the presented framework, residuals were calculated, and all local minima were extracted and inserted to the single-min-cut variable-layer graph-cut algorithm[8].

In difference to the previously introduced method[6], several modifications were applied:

Spatial resolution: The image can be downsampled to decrease the number of graph nodes and reduce noise sensitivity.

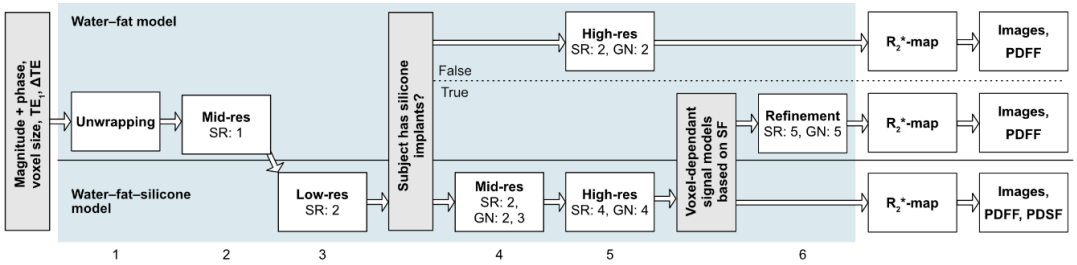

Fig. 2: Schematic diagram for the layered graph-cut method developed for field-mapping (blue area) in breast MRI. For each graph-cut layer, the layers used as prior for sampling range estimation (SR) and graph nodes insertion (GN) are denoted.

Signal model and regularization parameter: The graph-cut algorithm can be performed for different signal models (water–fat or water–fat–silicone) and regularization factors.

Field-map prior: Prior field-maps can be used as an initialization for the graph-cut algorithm by setting the sampling neighborhood or including the prior as graph nodes in the graph-cut algorithm.

The proposed method consists of multiple connected graph-cut layers with different properties summarized in Fig. 2. First, the unwrapped field-map range is found in a low-resolution layer. Subsequently, the resolution is increased, and it is determined based on the silicone fraction if silicone implants are present. If no silicone implants are present, a water–fat model is applied and a high-resolution field-map is computed. Otherwise, the water–fat and water–fat–silicone model is chosen voxel-wise based on the silicone fraction and a high-resolution field-map is computed similarly. R_2^*-maps, images and the proton-density fat fraction (PDFF) are calculated afterwards based on the field-map[9-11].

MR measurements were performed with a monopolar time-interleaved multi-echo gradient echo sequence[12] on a clinical 3T scanner with $N_{TE} = 6$, $TE_1 = 1.58$ ms, $\Delta TE = 1.28$ ms and 1.3 mm isotropic resolution (acquisition duration: 255 s). Only the first 4 echoes were used for water–fat–silicone separation. Results were compared with a clinical silicone-only scan with water and fat suppression and acquired voxel size of 1.25 x 1.88 x 3 mm³ (acquisition duration: 188 s).

Results

Figure 3 shows water, fat and silicone images and the field-map for a single subject. The axial and sagittal orientations are shown and compared to a clinical silicone-only scan. Silicone-separated images show similar sensitivity, higher resolution in the sagittal slice and better fat suppression compared to the silicone-only scan.

Discussion and Conclusion

Preliminary results show robust and fast water–fat–silicone separation for 4 echoes. The proposed method is significantly faster than a single graph-cut layer (computation time around 2-5 min dependent on hardware specifications) and increases robustness due to different image resolutions and sampling ranges.

References

1. Ding J, et al. *J Magn Reson Imaging*. 2018;48(4):971-981.
2. Borde T, et al. *Proc. Intl. Soc. Mag. Reson. Med. 29*. 2021:743.
3. Dimov AV, et al. *Magn Reson Med*. 2015;73(6):2100-2110.
4. Fatemi-Ardekani A, et al. *Med Phys*. 2009;36(12):5429-5436.
5. Schweser F, et al. *Proc. Intl. Soc. Mag. Reson. Med. 19*. 2011:1014.
6. Stelter JK, et al. *Proc. Intl. Soc. Mag. Reson. Med. 29*. 2021:3848.
7. Hernando D, et al. *Magn Reson Med*. 2008;59(3):571-580.
8. Boehm C, et al. *Magn Reson Med*. 2021;85(3):1697-1712.
9. Yu H, et al. *J Magn Reson Imaging*. 2007;26(4):1153-1161.
10. Reeder SB, et al. *J Magn Reson Imaging*. 2012;36(5):1011-1014.
11. Liu C-Y, et al. *Magn Reson Med*. 2007;58(2):354-364.
12. Ruschke S, et al. *Magn Reson Med*. 2017;78(3):984-996.

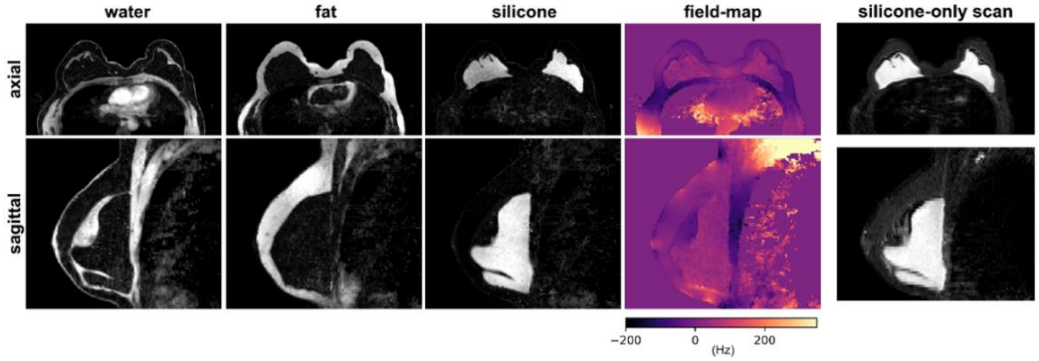

Fig. 3: In-vivo results for 4 echoes showing water–fat–silicone separation with high accuracy. The resolution of the silicone image is considerably improved in the sagittal slice due to the isotropic resolution compared to the silicone-only scan with water- and fat-suppression.

SPIRAL ^{7}Li MRI for in vivo neuroimaging of lithium in mice: a feasibility study

Tor R. Memhave[1,2,3*], Amir Moussavi[1], Susann Boretius[1,2,3]

[1] German Primate Center, Functional Imaging Laboratory, Göttingen, Germany
[2] Georg-August University of Göttingen, Göttingen, Germany
[3] International Max Planck Research School for Neurosciences, Göttingen, Germany
* e-mail: tmemhave@dpz.eu

Synopsis: We acquired *in vivo* ^{7}Li MR images after five weeks of lithium treatment from five wild-type mice. Using a 4-hour SPIRAL sequence, we found that lithium was detectable in all five mice. The ^{7}Li images were acquired at a resolution of 2×2×3 mm^3. We observed increased lithium in the central and ventral brain regions.

Zusammenfassung: In dieser Arbeit wurden in vivo ^{7}Li-MR Bilder nach fünfwöchiger Lithiumbehandlung von fünf Wildtyp-Mäusen aufgenommen. Unter Verwendung einer 4-stündigen SPIRAL-Sequenz konnten wir, in allen fünf Mäusen Lithium nachweisbar war. Die ^{7}Li-Bilder wurden mit einer Auflösung von 2×2×3 mm^3 aufgenommen. Es konnte eine erhöhte Lithium-Konzentration in den zentralen und ventralen Hirnregionen nachgewiesen werden.

Motivation

Lithium (Li) is a frontline drug in the treatment of bipolar disorder. However, despite clinical usage for over 50 years, the mode of action of Li is not fully understood. Knowledge of the *in vivo* distribution of Li in the brain, despite recent advances in Li imaging techniques, is still limited (1–4).

Li-7, 92.4% of Li, is a spin 3/2 nucleus, which has a relative sensitivity of 0.29. As Li is a trace element, we fed a Li-enriched diet to five wild-type mice. After 5 weeks of treatment we acquired *in vivo* ^{7}Li MRI using a 4-hour SPIRAL sequence. In this feasibility study, we present the first *in vivo* ^{7}Li images of the mouse brain.

Materials and Methods

Five C57BL6/N adult mice were fed a Li-enriched diet (0.3% Li_2CO_3 w/w) for five weeks and subsequently ^{7}Li MRI was acquired.

^{7}Li MRI was acquired using a 9.4T MR scanner (Bruker BioSpin) with a 30-cm horizontal bore and a BGA 12 gradient system. A dual-tuned, ^{1}H/^{7}Li, transmit-receive RF surface coil was used (Rapid Biomedical). ^{7}Li MRI was acquired with a SPIRAL sequence that had the following parameters: 2500 ms repetition time, 1.6 ms echo time, 7500 Hz acquisition bandwidth, 16×16 matrix size, 2-slices, 2×2×3 mm^3 voxel size, 5760 averages, and 4-hour acquisition time. The ^{7}Li MRI was overlaid on ^{1}H images acquired at an isotropic resolution of 0.5-mm using a fast low-angle shot (FLASH) sequence.

Image segmentation was performed by defining a threshold that optimized the inter-group variance (Otsu's method) (5). In practice this was realized in python using the *scikit-image* function *threshold_otsu*.

In figure 2, the ^{1}H images of all five mice were binarized and aligned by centroids. The average ^{7}Li images were resized using nearest neighbor interpolation and aligned along with the ^{1}H images. Partial-volume correction and coil signal profile correction were done at the resolution of the ^{7}Li images, 2×2×3 mm^3.

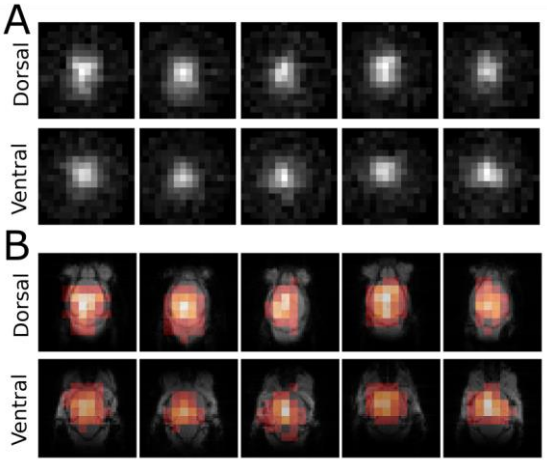

Figure 1: ^{7}Li MRI acquired from five mice, A. The ^{7}Li images were acquired in vivo using a 4-hour SPIRAL sequence. Segmented ^{7}Li images were overlaid on ^{1}H images, B, which showed that the signal arose, almost exclusively, from the brain.

Results

^{7}Li MRI allowed for *in vivo* detection of Li in all five mice, figure 1A. The signal-to-noise ratio was, as expected, higher in the dorsal than the ventral slice (5.87 vs. 5.50). The better SNR was accompanied by a lower inter-animal variation of the Li signal in the dorsal compared to the ventral slice. We note that in the segmented

^{7}Li images, figure 1B, the signal arose predominantly from the brain.

An overlay of the group average of ^{1}H and ^{7}Li images revealed that Li signal almost exclusively originated from the brain, figure 2A. The signal intensity was largest in the central brain regions of both the dorsal and ventral slice.

The ^{7}Li MR images showed a large signal intensity in the central brain regions, which may be the result of these voxels containing more tissue, relative to the edges of the brain. In order to remove this partial-volume effect, we binarized each ^{1}H image (brain tissue versus no tissue) and calculated the percentage of tissue in each voxel. The partial-volume corrected ^{7}Li image had improved signal quality near the edges of the brain, figure 2B.

We note that the signal-to-noise ratio was higher in the dorsal than ventral slice, which may result from the proximity of the dorsal slice to the surface coil. We therefore corrected for the RF coil signal intensity profile. The ^{7}Li image corrected this way revealed an increased Li signal in the ventral and central brain regions, figure 2C.

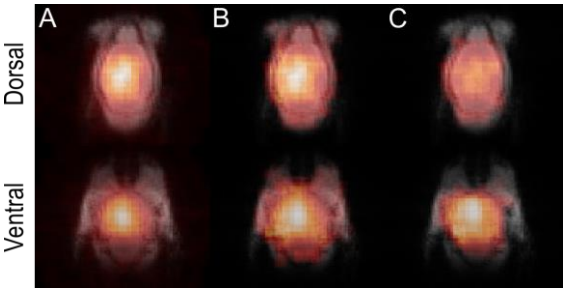

Figure 2: The average ^{7}Li image after centroid alignment, A. The ^{7}Li images were corrected for partial-volume effect, which increased the signal intensity near the edge of the brain, B. The ^{7}Li images were further corrected for the RF coil signal intensity profile, C.

Discussion

With the here proposed SPIRAL ^{7}Li MRI sequence a spatial resolution of 2×2×3 mm^{3} could be achieved within 4 hours.

This resolution is, to our knowledge, the highest currently reported for *in vivo* ^{7}Li MRI and even an improvement to those achieved in 36 hours on an *ex vivo* rat (1).

The signal-to-noise ratio of our SPIRAL ^{7}Li MRI was sufficient for *in vivo* Li imaging. However, despite a 4-hour acquisition time the spatial resolution was still limited.

As a result, we state with caution that our data indicated that Li was found in higher concentration in the ventral brain, contradicting *ex vivo* results from rats (1). Furthermore, we note that Li signal intensity was low in both the olfactory bulb and cerebellum. The olfactory bulb has previously been shown in *ex vivo* adolescent mice to have high concentrations of Li (4); however, it remains unclear whether adult and adolescent mice have different Li distributions. Previously reported lower Li concentrations in the cerebellum, especially in the white matter, are in accordance with our findings (1,6).

Conclusion

While *in vivo* neuroimaging of Li remains a challenge, we have presented the first *in vivo* ^{7}Li MRI of mice. The usage of SPIRAL encoding, compared with traditional Cartesian encoding, allowed for a higher signal-to-noise ratio, making *in vivo* ^{7}Li MRI feasible. It is our belief that while ^{7}Li MRI is still limited in resolution, it may in combination with other MR modalities and murine disease models help explain lithium's mode of action.

References

1. Stout J, Hanak AS, Chevillard L, et al. Investigation of lithium distribution in the rat brain ex vivo using lithium-7 magnetic resonance spectroscopy and imaging at 17.2 T. NMR Biomed 2017;30.

2. Stout J, Hozer F, Coste A, et al. Accumulation of Lithium in the Hippocampus of Patients With Bipolar Disorder: A Lithium-7 Magnetic Resonance Imaging Study at 7 Tesla. Biol. Psychiatry 2020;88:426–433.

3. Smith FE, Thelwall PE, Necus J, Flowers CJ, Blamire AM, Cousins DA. 3D 7Li magnetic resonance imaging of brain lithium distribution in bipolar disorder. Mol. Psychiatry 2018;23:2184–2191.

4. Zanni G, Michno W, Di Martino E, et al. Lithium accumulates in neurogenic brain regions as revealed by high resolution ion imaging. Sci. Rep. 2017;7:1–12.

5. Otsu N. A Threshold Selection Method from Gray-Level Histograms. IEEE Trans. Syst. Man. Cybern. 1979;9:62–66.

6. Heurteaux C, Ripoll C, Ouznadji S, Ouznadji H, Wissocq J-C, Thellier M. Lithium transport in the mouse brain. Brain Res. 1991;547:123–129.

Bestimmung von ultrakurzen T_2^* Relaxationszeiten

N. Egger,[1*] M. Müller, [1] B. Hensel, [2] M. Uder[1] und A. M. Nagel[1,3]

[1] Radiologisches Institut, Friedrich-Alexander Universität Erlangen-Nürnberg (FAU), Erlangen, Deutschland
[2] Max Schaldach-Stiftungsprofessur für Biomedizinische Technik (MSBT), Friedrich-Alexander-Universität Erlangen-Nürnberg (FAU), Erlangen, Deutschland
[3] Abteilung Medizinische Physik in der Radiologie, Deutsches Krebsforschungszentrum (DKFZ), Heidelberg, Deutschland
* nico.egger@uk-erlangen.de

Synopsis: In a comparative measurement, the relaxation times of cruciate ligament and patellar tendon were determined at three different field strengths. In addition, signal differences between single-echo and multi-echo measurements were demonstrated and investigated.

Zusammenfassung: In einer Vergleichsmessung wurden die Relaxationszeiten von Kreuzband und Patella-Sehne an drei verschiedenen Feldstärken bestimmt. Zudem wurden Signalunterschiede zwischen Single-Echo und Multi-Echo Messungen aufgezeigt und untersucht.

Motivation

Die UTE-Sequenz ermöglicht es, Signale von Geweben mit sehr kurzen transversalen Relaxationszeiten (≤ 1 ms), wie beispielsweise verschiedener Sehnen und Bänder des Knies, aufzunehmen. Dabei könnte das SNR der UTE-Aufnahmen möglicherweise durch Einsatz von höheren Magnetfeldstärken noch verbessert werden. Dies hängt allerdings stark davon ab, wie sich die Relaxationszeiten des untersuchten Gewebes für höhere Feldstärken verhalten. Aus diesem Grund wurden die T_2^*-Zeiten von Kreuzband und Patella-Sehne bei drei verschiedenen Feldstärken bestimmt. Da UTE-Sequenzen anfällig für Signalartefakte sind, wurden außerdem Signalunterschiede zwischen Single-Echo (SE) und Multi-Echo (ME) Messungen untersucht.

Material und Methoden

Die verwendete UTE-Sequenz basiert auf einem dreidimensionalen, radialen, dichte-angepassten Aufnahmeschema [1]. Zur Korrektur von Ungenauigkeiten des Gradientensystems wurden vor den eigentlichen Messungen Referenzmessungen gemäß [2] durchgeführt und die dadurch gemessenen Gradienten-Trajektorien zur Rekonstruktion der darauffolgenden Messungen verwendet. Der Vergleich zwischen SE und ME Messungen wurde bei einer Feldstärke von 3 T durchgeführt, wobei ein sphärisches Phantom verwendet wurde, welches eine dreiprozentige Agaroselösung enthält. Die SE Messung besteht aus fünf separaten Aufnahmen bei denen jeweils ein Echo zu einer Echozeit von TE = 0.1/6.5/13/19.5/26 ms aufgenommen wird. Bei der ME Messung werden dieselben Echos alle in einer einzelnen Messung aufgenommen, wobei nach jeder Auslese ein Rewinder-Gradient gefahren wird. Zur Darstellung möglicher Unterschiede wurde aus den Echos der beiden Aufnahmen der relative Signalunterschied ΔS bestimmt, der sich berechnet durch:

$$\Delta S(TE) = \frac{S_{\mathrm{Single}}(TE) - S_{\mathrm{Multi}}(TE)}{S_{\mathrm{Single}}(TE)}$$

Für die Vergleichsmessung der T_2^*-Zeiten von Patella und Kreuzband wurden an einem Probanden (m, 30 Jahre) Messungen an drei verschiedenen Feldstärken von 1.5 T, 3 T und 7 T durchgeführt. Zur Aufnahme des Signalzerfalls wurden dabei 12 SE Messungen mit Echozeiten zwischen 0.08 und 22 ms aufgenommen (Sequenzparameter einer SE Messung: Auflösung = $(0.75\ \mathrm{mm})^3$, FOV = $(140\ \mathrm{mm})^3$, TR = 28 ms, FA = 10 °, T_{RO} = 1 ms, Projektionen = 8000, TA = 4:08 min). Für die Auswertung wurde für jede Echozeit der Signalmittelwert innerhalb einer entsprechenden ROI berechnet und mit der in Matlab (R2017b, MathWorks, Natick, USA) implementierten *non-linear least squares* Methode gefittet. Als Fitfunktion wurde dabei ein bi-exponentielles Modell verwendet:

$$S(t) = S_0 \cdot \left(f_s \cdot e^{-\frac{t}{T_{2,s}^*}} + (1 - f_s) \cdot e^{-\frac{t}{T_{2,l}^*}} \right) + n$$

Ergebnisse

Der Vergleich von SE und ME Messung (Abbildung 1) zeigt, dass es ab dem zweiten Echo zu Signalunterschieden zwischen den beiden Aufnahmen kommt. Die Unterschiede steigen von Echo zu Echo an, sind innerhalb des Phantoms nicht homogen verteilt und treten sowohl mit positivem als auch negativem Vorzeichen auf. Die maximalen Signalunterschiede liegen in einem Bereich zwischen 20-30 %. In den Rohdaten der Messung konnte zudem ein über die Echos zunehmender Unterschied in den

Phasendaten zwischen SE und ME Messung festgestellt werden.

In Abbildung 2 a) sind ROI und zugehöriger Fit für die Messung der Patella-Sehne bei 3T dargestellt. Der bi-exponentielle Fit stimmt gut mit dem beobachteten Signalverlauf überein. Abbildung 2 b) zeigt die Mittelwerte und Standardabweichungen der Fit-Parameter die für Kreuzband und Patella-Sehne an den drei verschiedenen Feldstärken bestimmt wurden.

Diskussion

Für die Abweichungen der ME Daten zu den SE Daten konnten im Laufe der Arbeit keine endgültige Ursache sowie Lösung bestimmt werden. Allerdings deuten unsere Untersuchungen darauf hin, dass die Signalunterschiede durch Fehler in den Phasen-Daten der ME Messungen entstehen die möglicherweise durch Gradienten-induzierte Wirbelstromeffekte ausgelöst werden.

Die $T_{2,s}^*$-Zeiten der Patella-Sehne, die den geringsten Fehler aufweisen, deuten auf eine Abnahme der transversalen Relaxationszeit mit steigender Feldstärke hin.

Mögliche Ursachen der vergleichsweise hohen Fehler der restlichen Fit-Parameter könnten sowohl in dem hohen Undersampling-Faktor sowie in Bewegung des Probanden während der Messung liegen. Um diese Probleme zu verringern, sollten die dargestellten Signalabweichungen von ME Messungen für zukünftige Untersuchungen gelöst werden.

Literatur

1. Nagel AM, Laun FB, Weber MA, Matthies C, Semmler W, Schad LR. Sodium MRI using a density-adapted 3D radial acquisition technique. Magn Reson Med 2009;62(6):1565-1573.

2. Duyn JH, Yang Y, Frank JA, van der Veen JW. Simple correction method for k-space trajectory deviations in MRI. J Magn Reson 1998;132(1):150-153.

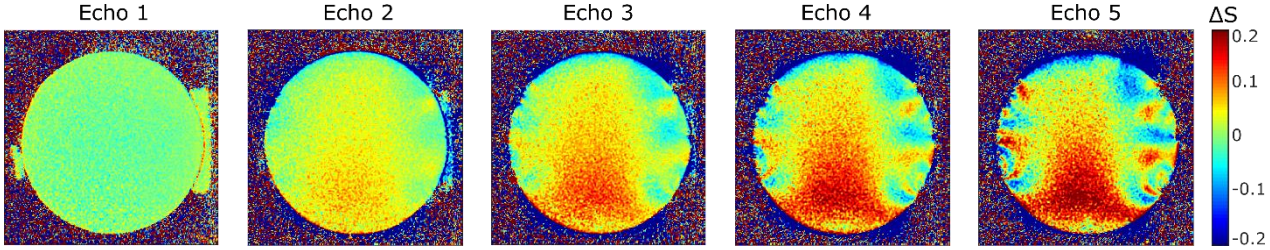

Abb. 1: Signalunterschiede ΔS, die zwischen den fünf Echos der SE und ME Aufnahmen (Auflösung = (0.75 mm)^3, TR = 33 ms, FA = 10 °, T_{RO} = 1 ms, Projektionen = 10000) bestimmt wurden, dargestellt für eine beispielhafte, koronale Schicht.

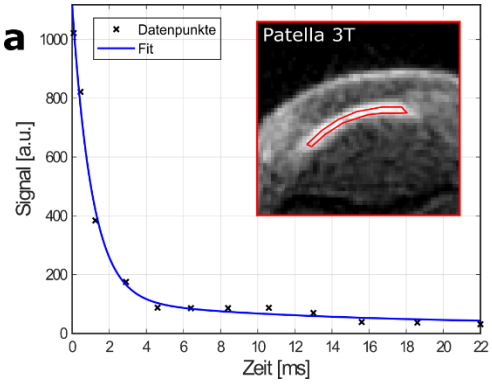

b

	Kreuzband			Patella-Sehne		
B_0 [T]	$T_{2,s}^*$ [ms]	$T_{2,l}^*$ [ms]	f_s [%]	$T_{2,s}^*$ [ms]	$T_{2,l}^*$ [ms]	f_s [%]
1.5	2.2 ± 0.6	11 ± 4	63 ± 14	1.31 ± 0.21	10 ± 8	89 ± 8
3	2.2 ± 0.4	8.8 ± 1.4	56 ± 10	1.07 ± 0.15	12 ± 11	92 ± 6
7	1.85 ± 0.25	7.7 ± 1.1	60 ± 8	0.70 ± 0.08	7 ± 4	88 ± 5

Abb. 2: a) ROI, zugehörige Signalmittelwerte und bi-exponentieller Fit der Patella-Sehne bei einer Feldstärke von 3 T. b) Relaxationsparameter, die mithilfe des bi-exponentiellen Fits für die zwei untersuchten Gewebearten an den drei verschiedenen Feldstärken bestimmt wurden.

Assessment of Whole-Body Fat Using Magnetic Resonance Imaging: Pilot Study and Validation in a Population-based Cohort

Kromrey ML[1], Laqua R[2], Hernando D[3], Effler J[1], Ittermann T[4], Friedrich N[5], Völzke H[4], Hoffmann RT[6], Hosten N[1], Kühn JP[6]

[1] Institute of Diagnostic Radiology and Neuroradiology, University Medicine, Greifswald, Germany
[2] Department of Diagnostic Radiology and Neuroradiology, University Medicine, Kiel, Germany
[3] Departments of Radiology, Medical Physics, Biomedical Engineering, Medicine, University of Wisconsin-Madison, Madison, WI, USA
[4] Institute for Community Medicine, University Medicine Greifswald, Greifswald, Germany
[5] Institut für Klinische Chemie und Laboratoriumsmedizin, University Medicine Greifswald, Greifswald, Germany
[6] Institute and Policlinic of Diagnostic and Interventional Radiology, Medical University, Carl-Gustav Carus, Dresden, Germany
*marie-luise.kromrey@uni-greifswald.de

Synopsis: In this study we determined whole-body fat volume using confounder corrected chemical shift encoded magnetic resonance imaging (CSI-MRI) and a newly developed segmentation algorithm. Fat content of different body compartments were successfully measured in all volunteers. Image evaluation by two readers showed the newly developed fat segmentation algorithm is a reliable approach for the assessment of the different tissue and organ fat contents. Correlation analyses with clinical proband data showed differences in distribution of fat compartments, especially between men and women.

Zusammenfassung: In dieser Studie stellen wir einen neu entwickelten Segmentierungsalgorithmus zur Bestimmung des Ganzkörperfettvolumens mittels confounder corrected chemical shift encoded magnetic resonance imaging (CSI-MRI) vor. Der Fettgehalt unterschiedlicher Körperkompartimente wurde mithilfe der Methode erfolgreich in allen Probanden ermittelt. Die Bildanalyse durch zwei Reader ergab, dass der angewendete Algorithmus eine robuste Methode zur Bestimmung des Fettgehaltes unterschiedlicher Gewebe und Organe ist. Korrelationsanalysen mit klinischen Probandendaten zeigten eine unterschiedliche Verteilung der Fettkompartimente, insbesondere zwischen Männern und Frauen.

Motivation

The increasing incidence of the metabolic syndrome is considered one of the most important challenges for health care systems in industrialized countries. Although the body mass index (BMI) is an accepted and widely used indicator of obesity, fat content and distribution have an important impact on the metabolic syndrome (1). Likewise, evaluation of fat compartments allows a more accurate prediction of metabolic risk than total body fat. Especially abdominal fat is strongly associated with insulin resistance and disease outcome(2-4). Furthermore, fat deposition in organs such as liver and pancreas impairs their metabolic function. A manual segmentation of fat compartments tends to be highly time consuming, making it impractical for clinical setting. Therefore, the purpose of this study was to develop an algorithm to assess fat compartments of the whole body and demonstrate its feasibility using whole-body CSI-MRI.

Materials and Methods

Four hundred sixty-six volunteers aged 36 to 87 years (259 women) underwent whole-body MRI including five-echo chemical shift encoded sequences acquired in 5 steps. After confounder correction, whole-body proton-density fat fraction was acquired. Based on tissue fat content, we developed a post-processing algorithm for segmentation of fat compartments on a preliminary validation cohort of 73 volunteers categorized according to their body mass index (BMI) into healthy (n = 25; BMI: 19.4 – 24.9), overweight (n = 24; BMI: 25.0 – 29.9) and obese (n = 24; BMI: 30.0 – 37.5). Using this algorithm, total body fat volume (TAT), subcutaneous fat volume (SAT), visceral fat volume (VAT), mediastinal fat volume (MAT) and liver fat content (LFC) were assessed. Robustness of the algorithm was tested by evaluation of inter- and intra-observer variability (n=73) by two observers using Bland-Altman analysis. Further, correlation with gender, age and factors of metabolic syndrome was undertaken.

Results

Intra-observer variability (mean bias (%) ± standard deviation) (TAT/SAT/FAT/LFC: -0.1±0.3/0.4±1.0/0.2±0.4/0.4±1.0) and inter-observer variability (TAT/SAT/FAT/LFC: 0.0±0.3/0.9±1.4/0.4±0.8/0.9±1.6) was small.

SAT, VAT, MAT and LFC demonstrated significant gender-related differences with women displaying higher subcutaneous fat, whereas men had higher visceral, mediastinal and liver fat. No significant difference was seen for total adipous tissue (p=0.21). After adjustment for age, sex and smoking status all fat compartments increased significantly with BMI, blood glucose and HbA1c level (p<0.05). No significant impact on fat compartments was detected for LDL cholesterol, whereas HDL cholesterol had a negative on all fat compartments.

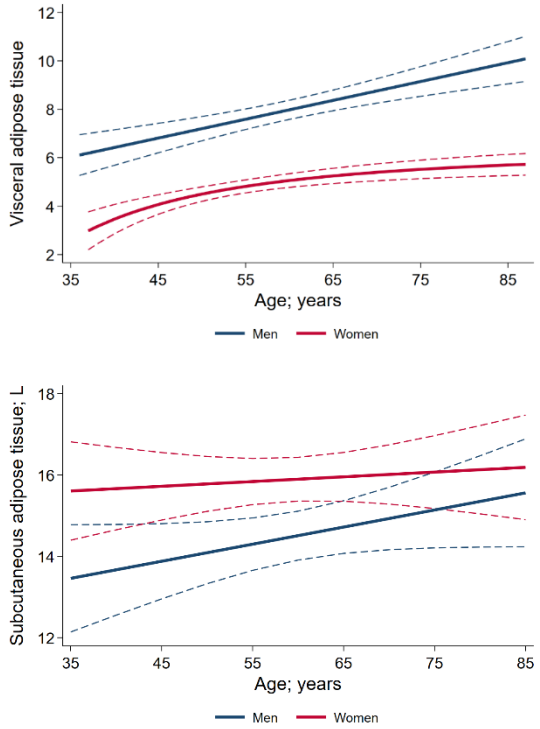

Fig. 1: Association of age and sex with visceral adipose tissue and subcutaneous adipose tissue.

Conclusion

CSI-MRI is a feasible approach to assess whole-body fat volume and fat compartments. The technique may offer new possibilities in imaging of metabolic disorders.

References

1. Vega GL, Adams-Huet B, Peshock R, Willett D, Shah B, Grundy SM. Influence of body fat content and distribution on variation in metabolic risk. J Clin Endocrinol Metab 2006;91(11):4459-4466.

2. Pascot A, Despres JP, Lemieux I, Bergeron J, Nadeau A, Prud'homme D, Tremblay A, Lemieux S. Contribution of visceral obesity to the deterioration of the metabolic risk profile in men with impaired glucose tolerance. Diabetologia 2000;43(9):1126-1135.

3. Bergman RN, Kim SP, Catalano KJ, Hsu IR, Chiu JD, Kabir M, Hucking K, Ader M. Why visceral fat is bad: mechanisms of the metabolic syndrome. Obesity (Silver Spring) 2006;14 Suppl 1:16S-19S.

4. Demerath EW, Reed D, Rogers N, Sun SS, Lee M, Choh AC, Couch W, Czerwinski SA, Chumlea WC, Siervogel RM, Towne B. Visceral adiposity and its anatomical distribution as predictors of the metabolic syndrome and cardiometabolic risk factor levels. Am J Clin Nutr 2008;88(5):1263-1271.

Mapping myelin content in ex-vivo MS brain tissue using short-T_2 MRI of the lipid-protein bilayer

E.L. Baadsvik,[1] M. Weiger,[1*] R. Froidevaux[1], W. Faigle,[2] B.V. Ineichen[2] and K.P. Pruessmann[1]

[1] Institute for Biomedical Engineering, ETH Zurich and University of Zurich, Zurich, Switzerland.
[2] Neuroimmunology and MS Research, Neurology Clinic, University Hospital Zurich and University of Zurich, Zurich, Switzerland.
* weiger@biomed.ee.ethz.ch.

Synopsis: Ultrashort-T_2 signal from white matter can be captured for imaging using dedicated short-T_2 techniques. In this work, such methods were applied to D_2O-exchanged human brain tissue from four donors diagnosed with multiple sclerosis to obtain 0.39 mm isotropic resolution MR images of the ultrashort-T_2 tissue components and a lower-resolution multi-TE image series used to produce maps of the relative content of myelin lipid-protein bilayer. The contrast in these images was compared with corresponding myelin-stained cryosections and photographs, yielding promising correlation.

Introduction

Myelin is vital to the development and function of the central nervous system, and, consequently, demyelinating disorders such as multiple sclerosis (MS) can have devastating effects. It would be of great interest for the diagnosis, treatment and monitoring of such diseases, as well as the study of demyelination and myelin repair, to noninvasively track myelin content.

Development of MRI techniques for myelin mapping has largely been focused on the unique relaxation properties of myelin water or on magnetisation transfer (1-3). However, with the advancement of short-T_2 imaging technology, approaches targeting the extremely rapidly decaying MR signal of the myelin lipid-protein bilayer have become feasible (4-7). The aim of the present work is to apply the method presented in Ref. (7) for mapping the myelin content of ex-vivo porcine brain to tissue from MS patients and validate the image findings with histological myelin staining.

Methods

Tissue slices (2-3 mm thick and around 15x15 mm^2) from four MS patients (UK brain bank) were investigated.

In order to produce images depicting primarily non-aqueous proton content, H_2O in the samples was exchanged with D_2O prior to imaging (similar procedure to Refs. (4,7)).

To capture signal from the myelin bilayer, dedicated short-T_2 techniques and hardware are needed. This work relied on a high-performance gradient system (8), fast transmit/receive switches (9) and a proton-free loop coil of 40 mm diameter. Two different imaging sequences were used, the zero-TE variant HYFI (10) (protocol 1, with amplitude coefficient 0.17 and target-T_2 of 50 µs) and single-point imaging (SPI) (11) (protocol 2). See Table 1 for scan parameters.

	FOV [mm]	Nom. res. [mm]	G [mT/m]	BW [kHz]	TE [µs]	RF pulse	TR [ms]	Avg.	Scan time [m:s]
1	50	0.39	200	425	10.9	2 µs hard	1	32	27:41
2	50	1.56	3.5-221	7.5-470	2000-33	2 µs hard	3	4	03:34

Table 1: Protocols for MRI of the myelin bilayer. Pulse power was adjusted for maximum signal yield, leading to flip angles of approximately 2º.

The SPI protocol, consisting of fourteen images acquired at different TE, captures signal decay over time. The behaviour of this decay was analysed by means of a fitting procedure, as described in Ref. (7). The underlying model contains three signal components of Lorentzian or super-Lorentzian lineshape (with T_2 or $T_{2,min}$, respectively), namely water (T_2 of 50 ms, chemical shift of 4.7 ppm), myelin bilayer (denoted uT_2-S, $T_{2,min}$ of ~10 µs) and residual ultrashort-T_2 signal (denoted uT_2-L, $T_{2,min}$ of ~100 µs).

Specific T_2 values of the non-aqueous components were found by fitting the average signal from normal-appearing white matter (WM) regions in samples 1 and 2. Maps of the amplitude contributions of each component were generated through voxel-by-voxel fitting where, to increase fit stability, all readily-determined parameters were fixed.

Tricubic interpolation was performed on all SPI data, reducing voxel size by a factor of 2, and an additional factor of 3 was applied for display purposes.

Subsequent to imaging, the samples were cryosectioned (10 µm) and underwent immunohistochemistry for myelin oligodendrocyte glycoprotein (MOG) with haematoxylin counterstain. MOG staining density is closely related to tissue myelin density.

Results

The $T_{2,min}$ times of the non-aqueous components were found to be 6.5 µs and 110 µs, which is in good agreement with expected values.

An example single-voxel fit is shown in Figure 1. The T_2 times of all three components were fixed, and the fit found the chemical shifts of the uT_2-S and uT_2-L components at 1.26 ppm and 2.12 ppm, respectively. The former corresponds well with the expected chemical shift of fat, supporting the claim that the uT_2-S component represents the myelin bilayer.

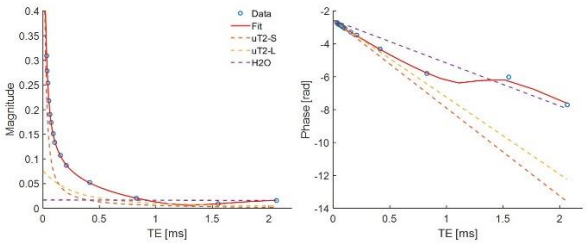

Fig. 1: Example of a single-voxel fit of the multi-TE data, showing normalised magnitude (left) and phase (right) evolution for a normal-appearing WM region in sample 1. After around 1 ms the water signal dominates.

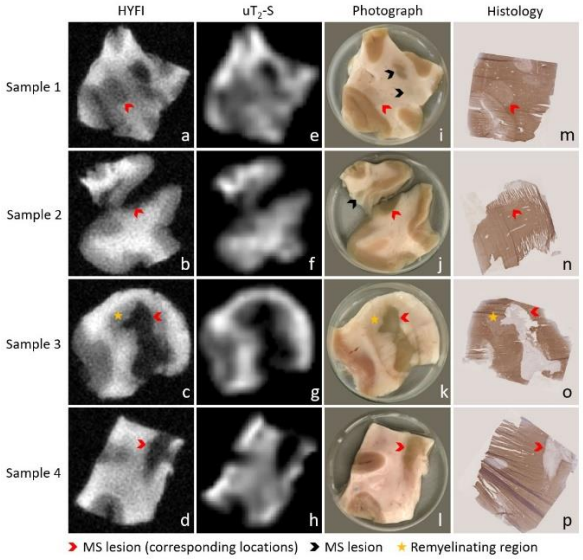

Fig. 2: Image series showing the correlation between MRI results, photographs and histology for all samples. a-d) High-resolution HYFI images, e-h) amplitude maps of the uT_2-S fit component, i-l) sample photographs, m-p) corresponding 10 µm cryosections with myelin staining using immunohistochemistry for MOG (brown) and haematoxylin counterstaining (purple).

Figure 2 presents MR results, visual photographs and myelin-stained cryosections for all samples. Note that as a result of the D_2O exchange, practically all signal in the MR images is non-aqueous. The HYFI images demonstrate the ability of dedicated short-T_2 imaging systems to image the non-aqueous components of brain tissue at high resolution, and the amplitude maps of the uT_2-S component are interpreted as depicting relative myelin content.

Both MR results show significant correlation with the sample photographs. Grey matter (GM) and WM are clearly distinguishable, with GM producing less MRI signal and giving lower uT_2-S amplitude than WM. MS lesions hardly produce signal, indicating a lack of detectable non-aqueous protons. Direct comparison of the MR images with the corresponding myelin-stained sections shows a clear correlation between MR signal intensity and MOG staining density. The amplitudes of the water and uT_2-L components are small compared to the uT_2-S component, constituting only around 2 % and 8 %, respectively.

Discussion and Conclusion

While the analysis of the SPI data gave conclusive results for the uT_2-S component representing the myelin bilayer, there is likely additional information present in the observed signal evolutions which is yet to be extracted. Further work should also include validation in samples not subjected to D_2O exchange and translation to in-vivo studies.

Overall, accessing the myelin bilayer through short-T_2 imaging methods was shown to be feasible also in human tissue. Notably, the MR image contrast enables depiction of MS lesions to a similar degree as histological MOG-staining.

References

1. Piredda GF et al. Magn Reson Med. 2021;85:627-652.
2. MacKay AL et al. Brain Plast. 2016;2:71-91.
3. Varma G et al. Magn Reson Med. 2015;73:614-622.
4. Wilhelm MJ et al. Proc Natl Acad Sci. 2012;109:9605-9610.
5. Du J et al. NeuroImage. 2014;87:32-41.
6. Seifert AC et al. NeuroImage. 2017;163:358-367.
7. Weiger M et al. NeuroImage. 2020;217:116888.
8. Weiger M et al. Magn Reson Med. 2018;79:3256-3266.
9. Brunner DO et al. J Magn Reson. 2016;263:147-155.
10. Froidevaux R et al. NMR Biomed. 2021.
11. Balcom BJ et al. J Magn Reson Ser A. 1996;123:131-134.

Partial Simultaneous Multi-Slice Acquisition of Combined T2-Weighted Imaging of the Human Brain and Cervical Spinal Cord*

Ying Chu,[1*] Jürgen Finsterbusch[1*]

[1] Systemische Neurowissenschaften, Universitätsklinikum Hamburg-Eppendorf, Hamburg, Deutschland
* y.chu@uke.de, j.finsterbusch@uke.de

Synopsis: In this study, combined fMRI T2*-weighted imaging of the human brain and cervical spinal cord has been accelerated by simultaneous multi-slice (SMS) imaging of the brain volume. The implementation has been tested and evaluated in vivo and shows a similar performance to non-accelerated combined and brain-only measurements. With the much shorter acquisition times achievable it could help to improve brain volume coverage of cortico-spinal fMRI.

Zusammenfassung: In dieser Studie wurde die kombinierte T2*-gewichtete fMRI-Bildgebung von Gehirn und zervikalem Rückenmark durch simultane Mehrschicht-Bildgebung (SMS) für das Gehirnvolumen beschleunigt. Die Implementierung wurde getestet und evaluiert und zeigte eine ähnliche Leistung wie eine nicht beschleunigte kombinierte und Gehirnmessung. Durch die verkürzte Messzeit kann das Gehirnvolumen in kombinierten Gehirn-Rückenmarksmessungen vergrößert werden.

Motivation and Introduction

Combined functional magnetic resonance imaging (fMRI) of the brain and cervical spinal cord (1) allows to assess the functional connectivity between these two regions, e.g., in pain processing (2) or sensory and motor function (3). In previous approaches (1), volume coverage and temporal resolution were limited, because the standard implementations of simultaneous multi-slice (SMS) (4) imaging are not compatible with two different slice groups and the SMS performance of typical coils in the neck region is low. In this study, this problem is addressed by implementing a “partial-SMS” approach in which only the brain volume is accelerated with SMS while the spinal cord volume is acquired conventionally. Experiments in vivo show a similar performance to non-SMS and brain-only SMS measurements, but with reduced minimum acquisition time.

Materials and Methods

Experiments were performed on a 3T whole-body MR system (PrismaFit, Siemens Healthineer) using a 64-channel head-neck coil. A healthy volunteer was investigated after his informed consent was obtained. EPI acquisitions with a 7/8 partial Fourier and GRAPPA with an acceleration factor of 2 and 36 reference lines were used for both volumes. Other EPI parameters are shown in Fig. 1. The minimum TRs are different for acquisitions with and without SMS; but to compare the performance, a fixed TR of 4177ms and flip angle of 86° was used to avoid different saturation effects.

	brain	spinal cord
number of slices	60	12
in-plane resolution	$2.0 \times 2.0\ mm^2$	$1.2 \times 1.2\ mm^2$
slice thickness	$2\ mm$	$3.5\ mm$
TE	$24\ ms$	$27\ ms$
SMS factor (brain)/minTR	$3 / 1975\ ms$	
	$- / 4177\ ms$	
FOV	$220\ mm$	$136\ mm$

Fig. 1: Important parameters of the EPI protocol

A dynamic update of the frequency and first order shim values was performed between the two volumes (see Fig. 2) as shown in a previous study (1) for all acquisitions.

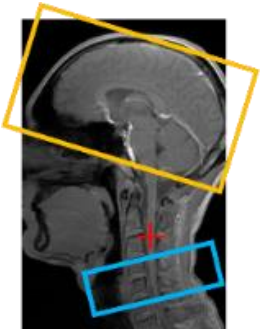

Fig. 2: Localizer image with position of isocenter (red cross) and brain (yellow) and spinal cord (blue) volumes

The image reconstruction pipeline was modified to ignore the SMS part of the reconstruction for spinal cord slices while brain slices pass the full pipeline including the SMS functionality.

For the evaluation, gray matter images are segmented with SPM12 and Matlab2020b.

SNRs were calculated from a series of 20 measurements.

Results

Brain and spinal cord example EPI are shown in Figure 3, which were obtained in a single measurement covering both volumes ("combined") with an SMS acceleration factor of 3 for the brain volume.

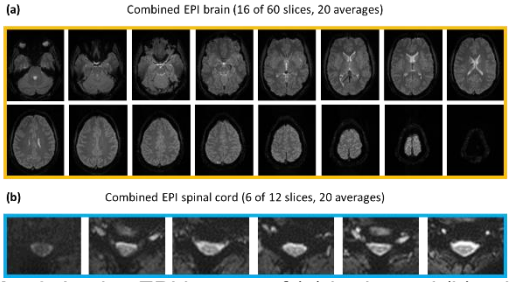

Fig. 3: In vivo EPI images of (a) brain, and (b) spinal cord using an acceleration factor of 3 for the brain volume only.

Figure 4 shows the MR images and SNR maps of gray matter of several slices in the brain volumes, which shows that the combined fMRI with an SMS factor of 3 for the brain volume has a very good image quality comparable to that of a single-volume acquisition, both without and with SMS. However, the minimum achievable TR is reduced from 4177ms to 1975ms.

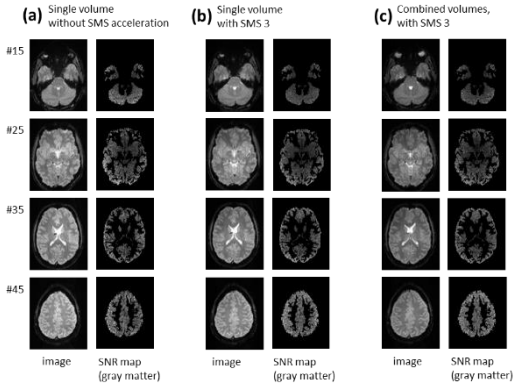

Fig. 4: Mean and SNR maps from gray matter comparison in brain volume.

The results of SNR measurements in vivo are summarized in Figure 5. Comparing single-volume and "combined" measurements for brain slices reveals no relevant difference in the whole brain volume for accelerations both without and with SMS which indicates that the partial acceleration of "combined" measurements provides the same performance as a single volume acquisition with the same SMS factor.

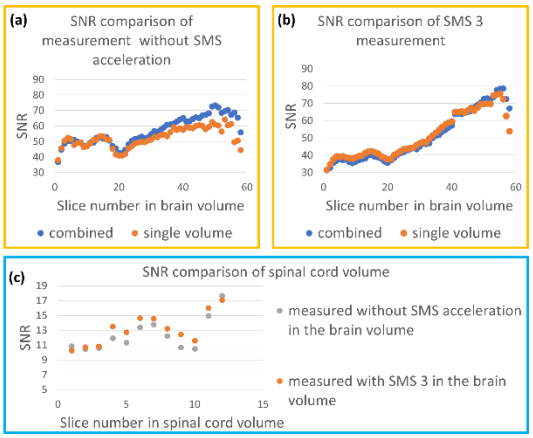

Fig. 5: SNR measurements in (a) gray matter map for brain and for (b) spinal cord volume

Discussion and Conclusion

In this study, simultaneous multi-slice acceleration of combined T2*-weighted acquisitions of the human brain and cervical spinal cord was implemented and tested for the brain volume ("partial-SMS"). The results show a similar image quality compared to both single-volume measurements covering the brain only and non-accelerated combined acquisitions. With the full image reconstruction being performed on-the-fly and a reduction of the image acquisition time by more than 50%, it may help to improve the temporal resolution and/or brain volume coverage of cortico-spinal fMRI.

References

1. Finsterbusch J, Sprenger C, Buchel C. Combined T2*-weighted measurements of the human brain and cervical spinal cord with a dynamic shim update. NeuroImage.2013;79:153-161

2. Tinnermann A, Geuter S, Sprenger C, Finsterbusch J, Büchel C. Interactions between brain and spinal cord mediate value effects in nocebo hyperalgesia. Science.2017;358:105-108

3. Vahdat S, Lungu O, Cohen-Adad J, Marchand-Pauvert V, Benali H, Doyon J. Simultaneous brain-cervical Cord fMRI reveals intrinsic spinal cord plasticity during motor sequence learning. PLoS Biol.2015;Jun30;13(6)

4. Barth M, Breuer F, Koopmans P, Norris D, Poser B. Simultaneous multislice (SMS) imaging techniques. Magn Reason Med. 2015;75(1):63-81

Evaluating diffusion dispersion across an extended range of b-values and frequencies using advanced OGSE methodology

Eric Seth Michael,[1*] Franciszek Hennel,[1] and Klaas Paul Pruessmann[1]

[1] Institute for Biomedical Engineering, ETH Zurich and University of Zurich, Zurich, Switzerland
*ericmich@biomed.ee.ethz.ch

Synopsis: To address the sensitivity limitations of oscillating gradient spin-echo (OGSE) diffusion imaging, a novel implementation of the sequence was developed by combining improved oscillating gradient waveforms, strong gradients, and spiral readouts and was utilized to investigate diffusion dispersion in the in vivo human brain. The methodology provided an enhanced depiction of diffusion dispersion, especially at higher b-values, and showed negligible downstream effects of a marginal flow sensitivity that was introduced by the improved OGSE shapes.

Motivation

Oscillating gradient spin-echo (OGSE) sequences offer additional insight into tissue microstructural properties compared to their pulsed gradient counterparts by permitting detection of the frequency dependence of diffusion (i.e., diffusion dispersion). However, OGSE is limited in terms of sensitivity due to the relatively low diffusion encoding strength and long echo times (TE) of the sequence. Toward higher b-values, OGSE can be helped by using a high-performance gradient system,[1] which can achieve stronger diffusion encoding (and/or higher frequencies) for otherwise equivalent acquisition parameters, and recently proposed gap-filled OGSE shapes,[2] which were shown to improve sensitivity in OGSE measurements. Shorter echo times, on the other hand, can be reached with spiral readouts.

To realize the associated benefits of said hardware- and sequence-based improvements, a novel OGSE implementation for in vivo human brain imaging is developed here by combining a high-performance gradient insert,[3] gap-filled oscillating gradient shapes, and spiral readouts. This methodology was utilized to evaluate diffusion dispersion in a yet unreached regime of frequencies (up to 125 Hz) and b-values (up to 1000 s/mm^2). Also, to explore the flow sensitivity introduced by gap-filled shapes, flow-compensated variants of these shapes are developed for experimental comparison.

Materials and Methods

Experiments were performed with a 3T Philips Achieva system (Philips Healthcare, Best, the Netherlands) equipped with the aforementioned high-performance gradient insert. Two healthy volunteers were scanned with PGSE DTI and OGSE DTI sequences with spiral readouts (TE = 95 ms) at b-values of 300, 500, and 1000 s/mm^2 and frequencies up to 125, 100, and 75 Hz, respectively. OGSE scans were performed at all b-values with gap-filled oscillating gradient waveforms providing increased diffusion sensitivity and at b = 300 and 1000 s/mm^2 with further modified gap-filled shapes that eliminate the flow sensitivity (see Figure 1).

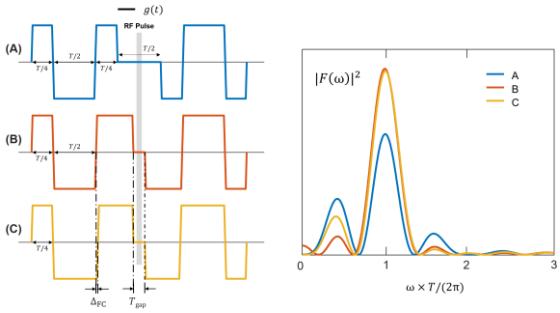

Fig. 1: Comparison of OGSE gradient waveforms and power spectra for (A) a standard OGSE shape, (B) an original gap-filled OGSE shape, and (C) a further modified gap-filled shape. Waveforms B and C are utilized here.

Image reconstruction was performed using an algorithm[4] that incorporated a third-order spherical harmonic model of the spatiotemporal magnetic field dynamics during readout. Mean diffusivity (MD) was calculated voxel-wise from the resulting images based on diffusion tensor fits. Consequently, diffusion dispersion maps were computed by fitting MD values to the power law relationship[5] $D(\omega) = \Lambda\omega^{\theta} + D_{\omega=0}$, where Λ is the diffusion dispersion rate, D(ω) is MD at frequency ω, $D_{\omega=0}$ is the PGSE diffusivity, and structural disorder parameter θ = 0.5 is assumed. Separate fits were performed for each b-value and for both cases of flow sensitivity.

Results

Figure 2 depicts MD maps corresponding to OGSE acquisitions with flow sensitivity; MD clearly increases with rising frequency and with decreasing b-value. Figure 3 captures these trends as pertains to the power law model, where Λ is depicted for each voxel. The parametric map quality greatly improves with in-

creasing b-value, as local homogeneity improves going from left to right. Figure 4 compares results between MD and diffusion dispersion fits for acquisitions with and without flow sensitivity at b = 1000 s/mm^2; both diffusion metrics are in agreement between the two cases.

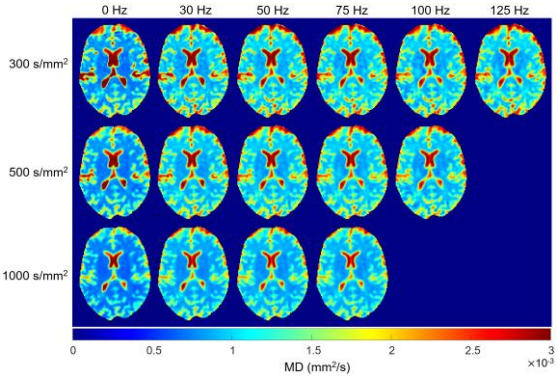

Fig. 2: MD maps of a representative slice for all b-values and frequencies.

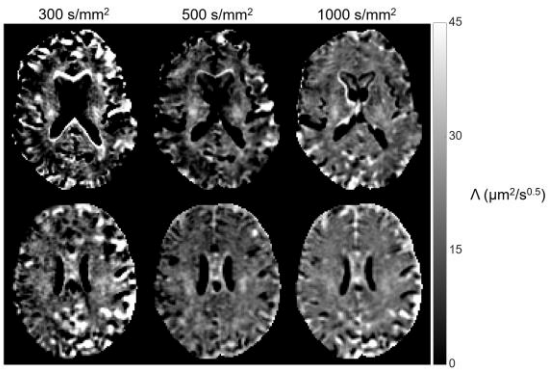

Fig. 3: Diffusion dispersion maps of two representative slices (different rows) for all b-values (different columns).

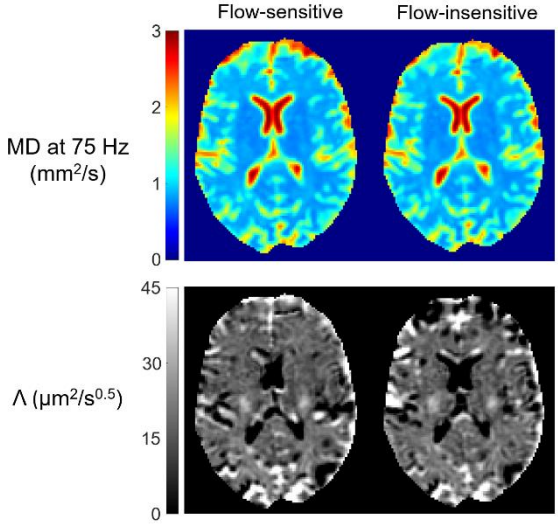

Fig. 4: MD (at 75 Hz) and diffusion dispersion maps for OGSE acquisitions with and without flow sensitivity at b = 1000 s/mm^2.

Discussion

The data indicate a clear advantage of higher b-values in measuring diffusion dispersion, for which the alternative is to probe higher OGSE frequencies. Evidently, the reduction in noise sensitivity of the underlying MD maps that results from higher b-values outweighs the decrease in the number of intermediate frequencies that can be sampled.

Furthermore, the OGSE data at higher b-values is less sensitive to pseudo-diffusive microcirculation, as MD values decrease with increasing b-value. A further reduction in perfusion bias could be expected for the flow-insensitive OGSE acquisitions; however, MD values and diffusion dispersion rates are in agreement between the two cases of flow sensitivity, with relative contrast maintained. These observations indicate that a marginal flow sensitivity is tolerable for the range of b-values used here.

Conclusion

The OGSE implementation employed here permitted lower TEs and higher b-values and frequencies in diffusion dispersion measurements. Imaging results based on this methodology demonstrate that such measurements chiefly benefit from higher b-values in terms of sensitivity.

References

1. Tan ET, Shih RY, Mitra J, et al. Oscillating diffusion-encoding with a high gradient-amplitude and high slew-rate head-only gradient for human brain imaging. Magn. Reson. Med. 2020;84:950-965.

2. Hennel F, Michael ES, Pruessmann KP. Improved gradient waveforms for oscillating gradient spin-echo (OGSE) diffusion tensor imaging. NMR Biomed. 2021;34:e4434.

3. Weiger M, Overweg J, Rösler MB, et al. A high-performance gradient insert for rapid and short-T2 imaging at full duty cycle. Magn. Reson. Med. 2018;79:3256-3266.

4. Wilm BJ, Barmet C, Pavan M, Pruessmann KP. Higher order reconstruction for MRI in the presence of spatiotemporal field perturbations. Magn. Reson. Med. 2011;65:1690-1701.

5. Arbabi A, Kai J, Khan AR, Baron CA. Diffusion dispersion imaging: Mapping oscillating gradient spin-echo frequency dependence in the human brain. Magn. Reson. Med. 2020;83:2197-2208.

Synchronous nonmonotonic changes in functional connectivity and white matter integrity in a rat model of sporadic Alzheimer's disease

Yujian Diao[1,2,#], Catarina Tristão Pereira[1,3,#], Ting Yin[1], Analina Raquel Da Silva[1], Bernard Lanz[2], Katarzyna Pierzchala[1], Carole Poitry-Yamate[1], Ileana Ozana Jelescu[1,*]

[1] Centre d'Imagerie Biomédicale, EPFL, Station 6, Lausanne 1015, Switzerland.
[2] Laboratoire d'Imagerie Fonctionnelle et Métabolique, EPFL, Lausanne, Switzerland
[3] Faculdade de Ciências da Universidade de Lisboa, Lisbon, Portugal.

First authors
* Corresponding author

Synopsis: Alzheimer's disease (AD) can be described as brain diabetes. We performed a longitudinal PET-MRI study of how brain insulin resistance affects functional connectivity and white matter microstructure in a rat model of sporadic AD. Rats exhibited early hyperconnectivity followed by hypoconnectivity in brain regions typical of AD, and intra-axonal damage also in a pattern of acute injury, transient recovery and chronic degeneration. This study highlights signature nonmonotonic trajectories resulting from brain insulin resistance and proposes clinically-feasible MRI biomarkers for AD.

Zusammenfassung: Die Alzheimer-Krankheit (AK) wurde als Diabetes des Gehirns beschrieben. Mittels einer longitudinalen PET-MRI-Studie wurde in einem sporadischen AK-Rattenmodell untersucht, wie die Insulinresistenz des Gehirns die funktionelle Konnektivität und die Mikrostruktur der weißen Substanz beeinflusst. AK-Ratten zeigten eine frühe Hyperkonnektivität, gefolgt von einer Hypokonnektivität in AK-typischen Hirnregionen, und eine intraaxonale Schädigung in einem Muster aus akuter Verletzung, vorübergehender Erholung und chronischer Degeneration. Diese Studie hebt charakteristische nicht-monotone Verläufe hervor, die aus zerebraler Insulinresistenz resultieren, und schlägt klinisch praktikable MRI-Biomarker für AK vor.

Motivation

Clinically, Alzheimer's disease (AD) is manifested by progressive memory loss and gradual decline in cognitive function. The characterization of the temporal progression of AD promises to provide an understanding of disease mechanisms, an effective disease staging and a window for therapeutic intervention. Hypometabolism of glucose in the brain has been taking the center stage as a key player in the onset of AD (1). Impaired brain insulin function has been reported to trigger AD pathology (2,3). Moreover, metabolic decline has been linked to impaired glucose transport and neuroinflammation (4,5). As it becomes well-established that diabetes makes the brain more susceptible to the aging process (6), AD pathology has been suggested to be a brain-specific type-III diabetes (7).

With the importance of brain glucose metabolism in AD being recognized, animal models of brain insulin resistance have been developed by an intracerebroventricular (icv) injection of streptozotocin (STZ). When delivered exclusively to the brain via the ventricles, this diabetogenic substance is thought to disrupt the brain insulin receptor system, thereby reducing glycolysis in the hippocampus and parieto-temporal cortex, but without causing systemic diabetes (8,9). Moreover, the icv-STZ rat model has demonstrated its potential to reproduce sporadic AD by the resemblance with the behavioral, neurochemical and structural changes found in the human AD brain (10–12). However, beyond anatomical data, this animal model has never been assessed with MRI, which could potentially offer significant insight into neurodegenerative processes.

Here we performed a longitudinal study in the icv-STZ rat model to quantitatively characterize alterations in functional connectivity and in white matter microstructure using resting-state functional (rs-fMRI) and diffusion MRI, respectively, as well as changes in brain glucose uptake captured by ^{18}FDG (fluorodeoxyglucose)-PET. This work serves the dual purpose of outlining pathological trajectories relevant for clinical studies and validating potent MRI-derived biomarkers to track neurodegeneration in human AD and diabetes populations.

Material und Methoden / Materials and Methods

All experiments were approved by the local Service for Veterinary Affairs. Male Wistar rats (N=17) (236±11 g at baseline) underwent a bilateral icv-injection of either streptozotocin (3 mg/kg, STZ group, N=9) or buffer (CTL group, N=8). MRI: Rats were scanned at 3 timepoints following surgery (Figure 1), on a 14T Varian

system (Abingdon, UK). Briefly, rats were anesthetized using isoflurane for initial setup and switched to medetomidine sedation (bolus: 0.1mg/kg, perfusion: 0.1mg/kg/h). Rs-fMRI data were acquired using a two-shot gradient-echo EPI sequence (TE/TR=10/800ms; Matrix: 64x64; FOV: 23x23mm2; 8 1.12-mm slices; 370 repetitions; TA=10'). Diffusion data were acquired using a PGSE-EPI sequence (4 b=0 and 3 b-shells b=0.8/1.3/2 ms/μm^2 with 12/16/30 directions; δ/Δ=4/27 ms; TE/TR=48/2500 ms, 9 1-mm slices, FOV=23x17mm^2, matrix=128x64). PET: List-mode data were acquired on a LabPET-4 small-animal scanner (Gamma Medica-Ideas Inc.) following tail vein delivery of ^{18}FDG (~50MBq) in non-fasted rats. Data between 30 and 50 minutes post-injection were reconstructed and Standardized Uptake Value (SUV)-normalized to generate a steady-state image.

Optimized data processing for rs-fMRI were developed separately (13) and included denoising (14), distortion correction (15), slice-timing correction, spatial smoothing (16), and removal of physiological noise following independent component (IC) analysis decomposition (17). FC matrices between 28 atlas-based ROIs were computed, co-varying for the global signal. The significance of group differences was tested using non-parametric permutation tests (N = 5000) with the Network-Based Statistics (NBS) Toolbox (18), with statistical significance retained at p = 0.05 after family-wise error rate (FWER) correction. Diffusion MRI images were denoised (14), Gibbs-ringing corrected (19) and EDDY-corrected (20). Diffusion and kurtosis tensors were calculated (21) and the White Matter Tract Integrity (WMTI)-Watson model (22) was estimated in WM voxels. Corpus callosum, cingulum and fimbria were automatically segmented using atlas-based registration. Average diffusion-derived metrics in each white matter ROI were compared between STZ and CTL groups at each timepoint using two-tailed Mann-Whitney U test, at α = 0.05 significance. Longitudinal changes within each group were assessed by one-way ANOVA and Tukey-Cramer correction, at α = 0.05 significance. PET datasets were registered to their corresponding MRI anatomical image with cross-correlation (23) using ANTs (24) and 26 ROIs were segmented. SUV images were normalized to mean SUV over the brain to obtain relative SUV (SUVr) maps corrected for inter-rat experimental variability (12). Regional differences in SUVr between STZ and CTL groups were evaluated at each timepoint (except at 2 weeks due to the small sample size) using one-tailed Mann-Whitney U test (STZ < CTL), at significance level of α = 0.05.

Ergebnisse / Results

The weight of all animals was measured before the icv-STZ injection (baseline) and at all timepoints before each MRI or PET scanning session. There was no difference between

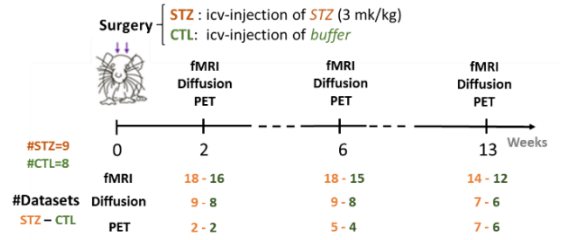

Figure 1. Experimental timeline. PET and MRI data were collected at 2, 6 and 13 weeks after icv-STZ injection. Two fMRI runs were acquired for each MRI session.

groups at baseline, but STZ rats had a significantly lower weight than CTL rats at 2, 6 and 13 weeks after the injection.

SUVr was reduced in STZ rats compared to

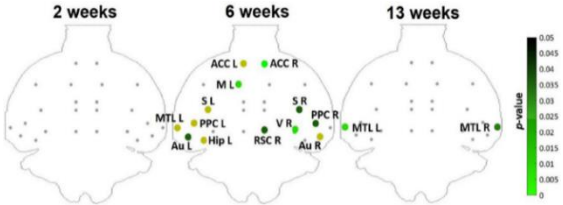

Figure 2. Group differences in SUVr at each timepoint. Green: ROIs with significantly lower SUV (p < 0.05 using one-tailed Mann-Whitney U test, STZ < CTL). Dark yellow: Trend of lower SUV (p < 0.1). Correction for multiple comparisons was not applied given the small number of animals per group. *ACC: anterior cingulate cortex; RSC: retrosplenial cortex;PPC: posterior parietal cortex; MTL: medial temporal lobe; Hip: hippocampus; Au: auditory; V: visual; S: somatosensory and M: motor cortices; L/R: left/right*

CTL rats, with different spatial patterns over time (Figure 2). The most pronounced differences were found at 6 weeks after injection, involving several regions typically affected in AD: anterior cingulate cortex (ACC), retrosplenial cortex (RSC), posterior parietal cortex (PPC), but also motor, somatosensory, auditory and visual cortices.

Significant group differences in functional connectivity were found at 2, 6 and 13 weeks after injection (Figure 3A). In Figure 3B, graph networks highlight the group differences in nodal connections. At 2 weeks, STZ rats dis-

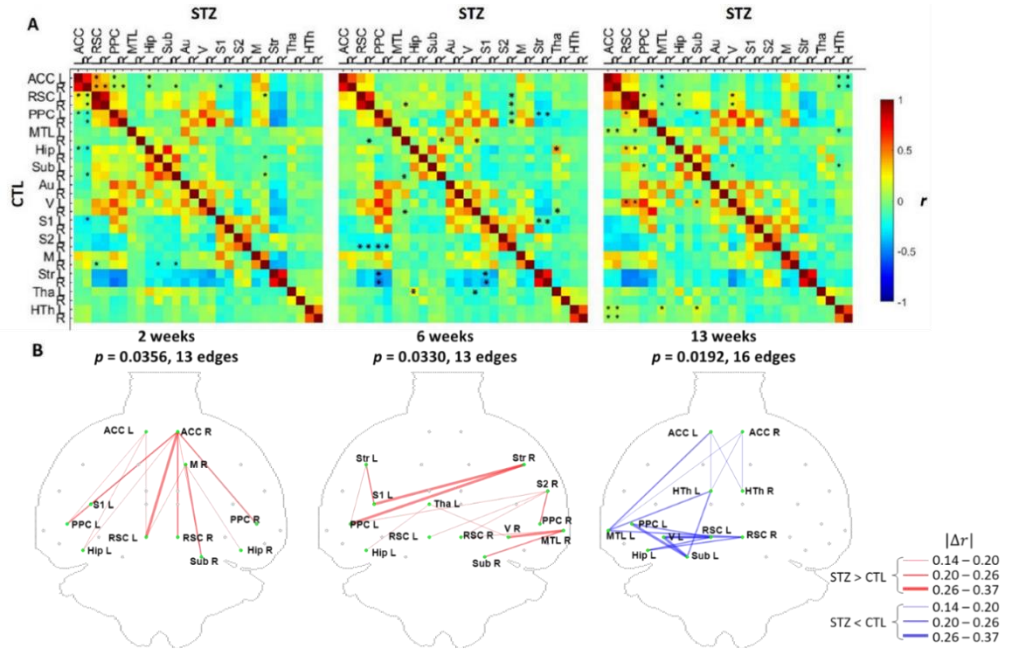

Figure 3. A) Hybrid average functional connectivity matrices at each timepoint (top-right half: STZ, bottom-left half: CTL). ∗ : $p < 0.05$ (FWER corrected) at a threshold of 2.2. B) Graph networks at each timepoint. Red (STZ > CTL) or blue (STZ < CTL) edges and green nodes indicate connections with significant difference. The line width of each edge represents the absolute difference in mean correlation coefficients | Δr|. The *p*-value for each network is given after FWER correction.

played hyperconnectivity, in the form of increased positive connectivity between the ACC and the RSC and decreased anti-correlation of the default mode network (DMN) (including the ACC, RSC, hippocampus and subiculum) to regions of the lateral cortical network (LCN) including S1 and the motor cortex, as compared to CTL rats. At 6 weeks, the main changes in STZ rats remained reduced anti-correlations between the DMN and LCN as well as striatum. At 13 weeks, there was a dramatic shift towards overall hypo-connectivity of the DMN in STZ rats. STZ rats thus exhibited a nonmonotonic trend in functional connectivity alterations, moving from hyperconnectivity within the DMN and less efficient dissociation between the DMN and LCN, to hypoconnectivity within the DMN. This switch occurred between the 6 and 13-week timepoints.

Diffusion Tensor Imaging (DTI) metrics revealed that STZ rats displayed lower fractional anisotropy (FA) in the corpus callosum at 2, 6 and 13 weeks after injection, in the fimbria at 2 and 13 weeks and in the cingulum at 13 weeks only (Figure 4). The WMTI-Watson biophysical model provided a more specific characterization

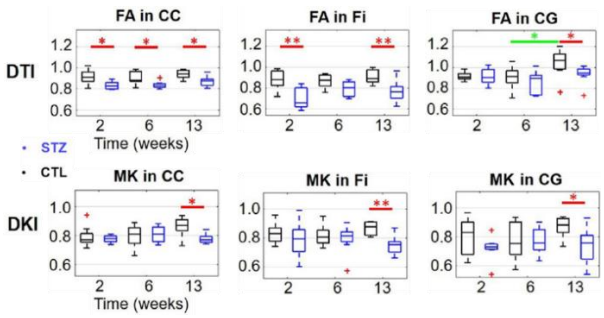

Figure 4. DTI and DKI estimates in three white matter ROIs (top row: corpus callosum (CC), middle row: fimbria of the hippocampus (Fi) and bottom row: cingulum (CG)). FA: Fractional Anisotropy, MK: Mean Kurtosis. Two-tailed Mann-Whitney U test for inter-group comparison (red bars) and one-way ANOVA with Tukey-Cramer correction for within-group comparison across time (green bars). ∗ : $p < 0.05$, ∗∗ : $p < 0.01$. + : outlier values (but not excluded from the analysis).

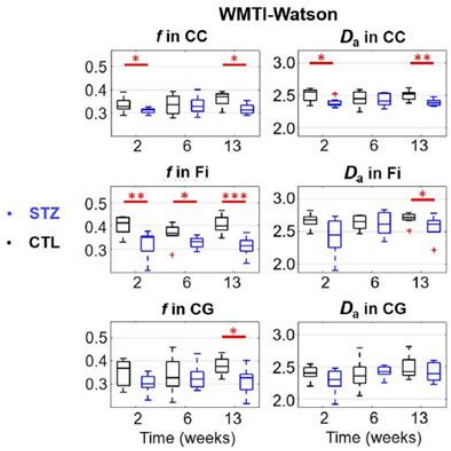

Figure 5. WMTI-Watson model estimates in three white matter ROIs (top row: corpus callosum (CC), middle row: fimbria of the hippocampus (Fi) and bottom row: cingulum (CG)). *f* : axonal water fraction , Da : intra-axonal parallel diffusivity . Two-tailed Mann-Whitney U test for inter-group comparison (red bars). ∗ : $p < 0.05$, ∗∗ : $p < 0.01$, ∗∗∗ : $p < 0.001$. + : outlier values (but not excluded from the analysis).

of white matter degeneration. In the corpus callosum, both axonal fraction *f* and intra-axonal diffusivity Da were reduced in the STZ group at 2 weeks and 13 weeks (Figure 5). In the fimbria, *f* was lower in the STZ group at all timepoints, being more accentuated at 13 weeks, when Da was also lower. In the cingulum, reduced *f* was found at 13 weeks. Overall, white matter integrity displayed a nonmonotonic trend with partial recovery at 6 weeks, most markedly in the fimbria but also in the corpus callosum. The 13-week timepoint appeared as one of the most widespread damage, with involvement of the cingulum bundle as well.

Diskussion / Discussion

The effects of brain insulin resistance on the pathological cascade have not been fully understood, and the present study attempts to characterize them by means of MRI-derived biomarkers for the first time. In this longitudinal assessment, FDG uptake, resting-state functional connectivity and white matter microstructure results agree in terms of spatio-temporal variations, and are consistent with our histological findings and with previous studies of cognitive decline and immunochemistry.

Icv-STZ animals displayed early hyper-connectivity within the DMN and impaired network dissociation between the DMN and LCN followed by hypo-connectivity within the DMN. Moreover, white matter degeneration was manifested as intra-axonal damage and demyelination, potentially leading to axonal loss and mainly affecting the corpus callosum and the fimbria of the hippocampus. It followed a sequence of early acute injury followed by transient partial recovery and late chronic degeneration. Structural and functional changes presented matching spatio-temporal patterns, with a turning point between 6 and 13 weeks, and were in agreement with existing literature.

PET data showed reduced FDG uptake in icv-STZ rats in brain regions typically involved in AD. The most pronounced differences in uptake were found at 6 weeks, but the development of earlier glucose hypometabolism in STZ rats is highly likely. Furthermore, STZ rats were on average already 70 g lighter than CTL rats at that timepoint. The significant weight difference supports the assumption of impaired brain glucose metabolism as early as 2 weeks and the use of alternative energy sources such as stored body fat, which when burnt results in a build-up of ketones.

Remarkably, we report "partial recovery" in terms of axonal integrity and functional hyperconnectivity at six weeks post-injection, in a context of marked FDG uptake differences at that timepoint. This observation supports the assumption that past the acute phase, the brain switches to other forms of energy, such as ketone bodies, as a means to maintain energy homeostasis and restore normal brain function(25). Interestingly, the same regions with reduced FDG uptake at 6 weeks after STZ injection eventually showed functional hypoconnectivity at 13 weeks, supporting the manifestation of a chronic phase of disease. Here, our data suggests that neurodegeneration resumes as pathological mechanisms approach a critical stage and can no longer be compensated for.

Schlussfolgerung / Conclusion

Our results support the hypothesis of impaired glucose metabolism as a key player in the onset of AD and the relevance of the icv-STZ animal models for pre-clinical AD research. This study (i) characterized the impact of brain glucose hypometabolism on brain microstructure and function, (ii), highlighted signature nonmonotonic trajectories in their evolution and (iii) proposed potent MRI-derived biomarkers translatable to human AD and diabetic populations to monitor disease progression and potential response to treatment.

References

1. Kuehn BM. In Alzheimer Research, Glucose Metabolism Moves to Center Stage. JAMA 2020;323:297–299 doi: 10.1001/jama.2019.20939.

2. Correia SC, Santos RX, Perry G, Zhu X, Moreira PI, Smith MA. Insulin-resistant brain state: the culprit in sporadic Alzheimer's disease? Ageing Res. Rev. 2011;10:264–273 doi: 10.1016/j.arr.2011.01.001.

3. Hölscher C. Insulin Signaling Impairment in the Brain as a Risk Factor in Alzheimer's Disease. Front. Aging Neurosci. 2019;11 doi: 10.3389/fnagi.2019.00088.

4. An Y, Varma VR, Varma S, et al. Evidence for brain glucose dysregulation in Alzheimer's disease. Alzheimer's & Dementia 2018;14:318–329 doi: 10.1016/j.jalz.2017.09.011.

5. Balducci C, Forloni G. Novel targets in Alzheimer's disease: A special focus on microglia. Pharmacological Research 2018;130:402–413 doi: 10.1016/j.phrs.2018.01.017.

6. Gudala K, Bansal D, Schifano F, Bhansali A. Diabetes mellitus and risk of dementia: A meta-analysis of prospective observational studies. Journal of Diabetes Investigation 2013;4:640–650 doi: 10.1111/jdi.12087.

7. de la Monte SM, Wands JR. Alzheimer's Disease is Type 3 Diabetes—Evidence Reviewed. J Diabetes Sci Technol 2008;2:1101–1113 doi: 10.1177/193229680800200619.

8. Nitsch R, Hoyer S. Local action of the diabetogenic drug, streptozotocin, on glucose and energy metabolism in rat brain cortex. Neuroscience Letters 1991;128:199–202 doi: 10.1016/0304-3940(91)90260-Z.

9. Plaschke K, Kopitz J, Siegelin M, et al. Insulin-Resistant Brain State after Intracerebroventricular Streptozotocin Injection Exacerbates Alzheimer-like Changes in Tg2576 AβPP-Overexpressing Mice. Journal of Alzheimer's Disease 2010;19:691–704 doi: 10.3233/JAD-2010-1270.

10. Kraska A, Santin MD, Dorieux O, et al. In vivo cross-sectional characterization of cerebral alterations induced by intracerebroventricular administration of streptozotocin. PLoS ONE 2012;7:e46196 doi: 10.1371/journal.pone.0046196.

11. Knezovic A, Osmanovic-Barilar J, Curlin M, et al. Staging of cognitive deficits and neuropathological and ultrastructural changes in streptozotocin-induced rat model of Alzheimer's disease. J Neural Transm (Vienna) 2015;122:577–592 doi: 10.1007/s00702-015-1394-4.

12. Heo J-H, Lee S-R, Lee S-T, et al. Spatial Distribution of Glucose Hypometabolism Induced by Intracerebroventricular Streptozotocin in Monkeys. JAD 2011;25:517–523 doi: 10.3233/JAD-2011-102079.

13. Diao Y, Yin T, Gruetter R, Jelescu IO. PIRACY: An Optimized Pipeline for Functional Connectivity Analysis in the Rat Brain. Front. Neurosci. 2021;15 doi: 10.3389/fnins.2021.602170.

14. Veraart J, Fieremans E, Novikov DS. Diffusion MRI noise mapping using random matrix theory: Diffusion MRI Noise Mapping. Magn. Reson. Med. 2016;76:1582–1593 doi: 10.1002/mrm.26059.

15. Smith SM, Jenkinson M, Woolrich MW, et al. Advances in functional and structural MR image analysis and implementation as FSL. Neuroimage 2004;23 Suppl 1:S208-219 doi: 10.1016/j.neuroimage.2004.07.051.

16. Friston KJ, Ashburner J, Kiebel SJ, Nichols TE, Penny WD. Statistical Parametric Mapping. In: ; 2007. doi: 10.1007/978-1-4615-1079-6_16.

17. Griffanti L, Douaud G, Bijsterbosch J, et al. Hand classification of fMRI ICA noise components. NeuroImage 2017;154:188–205 doi: 10.1016/j.neuroimage.2016.12.036.

18. Zalesky A, Fornito A, Bullmore ET. Network-based statistic: Identifying differences in brain networks. NeuroImage 2010;53:1197–1207 doi: 10.1016/j.neuroimage.2010.06.041.

19. Kellner E, Dhital B, Kiselev VG, Reisert M. Gibbs-ringing artifact removal based on local subvoxel-shifts. Magnetic Resonance in Medicine 2016;76:1574–1581 doi: 10.1002/mrm.26054.

20. Andersson JLR, Sotiropoulos SN. An integrated approach to correction for off-resonance effects and subject movement in diffusion MR imaging. NeuroImage 2016;125:1063–1078 doi: 10.1016/j.neuroimage.2015.10.019.

21. Veraart J, Sijbers J, Sunaert S, Leemans A, Jeurissen B. Weighted linear least squares estimation of diffusion MRI parameters: Strengths, limitations, and pitfalls. NeuroImage 2013;81:335–346 doi: 10.1016/j.neuroimage.2013.05.028.

22. Jespersen SN, Olesen JL, Hansen B, Shemesh N. Diffusion time dependence of microstructural parameters in fixed spinal cord. NeuroImage 2018;182:329–342 doi: 10.1016/j.neuroimage.2017.08.039.

23. Avants BB, Epstein CL, Grossman M, Gee JC. Symmetric diffeomorphic image registration with cross-correlation: Evaluating automated labeling of elderly and neurodegenerative brain. Medical Image Analysis 2008;12:26–41 doi: 10.1016/j.media.2007.06.004.

24. Avants BB, Tustison N, Song G. Advanced Normalization Tools (ANTS). 2011.

25. Yang H, Shan W, Zhu F, Wu J, Wang Q. Ketone Bodies in Neurological Diseases: Focus on Neuroprotection and Underlying Mechanisms. Front. Neurol. 2019;10 doi: 10.3389/fneur.2019.00585.

Optimierte Hintergrundunterdrückung für Arterial Spin Labeling bei 3 Tesla

Christian K. Eisen[1]*, Christian R. Meixner[1], Bernhard Hensel[2], Michael Uder[1] und Armin M. Nagel[1,3]

[1] Radiologisches Institut, Friedrich-Alexander-Universität Erlangen-Nürnberg (FAU), Erlangen, Deutschland
[2] Max Schaldach-Stiftungsprofessur für Biomedizinische Technik (MSBT), Friedrich-Alexander-Universität Erlangen-Nürnberg (FAU), Erlangen, Deutschland
[3] Abteilung Medizinische Physik in der Radiologie, Deutsches Krebsforschungszentrum (DKFZ), Heidelberg, Deutschland
*christian.eisen@uk-erlangen.de

Synopsis: This work proposes an optimization approach for background suppression of Arterial Spin Labeling (ASL) with multiple inversion pulses, which minimizes the signal for a broad T_1 range and enables post-processing without phase information. Thus, artefacts caused by the use of phase data within complex subtraction are reduced while perfusion image quality is greatly improved. The proposed optimization method results in a similar tSNR improvement as previous approaches with a less error-prone post-processing procedure.

Zusammenfassung: In dieser Arbeit wird ein Optimierungsansatz für die Hintergrundunterdrückung bei *Arterial Spin Labeling* (ASL) mit mehreren Inversionspulsen vorgeschlagen, der das Signal für einen breiten T_1-Bereich minimiert und eine Nachbearbeitung ohne Phaseninformation ermöglicht. So werden Artefakte, die durch die Verwendung der Phasendaten bei der komplexen Subtraktion auftreten, reduziert, während sich die Qualität der Perfusionsbilder stark verbessert. Die vorgeschlagene Optimierungsmethode führt zu einer ähnlichen tSNR-Verbesserung wie bei früheren Ansätzen, bietet jedoch eine stabilere Nachbearbeitung.

Motivation

Die Unterdrückung von statischem Gewebe bei ASL erhöht die Qualität des Perfusionssignals, da Hintergrundsignale trotz Subtraktion der Messpaare das Perfusionsbild negativ beeinflussen. Frühere Arbeiten haben bereits gezeigt, dass eine optimierte Hintergrundunterdrückung das Signal von statischem Gewebe auf weniger als 1 % reduzieren kann (1,2). Der hier vorgestellte Ansatz erweitert die bisherigen Methoden, indem durch eine entsprechende Optimierung keine Phaseninformationen und somit keine komplexe Subtraktion für die Nachbearbeitung notwendig ist. Damit einhergehende Effekte, wie z.B. Phasenrauschen oder *wrapping* Artefakte (3), können so vermieden werden.

Material und Methoden

Die longitudinale Magnetisierung M_z als Funktion der Relaxationszeit T_1 und den Inversionspulszeiten t_m (zeitliche Differenz zwischen der *saturation time TS* und Inversionspuls *m*) kann wie folgt ausgedrückt werden:

$$M_z(T_1,t_m)=1+(-1)^n(M_{z0}-1)\chi^n e^{\frac{TS}{T_1}} + 2\sum_{m=1}^{n}(-1)^m(\chi^m+\chi^{m-1})e^{\frac{t_m}{T_1}} \quad (1)$$

Hierbei ist n die Gesamtanzahl an Inversionspulsen, M_{z0} die initiale longitudinale Magnetisierung und χ die Inversionspulseffizienz. Die Optimierung umfasst eine zweistufige Minimierung der summierten Magnetisierungen im Betrag innerhalb des Bereiches 250 ms ≤ T_1 ≤ 4200 ms. Dabei müssen Beschränkungen erfüllt sein, sodass die Magnetisierungen von Blut ($T_{1,blood}$ = 1961 ms) (4) für die *label* und *control* Wiederholungen nach Formel (1) zum Auslesezeitpunkt nicht negativ sind.

Die Messungen wurden an einem 3T-MRT (Magnetom Prisma Fit, Siemens Healthcare GmbH, Erlangen, Germany) und mithilfe von drei gesunden Probanden (Alter zwischen 22 und 24 Jahren) durchgeführt. Das Messprotokoll umfasst eine pCASL Sequenz nach Alsop *et al.* (5) mit einer 2D EPI Auslese (TR = 5.4 s, TE = 25.0 ms, Auflösung = (3.0x3.0x4.0) mm, partial Fourier, GRAPPA, Bandbreite = 764 Hz/Px).

Alle Perfusionsbilder wurden mithilfe des zeitlichen Signal-zu-Rausch Verhältnisses (tSNR) in grauer Substanz quantitativ ausgewertet und verglichen.

Ergebnisse

Um den Mehrwert der hier präsentierten Methodik zu zeigen, wurden Perfusionsbilder ohne Hintergrundunterdrückung (Fig. 1a), mit optimierter Unterdrückung ohne die Beschränkungen für die finale Blutmagnetisierung (ohne und

mit komplexer Subtraktion) (Fig. 1b bzw. c) und optimierter Hintergrundunterdrückung mit den entsprechenden Beschränkungen (Fig. 1d) bestimmt. Des Weiteren wurden zugehörige tSNR Karten ermittelt (Fig. 2). Die mittlere tSNR Verbesserung durch eine optimierte Hintergrundunterdrückung nach bestehenden Verfahren beträgt 78.5% ±10.9%, wohingegen der Ansatz dieser Arbeit 74.1% ±32.4% erzielt.

Schlussfolgerung

Die resultierenden Perfusionsbilder und tSNR Verbesserungen der präsentierten Methode führen zu einer vergleichbaren Qualität wie bisherige Ansätze. Allerdings können mit den Phasendaten einhergehende Quellen für Artefakte durch alleinige Verwendung der Magnitudeninformation bei der Nachbearbeitung vermieden werden. Daher ist der vorgestellte Ansatz zur Optimierung der Hintergrundunterdrückung eine sinnvolle Ergänzung für verlässliche und akkurate ASL Perfusionsbildgebung.

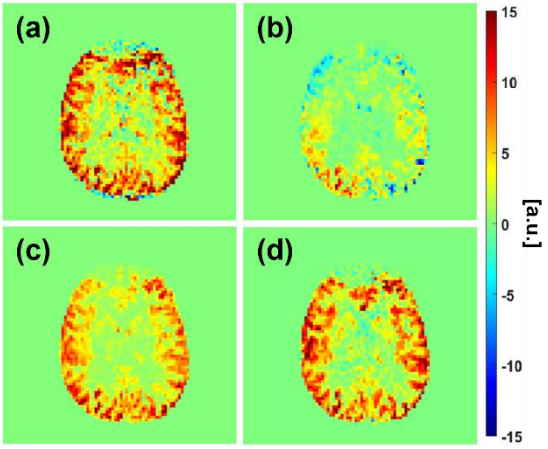

Fig. 1: Vergleich der ermittelten Perfusionsbilder.
(a) ohne Hintergrundunterdrückung
(b) mit Unterdrückung nach Vorbild bisheriger Ansätze, ohne Phaseninformation
(c) mit Unterdrückung nach Vorbild bisheriger Ansätze, mit Phaseninformation
(d) mit Unterdrückung nach dem in dieser Arbeit präsentierten Ansatz, ohne Phaseninformation

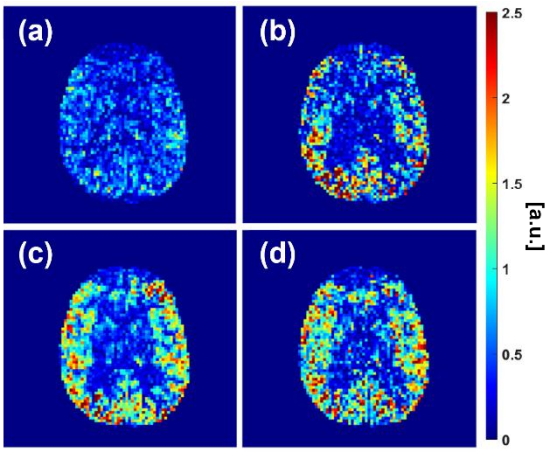

Fig. 2: Vergleich der zugehörigen tSNR Karten.
(a) ohne Hintergrundunterdrückung
(b) mit Unterdrückung nach Vorbild bisheriger Ansätze, ohne Phaseninformation
(c) mit Unterdrückung nach Vorbild bisheriger Ansätze, mit Phaseninformation
(d) mit Unterdrückung nach dem in dieser Arbeit präsentierten Ansatz, ohne Phaseninformation

References

1. Maleki N, Dai W, Alsop DC. Optimization of background suppression for arterial spin labeling perfusion imaging. MAGMA. 2012;25(2):127-133.

2. Mani S, Pauly J, Conolly S, Meyer C, Nishimura D. Background suppression with multiple inversion recovery nulling: applications to projective angiography. Magn Reson Med. 1997;37(6):898-905.

3. Garcia DM, Duhamel G, Alsop DC. Efficiency of inversion pulses for background suppressed arterial spin labeling. Magn Reson Med. 2005;54(2):366-372.

4 Rooney WD, Johnson G, Li X, et al. Magnetic field and tissue dependencies of human brain longitudinal 1H2O relaxation in vivo. Magn Reson Med. 2007;57(2):308-318.

5 Alsop DC, Detre JA, Golay X, et al. Recommended implementation of arterial spin-labeled perfusion MRI for clinical applications: A consensus of the ISMRM perfusion study group and the European consortium for ASL in dementia. Magn Reson Med. 2015;73(1):102-116.

NN-driven mapping of multiple diffusion metrics at high to ultra-high resolution using the bSSFP frequency profile

Florian Birk,[1*] Felix Glang,[1] Alexander Loktyushin,[1,2] Christoph Birkl,[3] Philipp Ehses,[4] Klaus Scheffler[1,5] and Rahel Heule[1,5]

[1] High Field Magnetic Resonance, Max Planck Institute for Biological Cybernetics, Tübingen, Germany.
[2] Empirical Inference, Max Planck Institute for Intelligent Systems, Tübingen, Germany.
[3] Department of Neuroradiology, Medical University of Innsbruck, Innsbruck, Austria.
[4] German Center for Neurodegenerative Diseases (DZNE), Bonn, Germany.
[5] Department of Biomedical Magnetic Resonance, University of Tübingen, Tübingen, Germany.
* florian.birk@tuebingen.mpg.de

Synopsis: Asymmetries in the bSSFP frequency profile comprise rich information about microstructural tissue properties and white matter fiber orientation. A neural network-driven approach is presented to simultaneously map multiple diffusion metrics from phase-cycled bSSFP data acquired at 3T and 9.4T.

Zusammenfassung: Asymmetrien im bSSFP Frequenzprofil enthalten reichhaltige Informationen über mikrostrukturelle Gewebeeigenschaften und Faserorientierung der weißen Substanz. Wir stellen einen neuartigen Ansatz vor, der auf neuronalen Netzen basiert, um gleichzeitig mehrere Diffusionsmetriken aus phasenzyklischen bSSFP-Daten bei 3T und 9.4T abzubilden.

Motivation

The pulsed-gradient spin-echo echo-planar-imaging (SE-EPI) sequence is predominantly used for diffusion-weighted imaging (DWI). However, strong image distortions in the presence of magnetic field inhomogeneities and spatial blurring due to long echo trains complicate volumetric brain coverage using DWI, especially at ultra-high field strength.

While diffusion tensor imaging (DTI) is commonly used to visualize anisotropies in the tissue microenvironment and delineate WM fiber pathways, the phase-cycled balanced SSFP (bSSFP) profile was shown to also reflect information about tissue anisotropies. Miller et al. observed different degrees of asymmetry depending on the underlying intravoxel frequency distribution for each tissue type and found highest bSSFP asymmetries in highly anisotropic WM tracts oriented perpendicular to B0 (1-2). These findings suggest significant correlations of the bSSFP asymmetry index (AI) with DTI metrics, such as the fractional anisotropy (FA), reflecting the strength of tract directionality (2). Figure 1 illustrates correlations of the bSSFP profile and the entangled AI with DTI metrics, measured within the scope of the proposed work.

The inherent sensitivity to tissue microstructure, combined with a mixed dependence on both T1 and T2, as well as the ability to enable distortion-free volumetric imaging with high signal-to-noise-ratio (SNR) efficiency in short scan times (3) make phase-cycled bSSFP an interesting tool for multi-parametric mapping of various MR quantities (4).

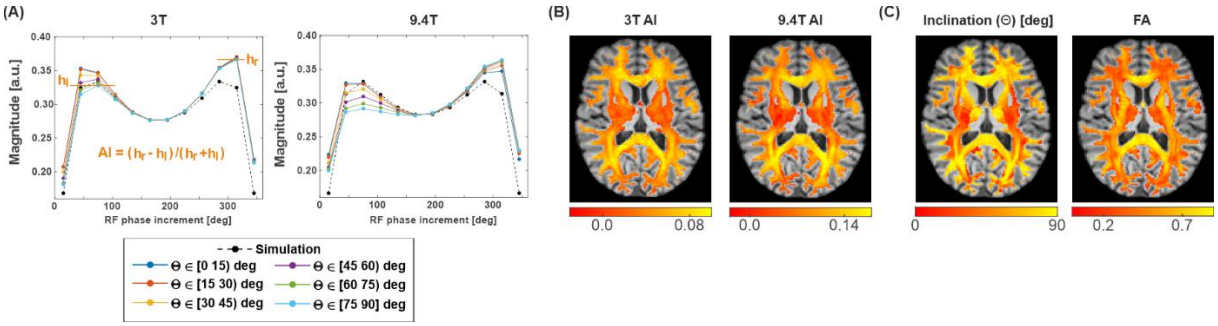

Fig. 1: (A) The bSSFP profile assessed in WM at 3 T and 9.4 T for different ranges of the inclination angle Θ (≡ angle between principal fiber direction and B0). (B) AI maps obtained at 3 T and 9.4 T and (C) maps of the inclination angle and FA, registered and overlaid onto the T1-weighted anatomical image.

Materials and Methods

A 12-point bSSFP phase-cycling scheme with high-resolution whole-brain coverage was employed at 3 T (1.3 x 1.3 x 1.3 mm^3) and 9.4 T (0.8 x 0.8 x 0.8 mm^3) for NN input, with scan times of 10-11 min and 9-10 min, respectively.

Low-resolution (1.4 x 1.4 x 3.0 mm^3) target diffusion data were derived based on diffusion-weighted SE-EPI scans, i.e., mean, axial, and radial diffusivity (MD, AD, RD) and FA with scan times of around 15 min. To provide matched NN input data, the high-resolution 3 T and 9.4 T bSSFP phase-cycles were registered and downsampled to the lower-resolution 3 T DTI data. Multilayer perceptrons, i.e., fully connected feedforward NNs were trained voxelwise. The training data contained ~590.000 voxels from four subjects; 20% of these voxels were used for validation purposes during training.

Results

As apparent from Figure 2, the NN predictions for a test subject not included in NN training yield highly reliable results in WM and GM structures for MD. The quantification of FA, AD, and RD is overall in good agreement with the reference but the dependence of these parameters on WM anisotropy is somewhat biased, e.g., in corpus callosum. Application of the NN to high-resolution input data provides whole-brain maps with rich structural details.

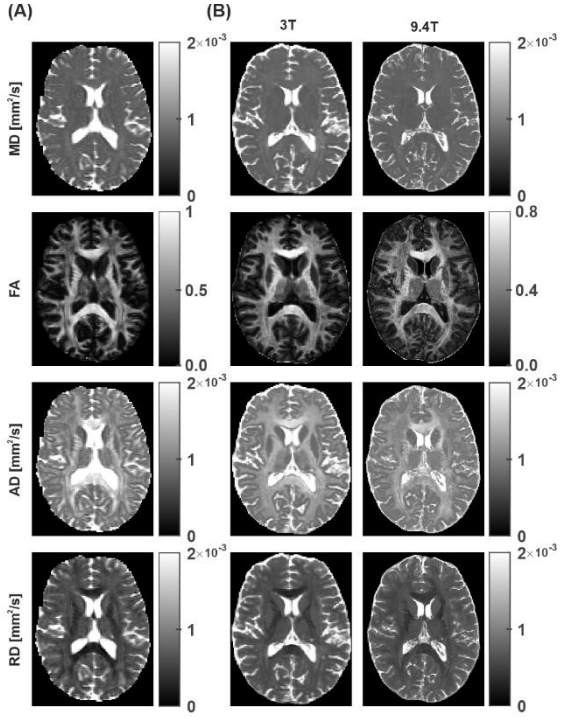

Fig. 2: (A) Reference data obtained with standard SE-EPI-based DTI fitting compared to (B) the NN predictions for 12-point phase-cycled bSSFP data of test subject 1, not included in NN training and acquired at field strengths of 3 T (middle) and 9.4 T (right).

Discussion

This proof-of-principle study indicates the high potential of NNs to predict high-resolution volumetric maps of multiple diffusion metrics jointly based on phase-cycled bSSFP input data at high to ultra-high field strengths (cf. Fig. 2). The trained NNs demonstrate their general ability to reliably estimate scalar diffusion measures (here, MD, FA, AD, RD) with isotropic resolution of 1.3 x 1.3 x 1.3 mm^3 and 0.8 x 0.8 x 0.8 mm^3 at 3 T and 9.4 T, respectively, yielding whole-brain coverage in scan times of only about 10 min for a 12-point phase-cycling scheme.

Common DTI sequences such as SE-EPI are barely applicable at an ultra-high field strength of 9.4 T due to the presence of strong B0 field inhomogeneities inducing image distortions and provide generally only limited anatomical coverage at rather low resolution. This adds considerable value to the proposed NN-driven approach, which is able to infer high-resolution distortion-free maps of various diffusion metrics with high structural information content from phase-cycled bSSFP input data within a processing time of only a few seconds and scan times on the order of 10 min.

Conclusion

The proposed NN-driven approach shows potential to provide distortion-free high-resolution whole-brain maps of multiple diffusion metrics at high to ultra-high field strengths in clinically relevant scan times.

References

1. Miller KL. Asymmetries of the balanced SSFP profile. Part I: Theory and observation: Balanced SSFP Asymmetry: Theory. Magn. Reson. Med. 2010;63:385–395.

2. Miller KL, Smith SM, Jezzard P. Asymmetries of the balanced SSFP profile. Part II: White matter: Asymmetries of the Balanced SSFP Profile. Part II: White Matter. Magn. Reson. Med. 2010;63:396–406.

3. Scheffler K, Lehnhardt S. Principles and applications of balanced SSFP techniques. Eur. Radiol. 2003;13:2409–2418.

4. Heule R, Bause J, Pusterla O, Scheffler K. Multi-parametric artificial neural network fitting of phase-cycled balanced steady-state free precession data. Magn. Reson. Med. 2020;84:2981–2993.

Fusion of ultra-high-field DTI and 3D mesoSPIM microscopy for white matter tractography in mice

Maria Karatsoli[1,2], Rahel Kaestli[1], Mark-Aurel Augath[3], Theofanis Karayannis[1] and Andras Jakab[2,4*]

[1] Brain Research Institute, University of Zürich, Zürich, Switzerland
[2] Center for MR-Research, University Children's Hospital, Zürich, Switzerland
[3] Preclinical Imaging Center, ETH Zürich, Zürich, Switzerland
[4] Neuroscience Center Zürich, Zürich, Switzerland

* andras.jakab@uzh.ch, Steinwiesstrasse 75, 8032 Zürich, Switzerland

Synopsis: We present a method for the reconstruction of fiber pathways in a joint space consisting of ultra-high-field diffusion tensor imaging (DTI) and whole-mount, 3D light-sheet microscopic images in mice. The estimation of axonal orientation distribution functions (aODF) was achieved in both modalities, which allowed for probabilistic tractography of major white matter structures. Our method provides valuable ground truth information for validation DTI and tractographic procedures.

Zusammenfassung: Wir präsentieren eine Methode, die die Rekonstruktion von Nervenfaserverbindungen in einem gemeinsamen Koordinatensystem, bestehend aus Ultrahochfeld Diffusionstensor MRT (DTI) und 3D Lichtscheibenmikroskopie in denselben transgenen Mäusen ermöglicht. Die in beiden bildgebenden Modalitäten durchgeführte Berechnung der axonalen Orientierungsverteilungsfunktionen (aODF) hat Daten zur Diffusionstraktographie geliefert. Unsere Methode ist wertvoll für die Charakterisierung der Gehirnkonnektivität und liefert auch Ground-Truth Validierungsdaten für DTI.

Motivation

Mapping neural connections is a critically important task for understanding the processes that underlie neuronal functions in normal and pathological conditions. In humans, to date, technical obstacles and ethical considerations have prohibited whole-brain connectivity mapping at the level of individual synapses and neurons. While invasive tracing of neuronal connections is possible in animal studies, whole-brain-level mapping of system-wide connectivity is time- and resource-consuming, elusive effort, and therefore not applicable for any study. Diffusion tensor magnetic resonance imaging (DTI) and tractography may offer unique insights into the (macro-)connectome-level organization of the brain, the spatial resolution and anatomical accuracy is limited.

The overarching goal of our work was to overcome the limitations of DTI by developing a computational image analysis framework fusing microscopy and DTI.

Materials and Methods

Seven adult mice from the Thy1-YFP transgenic line (P58-P66) were used in the study. These mice express a fluorescent protein in the somatosensory as well as in thalamic and other central neurons. The mice were anaesthetized and transcardial perfusion was performed using 4% PFA. We followed the CLARITY tissue clearing protocol (1).

Prior to clearing, the PFA-fixed post mortem brains were scanned on a 9.4T Bruker BioSpec 94/30 MR scanner equipped with a cryogenic coil. For DTI, we used an echo-planar imaging sequence with 64 diffusion encoding pulsed magnetic gradient directions (b=2000 s/mm^2) and 5 B_0 images. An isotropic image voxel resolution of 100 μm was achieved. Scanning time was 12 hours per brain.

DTI data was pre-processed using standard algorithms in the FDT tool of the FSL software library. DTI was corrected for eddy-induced artifacts.

Whole-mount, cleared brains were imaged on the mesoSPIM microscope (2), which offers near isotropic resolution and reduced shadow artifacts. An in-plane resolution of 8 μm and slice distance of 4 μm was used for imaging. The specifications are summarized in **Table 1.**

Laser	Filter	Light sheet	Zoom
515 nm	515 nm LP	Left and right	0.8 x
488 nm	515 nm LP	Left and right	0.8 x
488 nm	515 nm LP	Left	2 x
647 nm	Quadru-pleblock	Left and right	0.8 x

Table. 1: MesoSPIM acquisition details.

We excluded 3 datasets due to insufficient quality of the labeling. 4 of the 7 mesoSPIM datasets underwent the following processing

steps. First, we averaged the left and right light sheet images to achieve homogenous illumination across the whole image. Local image intensity homogenization and re-orientation to a standard direction was performed in ImageJ.

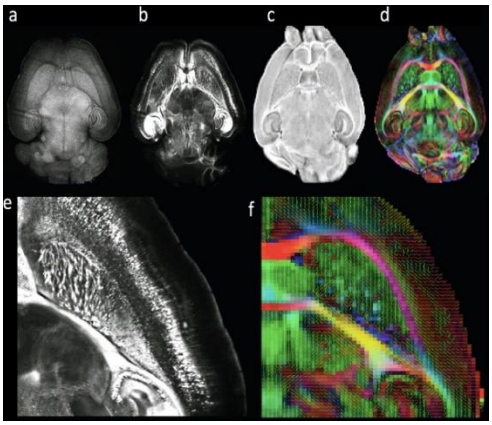

Fig. 1: MesoSPIM microscopy and DTI of a Thy1-YFP mouse. a: reference mesoSPIM image, b: YFP signal image, c: mean DWI image, d: colorized fractional anisotropy image. e-f: zoom-in images of sensorymotor areas and the striatum.

Next, we estimated the axonal orientation distribution functions (aODF). In the high-resolution mesoSPIM images, 3D orientation-sensitive Gabor filter kernels with tubular shaped, elongated Gaussian kernels were used. This filter responded to image texture features of a given orientation and a given width, optimized for the axons visible on the mesoSPIM images. The aODF data, where a filter response (amplitude) was associated with a given spatial angle, was modeled by spherical harmonic functions (SH) to allow easier computation and to model noise. We then down-sampled the SH data to an image resolution of 50 μm isotropic by ignoring voxels that contained no labeled axons.

SH data was processed in the MRtrix software package for computational tractography. Fiber trajectories were estimated by using second-order integration over fiber orientation distributions, implemented as the iFOD in MRtrix (3). The same procedure to estimate SH aODF from the DTI amplitudes was followed in case of the DTI data (**Fig. 1**).

Results

Qualitative analysis revealed a moderate overlap of high diffusion anisotropy in axonal bundles otherwise intensively labeled with YFP. This was particularly strong for corticospinal neurons as well as hippocampal connections (**Fig. 1**). A weaker visual correlation was found for callosal fibers. Tractography from the internal capsule was similar in both modalities. However, DTI revealed spurious connections taking a turn into the corpus callosum (false positivity), and fibers were terminated before reaching the cortical plate. In the mesoSPIM based tracking, we were able to follow the trajectories until the cortical termination (**Fig. 2**).

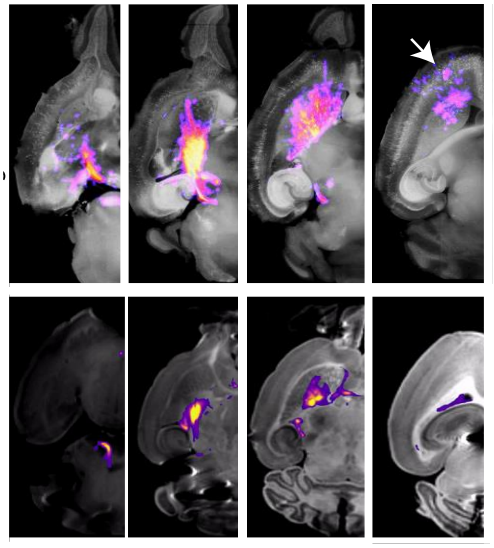

Fig. 2: Tractography in mesoSPIM data (first row) and DTI (second row). White arrow: cortical termination of fibers.

Conclusions

In our study, instead of tracing the elaborate network of neurons individually after invasive tracing, fiber trajectories were statistically estimated based on local fiber orientations. This method therefore accumulates information from to micro-scale to reconstruct macro-scale connectivity. Since the axons are directly visualized in 3D-FLSM, there is no need for a fiber response function, as it would be needed in typical DTI processing. The aODF amplitudes can be visually estimated from the image. In our study, we provided a joint reference space of mesoSPIM and DTI data in the same mice, which can be used to correlate diffusion anisotropy of fiber tractography results either based on microscopy or DTI. In the future, this dataset has to potential to serve whole-brain connectomic studies, or to inform tractography algorithms with micro-scale aODF information.

References

1. Chung K, Wallace J, Kim SY, et al. Structural and molecular interrogation of intact biological systems. Nature 2013; 16:332-337.

2. Voigt F, Kirschenbaum D, Platonova E. et al. The mesoSPIM initiative: open-source light-sheet microscopes for imaging cleared tissue. Nat Methods 2019;16:1105–1108.

3. Tournier J, Calamante F, Connelly A: MRtrix: Diffusion tractography in crossing fiber regions. Int J Imaging Syst Technol 2012; 22:53-66

Removing T2 blurring in RARE sequences by using a DenseNet

Hoai Nam Dang[1*], Jonathan Endres[1], Simon Weinmüller[1], Alexander Loktyushin[2], Felix Glang[2], Klaus Scheffler[2], Arnd Doerfler[1], Andreas Maier[3], Moritz Zaiss[1,2]

[1] Department of Neuroradiology, Universitätsklinikum Erlangen, Friedrich-Alexander Universität Erlangen Nürnberg, Germany.
[2] Magnetic Resonance Center, Max-Planck-Institute for Biological Cybernetics, Tübingen, Germany.
[3] Department of Computer Science, Friedrich-Alexander Universität Erlangen Nürnberg, Germany.

* HoaiNam.Dang@uk-erlangen.de

Synopsis: We propose a method to reduce blurring in RARE sequences along phase encoding direction due to T2 decay during k-space acquisition. A convolutional neural network is employed to map simulated RARE images to the transversal magnetization of the central echo.

Motivation

In fast imaging techniques, like Rapid Imaging with Refocused Echoes (RARE) sequences [1], the short T2 values of different tissues of interest are comparable to the echo-train duration, which results in significant T2 decay during the k-space acquisition. Each echo or k-space sample along the phase encoding direction is thus collected at a different point along the T2-decay curve; the transverse magnetization is constantly changing throughout the acquisition (Fig.1). In FFT reconstruction of centric-reorderd RARE sequences, this leads to a T2- dependent and thus a complicated tissue dependent blurring. In this work, we propose a method to reduce this blurring by utilizing a Convolutional Neural Network and blurring-free transverse magnetization as a target.

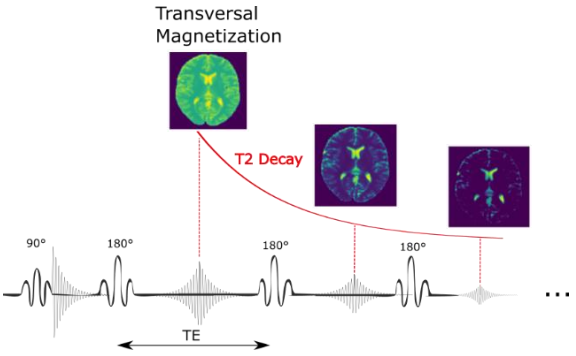

Fig. 1: The T2 decay of refocused echoes along the phase encoding direction is illustrated in this diagram. The transversal magnetization represents the signal contributions of all voxels at a specific time point.

Materials and Methods

Signal simulations were performed by using an Extended Phase Graph (EPG) algorithm [2] implemented in the MRzero framework [3]. A centric-reorderd RARE sequence with a matrix size = (96x96) was used in the simulation. The sequence was repeated with two different echo times TE1 = 17.28ms and TE2 = 19.28ms, respectively. The forward simulation outputs RARE images, and in addition the transversal magnetization, which has the same T2w contrast, but is free from any spatial blurring and forms the target for the neural network. The training data consists of synthetic brain data acquired from the BrainWeb [4] database filled with *in vivo*-like tissue parameters. Each training sample is further augmented by random rotations and cropping at varying spatial location. In total 10,000 training samples are generated. To incorporate prior knowledge the simulated RARE images were multiplied in the frequency domain with the inverse k-space filter as a known operator [5] given by the T2 decay during the echo train: $K_{n,T2} = \exp(\frac{n*2TEd}{T2})$, with $n \in [0, Nrep-1]$ and $T2 \in$ [79.6ms, 110ms, 1500ms], which are estimations of T2 values for white matter, grey matter and cerebrospinal fluid. By applying the inverse k-space filter, signals from the corresponding tissue type are roughly free of blurring, but still overlapped by blurred signals of other tissue types. The remaining task of network is to decouple these signals to acquire a deblurred image (Fig.2). For the architecture of the convolutional neural network a DenseNet [6] is employed and a $\perp$-loss (perpendicular loss) [7] is being used.

Results

For validation of the proposed method, an unseen dataset is used for inference with the trained network. In the simulated RARE images (Fig.3 a,b) blurring in the phase encoding direction (anterior->posterior) is clearly visible. The T2 blurring is strongly reduced in the prediction of the neural network (Fig.3 d) with sharp edges around the border of the brain and at tissue interfaces. Further, the overall contrast matches the target transversal magnetization (Fig.3 c) to a high degree (RMSE=0.131, SSIM=0.52).

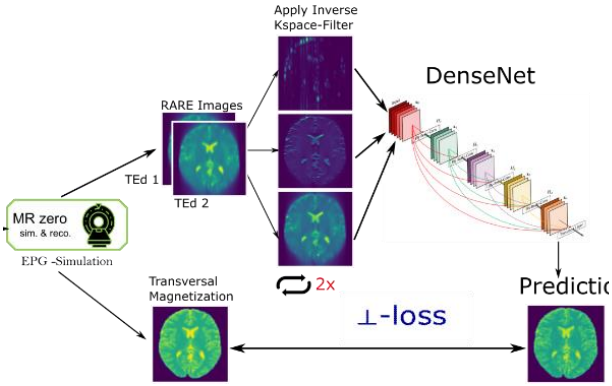

Fig. 2: An overview of the proposed method is shown in this diagram. A RARE sequence is simulated with two different TEd and subsequently an inverse k-space filter is applied. Prediction of the DenseNet is compared to the target transversal magnetization by using a perpendicular loss.

However, the prediction also exhibits some additional high frequency noise in the image. This homogenous noise could be further improved by applying a pretrained DnCNN denoising network (RMSE=0.0129, SSIM=0.62).

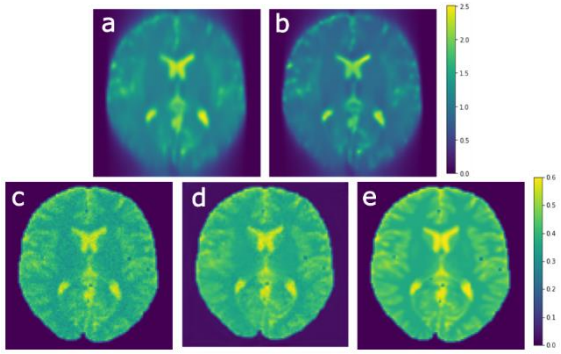

Fig. 3: Simulated test set of a RARE sequence with TE1 = 17.28ms (a) and TE2 = 19.28ms (b) . The prediction of the neural network without (c) and with additional DnCNN denoising (d) yields a good prediction of the transverse magnetization target (e).

Discussion

By utilizing a convolutional neural network blurring in phase encoding direction induced by T2 decay in a centric RARE could be successfully suppressed. In the predicted images additional noise can be observed, which might be due to amplification of high frequency information. This is expected as high frequencies are acquired last and experienced strongest T2 decay and thus lowest SNR.

The used fixed inverse k-space filter could be biased with respect to the T2 values of the object, which could introduce systematic errors. A possible solution could be to allow the neural network to learn the k-space filter directly from the underlying data instead of applying it explicitly. Such a task is closely related to actual prediction of pixelwise T2 values. Hence, for future work extending the proposed method to estimating additionally a T2 map would be a suitable step. Using variable flip angle trains has been proposed to reduce T2 blurring in RARE sequences [8]. This approach can also be included in our MRzero framework to optimize simultaneously flip angles and the deblurring neural network parameters. A further aim would be to release the requirement of two measurements with different TEd values to a single measurement. De-Ringing of linear-reordered RARE sequences can be approached with the same method.

Conclusion

We demonstrated the removal of T2-induced blurring in centric RARE sequences by using two measurements with different TEd values with an applied inverse k-space filter as input to a convolutional neural network.

References

1. Hennig J, Nauerth, A. and Friedburg, H. (1986), RARE imaging: A fast imaging method for clinical MR. Magn Reson Med, 3: 823-833.

2. Weigel M. Extended phase graphs: dephasing, RF pulses, and echoes-pure and simple. Journal of Magnetic Resonance Imaging. 2015 Feb;41(2):266-95.

3. Loktyushin A, et al. MRzero - Automated discovery of MRI sequences using supervised learning. Magn Reson Med. 2021; 86: 709– 724.

4. http://www.bic.mni.mcgill.ca/brainweb/.

5. Maier AK, et al. Learning with known operators reduces maximum error bounds. Nature machine intelligence. 2019 Aug;1(8):373-80.

6. Huang G, et al. Densely connected convolutional networks. InProceedings of the IEEE conference on computer vision and pattern recognition 2017 (pp. 4700-4708).

7. Terpstra M, et al. Rethinking complex image reconstruction: ⊥-loss for improved complex image reconstruction with deep learning. In Proc. ISMRM & SMRT Annual Meeting & Exhibition (Online, 2021).

8. Hennig J, Weigel M, Scheffler K. Multiecho sequences with variable refocusing flip angles: optimization of signal behavior using smooth transitions between pseudo steady states (TRAPS). Magn Reson Med. 2003 Mar;49(3):527-35.

Posters
(P1-P14)

fMRI comparison of optogenetic and electrical stimulation in the mouse hippocampus

Nikolaos Molochidis[1], Enya Paschen[2], Carola Haas[2,3] and Niels Schwaderlapp[1]

[1] Department of Radiology, Medical Physics, Faculty of Medicine, Medical Center University of Freiburg, University of Freiburg, Freiburg, Germany
[2] Experimental Epilepsy Research, Department of Neurosurgery, Medical Center University of Freiburg, Faculty of Medicine, Freiburg, Germany
[3] Center for Basics in NeuroModulation, Faculty of Medicine, University of Freiburg, Freiburg, Germany.

Synopsis: In this study, we used fMRI to analyse the brain–wide activation patterns upon optogenetic and electrical stimulation in mice. Both modalities targeted the right dorsal hippocampus, with the optogenetic stimulation being cell-specific to the granule cells of the dentate gyrus. Common to both stimulations were the recruitment of the hippocampal-entorhinal network. However, the electrical stimulation activated additional areas in the frontal part of the brain.

Zusammenfassung: In dieser Studie wurde mittels fMRT die Gehirnweite Aktivierung von optogenetischer und elektrischer Stimulation in Mäusen untersucht. Stimuliert wurde mit beiden Methoden der rechte dorsale Hippocampus. Mit der Optogenetik wurden zellspezifisch die Körnerzellen des Gyrus dentatus stimuliert. Beide Stimulationen führten zu einer Aktivierung des Hippocampalen-Entorhinalen Netzwerkes. Die elektrische Stimulation allerdings zeigte noch weitere Aktivierungen insbesondere im frontalen Bereich des Gehirns.

Motivation

Optogenetic-fMRI has become a popular method to study induced activity and brain-wide networks in rodents. On the one hand, optogenetics may be applied to study basic neuroscience, e.g. which networks are recruited upon hippocampal stimulation (1), but also to study related disease mechanisms and possible treatments (2-3).

However, as optogenetics per se is not clinically feasible, possible findings based on optogenetics would have to be realized by electrical stimulation eventually. This implies the question how comparable the two modalities are.

In our study we are using fMRI to compare the brain-wide responses upon electrical and optogenetic stimulation of the mouse hippocampus, a brain area of high importance for diseases like temporal lobe epilepsy for example.

Materials and Methods

The right dorsal hippocampus (dHC) was targeted with electrical and optogenetic stimulations during fMRI. An optical fiber and custom-made MRI-compatible electrodes were implanted in Ai32-Rbp4Cre mice (n=6); One stimulation electrode was implanted in the right dHC, one recording electrode in the left dHC, two electrodes over the frontal cortex served as reference and ground.

Four out of these six mice expressed ChR2 in the granule cells of the dentate gyrus and were used for optogenetic stimulation (blue light 460nm, Prizmatix, USA/Canada). The MRI measurements were conducted on a 7T small animal system equipped with a CryoProbe (Bruker, Germany). During the scans, animals were sedated with medetomidine. All experiments were conducted according to federal/institutional guidelines.

FMRI data were acquired with a GE-EPI sequence (TR=1.5s, TE=14, 23, 32 and 41ms, matrix 64x40, resolution 0.28x0.28mm^2, 12 slices, thickness 0.8mm). The four echo images were combined into a single time-series (4).

FMRI preprocessing (motion correction, spatial and temporal filtering), single subject and group level analysis was done with FSL (FMRIB, Oxford, UK).

The stimulation design consisted of five blocks with 1-2s duration (10Hz) and 60s rest. The amplitude for electrical stimulation was 200µA and ca. 90mW/mm^2 for the optogenetic pulses. Additionally, a single stimulation block of 10s (10Hz) was applied.

Results

Optogenetic stimulation yielded robust BOLD responses in the right and left HC and entorhinal cortex (EC). The 2s optogenetic stimulation showed in single subjects also subcortical responses in the frontal part of the brain, which however was not reflected in the group analysis (Fig.1). Overall, the optogenetic results are in agreement with Weitz et. al., 2015 (1).

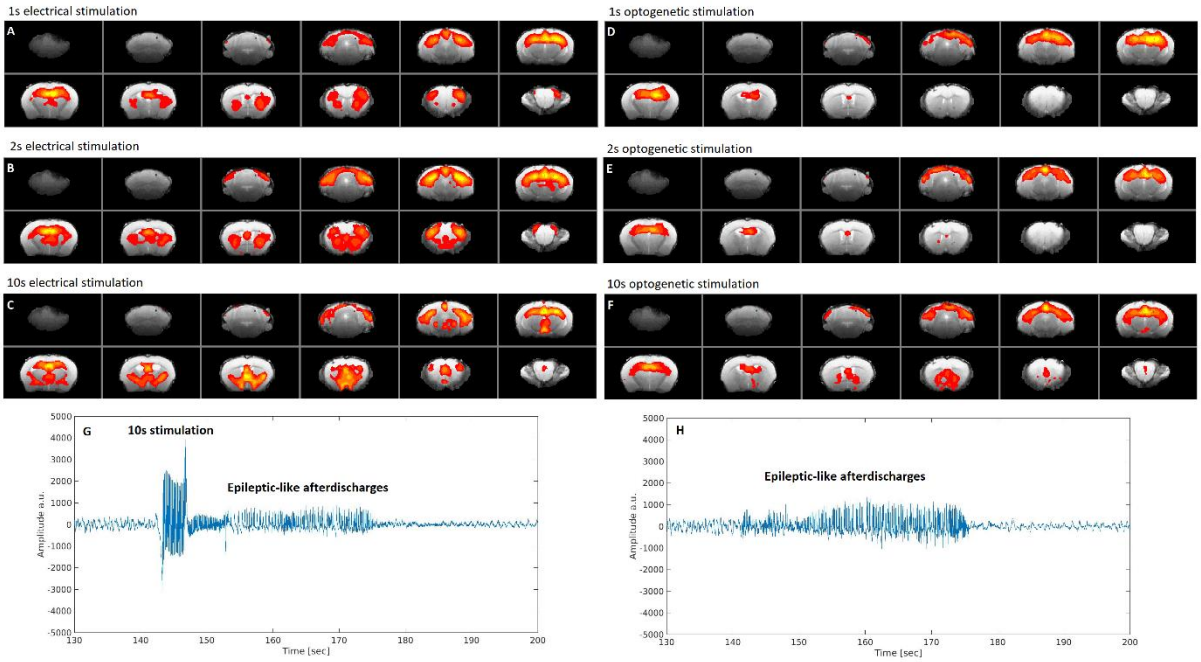

Fig. 1: Responses to electrical or optogenetic stimulation in the mouse hippocampus. (A-C) fMRI response to electrical stimulations with 1s (A, n=6), 2s (B, n=5) and 10s (C, n=6) durations. (D-F) Optogenetic stimulations with 1s (A, n=4), 2s (B, n=4) and 10s (C, n=3) durations. Group level fMRI with voxel-wise corrections at p 0.05, overlaid on a reference RARE image. (G, H) EEG showed epileptiform activity after 10s of electrical (G) or optogenetic (H) stimulations, respectively.

The electrical stimulations also revealed responses in the right and left HC, with a more bilateral recruitment of the EC as compared to the optogenetic stimulation. The most obvious difference to the optogenetic stimulation is the additionally induced activity in frontal areas, such as pallidum and striatum, somatosensory cortex, hypothalamus and nucleus accumbens.

Discussion

The direct comparison of the two stimulation methods is hindered because the respective stimulation amplitudes have an impact on the results but are difficult to compare across the modalities. We addressed this issue by keeping all parameters fixed and only increasing the stimulation time. This revealed two stimulation regimes with short stimulations (1-2s) yielding “normal” activity and longer stimulations (10s) yielding epileptiform activity. In all conditions, the electrical stimulation showed recruitment of brain areas that were not activated by the optogenetic stimulation.

Conclusion

Besides showing similarities - the recruitment of the hippocampal network - we could highlight different activation patterns upon optogenetic or electrical stimulation. FMRI is an important tool to reveal these brain-wide differences.

References

1. Weitz AJ et. al., Optogenetic fMRI reveals distinct, frequency-dependent networks recruited by dorsal and intermediate hippocampus stimulations. NeuroImage 2015; 107: 229-241

2. Krook-Magnuson E. et al., On-demand optogenetic control of spontaneous seizures in temporal lobe epilepsy. Nat Commun 2013; 4:1376

3. Paschen E. et al., Hippocampal low-frequency stimulation prevents seizure generation in a mouse model of mesial temporal lobe epilepsy. eLife 2020; 9:e54518

4. Poser B.A. et. al., BOLD contrast sensitivity enhancement and artifact reduction with multi-echo EPI: Parallel-acquired inhomogeneity-desensitized fMRI. Magn Reson Med. 2006; 55(6):1227-35

Acknowledgements

This work was supported by BrainLinks-BrainTools, Federal Ministry of Economics, Science and Arts of Baden-Württemberg within the sustainability program for projects of the excellence initiative II and the DFG (Grant LE 3437/3-1).

The next snapshot CEST for fast 3D APTw imaging at 3T

Patrick Liebig,[1] Maria Sedykh[2], Kai Herz[3,4], Moritz S. Fabian[2], Angelika Mennecke[2], Manuel Schmidt[2], Arnd Dörfler[2], and Moritz Zaiss[2, 3]*

[1] Siemens Healthcare GmbH, Erlangen, Germany

[2] Department of Neuroradiology, Universitätsklinikum Erlangen, Friedrich-Alexander Universität Erlangen Nürnberg, Germany

[3] Magnetic Resonance Center, Max-Planck-Institute for Biological Cybernetics, Tübingen, Germany

[4] Department of Biomedical Magnetic Resonance, University of Tübingen, Tübingen, Germany

* moritz.zaiss@uk-erlangen.de

Synopsis: We present a fast whole-brain APTw CEST MRI sequence extending the snapshot CEST approach by undersampled acquisition and compressed sensing reconstruction. This allows push-button whole-brain APTw imaging with online reconstruction for clinical research at 3T.

Motivation

Amide proton transfer weighted imaging is a metabolic MRI technique based on chemical exchange saturation transfer (CEST) with the ability of tumor detection and subtyping[1]. CEST MRI suffers from long preparation times and consequently long acquisition times (~5 mins) as well as the interplay of the acquisition onto the preparation state itself. To reduce acquisition time, the snapshot CEST approach has been suggested[2], as a way to acquire the entire 3D volume after only one preparation block. This reduces the acquisition time to an absolute minimum. Furthermore, snapshot CEST completely disentangles the preparation from the readout block, giving freedom to optimally design the preparation block for the contrast desired. Herein, we show an optimized sequence and protocol for snapshot APTw CEST imaging. By using compressed sensing, we could extend the volume and resolution of the snapshot GRE CEST to whole brain acquisition, which before has been limited to a smaller slab.

Materials and Methods

All MRI scans were performed at a Siemens PRISMA scanner (3T) with a 64 channel head coil after written informed consent of the healthy volunteers and patients.

The snapshot CEST sequence consist of an APTw preparation phase following the Pulseq-CEST[3] standard **APTw_001**[4] with a pulsed rf irradiation of 2 s duration at 90% rf duty cycle and a $B_{1,rms}$ of 2 µT. A 3D GRE (2x2x5mm, FA=8°, TE/TR = 2ms/4ms), with 8-fold undersampled acquisition following a variable density poisson disk centric-out in the two phase encoding directions is used fir readout of the prepared magnetization. A 4D coupled reconstruction with L1 regularisation was running on GPU. The regularisation factor along the offset dimension is set to 0. Coil sensitivities were estimated using ESPIRiT. Reconstruction times are 3- 5 minutes depending on the matrix size as well as the number of offsets. Different numbers of offsets between 30 for full Z-spectrum acquisition and 6 offsets around 3.5ppm were used. Minimal possible acquisition time was ~1min. APTw contrast was achieved by asymmetry analysis evaluated at 3.5 ppm.

Results

Comparing APTw images obtained with snapshot CEST to the literature reveals that published results of healthy volunteers show a relatively homogenous (green) image, whereas our obtained images showed quite some gray-white matter contrast (Figure 1a). This is actually a visualization issue, solved by using the same rainbow colormap windowed from -5% to +5% (Figure 1b).

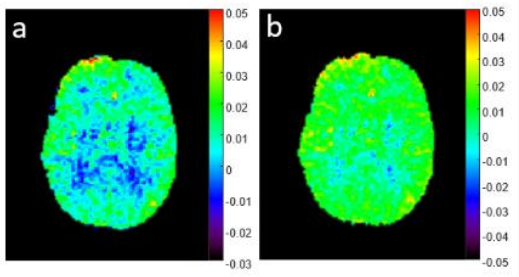

Figure 1: Previously published APTw imaging in a healthy volunteer by MTRasym(3.5 ppm, B1rms =2 µT). (a) and (b) is the exact same image just with different windowing of the rainbow colormap. (b) shows the homogeneous green background known from other published work.

As noise is still visible in Figure 1, we further improved the CNR of the method by following the snapshot readout protocol of dynamic glucose-enhanced imaging at 3T by Herz et al.[5] and increased the flip angle to 8° and the voxel size to 2x2x5 mm. As seen in Figure 2c this yields more CNR compared to higher resolutions (Figure 2ab). The flip angle can also be

slightly increased without causing too much blurring, yielding also higher CNR (Figure 2ab).

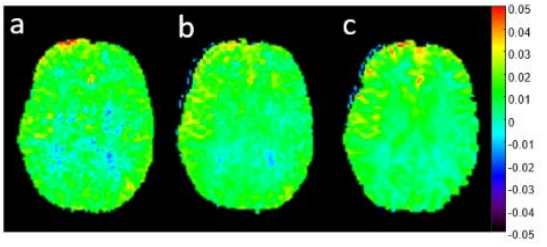

Figure 2: Comparison of APTw images upon change of flip angle and voxel size. (a) 1.7x1.7x5mm, FA=6°, (b) 1.7x1.7x5mm, FA=9°, and (c) 2x2x5mm, FA=7°.

Figure 3 shows the comparison of the previous slab-selective fully-sampled snapshot CEST sequence and the whole-brain compressed sensing snapshot CEST with the same optimized APTw parameters. The optimized protocol could be applied in a patient with a high-grade glioblastoma (Figure 4). APTw imaging shows the typical hyperintensity in the tumor area[1].

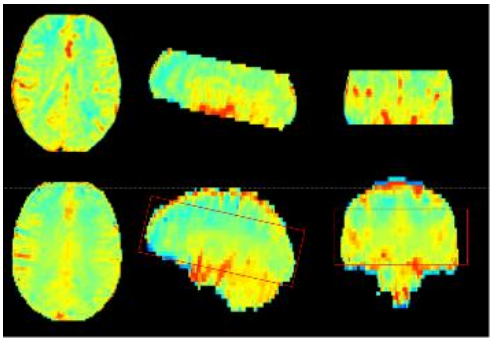

Figure 3: Validation of the whole-brain compressed sensing snapshot APTw-MRI sequence (bottom) with conventional snapshot APTw (top). Whole-brain coverage as seen in the transversal, sagittal and coronal view is now possible.

Discussion

The previous snapshot CEST approach could be extended to whole-brain coverage without time penalty by undersampled acquisition and compressed sensing reconstruction.

An optimized protocol yields APTw images with decent CNR at 3T. With an optimized subsampling in frequency domain, we accelerate the whole-brain APTw method to an acquisition time below 1 minute. TSE-based sequences with comparable coverage typically take 5-10 minutes[1]. The B0-corrected asymmetry analysis runs online, thus, APTw images are directly provided at the scanner making this sequence and protocol a push button tool for clinical researchers.

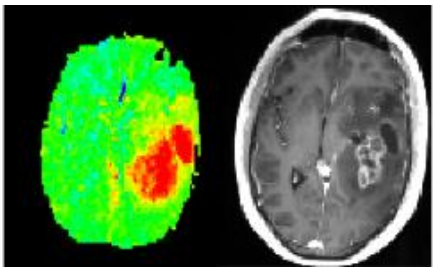

Figure 4: APTw image (left) and post.contrast T1w-MRI (right) of a tumor patient shows that the snapshot APTw MRI highlights the tumor area in red in contrast to healthy tissue which appears green.

Conclusion

Undersampled acquisition and compressed sensing reconstruction allows for increasing the volume coverage of the snapshot CEST approach for whole brain imaging. With this sequence, a fast snapshot APTw imaging was realized and validated for its ability to detect brain tumors.

References

1. Zhou J, et al. *J Magn Reson Imaging*. 2019;50(2):347-364. doi:10.1002/jmri.26645

2. Zaiss M, et al. NMR Biomed. 2018 Apr;31(4):e3879. doi: 10.1002/nbm.3879.

3. Herz et al. Pulseq-CEST: T *Magn Reson Med*. 2021; 00: 1– 14. https://doi.org/10.1002/mrm.28825

4. https://github.com/kherz/pulseq-cest-library/tree/master/seq-library/APTw_3T_001_2uT_36SincGauss_DC90_2s_braintumor

5. Herz et al. *Magn Reson Med*. 2019; 82: 1832– 1847. https://doi.org/10.1002/mrm.27857

Entwicklung und in-vitro-Evaluation einer GlucoCEST-Sequenz an klinischen 3 T MR-Scannern

Tobias Krähling,[1*] Jochen Bauer[2] und Verena Hoerr[1]

[1] AG Hybrid MRI Physics, Klinik für Radiologie, UK Münster, Münster, Deutschland.
[2] Translational Research Imaging Center, Klinik für Radiologie, UK Münster, Münster, Deutschland.
* Email: tobias.kraehling@uni-muenster.de.

Synopsis: A self-developed CEST sequence with multiple saturation pulses and FLASH imaging was evaluated for the measurement of glucose on two clinical 3 T scanners. Here, it is shown that integration over the entire z-spectrum, leads to a linear relationship to glucose concentration, with comparable slopes on both scanners. Our results also demonstrate that a higher B_1 field is advantageous. This method shows potential to be used in vivo as an easy-to-use technique for glucose quantification.

Zusammenfassung: Es wurde eine selbstentwickelte CEST-Sequenz mit mehreren Sättigungspulsen und FLASH-Bildgebung für die Messung von Glukose an zwei klinischen 3 T-Scannern evaluiert. Hier zeigt sich, dass mittels einer Integration über das gesamte z-Spektrum ein linearer Zusammenhang mit vergleichbaren Steigungen auf beiden Scannern zur Glukosekonzentration besteht. Ein höheres B_1-Feld erwies sich hierfür als günstig. Diese Methode zeigt Potential, auch in vivo als einfach anzuwendende Technik für die Glukosequantifizierung eingesetzt werden zu können.

Motivation

Chemical Exchange Saturation Transfer (CEST) ist eine Messmethode, die einen molekülspezifischen Kontrast ermöglicht und sich auch zum Nachweis und zur Quantifizierung von verschiedenen Molekülgruppen bei niedrigen Konzentrationen eignet. [1] Das Basisprinzip hinter der CEST-Methode ist die selektive Sättigung von Wasserstoffprotonen des nachzuweisenden Moleküls, die eine gegenüber Wasser verschobene Resonanzfrequenz aufweisen und die Übertragung dieser Sättigung auf Wasserprotonen mittels chemischem Austausch. Die Detektion und Quantifizierung erfolgt hierbei indirekt über die Messung des Wassersättigungssignals in Abhängigkeit der Sättigungsfrequenz.

Für viele Pathologien wie Entzündungen, Tumorerkrankungen, Hirninfarkt oder neurodegenerative Veränderungen stellt die Pharmakokinetik und Metabolismus von Glukose einen sensitiven Biomarker dar. Durch Verabreichung von Glukoselösung als Kontrastmittel können Veränderungen der Glukosekonzentration mittels CEST bestimmt werden. [2] Hierfür wurde eine neue Pulssequenz auf zwei humanen 3 T MR-Scannern entwickelt und zunächst *in vitro* überprüft.

Material und Methoden

Die Messungen erfolgen an zwei 3 T MR-Scannern (Siemens Biograph mMR VE11P und Prisma^{fit} VE11E) mit einer selbstgeschriebenen Pulssequenz unter Verwendung der Kopfspule. Die Sequenz besteht aus einem CEST Präparationsmodul und einem 2D FLASH-Modul für die Bildgebung (Abb. 1). Das entwickelte CEST-Modul erlaubt die Anzahl und Pulsform der RF-Sättigungspulse, die Pulslänge, Abstand zwischen den Pulsen und das B_1-Feld zu variieren. Für jede akquirierte k-Raum-Linie wird die CEST-Präparation vorab durchgeführt, als Beschleunigungstechnik ist GRAPPA implementiert. Verwendete Standardparameter für die Bildgebung sind: TR 1000 ms; TE 30 ms; FOV 80×80 mm²; Matrix 32×32; Einzelschicht mit 5 mm; iPAT 4.

Über alle Messungen konstante Parameter für das CEST-Modul waren: Frequenzoffset -500 – 500 Hz; Schrittweite 20 Hz; Pulsform Gauss; Pulsbreite 100 ms; Pulsanzahl 5; Abstand zwischen Pulsen 1 ms. Zusätzlich wurde bei einem Offset von 4000 Hz ein Referenzbild akquiriert. Bild- und Datenanalyse erfolgen mittels Fiji ImageJ und OriginPro 2020 (OriginLab Cor., Northampton, USA), wobei die inversen z-Spektren für eine ROI über $nMPV = (1 - S/S_{Ref}) \times 100$ und die Asymmetriespektren über $dnMPV = nMPV(\omega) - nMPV(-\omega)$ ermittelt wurden.

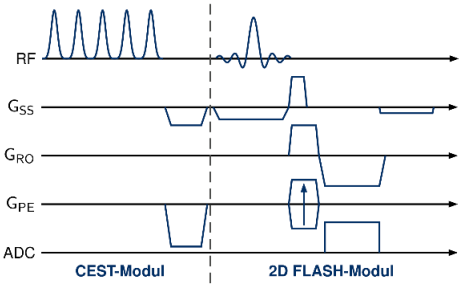

Abb. 1: Pulsdiagramm der selbstentwickelten Sequenz mit CEST-Präparationsmodul und 2D FLASH-Modul für die Bildgebung.

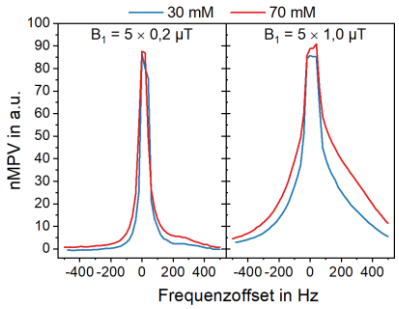

Abb. 2: Inverse z-Spektren für 30 mM und 70 mM Glukose und zwei B_1-Felder, gemessen am Siemens Biograph mMR.

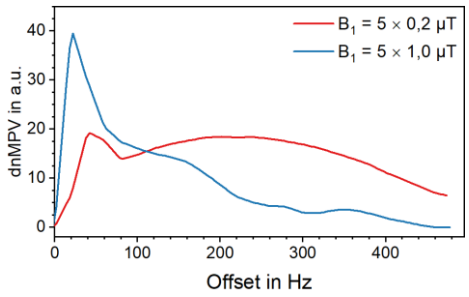

Abb. 3: Asymmetriespektrum für 70 mM bei niedrigem und hohem B1-Feld, gemessen am Siemens Biograph mMR.

Als Proben wurden Glukoselösungen in zweifach-destilliertem Wasser mit Konzentration zwischen 5 und 70 mM Glukose in Glasflaschen verwendet.

Ergebnisse

Die Variation des B_1-Feldes der Sättigungspulse führt bei höherem B_1-Feld zu einer Verbreiterung der Peaks, insbesondere des Wasserpeaks (Abb. 2). Wasser- und Glukoseresonanzen (bei 0,5, 1,2, 1,8 und 2,4-2,8 ppm) überlagern sich bei hohem B_1-Feld derart, dass eine spektrale Trennung nicht möglich ist, wohingegen bei niedrigem B_1-Feld einzelne Resonanzen noch erkennbar sind (Abb. 3). Unterschiede im spektralen Auflösungsvermögen zwischen Biograph mMR und Prisma^{fit} sind nicht zu erkennen.

Zur Überprüfung des Antwortverhaltens auf Konzentrationsänderungen wurden Konzentra

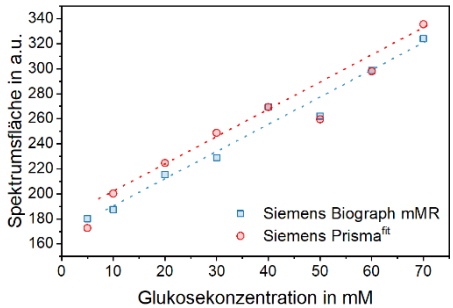

Abb. 4: Abhängigkeit der Spektrumsfläche über das gesamte Abtastintervall in Abhängigkeit von der Glukosekonzentration für B_1 = 5 ×1,0 µT.

tionen zwischen 5 und 70 mM an beiden MR-Scannern untersucht und das gesamte z-Spektrum integriert (Abb. 4). Beide Systeme zeigen hier einen linearen Zusammenhang mit ähnlicher Steigung. Die Reproduzierbarkeit der Quantifizierungsmethode wurde durch Wiederholungsmessungen an verschiedenen Tagen überprüft. Zudem wurde variiert: Empfangsspule (Kopf auf Body-Array/Spine) und Schrittweite (20 Hz auf 40 Hz und 100 Hz). Die Streuung der Messwerte lag bei max. 6 %.

Diskussion

Durch die PET-Komponente beim Biograph mMR sind zunächst Verbreiterungen des Spektrums aufgrund höherer Wirbelstromeffekte zu erwarten, die jedoch im Vergleich zum Prisma nicht bestätigt werden konnten. Vielmehr zeigt das B_1-Feld einen stärkeren Effekt auf die Verbreiterung der Peaks im Spektrum. Hohe B_1-Felder führen zwar zu einer deutlichen Verbreiterung (Abb 1), bei Konzentrationsveränderungen ist hierdurch aber eine größere Änderung der gesamten Peakfläche verbunden, die zu einer geringeren Streuung und höheren Sensitivität führt. Für die Glukosequantifizierungen über die Integration des gesamten Spektrums sollten daher eher höhere B_1-Felder verwendet werden.

Nachteil ist jedoch, dass hiermit auch andere Moleküle als Glukose erfasst werden, deren Einfluss auf die Quantifizierung weiter untersucht werden muss. Des Weiteren sind pH-Änderungen unterschiedliche Glukosekonzentrationen nicht berücksichtigt. Um die vorgestellte Methode auch auf in vivo-Messungen übertragen zu können, muss der lineare Zusammenhang zwischen Konzentration und Spektrumsfläche unter Verwendung verschiedener Pufferlösungen verifiziert werden.

Schlussfolgerung

Mit der entwickelten CEST-Sequenz ist eine in-vitro Konzentrationsbestimmung von Glukose an 3T-Scannern möglich. Ein Anfitten von Peaks ist hierfür nicht notwendig, sondern kann durch Integration der gesamten Spektrumsfläche erfolgen.

Referenzen

1. van Zijl PC, Yadav NN. Chemical exchange saturation transfer (CEST): what is in a name and what isn't? Magn. Reson. Med. 2011;65:927-948.

2. Jones KM, Pollard AC, Pagel MD. Clinical applications of chemical exchange saturation transfer (CEST) MRI. J. Magn. Reson. Imaging 2018,47:11-27.

^{7}Li-/^{1}H-Messaufbau für tierexperimentelle Anwendungen

Marco Deckers,[1] Tor Rasmus Memhave,[1] Jens Gröbner[2], Susann Boretius[1,3] und Amir Moussavi[1]

[1] Abteilung Funktionelle Bildgebung, Deutsches Primatenzentrum GmbH, Leibniz-Institut für Primatenforschung, Göttingen, Deutschland.
[2] Fachbereich Elektrotechnik und Informationstechnik, Fachhochschule Südwestfalen, Deutschland
[3] Johann-Friedrich-Blumenbach Institut für Zoologie und Anthropologie, Georg-August-Universität, Göttingen, Deutschland
* E-Mail: mdeckers@dpz.eu

Synopsis: This work deals with the development and optimization of surface coils for experiments in small animals. Especially in the field of X-nuclei (all nuclei except ^{1}H) there are many possibilities for optimization with regard to the lower gyromagnetic ratio and the significantly lower sensitivity compared to hydrogen. Preliminary results demonstrate the feasibility of *in vivo* lithium imaging in mice using the introduced coil setup.

Zusammenfassung: Diese Arbeit befasst sich mit der Entwicklung und Optimierung von Oberflächenspulen für tierexperimentelle Anwendungen im Kleintierbereich. Gerade auf dem Gebiet der X-Kerne (alle Kerne außer ^{1}H) bedarf es im Hinblick auf das geringere gyromagnetische Verhältnis und der deutlich geringeren Sensitivität im Vergleich zum Wasserstoffkern weiterer Optimierungen. Erste in vivo Messungen in der Maus verdeutlichen das Potential des Messaufbaus für zukünftige Studien.

Motivation

Durch die Verwendung sogenannter X-Kerne (z.B. ^{7}Li, ^{31}P) anstatt der üblicherweise in der Magnetresonanztomographie verwendeten Wasserstoffkerne (^{1}H) lassen sich die Spezifität und Anwendungsmöglichkeiten dieses Bildgebungsverfahrens deutlich erweitern. So ermöglicht beispielsweise die Detektion von ^{7}Li dessen Verteilung im Gehirn nach entsprechender Lithium-Therapie bei Patienten mit bipolarer Störung [1] zu bestimmen. Um zudem strukturelle Information zu erhalten, wird üblicherweise eine X-Kernspule mit einer ^{1}H-Spule kombiniert. Das Ziel dieser Arbeit ist es, eine einzel-resonante X-Kern-Oberflächenspule (^{7}Li) für tierexperimentelle Anwendungen zu entwickeln, die in Kombination mit einer ^{1}H-Volumenspule sowohl strukturelle als auch metabolische Information des zu untersuchenden Objektes liefert.

Material und Methoden

Alle Experimente wurden an einem tierexperimentellem MR-System (BioSpec 94/30, Bruker BioSpin MRI) durchgeführt. Abbildungen 1 zeigt das Schaltungsnetzwerk des verwendeten Spulenaufbaus. Der Spulenring (14x20 mm) ist an das zu untersuchende Kleintier (Maus) angepasst und umgibt somit das Gehirn vollständig. Um das Signal-zu-Rausch Verhältnis weiter zu verbessern, wurde zudem eine Segmentierung des Spulenrings vorgenommen. Diese soll für eine Reduzierung der elektrischen Verluste und eine bessere Einstrahlung des Hochfrequenzimpulses sorgen [2]. Zudem kann damit der Gütefaktor der Spule im Vergleich zu nichtsegmentierten Spulen erhöht werden [3]. Um das optimale Verhältnis von Spulendurchmesser und Anzahl der Segmentierungen zu ermitteln, wurden Spulen mit unterschiedlicher Anzahl an Segmentierungen konstruiert. Die Anpassungsnetzwerke wurden durch Simulationen mit Ansoft Designer SV und Smith-Chart V4.1 berechnet. Um eine optimale Anpassung im MR-System zu gewährleisten, wurden variable Kapazitäten und Induktivitäten im Anpassungsnetzwerk („Matching- & Tuning“ –Netzwerk) verwendet.

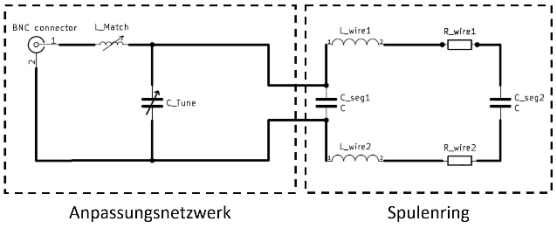

Abbildung 1: Schaltungsdiagramms einer 2-fach segmentierten Spule.

Zusätzlich zur Oberflächenspule wurde ein Mantelwellenfilter benutzt, um äußerliche Störeinflüsse zu vermeiden beziehungsweise zu verringern. Der endgültige Aufbau aus dem Anpassungsnetzwerk und des Spulenrings wurde dann auf einem 3D-Modell integriert, sodass dieser dann im MR-System befestigt werden konnte. Für die Positionierung als auch der strukturellen Darstellung der Probe dient eine 86 mm ^{1}H-Volumenspule.

Die systematische Evaluation der verschiedenen Spulen erfolgte mittels lokalisierter Spektroskopie (ISIS: TR = 2,5 s, Bandbreite = 10 kHz, 256 Datenpunkte, Voxelgröße = 6x5x8 mm^{3}) einer LiCl-Probe (100 mM). Mit der besten Spu-

lenkonfiguration wurden dann in vivo Messungen in Wildtyp-Mäusen (5 Wochen nach Lithium-Gabe über das Futter) durchgeführt (Spiral: TR = 2,5 s, TE = 1,6 ms, räumliche Auflösung = 2x2x3 mm^3, Messdauer = 4 Std.)

Ergebnisse

Abbildung 2 verdeutlicht den Einfluss der Segmentierung auf das gemessene Spektrum. Es ist ein deutlicher Anstieg des MR-Signals in Relation zur Anzahl der Segmente zu beobachten. Eine Empfangsspule mit vier Segmenten war Aufgrund der Größe der Spule und Schwierigkeiten im Anpassungsnetzwerk nicht realisierbar. Bei Betrachtung des SNRs stellte sich heraus, dass für den gewählten Spulendurchmesser von ca. 14x20 mm die 2-fach segmentierte Oberflächenspule die optimale Konfiguration darstellt.

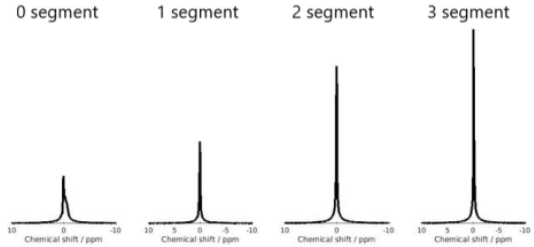

Abbildung 2: Lokalisierte Spektren der jeweiligen Spulenkonfiguration.

In Abbildung 3 ist die Homogenität des erzeugten Hochfrequenzimpulses für die 2-fach segmentierte Spule abgebildet.

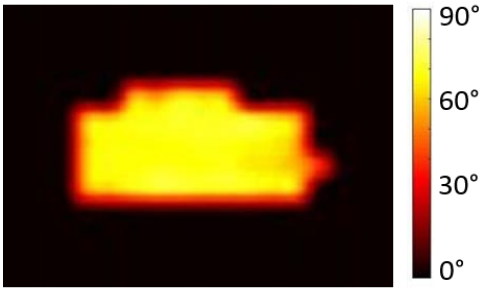

Abbildung 3: B1+-Karte der 2-fach segmentierten Spule.

Für in vivo Aufnahmen in der Maus haben wir uns somit für die 2-fach segmentierte Version des Spulenaufbaus entschieden. Abbildung 4 zeigt sowohl die Konzentrationsverteilung von Lithium im Mäusehirn, als auch die mittels der ^{1}H-Volumespule aufgenommene strukturelle Darstellung.

Diskussion

In dieser Arbeit wurden verschiedene Entwicklungsschritte zur Konstruktion eines Spulenaufbaus für X-Kerne durchlaufen und die entwickelte Spule für tierexperimentelle Anwendungen optimiert. Sowohl die Form bzw. Größe der Empfangsspule als auch die Segmentierung des Spulenrings wurde auf die Gegebenheiten und Erfordernisse der Maus angepasst. Durch Vergleichsmessungen wurde der optimale Spulenaufbau ermittelt und erste in vivo Aufnahmen an der Maus durchgeführt. B1+-Karten verdeutlichen zudem die Homogenität des erzeugten Hochfrequenz-impulses. Aktuelle weiterführende Arbeiten beinhalten neben einer zusätzlichen Optimierung des Spulenaufbaus auch ein Vergleich mit herkömmlich verfügbaren doppelresonanten Spulen.

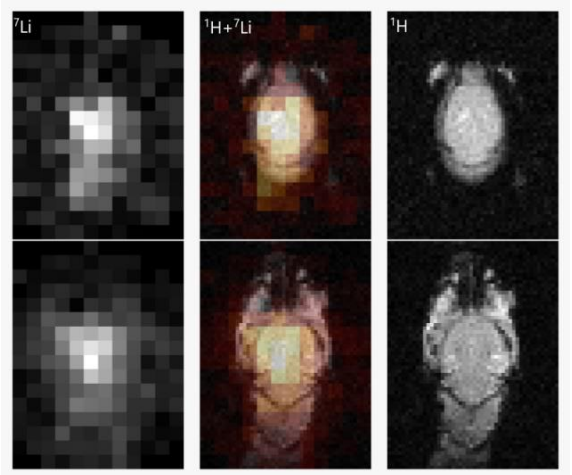

Abbildung 4: links) ^{7}Li-Aufnahmen in der Maus. rechts) Strukturelle Darstellung des Gehirns mittels ^{1}H. Mitte) Überlagerung der beiden Aufnahmen.

Schlussfolgerung

Erste in vivo Aufnahmen verdeutlichen das Potential des hier vorgestellten Spulenaufbaus für tierexperimentelle Anwendungen. In Abhängigkeit von der zu realisierenden Geometrie der Spule hat die gewählte Anzahl an Segmentierungen einen signifikanten Einfluss auf das SNR. Individuelle Spulenlösungen können gerade im Bereich der X-Kern-Bildgebung einen hohen Mehrwert für die Datenqualität bedeuten.

Referenzen

1. Schlegel, Medizinische Physik. Springer-Verlag GmbH, 2018

2. Joel Mispelter et. Al., NMR Probeheads For Biophysical und Biomedical Experiments, Imperial College Press, 2009

3. F. David Doty et. Al., Radio frequency coil technology for small-animal MRI, Wiley Inter-Science, 2006

Optimierte IR-DWI Aufnahmeparameter für ein 2-Kompartimentmodell der Prostata

Felix Gloger[1*], Tobit Führes[1], Andreas Riexinger[1], Jan Martin[1,2], Martina Murr[1,3], Sebastian Bickelhaupt[1], Bernhard Hensel[4], Michael Uder[1], Frederik Laun[1]

[1] Radiologisches Institut, Universitätsklinikum Erlangen, Friedrich-Alexander-Universität Erlangen-Nürnberg (FAU), Erlangen, Deutschland
[2] Physical Chemistry, Lund University, Lund, Schweden
[3] Department für Radioonkologie, Sektion Biomedizinische Physik, Eberhard-Karls Universität Tübingen, Tübingen, Deutschland
[4] Zentrum für Medizinische Physik und Technik, Friedrich-Alexander-Universität Erlangen-Nürnberg (FAU), Erlangen, Deutschland

* Felix Gloger, Universitätsklinikum Erlangen, Maximiliansplatz 3, 91054 Erlangen, Deutschland, felix.gloger@extern.uk-erlangen.de .

Zusammenfassung: Für ein 2-Kompartiment Modell zur Beschreibung der Diffusion in der Prostata wurden b-Werte und TI-Zeiten numerisch optimiert. Die optimierten b-Werte waren: 20, 260, 300, 640, 920, 1840, 1920, 2000 s/mm² und die optimierten TI-Zeiten waren 0, 0.20, 0.25, 0.95, 1.25, 1.40, 2.60, 3.35, 3.60, 4.30, 4.85, 5.00 s.

Motivation

Die quantitative MRT zielt darauf ab, physikalische Parameter zu messen, die den MR-Kontrast beeinflussen, wie beispielsweise die Relaxationszeiten T_1 und T_2 und den scheinbaren Diffusionskoeffizienten (ADC, engl. Apparent Diffusion Coefficient) [1]. Z.B. stellt die Messung von ADC-Karten in der Diagnostik des Prostatakarzinoms derzeit ein zentrales Element gemäß der PI-RADS Leitlinien dar [2].

Eine Erweiterung dieses klassischen Ansatzes, einzelne physikalische Parameter zu messen, stellt die multi-dimensionale MRT dar, die auf die Messung mehrerer physikalischer Parameter und deren Korrelationen abzielt [3].

Durch diesen multidimensionalen Ansatz können einerseits die Parameter biophysikalischer Gewebemodelle besser gemessen werden. Andererseits kann die auftretende Degeneration, d.h. die Unmöglichkeit, die Modell-Parameter zu bestimmen, da mehrere Modell-Parameter die gleichen Signalkurven erzeugen, teils überwunden werden [4].

Diese Arbeit basiert auf der Hypothese, dass die Wasserdiffusion in der Prostata durch ein 2-Kompartimentmodell beschrieben werden kann; und dass dessen Parameter mittels IR-diffusionsgewichteter MRT gemessen werden können (IR, engl., Inversion Recovery). Die Prostata soll in diesem Modell durch ein Gewebe-Kompartiment und durch ein Flüssigkeits-Kompartiment beschrieben werden.

Da die quantitative mehrdimensionale MRT sich noch schwieriger gestaltet als die eindimensionale quantitative MRT, ist die Verwendung eines optimierten Messprotokolls unabdingbar. Ziel dieser Arbeit war deshalb die Erstellung eines optimierten Satzes an Inversionszeiten TI und Diffusionswichtungen b für die Messung der Parameter des 2-Kompartiment-Prostata-Modells.

Material und Methoden

Das 2-Kompartiment-Modell wird durch folgende Signalgleichung beschrieben

$$S(b,TI) = S_{0,\mathrm{G}} \cdot \left(1 - 2e^{-\frac{TI}{T_{1,\mathrm{G}}}}\right) \cdot \exp(-bD_{\mathrm{G}}) + S_{0,\mathrm{F}} \left(1 - 2e^{-\frac{TI}{T_{1,\mathrm{F}}}}\right) \cdot \exp(-bD_{\mathrm{F}}).$$

$S_{0,\mathrm{G}}$ und $S_{0,\mathrm{F}}$ beschreiben dabei die T_2-gewichteten Signale des Gewebe-Kompartiments (= G) und des Flüssigkeits-Kompartiments (= F). $T_{1,\mathrm{G}}$ und $T_{1,\mathrm{F}}$ sind die T_1-Zeiten und D_{G} und D_{F} die ADCs der zwei Kompartimente. Die Optimierung wurde für einen festen Satz an Modellparametern durchgeführt: $S_{0,\mathrm{G}}$ = 200, $S_{0,\mathrm{F}}$ = 100, $T_{1,\mathrm{G}}$ = 1.5 s, $T_{1,\mathrm{F}}$ = 3.0 s, D_{G} = 0.8 mm²/s, D_{F} = 3.0 mm²/s, SNR = 100, für den Fall, dass 96 Signalaufnahmen erfolgen. Folgende Verteilungen der Zahl der b-Werte und TI-Zeiten wurden verwendet: (2, 48), (4, 24), (8, 12), (12, 8), (24, 4), (48, 2).

Für die Optimierung wurden zufällig 100 000 b-TI-Verteilungen erzeugt (erlaubte Werte: b = 0, 20, …, 2000 s/mm², TI = 0, 0.05, …, 6 s). Zum Vergleich wurden Verteilungen mit äquidistant verteilten b- und TI-Werten betrachtet. Bei den äquidistanten Verteilungen wurde zudem eine

Optimierung der Startwerte für den Fit durchgeführt, da der Fit sonst instabil war.

Für die Güte der b-TI-Verteilungen wurde die Summe der relativen Fehler der Modellparameter (im Vergleich zum jeweils wahren Wert) in wiederholten Fits verwendet. Die nach diesem Kriterium besten Verteilungen wurden gemäß des in Abb. 1 dargestellten Schemas bestimmt.

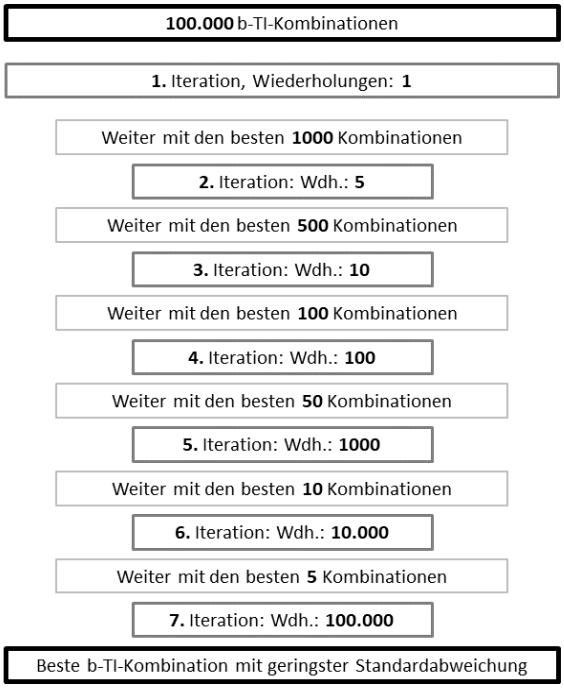

Abb. 1: Der Optimierungsprozess.

Ergebnisse

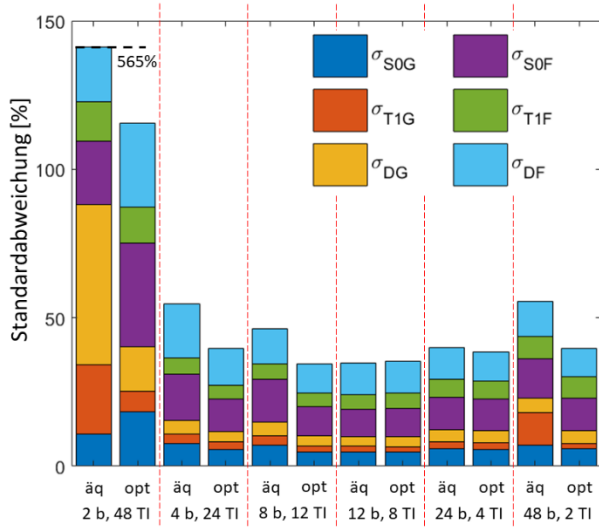

Abb.2: Relativer Fehler der Modellparameter. äq = äquidistant verteilte Aufnahmeparameter, opt = optimierte Aufnahmeparameter. Der größte Fehlerbalken wurde auf ein Viertel gestaucht.

Die b-TI-Verteilung mit der kleinsten Summe der relativen Fehler der Modellparameter war:

b [s/mm²] = 20, 260, 300, 640, 920, 1840, 1920, 2000.

TI [s] = 0, 0.20, 0.25, 0.95, 1.25, 1.40, 2.60, 3.35, 3.60, 4.30, 4.85, 5.00.

In Abb. 2 sind die relativen Fehler der Modell-Parameter abgebildet. Solange mehr als zwei b-Werte verwendet werden, ist der Unterschied zwischen den Verteilungen recht gering. Alle Modellparameter können mit den optimierten b-TI-Verteilungen mit einem relativen Fehler < 10% gemessen werden. Der Fehler der Parameter des Gewebe-Kompartiments ist um etwa einen Faktor drei größer, was dem Verhältnis $S_{0,G}/S_{0,F}$ entspricht. Der relative Fehler reduziert sich in den meisten Fällen wesentlich im Vergleich zur äquidistant verteilten b-TI-Verteilung.

Diskussion

Die durchgeführte Optimierung war erfolgreich und es sollten eher optimierte als äquidistant verteilte Aufnahmeparameter verwendet werden. Nichtsdestotrotz schneiden die äquidistanten Verteilungen erstaunlich gut ab. Die Anzahl der verwendeten b- und TI-Werte ist letztendlich wichtiger als die genaue Verteilung der Werte.

Eine Limitation des hier verwendeten Optimierungsansatzes ist, dass nur ein fester Satz an Modellparametern verwendet wurde. Eine weitergehende Optimierung mit Modellparametern, die aus einer sinnvollen Verteilung gezogen werden, würde diese Limitation überwinden.

Schlussfolgerung

Für die weitergehende Evaluierung des 2-Kompartiment-Modells der Prostata sollten optimierte b-TI-Verteilungen verwendet werden. Nächster Schritt ist die Evaluierung an gesunden Probanden.

References

1. Seiberlich N, Gulani V. Quantitative Magnetic Resonance Imaging, Advances in Magnetic Resonance Technology and Applications, Volume 1, 2020

2. Gupta RT, Mehta KA, Turkbey B, Verma S. PI-RADS: Past, present, and future. J Magn Reson Imaging. 2020 Jul;52:33-53.

3. Laun FB, Multidimensionale diffusionsgewichtete Magnetresonanztomographie, Zeitschrift für Medizinische Physik, Volume 30, Issue 1, 2020

4. Novikov, DS, Kiselev, VG, Jespersen, SN. On modeling. Magn Reson Med. 2018; 79: 3172-3193.

Dependence of Biexponential IVIM Parameters on the Number of Slices in the Liver

Martin Loh[1*], Tobit Führes[1], Bernhard Hensel[2], Michael Uder[1], and Frederik Bernd Laun[1]

[1] Radiologisches Institut, Universitätsklinikum Erlangen, Friedrich-Alexander-Universität Erlangen-Nürnberg (FAU), Erlangen, Deutschland.
[2] Zentrum für Medizinische Physik und Technik, Friedrich-Alexander-Universität Erlangen-Nürnberg (FAU), Erlangen, Deutschland.
* Martin Loh, Universitätsklinikum Erlangen, Maximiliansplatz 3, 91054 Erlangen, Deutschland, martin.loh@extern.uk-erlangen.de

Synopsis: The dependence of intravoxel incoherent motion (IVIM) parameters on the number of acquired slices is examined measuring the livers of nine healthy volunteers. Although the perfusion fraction showed a slight decrease in the many slice setting, no significant change was found. For D and D^*, no statistically significant dependencies occurred, as well.

Motivation

Intravoxel incoherent motion (IVIM) is a method in diffusion-weighted imaging, which not only considers tissue diffusivity, but also signal stemming from blood perfusion. The IVIM effect becomes noticeable for small b-values (b < 150 s/mm²), where a strong signal decay of the blood compartment is observed.

Mathematically, the signal can be described by a biexponential function:

$$S(b) = S_0 \cdot [(1-f)\exp(-bD) + f\exp(-bD^*)],$$

where $S(b)$ describes the diffusion-weighted signal, S_0 the signal at b = 0, D the diffusion coefficient, f the perfusion fraction, and D^* the pseudodiffusion coefficient.

As IVIM studies are regularly performed with varying acquisition parameters, the question arises, how far obtained results are comparable. For example, it is known that the strong dependency of f on echo time TE is one factor that must be taken into account [1].

History generally matters in MRI, but it matters in particular if saturation effects on flowing magnetization are of relevance; an effect that is made use of regularly in MR angiography [2]. Such saturation effects, however, are largely ignored in the context of IVIM studies.

This study aimed to reveal whether such saturation effects are of importance in IVIM examinations of the liver. For that purpose, we acquired data once with few slices and once with many slices. We thought that acquiring the data with few slices should reduce potential saturation effects and that therefore any difference in measured IVIM parameters between these acquisition setups would reveal a potential impact of saturation effects.

Materials and Methods

Diffusion-weighted image data of the liver of 9 healthy volunteers (2 female, 7 male, age between 21 and 30 years) were acquired at 3 T (Magnetom Prisma, Siemens Healthcare, Erlangen, Germany). The measurements were divided into two parts.

First, data with 4 slices in transversal orientation were acquired (referred to as few slices).

Second, data were acquired with a high number of slices covering the entire liver (24-27 slices depending on the liver size of the particular subject) in transversal orientation.

The slice thickness was always 5 mm. Spacing between slices of 25 mm was used for the measurements with few slices, and 1 mm for the image acquisition with the higher number of slices. Image acquisition was performed in free breathing.

Data were collected for three orthogonal diffusion directions and two sets of b-values ranging from 0 s/mm² to 800 s/mm². The first set (20 b-values) was used for the first five volunteer measurements. After re-evaluation, the second set was used for the remaining acquisitions consisting of 16 b-values. TE and TR were set to 60 ms and 3600 ms, respectively. TR was set to the lowest possible value.

The data evaluation was performed in Python 3.8. A region of interest (ROI) was drawn in the liver parenchyma of the right liver lobe for each slice separately sparing major vessels and was evaluated by computing the median of the included voxel signals. Next, for each b-value, the mean signal over all three diffusion directions was computed.

Finally, the resulting signals were normalized to the signal at b = 0 and biexponential fitting using the normalized signals was performed.

Thus, one value per slice was obtained for each IVIM parameter.

In order to check statistical significance, the unpaired t-test and the Mann-Whitney U test were applied in case of normally and non-normally distributed data, respectively. Normality was assessed with the Shapiro-Wilk test.

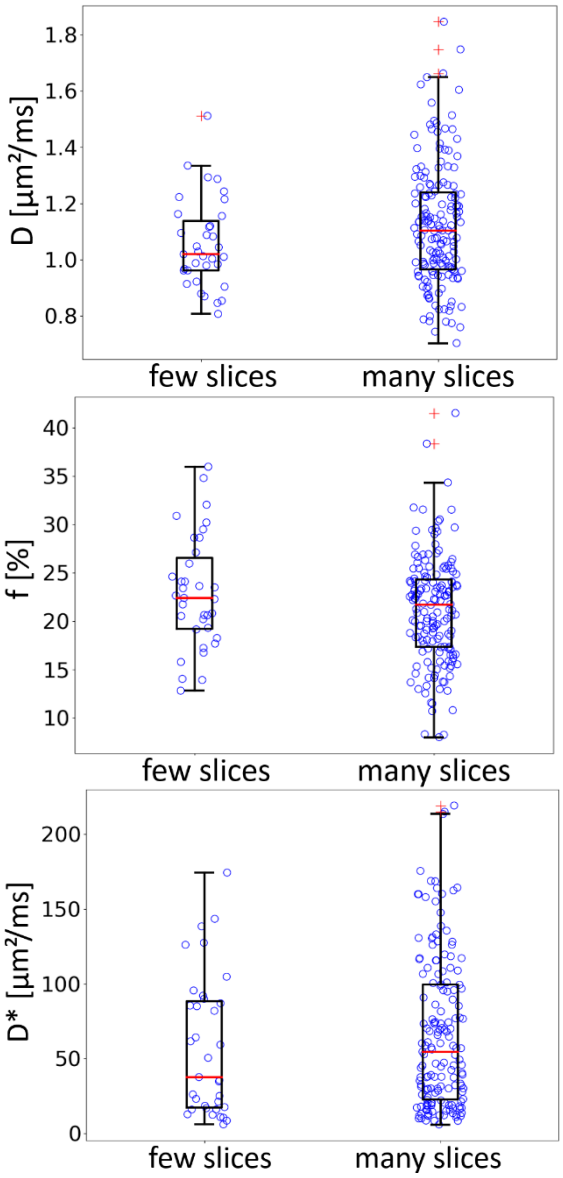

Fig. 1: Boxplots of the IVIM parameters for measurements of 4 slices ('few slices') and the many slice setting in transversal orientation ('many slices'). Data points are shown in blue, outliers are marked as red '+'-signs. The red line marks the respective median, the box indicates the interquartile range (IQR) and whiskers indicate all data lying within 1.5 x IQR.

Results

The obtained IVIM parameters are displayed as boxplots in Fig. 1 (each data point represents one slice). The median of values of D for all slices ranged from 1.02 µm²/ms (few slices) to 1.10 µm²/ms (many slices). The median of f ranged from 21.7 % (many slices) to 22.4 % (few slices). The median of D^* was 38 µm²/ms for the few slice setting and 55 µm²/ms in the many slice setting. Statistical analysis yielded no statistical significance for all three parameters (p_D = 0.09, p_f = 0.09, p_{D^*} = 0.5).

Discussion

This study showed that saturation effects may only play a minor role in IVIM studies of the liver. One would expect that f were most affected by saturation effects as it essentially is a representation of the relaxation-time weighted blood volume. We also observed a slight decrease of f in the many-slice experiment, but this effect was not significant. It seems that blood flows in the examined region at a faster pace than that it is saturated. With our setting, a slice is saturated every 3.6 s and the circulation time of blood through the whole human body varies roughly between 10 s to 25 s [3]. It is thus not unreasonable that the majority of the blood is exchanged once in the 3.6 s and then recovers to equilibrium magnetization while traveling through the body. It appears that the blood flow from the saturated slice to the neighbouring slice is not of major importance with our many-slice setting.

Conclusion

This work revealed no significant dependencies of the biexponential IVIM parameters on the slice number. We thus conclude that a straightforward comparison of IVIM parameters acquired with different slice settings should be possible. This may, however, be different if a much shorter repetition time is used.

References

1. Lemke A, Laun FB, Simon D, Stieltjes B, Schad LR. An in vivo verification of the intravoxel incoherent motion effect in diffusion-weighted imaging of the abdomen. Magnetic resonance in medicine. 2010;64(6):1580-1585.

2. Friedli JL, Cynthia BP. Evaluation of variable-angle uniform signal excitation, tilted optimized nonsaturating excitation, and flat radio-frequency pulses in free-breathing non-contrast-enhanced pulmonary MR angiography. Radiology. 1997;202(3):863-867

3. Puskas Z, Schuierer G. Determination of blood circulation time for optimizing contrast medium administration in CT angiography. Der Radiologe. 1996;36. Jg.,9:750-757

Orientierungsverteilung der Faserrichtungen in weißer Hirnsubstanz

Lucian Spitzner[1], Patricia Ulloa[1], und Martin A. Koch[1]

[1] Institut für Medizintechnik, Universität zu Lübeck, Lübeck, Deutschland.

Synopsis: Using diffusion MRI data and the tensor model, the axon fibre dispersion in human white brain matter was examined. Using a rotation of the diffusion tensor, an estimation for the angle between two assumed strands of axon fibres per voxel could be made. The results indicate that the structure of certain brain regions, such as the corticospinal tract, could be visualized, but the absolute dispersion angles may be inaccurate.

Zusammenfassung: Es wurde untersucht, ob mittels diffusionsgewichteter MRT eine Abschätzung der Faserstreuung in weißer Hirnsubstanz möglich ist. Der Einfluss eines zweiten Bündels an Fasern wurde mittels Rotation von Tensordaten simuliert. Unter der Annahme von zwei Faserbündeln erlaubt dies eine Abschätzung des Streuungswinkels für jedes Voxel eines Datensatzes. In den Ergebnissen sind Strukturen von Hirnregionen, wie z. B. der Pyramidenbahn, zu erkennen. Jedoch sind die absoluten Winkel ungenau.

Motivation

Diffusiongewichtete Bildgebung (eng.: diffusion-weighted imaging, DWI) ist eine Kategorie der Magnetresonanzbildgebung (eng.: magnetic resonance imaging, MRI), bei der Diffusionsprozesse in Gewebe in vivo analysiert werden können. Nach der klassischen Pulssequenz von Stejskal und Tanner (1) kann hierbei unter Verwendung von Gradientenfeldern Rückschluss auf die mikroskopischen Ortsänderungen von Spins gemacht werden. Heute wird DWI in der Diagnostik u. A. zur Erkennung von Schlaganfällen genutzt.

Nach Mitra (2) ist es möglich über die sogenannte doppelt-diffusionsgewichtete Bildgebung (eng.: double diffusion encoding, DDE), Informationen über die Geometrie von Poren zu gewinnen. Hierbei werden Paare von Gradientenpulsen in unterschiedlichen Richtungen verwendet. Der Vergleich zwischen den Signalen bei parallelen und senkrechten Feldgradienten erlaubt dann eine Aussage über die Porenform.

Diese Größenbestimmung ist besonders einfach, wenn alle Axone senkrecht auf der Ebene der beiden Feldgradienten stehen. Für schräg liegende Fasern kann das arithmetische Mittel von zwei um 90° zueinander gedrehten Messungen gebildet werden, um den Einfluss der schrägen Fasern herauszurechnen (3). Dies funktioniert jedoch nur unter der Voraussetzung, dass nicht mehrere Orientierungen von Faserbündeln innerhalb eines Voxels vorliegen, wie z. B. wenn Faserbündel sich aufteilen oder kreuzen.

Um den Nutzen der Methode einzuschätzen, wurde die Orientierungsverteilung von Axonen in weißer Hirnsubstanz untersucht. Dafür wurde das Tensormodell der Diffusion verwendet.

Material und Methoden

Richtungsabhängige Diffusionsprozesse können mithilfe eines Tensors zweiter Stufe charakterisiert werden. Die Diffusion kann dabei z. B. durch Zellwände in einer Raumrichtung begrenzt, in einer anderen Richtung scheinbar frei sein. Dabei ist die Teilchenstromdichte abhängig von der Teilchenkonzentration und dem Diffusionstensor, welcher durch eine symmetrische 3x3-Matrix repräsentiert wird.

In der Diffusionstensorbildgebung (eng.: diffusion tensor imaging, DTI) werden für verschiedene Richtungen des Feldgradienten verschiedene Richtungen des Diffusionsprozesses gemessen. Aus mindestens sechs verschiedenen diffusions-gewichteten Messungen und einer nicht diffusions-gewichteten Messung kann dann voxelweise der Diffusionstensor bestimmt werden. Die symmetrische Matrix kann diagonalisiert werden, um Eigenwerte und Eigenvektoren zu erhalten. Dabei wird angenommen, dass die Hauptfaserrichtung in einem Voxel in Richtung des Eigenvektors mit dem größten Eigenwert zeigt. Hier zeigt sich direkt eine Schwäche des Tensormodells: es wird angenommen, dass pro Voxel nur eine Hauptfaserrichtung existiert. Für jedes Voxel mit mehr als einer Orientierung von Axonenbündeln entspricht das Signal der Summe der Signale der einzelnen Faserbündel und der errechnete Tensor kann die enthaltenen Richtungen nicht darstellen.

Um aus vorhandenen DTI-Daten Informationen über die Orientierungsverteilung zu gewinnen, wurde zu Daten eines Voxels, welches in guter Näherung nur eine Orientierung von Axonen enthält, eine zweite Orientierung über eine Simulation hinzugefügt. Dazu wurde ein Voxel

mit hoher fraktioneller Anisotropie (FA) ausgewählt (Seed-Voxel). Dieser Wert kann aus dem Tensor errechnet werden und ist ein Indiz dafür, wie unterschiedlich die Diffusionsgeschwindigkeiten in verschiedenen Richtungen sind. Voxel mit hoher FA sind geprägt von paralleler Faserstruktur und mit nur einer Orientierung der Faserrichtung.

Der Tensor des Seed-Voxels wurde unter Verwendung einer Rotationsmatrix rotiert. Dies entspricht der Rotation des sog. Diffusionsellipsoids. Dieses Ellipsoid wird aus den Eigenwerten des Diffusionstensors berechnet und hilft zur Visualisierung des Grades der Anisotropie der Diffusion. Für isotrope Diffusion entspricht das Diffusionsellipsoid einer Kugelfläche, für sehr anisotrope Diffusion einem prolaten Ellipsoid. Als Rotationsachse für die Rotation des Tensors wurde der Eigenvektor mit dem kleinsten Eigenwert gewählt.

Aus dem rotierten Tensor wurde wieder das Signal berechnet, welches der Tensor unter den gegebenen Magnetfeldern erzeugte. Dieses simulierte Signal wurde dann arithmetisch mit dem ursprünglichen Signal des Voxels gemittelt. Im nächsten Schritt wurde dann aus dem gemittelten Signal wieder ein neuer Tensor berechnet, welcher nun von dem Drehwinkel abhängig ist. Aufgrund unserer Wahl der Rotationsachse spiegelt sich die Rotation in den Eigenwerten λ_1 und λ_2 wider (bei $\lambda_1 > \lambda_2 > \lambda_3$). Für den ursprünglichen Tensor war $\lambda_1 >> \lambda_2$. Für einen Rotationswinkel von 90° wird für den Tensor des gemittelten Signals $\lambda_1 \approx \lambda_2$ erwartet.

Für verschiedene Drehwinkel erlaubt dies eine Abschätzung des Winkels zwischen zwei Orientierungen von Fasern abhängig vom Verhältnis der Eigenwerte. Diese Zuweisungen hängen außerdem von dem gewählten Seed-Voxel ab. In den DTI-Daten lag das Voxel mit der höchsten FA nicht in Regionen weißer Hirnsubstanz, sondern war durch Rauschen im zerebralen Kortex bedingt. Daher wurden die Seed-Voxel per Hand nach ihrer FA, in der Pyramidenbahn und im Corpus callosum gewählt. Die Pyramidenbahn ist für Porenbestimmung aufgrund ihrer Rolle in degenerativen neuronalen Erkrankungen interessant (4). Beide Strukturen enthalten dichte, parallele Axonbündel.

Ergebnisse

Wie beschrieben wurde die Methode für verschiedene Seed-Voxel angewendet und der Winkel bestimmt.

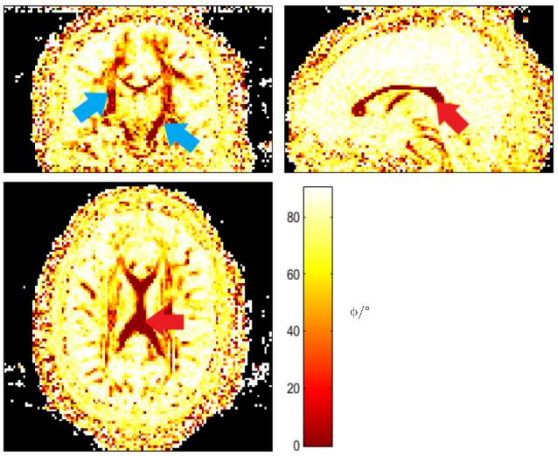

Abb. 1: Berechneter Winkel zwischen den zwei angenommenen Faserorientierungen je Voxel. Die roten Pfeile zeigen das Corpus callosum, die blauen Pfeile zeigen die Pyramidenbahn.

In Abb. 1 ist die Winkelberechnung für ein Seed-Voxel in der medialen Pyramidenbahn zu sehen.

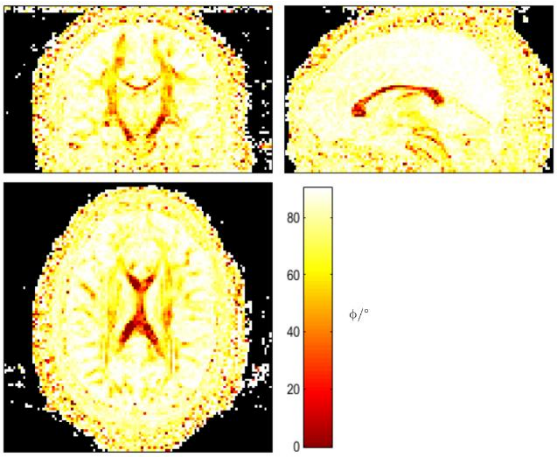

Abb. 2: Berechneter Winkel zwischen den zwei angenommenen Faserorientierungen je Voxel. Der Seed-Voxel liegt in der inferioren Pyramidenbahn.

Abb. 2 zeigt die Winkelberechnung für ein Seed-Voxel in der inferioren Pyramidenbahn. Wie erwartet zeigen Abb. 1 und Abb. 2 die Bereiche mit weißer Hirnsubstanz mit niedrigeren Winkeln an.

Für das Seed-Voxel in der inferioren Pyramidenbahn wurde schichtweise der durchschnittliche Winkel bestimmt. Das Ergebnis ist in Abb. 3 zu sehen.

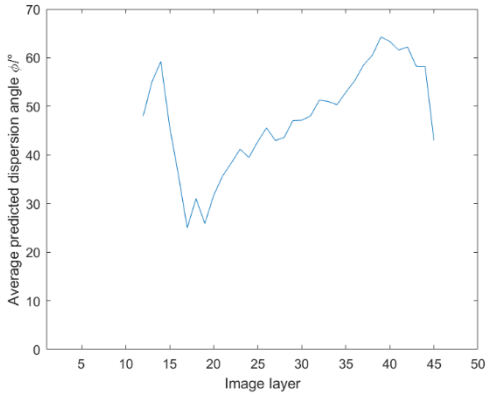

Abb. 3: Durchschnittlicher Winkel (vertikale Achse) pro Bildschicht (horizontale Achse) zwischen zwei Orientierungen von Fasern in der Pyramidenbahn. Das Seed-Voxel liegt in der inferioren Pyramidenbahn.

Diskussion

Für die Pyramidenbahn ist die auffächernde Struktur für beide Seed-Voxel erkennbar. Während Details aus der Struktur ähnlich sind, unterscheiden sich die zugewiesenen Winkel stark, abhängig von der FA des Seed-Voxels. Dies ist auf die Inkompatibilität des Tensormodells mit mehreren Faserrichtungen zurückzuführen.

Eine weitere Möglichkeit besteht darin, eine andere diskrete Anzahl von Fasern pro Voxel anzunehmen. Für z. B. drei Orientierungen könnte der dritte Eigenwert berücksichtigt werden: abhängig von den Eigenwerten könnte dem Voxel sowohl entweder ein, zwei oder drei Orientierungen als auch die entsprechenden Winkel zugeordnet werden.

Die Annahme, dass hohe FA gleichbedeutend mit dem Vorhandensein nur einer Orientierung ist, ist eine starke Vereinfachung. Da die FA nicht nur von der Orientierung, sondern auch von der Dichte der Faserstruktur beeinflusst wird, kann es z. B. für zwei Orientierungen von Fasern mit hoher Faserdichte eine höhere FA als für eine Orientierung mit geringerer Faserdichte geben. Dies führt zu Fehlern in der Berechnung.

Der Vergleich mit einer Studie von Sotiropoulos et. al. (5) legt nahe, dass die berechneten Winkel entweder zu groß sind oder nicht von Faseraufteilung, sondern von Faserkreuzungen stammen. Dies wird unterstützt durch die Annahme, dass Faseraufteilung nicht in scharfen Knicks stattfindet (6). Da die errechneten Winkel teilweise sehr groß sind, deutet dies auf Fehler der Methode hin.

Schlussfolgerung

Die Methode der Rotation des Tensors zeigt grobe Strukturen der weißen Gehirnmasse auf. Jedoch sind die Angaben für die Winkel zwischen Faserbündeln ungenau. Da auch Wissen über die ungefähre Anzahl von Faserorientierungen pro Voxel fehlt, ist eine genauere Untersuchung und Ausarbeitung der Methode notwendig, bevor diese verlässliche Ergebnisse produzieren kann.

References

1. Stejskal EO, Tanner JE, Spin Diffusion Measurements: Spin Echoes in the Presence of a Time-Dependent Field Gradient. J. Chem. Phys. 1965;42:288–292.

2. Mitra PP, Multiple wave-vector extensions of the NMR pulsed-field-gradient spin-echo diffusion measurement. Phys. Rev. B 1995;51:15074–15078.

3. Ulloa P, Wottschel V, Koch MA, Studying the extracellular contribution to the double wave vector diffusion-weighted signal. Curr. Dir. Biomed. Eng. 2015;1:240–244.

4. Koch MA, Finsterbusch J, Double Wave Vector Diffusion Weighting in Wallerian Degeneration. Proc. 20th Annual Meeting ISMRM 2012;3564.

5. Sotiropoulos SN, Behrens TEJ, Jbabdi S, Ball and rackets: Inferring fiber fanning from diffusion-weighted MRI. NeuroImage 2012;60: 1412–1425.

6. Lazar M, Mapping brain anatomical connectivity using white matter tractography. NMR Biomed 2010;23:821–835.

Investigation of changes in flow velocity due to wall motion on 3D printed tubes using 2D PC MRI

Isil Unal[1], Duygu Dengiz[2], Eckhard Quandt[2], Mona Salehi Ravesh[1], Jan-Bernd Hövener[1], Mariya Pravdivtseva[1], and Olav Jansen[1]

[1] Section Biomedical Imaging, Molecular Imaging North Competence Center (MOIN CC), Department for Radiology and Neuroradiology, University Medical Center, Kiel, Germany; Department for Radiology and Neuroradiology, University Hospital Schleswig-Holstein, Campus Kiel, Germany.

[2] Institute for Materials Science, Faculty of Engineering, University of Kiel, Germany.

Synopsis: Blood flow, which is the leading to aneurysm rupture, can be measured 2D PC MRI using 3D printed flow models with elastic wall in-vitro which mimics the cerebral arteries. In this study, material which has similar elastic modulus to cerebral arteries were used to investigate the effect of wall elasticity to the flow parameters. 2D PC MRI measurements were performed with rigid and elastic tubes and wall motion was imaged using CINE MRI.

Zusammenfassung: Der Blutfluss, der zur Ruptur des Aneurysmas führt, kann in der 2D PC MRT mit 3D-gedruckten Strömungsmodellen mit elastischer Wand in-vitro gemessen werden, die die Hirnarterien nachahmt. In dieser Studie wurde Material verwendet, das einen ähnlichen Elastizitätsmodul wie zerebrale Arterien aufweist, um den Einfluss der Wandelastizität auf die Strömungsparameter zu untersuchen. 2D-PC-MRT-Messungen wurden mit starren und elastischen Röhren durchgeführt und die Wandbewegung wurde mit CINE-MRT abgebildet.

Motivation

A cerebral aneurysm is a severe disease that leads to death in about 50 % of all cases if a rupture occurs [1]. To prevent this outcome, aneurysms at risk need to be identified and treated. Blood flow appears to be one of the most critical factors leading to aneurysm rupture [2]. It can be detected in vivo using 2D Phase Contrast (PC) MRI, but there is no clear understanding yet which of the flow parameters such as flow rate, pressure and wall shear stress are decisive. 3D models of aneurysms allow to tests novel treatment strategies in vitro. The emerging technique of 3D printing allows to produce patient derived models. The most commonly used printing materials, however, are rigid and don't mimic the elastic properties of the vessel wall well. Thus our first goal is to measure flow rate in a straight tube with a rigid wall using 2D PC MRI technique. Our second goal is to determine the material that can mimic the brain arteries in order to examine the effect of vascular wall elasticity on flow. Last goal is to image and quantify vessel wall motion using CINE MRI.

Material und Methoden / Materials and Methods

Determination of Elastic Modulus: We investigated three kinds of commercially available material with different shore and elasticity values claimed by the manufacturer as 'Rigid' (78D shore), 'Flexible' (80A shore), and 'Elastic' (50A shore) photoreactive resins (Formlabs, USA). Tensile test (Zwick Roell Z05, Fürstenfeld, Austria) was applied to the 25x5x1 mm³ flexible and 18 elastic samples were oriented to the building platform with the angles α = 0°, 45° and 90° at 24 °C.

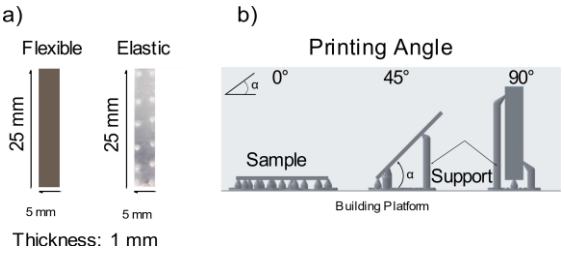

Fig. 1: 25x5x1 mm³ tensile test samples printed with flexible and elastic (a) and schematic view of printing setup (b).

Measuring the Flow Velocity and quantification of area change due to pulsatile flow in 3D Printed Straight Tubes: Straight tubes with rigid and elastic materials were produced using 3D printer with inner diameter 6mm and wall thickness 1 mm (elastic tube) (Fig.2). The flow models were placed in agarose gel and integrated in a flow loop filled with a glycerol-water mixture (40/60 %) to mimic blood flow. The tubes were supplied with a pulsatile (cardiac) flow of 250 ml/min using a cardiac pump (5000 Hz PD-1100, BDC Laboratories, USA) at 24 °C. Flow velocities in the middle of the tubes were measured using 2D PC MRI (Ingenia CX, 5.6.1, Philips Healthcare, Netherlands) in rigid and elastic tubes with 20 phases in one cardiac flow (60 bpm). Wall motion in elastic tube was imaged in real-time using CINE MRI (Compressed

SENSE Balanced TFE sequence) Image Processing and area change due to the pulsatile flow was made and quantified using an open source software ImageJ.

Ergebnisse / Results

Tensile Test: Tensile test were successfully performed. Elastic modules of 18 samples were obtained individually. Values of 12 samples were changing between 0.75 ± 0.25 MPa which is the value of real artery in literature [5] as shown in Fig. 2. According to the results 0° oriented elastic sample is very close to the elastic modulus of real artery with 0,76 MPa. Tubes were produced with 0° orientation.

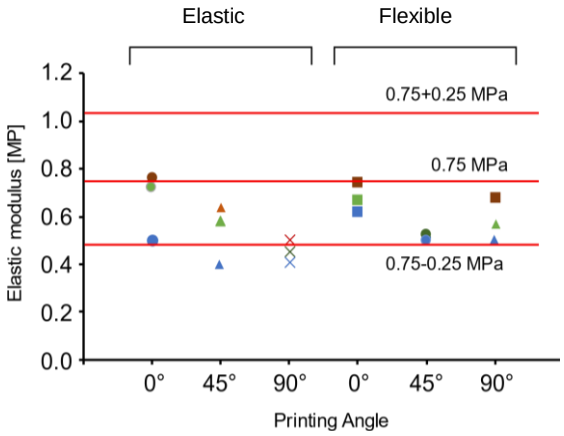

Fig. 2: Elastic modulus of samples with respect to the real artery (0,75 ±0,25 MPa [2])

Flow Velocity Measurement: After performing the 2D PC MRI measurement two different Mean flow velocities were obtained for rigid and elastic tube as shown in Fig. 3.

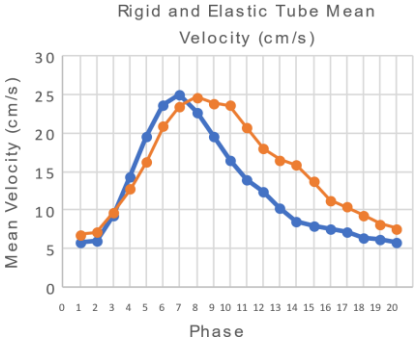

Fig. 3: Flow mean velocities in rigid (blue) and elastic (orange) tubes in one cardiac cycle with 20 phases (frames).

Tube cross-sectional Area Change due to pulsatile flow: Images obtained from the CINE imaging each frames (20) were smoothed and thresholded due to the high signal intensity of flow; then pixels were counted by ImageJ pixel counting script (Fig.4).

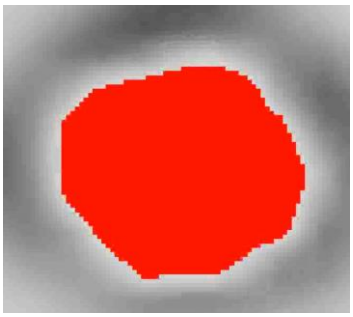

Fig. 4: One of the frame thresholded.

Total area of pixels was measured using measuring module of ImageJ for each of frames. Area change was obtained for each frame between two cardiac phases as shown in Fig. 5.

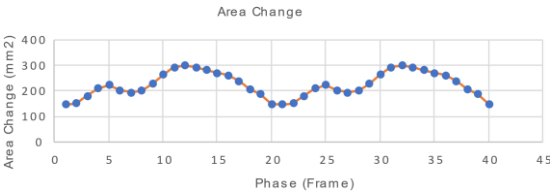

Fig. 5: Area change in elastic tube due to the pulsatile flow between 2 cardiac phases and 40 frames.

Diskussion / Discussion

The change in the elastic modulus of the samples showed that the printing angle was effective on elasticity and it is convenient to use elastic resin to obtain similar mechanical properties to real cerebral artery. According to the result in flow velocity in Fig. 3 mean velocity changes due to the periodic increase and decrease the cross-sectional area.

Schlussfolgerung / Conclusion

We found two commercially available 3D printing material which allowed to produce the flow models with elastic properties close to the human vessel. Wall motion was images in real-time using CINE MRI and quantified the area change using ImageJ software.

References

1.Brain Aneurysm Statistics and Facts. Brain AneurysmFoundation. https://www.bafound.org

2. Kamdaeng, T. et.al. Arterial stiffness identification of human carotid artery using the stress-strain relationship in vivo, UltraSonic 2012:52/3;402-411.

Flow quantification with MRI in the presence of flow diverter stents

Eva Peschke [1*], Mariya Pravdivtseva [1], Olav Jansen [2], Jan-Bernd Hövener[1]

[1] Section Biomedical Imaging, Molecular Imaging North Competence Center (MOIN CC), Department of Radiology and Neuroradiology, University Medical Center Schleswig - Holstein, Kiel University, Kiel, Germany
[2] Department of Radiology and Neuroradiology, University Medical Center Schleswig - Holstein, Kiel University, Kiel, Germany

*eva.peschke@rad.uni-kiel.de

Synopsis: Flow MRI is a promising tool to assess the efficacy of flow diverter stents. Here, we evaluated the adverse effect of three different stents at 3T and 7T. On GRE-MRI, distortions occurred. On flow MRI, velocities varied only at the stent, but not before and after and in a control next to it. Thus, flow MRI may be well suited to image flow in the vicinity of stents, but care has to be taken in their proximity.

Zusammenfassung: Die Fluss-MRT ist ein vielversprechendes Werkzeug zur Beurteilung der Wirksamkeit von flow diverter stents. Hier haben wir die nachteiligen Auswirkungen von drei verschiedenen Stents bei 3T und 7T untersucht. Auf GRE-MRI traten Verzerrungen auf. Im Fluss-MRT variierten die Geschwindigkeiten nur am Stent, nicht aber davor und danach und in einer Kontrolle daneben. Daher kann die Fluss-MRT gut geeignet sein, um den Fluss in der Nähe von Stents abzubilden. In deren Nähe hingegen, muss man vorsichtig sein.

Motivation

Aneurysms are expansions of blood vessel which can rupture, leading to potentially fatal brain hemorrhage. Flow diverter stents (FD) are used to treat these aneurysms, preventing the blood to flow in the aneurysm sack. Flow imaging is a direct way to assess the treatment outcome. 4D flow MRI is well established to do so, but the impact of the metallic FDs on flow MRI has to be investigated further. Here, we evaluated the impact and artifacts of different FDs on quantitative flow MRI.

Materials and Methods

Two silicone tubes (ID: 4 mm) were placed in a water container, one tube receiving a FD, the other serving as control (FD1: Derivo, Acandis; FD2: P64, Phenox; FD3: Silk, Balt Extrusion). The tubes were placed in parallel to B_0 and supplied with water at a mean flow of 1.77 ml/s and a mean velocity of 14.15 cm/s (calibrated with ME6PXN325; Transonic System Inc.). MRI was acquired at 3T (32-channel volume head coil, Ingenia CX, Philips) and 7T (72 mm volume coil, Biospec, Bruker).
The flow was measured with 2D and 3D phase contrast sequences at 3T (TR=7 ms, TE=4.5 ms, Bw=443 Hz/Px, resolution=0.26x0.26 mm²) and 7T (TR=15 ms, TE=3,9 ms, Bw= 158 Hz/Px, resolution=0.136x0.136 mm²).
For the used sequence at 7T, the resulting signal intensities of the image were automatically transformed to velocity values, for 3T post processing was performed with GTFlow (Gyrotools,Switzerland).

Results

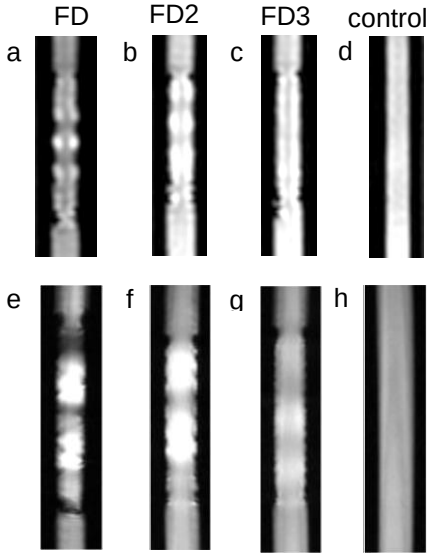

Fig. 1: T1w MRI of tubes with and without FDs at 3 T (a-d) and 7 T (e-g). Note the distortions, visible by hypo- and hyperintensities along the stents

All FDs were found to induce artifacts on the 4D Flow magnitude (3T) and T1w Flash (7T) MRI images (Fig. 1), manifesting as distortions, hypo- and hyperintensities along the devices. FD1 showed the largest distortions or signal voids, while FD3 showed least. The reference tube, at a distance of 2.5 cm, was not affected in an apparent way.

The flow measurements in 2D and 3D were repeated three times for 7T MRI to determine the reproducibility of the flow measurements as well as the comparability with the calibrated value of the flow pump for the control tube. It could be shown that the measurements are reproducible and are in the range of the calibrated value.

While the velocities in the control tube where slightly overestimated, both for 3T and 7T, the velocities at the non-distorted positions before and after the stent were slightly underestimated.

The velocities along the FDs were found to vary up to 50 % (Fig. 2). Again, FD1 exhibited the largest variations, while FD3 showed least. Notable, the variations were pronounced at the ends of the devices, where radiopacity markers were placed for FD1 and FD2. The least variations were found for FD3 at 7T.

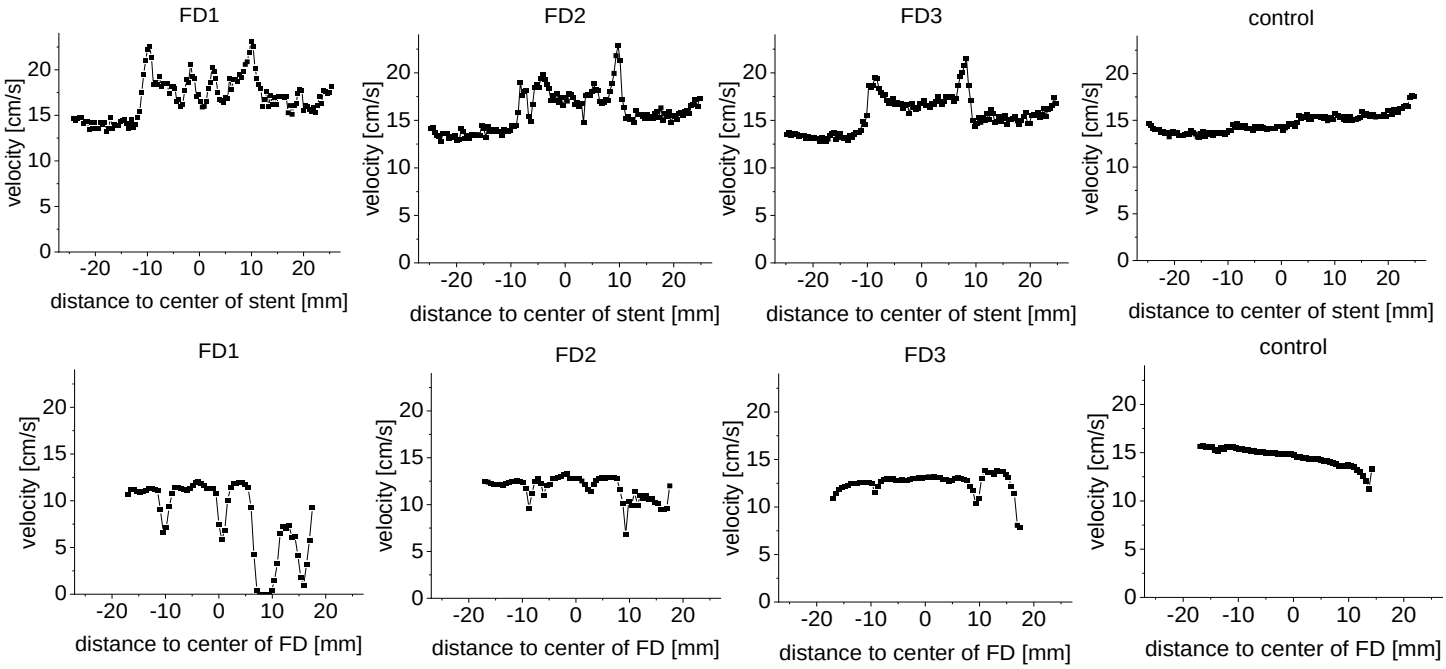

Fig. 2: 4D Flow (3T, upper row) and 3D-PC (7T, lower row) MRI for the three different FD with marked position of the stent.

Discussion

As the FDs affected the GRE MRI, similar effects were expected on PC MRI. The visible distortions of the FD are caused by metallic artifacts. The FD induce local distortions of the magnetic field, which leads to hypo- and hyperintensities along the stent.
Further analysis of the flow measurements showed, that the flow itself is less affected than the velocity, this still has to be evaluated for 7T.

While the velocities of the 3D PC results are especially prone to be affect at the beginning and at the end of the stent, the 2D PC results are less affect at those positions.
The artifacts are likely to be attributed to the composition of the FDs, especially the x-ray markers. FD3 showed the least artifacts and had only four helical markers and no point markers at the ends. FD1 showed the most artifacts consisting of wires with a platinum core and three x-ray markers at each end.

Conclusion

While flow Diverter stents don't forbid MRI, the results have to interpreted with care as artefacts are introduced. Still, flow MRI may be useful for evaluating treatment success, especially if FDs with little artifacts are chosen, or sequences are optimized to reduce the artifacts.

Acknowledgements

We acknowledge support from GRK 2154/1, Kiel University, Medical Faculty for MOIN CC (ERDF grant and Zukunftsprogramm Wirtschaft 122-09-053).

References

1. Bouillot P, Brina O, Delattre BMA, et al. Neurovascular stent artifacts in 3D-TOF and 3D-PCMRI: Influence of stent design on flow measurement. Magnetic Resonance in Medicine 2019;81:560–572 doi: 10.1002/mrm.27352.

Automatische Segmentierung des fibroglandulären Gewebes mittels U-Nets in der diffusionsgewichteten Bildgebung

Astrid Müller[1*], Frederik B. Laun[1], Mona Pistel[1], Michael Uder[1], Rolf Janka[1], Andreas Maier[2], Sabine Ohlmeyer[1], Evelyn Wenkel[1], Sebastian Bickelhaupt[1]

[1] Radiologisches Institut, Universitätsklinikum Erlangen, Friedrich-Alexander-Universität Erlangen-Nürnberg (FAU), Erlangen, Germany.

[2] Department of Computer Science, Friedrich-Alexander-Universität Erlangen-Nürnberg (FAU), Erlangen, Germany.

* Astrid.Mueller@uk-erlangen.de, Astrid Müller, Maximiliansplatz 3, 91054 Erlangen, Germany.

Zusammenfassung: Es wurden zwei U-Nets für die Segmentierung des fibroglandulären Gewebes der weiblichen Brust in der diffusionsgewichteten Mammabildgebung trainiert und verglichen. Das FGT wird mit beiden U-Nets zum Großteil korrekt segmentiert.

Motivation

Die diffusionsgewichtete Bildgebung (DWI) ermöglicht in der Magnetresonanztomographie (MRT)[1] die Kartierung des Diffusionsverhaltens von Wassermolekülen im Gewebe. Die DWI findet unter anderem in der Mammadiagnostik Anwendung, hierbei ist neben der Detektion von suspekten Läsionen auch die Beurteilung des fibroglandulären Drüsengewebes (FGT, engl., fibroglandular tissue) von Bedeutung[2]. Neben der visuellen Betrachtung der diffusionsgewichteten Bilder lassen sich durch Verwendung unterschiedlicher Diffusionswichtungen (b-Werten) quantitative Parameter wie der ADC[1] (engl., „apparent diffusion coefficient“) im FGT ableiten, um sie z.B. nachfolgend zu analysieren. Hierzu ist eine standardisierte und valide Segmentierung des FGTs notwendig. Da die Struktur des FGTs sehr komplex ist, entsteht bei manuellen Segmentierungen ein erheblicher Zeitaufwand. Zudem ist die visuelle Repräsentation in den b-Werten unterschiedlich.

Ein vielversprechender Ansatz für die automatisierte Segmentierung des FGTs in der diffusionsgewichteten Bildgebung ist die semantische Segmentierung mittels des U-Net, einem neuronalen Netz, welches speziell für die medizinische Bildverarbeitung konfiguriert wurde[3].

Material und Methoden

Die Studie wurde retrospektiv nach Einholung eines positiven Ethikvotums durchgeführt. Es wurden insgesamt $n = 78$ DWI-MRT Untersuchungen aus dem Zeitraum von 2015 bis 2019 in die Studie eingeschlossen ($n = 48$ Training, $n = 30$ Test). Die MRT-Untersuchungen wurden auf den SIEMENS MAGNETOM-Geräten Aera, Skyra fit, Vida und Avanto durchgeführt.

Es wurden zwei U-Nets auf ihre Fähigkeit das FGT auf DWI-MRT ($b = 800\ s/mm^2$) Daten zu segmentieren untersucht:

U-Net$_1$ wurde mit $n = 250$ DWI-Einzelschichten von $n = 19$ Probandinnen, akquiriert mit $n = 3$ unterschiedlichen EPI-DWI-Sequenzen trainiert. Die zugehörigen Referenzmasken wurden durch Clustern mit dem k-Means-Algorithmus und Gaussian-Mixture-Models generiert.

Für das Training des zweiten U-Net, U-Net$_2$, wurden $n = 127$ Referenzmasken ersetzt durch Segmentierungen, generiert durch U-Net$_1$ von $n = 29$ Probandinnen, akquiriert mit $n = 8$ unterschiedlichen EPI-DWI-Sequenzen.

Beide Datensätze wurden jeweils durch Datenaugmentation auf einen Datensatz von 3250 DWI-Bildern erweitert und anschließend in 80% Trainings- und 20% Validierungsdaten aufgeteilt. Die Segmentierungsleistung der U-Netze wurde folgend an einem Testdatensatz von $n = 30$ Mamma-DWI-Sequenzen ($b = 800\ s/mm^2$) mittels zweier Likert-Skalen (Tab. 1) von einem Reader (A.M.) visuell für alle Einzelschichten evaluiert. Die Likert-Skalen-Werte der einzelnen DWI-Bilder wurden je Probandin und Skala addiert und anschließend durch die Anzahl der jeweiligen Schichten dividiert. Die Ergebnisse der Likert-Skalen-Evaluierung wurden mittels Wilcoxon-Vorzeichen-Rang-Test evaluiert. Das Signifikanzniveau wurde mit $\alpha = 0.05$ gewählt.

Tab. 1: Likert-Skalen

Skala	*Vollständigkeit der FGT Segmentierung*	*Inkorrekte Segmentierung*
1	Keine	Großflächig
2	Vereinzelte Voxel	Gehäuft kleinflächig
3	Teilweise	Kleinflächig
4	Größtenteils	Vereinzelte Voxel
5	Nahezu vollständig, falls vorhanden	Keine

Ergebnisse

Die Vollständigkeit der FGT-Segmentierung der beiden U-Netze war weitgehend identisch (Abb. 1). Der mediane Likert-Wert für die FGT-Segmentierung für U-Net$_1$ war 4.13, für U-Net$_2$ 4.18 ($p = 0.6811$). Allerdings waren inkorrekte Segmentierungen bei U-Net$_2$ seltener zu finden als bei U-Net$_1$ ($p = 0.0005$)

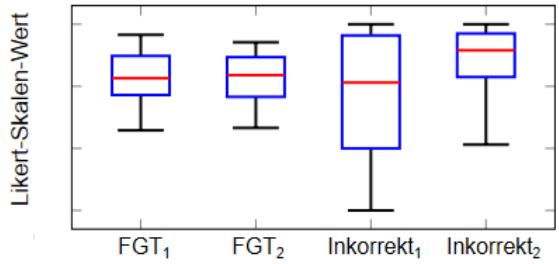

Abb. 1: Auswertung der Likert-Skalen Bewertungen von U-Net$_1$ und U-Net$_2$ der 30 Probandinnen

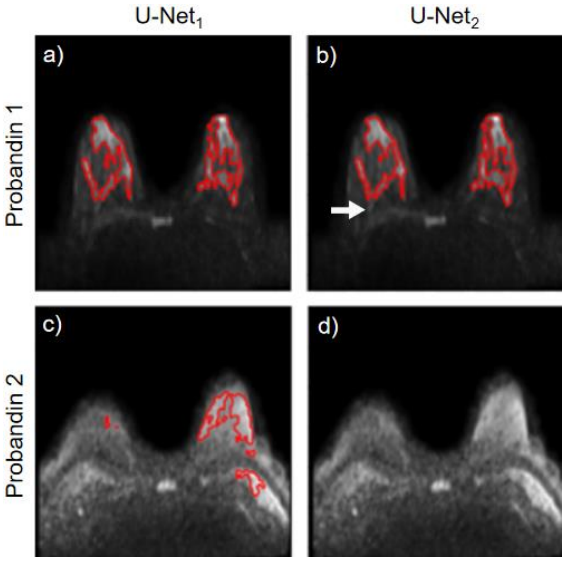

Abb. 2: Korrekte FGT-Segmentierung durch U-Net$_1$ (a) und U-Net$_2$ (b), inkorrekte Segmentierung durch U-Net$_1$ (c) im Vergleich dazu U-Net$_2$ (d)

Abbildung 2ab zeigt eine Schicht, auf der beide U-Nets das FGT bis auf den kleinen durch den weißen Pfeil markierten Bereich sehr gut segmentierten (Likert-Skalen-Werte: $\text{U-Net}_1 = 5$, $\text{U-Net}_2 = 5$). Abbildung 2cd zeigt einen Fall, bei dem Fett- und Muskelgewebe von U-Net$_1$, im Gegensatz zu U-Net$_2$, inkorrekt als FGT segmentiert wurde (Likert-Skalen-Werte: $\text{U-Net}_1 = 1$, $\text{U-Net}_2 = 5$).

Diskussion

In der vorliegenden Arbeit wurde die Fähigkeit unterschiedlicher U-Net Architekturen, das FGT in DWI-MRT Aufnahmen zu segmentieren, evaluiert. Beide Architekturen konnten das FGT größtenteils korrekt segmentieren, jedoch war keiner der Ansätze in der Lage, eine ausnahmslos perfekte Segmentierung zu erreichen. U-Net Ansatz 1 zeigte hierbei eine größere Anfälligkeit für inkorrekte Segmentierungen.

Ursächlich für die noch vorhandenen fehlerhaften Segmentierungen könnte unter anderem die komplexe Struktur und die hohen Unterschiede in der Signalintensität des FGTs bei hohen b-Werten sein. Ebenso ist die vorhandene Menge an Trainingsdaten im vorliegenden Ansatz limitiert gewesen, diese soll in weiterführenden Ansätzen deutlich erhöht werden. Neben der derzeit genutzten Referenz anderer semi-automatischer Segmentierungstechniken sollen zudem manuell eingezeichnete FGT-Segmentierungen unterschiedlicher DWI-Sequenzen erstellt werden, um eine Evaluation der Segmentierungsleistung mit verschiedenen Referenzmetriken zu ermöglichen. Ebenso sollte untersucht werden, inwiefern die Segmentierungsansätze für unterschiedliche b-Werte generalisiert werden können, da bei höheren b-Werten ein deutlicher Signalabfall des FGTs vorhanden ist, der die trainierten Netze vor Herausforderungen stellen kann.

Schlussfolgerung

Die untersuchten U-Netze waren in der Lage, das FGT auf DWI-MRT Daten größtenteils korrekt zu segmentieren, zeigten jedoch auf Basis des vorhandenen Trainingsdatensatzes noch deutliche Limitationen in der Segmentierungsleistung, die in weiterführenden Ansätzen mit größeren Datenmengen adressiert werden sollen.

References

1. Wenkel E, Uder M, Janka R. Diffusionsgewichtete Brustbildgebung. Radiologe. 2014;54:224–232.

2. Arasu AV, Miglioretti DL, Sprague BL, et al. Population-Based Assessment of the Association Between Magnetic Resonance Imaging Background Parenchymal Enhancement and Future Primary Breast Cancer Risk. J Clin Oncol. 2019;37(12):954–963.

3. Ronneberger O, Fischer P, Brox T. U-Net: Convolutional Networks for Biomedical Image Segmentation. MICCAI 2015. 2015;9351:234-241.

Super-selective pseudocontinuous arterial spin labeling MRI and angiography in Moyamoya disease

Patricia Ulloa,[1*,2] Johannes Hensler[1], Jan-Bernd Hoevener[1,2] und Olav Jansen[1]

[1] Department of Radiology and Neuroradiology, University Hospital Schleswig-Holstein, Kiel, Germany
[2] Biomedical section, Molecular Imaging North Competence Center (MOINCC), Kiel, Germany
* patricia.ulloaalmendras@uksh.de

Synopsis: Moyamoya disease requires constant monitoring of hemodynamic parameters, specially before and after treatment. Non-invasive imaging techniques are essential for such cases. Super-selective pseudocontinuous arterial spin labeling (ss-pCASL) allows vessel-specific blood perfusion mapping non-invasively. It also allows selective vessel angiography without using an exogenous contrast agent. Here, ss-pCASL perfusion maps and angiography are investigated in a Moyamoya patient.

Zusammenfassung: Die Moyamoya-Krankheit erfordert eine ständige Überwachung, besonders vor und nach der Behandlung. Nicht-invasive bildgebende Verfahren sind für solche Fälle unerlässlich. Das superselektive pseudocontinuous arterial spin labeling (ss-pCASL) ermöglicht ein nicht-invasives gefäßspezifisches Blutperfusions-mapping. Es erlaubt auch eine selektive Gefäßangiographie ohne Verwendung eines exogenen Kontrastmittels. Hier werden ss-pCASL-Perfusionskarten und Angiographie bei einem Moyamoya-Patienten untersucht.

Motivation

Moyamoya disease (MMD) is a very uncommon condition, characterized by a progressive stenosis of the internal carotid arteries (ICA). It is diagnosed by examining the vessel wall for pathological markers and stenosis formation using invasive techniques, such as catheter angiography[1]. The usual treatment for MMD is extracranial-intracranial bypass surgery, which has improved patient recovery, preventing rebleeding and hemodynamic stress[2]. Therefore, the non-invasive monitoring of the patients' hemodynamic response before and after treatment is crucial.

Arterial spin labeling (ASL) is a magnetic resonance imaging (MRI) technique that allows non-invasive quantification of blood perfusion. Because of its non-invasive nature, it is a viable alternative to X-ray-based digital subtraction angiography (DSA), specially for kidney-compromised patients, pediatric population, or cases that require constant monitoring.

In ASL, perfusion maps are obtained by acquiring an image with magnetically labeled blood and one without. The labeling is performed by exciting the inflowing blood in a plane proximal to the imaging volume. After the labeling, some time is allowed for the labeled blood to arrive at the tissue of interest before imaging is performed. A measure for tissue perfusion can be obtained calculating based on the difference between control and label image.

There are several ASL techniques described in the literature that may be classified by how the label is done. Pseudo-continuous ASL (pCASL) is the preferred method for clinical applications in the brain[3]. However, pCASL-based perfusion maps show contributions from all vessles supplying the brain. Super-selective pCASL (ss-pCASL)[4] is an alternative to map the perfusion induced by selected vessels. The selection is achieved by tilting and roating the labeling plane, such that the labeling is most effective at its center, where the desired artery is placed (using a pseudo-randomized magnetic field gradient scheme combined with the RF pulses). The same method can be used to acquire angriographies of selected vessels.[5]

Ss-pCASL has been used previously in monito-ring MMD[6], showing its clinical applicability.

Here, ss-pCASL perfusion maps and ss-pCASL angiography were used to study the perfusion territories of a Moyamoya patient.

Material und Methoden / Materials and Methods

ss-pCASL was implemented on a 3-Tesla clinical system (Ingenia, Philips Healthcare, Best, The Netherlands) using a 32-channel head coil. The super-selective label positioning was performed over a Time-of-Flight (ToF) image. The measurement parameters for pCASL and ss-pCASL perfusion maps were label duration: 1.8 s, post-labeling delay: 2.0 s, 3D GraSE readout with TE/TR: 13 ms/3.7 s, FOV: 240x240x96 mm^3, voxel size: 3.75x3.75x

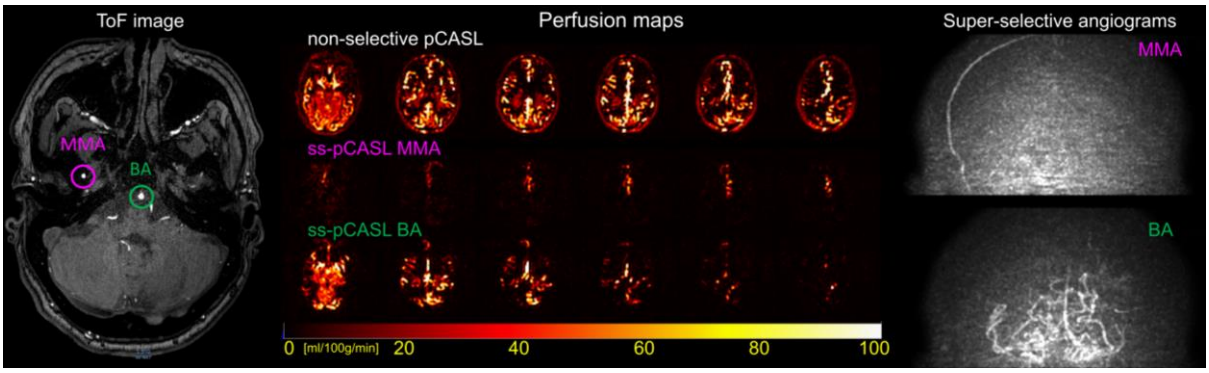

Fig. 1: ss-pCASL MRI application in Moyamoya disease (male, 36 y). **ToF MRI** shows the labeling positioning in the right MMA and basilar artery (BA). **Perfusion maps** Non-selective (top), and ss-pCASL MMA and BA perfusion maps of the patient, showing abnormal perfusion. **Ss-pCASL generated angiograms** (ss-angiograms) of the MMA and BA.

6 mm^3, fat suppression: SPIR and 6 repetitions. For the ss-angiograms the parameters were FOV: 240x240x10 mm^3, voxel size: 1x1x1 mm^3 3D TFE, TE/TR: 2.3/4.6 ms, flip angle: 8º, Each ss-pCASL examination takes 5 min approx. Perfusion maps were calculated using Matlab 2020a (The Mathworks, Natick, MA).

Ergebnisse / Results

The perfusion maps show abnormal perfusion of bilateral anterior cerebral artery territories by right MMA (Fig. 1). Collateralization of bilateral middle cerebral artery territories by basilar artery and subsequent posterior cerebral arteries are also observed. This due to chronic occlusion of bilateral internal carotid and middle cerebral arteries in MMD. In the ss-angiogram the MMA is dilated on its course to anterior-territories and vertebro-basilar territory is extended to both middle cerebral artery territories.

Diskussion / Discussion

Assessment of brain perfusion and vessel perfusion territories is critical in the understanding and surgical planning of MMD. ss-pCASL applications to MMD patients is an active field of research [6].

In this work, an MMD patient was examined using ss-pCASL perfusion and angiography. It was possible to identify the perfusion territories of the MMA and BA, proving the applicability of ss-pCASL in the monitoring of MMD in clinical compatible scan times. As ss-pCASL is non-invasive can be repeated multiple times for continuous monitoring, and it is also compatible with patients where exogenous contrast agents are not recommened. Another adventage is that it requires a minimum knowledge of cerebral vasculatory for correct planning.

Schlussfolgerung / Conclusion

Ss-pCASL is a non-invasive alternative to distinguished individual vessel territories that can support MMD patients' continuous monitoring and treatment planning.

References

(1) Fujimura, M.; Bang, O.; Kim, J. Moyamoya Disease. *Front. Neurol. Neurosci.* **2016**, *40*, 204--220.

(2) Soldozy, S.; Costello, J. S.; Norat, P.; Sokolowski, J. D.; Soldozy, K.; Park, M. S.; Tvrdik, P.; Kalani, M. Y. S. Extracranial-Intracranial Bypass Approach to Cerebral Revascularization: A Historical Perspective. *Neurosurg Focus* **2019**, *46*, 8.

(3) Alsop, D. C.; Detre, J. A.; Golay, X.; Günther, M.; Hendrikse, J.; Hernandez-Garcia, L.; Lu, H.; MacIntosh, B. J.; Parkes, L. M.; Smits, M. Recommended Implementation of Arterial Spin Labeled Perfusion MRI for Clinical Applications: A Consensus of the ISMRM Perfusion Study Group and the European Consortium for ASL in Dementia. *Magn. Reson. Med* **2015**, *73*, 102–116.

(4) Helle, M.; Norris, D. G.; Rüfer, S.; Alfke, K.; Jansen, O.; van Osch, M. J. P. Superselective Pseudocontinuous Arterial Spin Labeling. *Magn. Reson. Med.* **2010**, *64* (3), 777–786.

(5) Lindner, T.; Jensen-Kondering, U.; van Osch, M. J. P.; Jansen, O.; Helle, M. 3D Time-Resolved Vessel-Selective Angiography Based on Pseudo-Continuous Arterial Spin Labeling. *Magn. Reson. Imaging* **2015**, *33* (6), 840–846.

(6) Sollmann, N.; Liebl, H.; Preibisch, C.; Zimmer, C.; Helle, M.; Obara, M.; Kirschke, J. S.; Kaczmarz, S. Super-Selective ASL and 4D ASL-Based MR Angiography in a Patient with Moyamoya Disease: Case Report. *Clin. Neuroradiol.* **2020**.

Schnellere MR-Bildgebung des Kniegelenkes mit Compressed SENSE und künstlicher Intelligenz

Andra-Iza Iuga[1]*, Philip Santiago Rauen[1], Florian Siedek[1], Nils Große-Hokamp[1], Kristina Sonnabend [1,2], David Maintz[1], Grischa Bratke[1]

[1] Institut für Diagnostische und Interventionelle Radiologie, Medizinische Fakultät und Universitätsklinikum Köln, Universität zu Köln, Köln, Deutschland

[2] Philips Healthcare Germany, Hamburg, Germany

Synopsis: Innovations in accelerating image acquisition are a key factor in reducing the cost of individual MRI scans while maintaining diagnostic quality. Combining compressed SENSE with a newly developed deep learning-based algorithm using Convolutional Neural Networks allows a reduction in scan time for 2D imaging of the knee of up to 64%.

Zusammenfassung: Beschleunigte MRT-Sequenzen sind ein Schlüsselfaktor für die Senkung der Kosten der MRT-Untersuchungen bei gleichbleibender diagnostischer Qualität. Die Kombination von Compressed SENSE mit einem neu entwickelten Deep-Learning-basierten Algorithmus unter Verwendung von Convolutional Neural Networks ermöglicht eine Reduzierung der Scanzeit für die 2D-Bildgebung des Kniegelenkes von bis zu 64%.

Motivation

Beschleunigte MRT- Sequenzen sind ein Schlüsselfaktor zur Reduzierung der Kosten einzelner Scans bei gleichbleibender diagnostischer Qualität. (1) Techniken, die eine unvollständige Abtastung des k-Raums verwenden, sind in erheblichem Ausmaß von dem gewählten Rekonstruktionsalgorithmus abhängig um eine ähnliche Bildqualität zu erreichen. Ziel dieser Studie war es, die klinische Umsetzbarkeit der Verwendung von Compressed SENSE (CS) in Kombination mit einem neu entwickelten Deep-Learning-basierten Algorithmus unter Verwendung von Convolutional Neural Networks (CS-AI) (2) zur Beschleunigung der 2D-Bildgebung des Kniegelenkes zu untersuchen.

Material und Methoden

In dieser prospektiven Studie wurden 20 gesunde Probanden mit einem 3-Tesla-MRT-Scanner (Ingenia, Philips, Best, Niederlande) gescannt. Alle Probanden erhielten eine nicht beschleunigte fettgesättigte sagittale 2D-Protonendichte-Sequenz (PD) (CS 1) und vier beschleunigte Sequenzen: CS 2, CS 3, CS 4 und CS 6. Die Bilder wurden mit dem konventionellen CS und dem neuen CS-AI-Algorithmus für alle Beschleunigungsfaktoren rekonstruiert. Zwei unabhängige Auswerter bewerteten alle Aufnahmen unter Berücksichtigung der Gesamtbildqualität, des vorderen Kreuzbandes (VKB), des hinteren Kreuzbandes (HKB), der Menisken, des Knorpels, des Knochens und der Artefakten anhand einer 5-Punkte-Likert-Skala. Zu den objektiven Analysen gehörte außerdem die Berechnung des Signal-Rausch- (SNR) und des Kontrast-Rausch-Verhältnisses (CNR). Der Friedman- und Dunn's-Mehrfachvergleichstest wurde für ordinale Daten verwendet, während ANOVA und der Tukey-Kramer-Test für kontinuierliche Daten angewendet wurden. Cohens Kappa wurde für die Interrater-Reliabilität berechnet.

Ergebnisse

Die Scanzeiten der Sequenzen waren: CS 1: 317 s; CS 2: 165 s; CS 3: 114 s; CS 4: 89 s; CS 6: 63 s. Die AI-basierte Rekonstruktion ermöglichte eine Reduktion der Scanzeit von bis zu ca. 64 % im Vergleich zu den beschleunigten Sequenzen (CS-AI 3). Mit Ausnahme von Artefakten war die subjektive Bewertung für CS-AI bei mindestens einem Beschleunigungsfaktor signifikant höher als bei konventionellem CS. Die CS-AI Sequenzen wurden für alle Beschleunigungsfaktoren und alle Kriterien mit statistischer Signifikanz für Knorpel (Faktor 3 und 4), VKB (Faktor 3), HKB (Faktor 3), Menisken (Faktor 3), Knochen (Faktor 2 und 3) und Gesamtbildeindruck (Faktor 3 und 4) besser bewertet als die zeitäquivalente CS Sequenzen. SNR und CNR erwiesen sich für alle CS-AI-Rekonstruktionen signifikant besser (alle $p<0,05$).

Diskussion

Die Ergebnisse zeigen, dass die Kombination von CS mit dem neu entwickelten Deep-Learning-basierten Algorithmus (CS-AI) der konventionellen CS-Rekonstruktion überlegen ist und daher höhere Beschleunigungen bei unveränderter Bildqualität ermöglicht. Nach bestem Wissen ist unsere Studie die erste, die die klinische Einsetzbarkeit des neu entwickelten hybriden Deep-Learning-basierten Algorithmus unter Verwendung von Convolutional Neural Networks (CS-AI) untersucht. (2,3) Der Algorithmus scheint robust genug zu sein, um als neue Referenz in der klinischen Routine eingesetzt zu

werden, da er für alle getesteten subjektiven und objektiven Kriterien überlegene Ergebnisse aufwies. Die wichtigsten Limitationen dieser Studie sind die kleine Stichprobengröße und die Tatsache, dass zu diesem Zeitpunkt nur gesunde Probanden eingeschlossen wurden. Zukünftige Arbeite sollte größere Mengen an Probanden sowie Patienten berücksichtigen, um verschiedene Kniepathologien und die Übertragbarkeit in die klinische Routine zu analysieren.

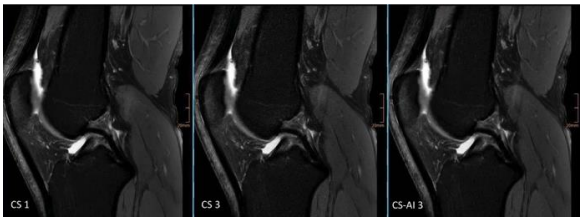

Fig. 1: Vergleich der nicht beschleunigten fettgesättigten 2D PD Sequenz (CS 1) mit der konventionellen CS und der neuen CS-AI-Bildrekonstruktion für Beschleunigungsfaktor 3. Es lässt sich nahezu kein Unterschied zwischen der Referenz CS 1 und CS-AI 3 feststellen.

Schlussfolgerung / Conclusion

Die AI-basierte Rekonstruktionen zeigen für allen untersuchten Kriterien eine bessere Leistung als die konventionelle CS für alle getesteten Beschleunigungsfaktoren. Die Kombination von Compressed SENSE mit dem neu entwickelten Deep-Learning-basierten Algorithmus ermöglicht eine Reduzierung der Scanzeit für die 2D-Bildgebung des Kniegelenkes von bis zu 64%.

References

1. Hollingsworth KG. Reducing acquisition time in clinical MRI by data undersampling and compressed sensing reconstruction. Phys. Med. Biol. 2015 doi: 10.1088/0031-9155/60/21/R297.

2. Pezzotti N, De Weerdt E, Yousefi S, Staring M. Adaptive-CS-Net: FastMRI with Adaptive Intelligence. arXiv:1912.12259 2019.

3. Pezzotti N, Yousefi S, Elmahdy MS, et al. An Adaptive Intelligence Algorithm for Undersampled Knee MRI Reconstruction. IEEE Access 2020 doi: 10.1109/access.2020.3034287.

Simultaneous mapping of B_0, B_1 and T_1 for the correction of CEST-MRI contrast

Kerstin Heinecke*[1]

[1] Quantitative MRI, Biomedical Magnetic Resonance, Medical Physics and Metrological Information Technology, Physikalisch-Technische Bundesanstalt, Braunschweig and Berlin, Germany
* kerstin.heinecke@ptb.de

Synopsis: The small signal in CEST-MRI is highly susceptible to B_0, B_1 and T_1, so it is crucial to correct for these parameters to determine the isolated CEST contrast. This thesis shows promising results for a new method for simultaneous mapping of these parameters, as opposed to the conventional individual scans, using a CEST-like sequence and a neural network analysis. As part of this WANTED framework for CEST-correction, a new tool for improved development and analysis of (CEST-)MRI experiments was established.

Zusammenfassung: CEST-MRT beruht auf kleinen Signalen, die empfindlich auf B_0, B_1 und T_1 reagieren. Diese Parametereinflüsse müssen korrigiert werden, wofür konventionell einzelne Scans je Parameter notwendig sind. Diese Arbeit zeigt eine neue Methode mit erfolgsversprechenden Ergebnissen, die alle drei Parameter gleichzeitig kartiert. Hierfür wird eine Sequenz ähnlich zu CEST-MRT genutzt und mit einem neuronalen Netz ausgewertet. Als Teil dieses WANTED Framework für CEST-Korrektur wurde eine neue Umgebung für die verbesserte Entwicklung und Analyse von Experimenten in CEST-MRT geschaffen.

Motivation and Background

Modern techniques of Magnetic Resonance Imaging (MRI) are no longer limited to qualitative black and white contrast imaging of Hydrogen properties, which only allowed vastly experienced radiologists the detection of structural differences. Functional MRI, diffusion MRI and MR fingerprinting are among the rising methods to enable the imaging of different tissue properties and the rise of quantitative MRI. Another recent technique, Chemical Exchange Saturation Transfer (CEST), has gained a lot of interest, enabling the imaging of low concentrated solubles. This method relies on the detection of small signals, which can be strongly influenced by field inhomogeneities and tissue parameters. To improve the correction pipelines of these influences, this thesis proposed and investigated a new method for simultaneous mapping of the static magnetic field B_0, the radio-frequency field B_1 and the longitudinal relaxation time T_1 to overcome limitations of conventional mapping methods.

In CEST-MRI, the solute's protons are saturated using a preparation radio-frequency pulse at the solute's resonance frequency. The resulting signal changes would be too small for direct detection, but a continuous proton exchange between the solute pool and the main water pool during saturation results in an accumulation of saturated protons. Thus, after a sufficient pulse duration, small solute concentrations can be detected indirectly via the water pool. CEST is analyzed with Z-spectra, plotting the saturated water signal normalized by the water signal without saturation as a function of the saturation frequency offset. Competing magnetization transfer mechanisms also influence the spectra, but can be compensated in specific contrasts like MTR_{asym} and MTR_{Rex} (1).

These contrasts open the possibility to image the target solute, which can, for example, enable clearer determination of pathological tissues. The successful application of CEST-MRI, however, greatly depends on the data post-processing pipeline to correct for signal distortions. The signal's strong susceptibility to field inhomogeneities can result in shifted (B_0) or scaled (B_1) Z-spectra. Additionally, the CEST effect directly depends on the relaxation time, resulting in strong effects of T_1 on the spectra. Generally, the use of high-field MR scanners is beneficial for CEST-MRI, as the chemical shift differences increase proportionally, improving the distinction of the CEST signal from the direct water saturation. Unfortunately, B_0 and B_1 field inhomogeneities also increase with higher field strengths. Thus, it is crucial to correct for B_0 shift, B_1 inhomogeneities and T_1 times to isolate the desired CEST contrast.

To enable the correction of the Z-spectra, maps of the parameters are needed. Conventionally, three individual scans with different set-ups are required to map each parameter individually, which is time-consuming and inefficient. Popular methods in CEST applications are water saturation shift referencing (WASSR) (2) and B_1 mapping by

Bloch-Siegert shift (BSS) (3), and T_1 can, for example, be mapped using a saturation or inversion recovery sequence. Schuenke et. al. developed a method for simultaneous water shift and B_1-mapping (WASABI) (4), using a CEST-like sequence. The WASABI spectra allow an analytical fit of the B_0 shift and B_1. Although the spectra show a correlation with T_1, this information has not yet been exploited, as the full analytical equation is complicated by additional terms to the WASABI fit. The terms for the relaxation times must be approximated and the function is not always differentiable, which can lead to unreliable results in a conventional fitting approach.

To overcome these limitations, a T_1-prepared WASABI sequence (WASABITI) was developed and a neural network (NN) was implemented to analyze the spectra. Machine learning has become an established data analysis tool and has been successfully applied to similar projects in CEST-MRI, as for example in the deepCEST approach (5). Thus, it was hypothesized, that with this new WASABITI sequence, B_0, B_1 and T_1 could be mapped simultaneously and the NN analysis would yield improved results as opposed to the analytical fit. This thesis investigated this novel method and prepared its further development for successful application in CEST-MRI.

Methods

The new MR sequence for simultaneous mapping of B_0, B_1 and T_1 was designed in the Pulseq "Open format for MR sequences" (6) using PyPulseq (7). To enhance T_1 sensitivity and spoil residual magnetization, the WASABI (4) sequence was extended by a T_1 preparation block to spoil residual longitudinal magnetization after each offset. This sequence, combined with a 2D gradient echo readout, was used in a scanner experiment, using a phantom consisting of 12 vials with different T_1 times.

For the virtual experiments, the WASABI Analysis Network with T_1 Evaluation for Data post-processing (WANTED) framework was developed. It consists of a complete simulation tool for scan-like virtual experiments, the NN and its functionalities, analytical fit functions, correction algorithms and scripts for different use-cases, including data post-processing.

Two open source simulation tools were developed over the course of this thesis, solving the full Bloch-McConnell equation system. Firstly, pypulseq-cest (8) is a Python interface for the C++ based pulseq-cest (9).Additionally, the purely Python based BMCTool (10) was developed for simplified adaptions during the development process in this project. In cooperation with the pulseq-cest project and the pulseq-cest-library, a platform to share simulation and Pulseq files, a shared input and output pipeline was established, working towards reproducibility of CEST-experiments (11). It consists of human-readable and shareable Pulseq-files and configuration files in the YAML-format (12).

Scan-like simulations were enabled by the self-developed BMCPhantom package, which allows the easy set-up of virtual phantoms. It takes a slightly extended input of the simulation tools, again promoting reproducibility and shareability. A stack of arrays defines the parameters for pixel-wise simulation of the desired configuration. Fig. 1 shows the phantom used in this thesis, designed for brain-scan-like simulations with broad parameter ranges. It has high field inhomogeneities, compartments of four different brain tissue-like parameters, Gaussian noise and CEST pool fractions for the virtual CEST experiment.

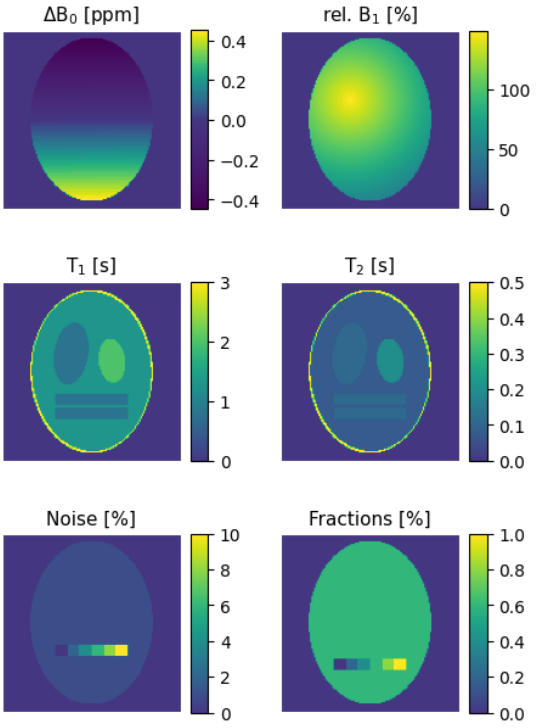

Fig. 1: Virtual phantom with parameter definitions: (Top to bottom) B_0 shift in ppm and relative B_1 in %, T_1 and T_2 in s, and Gaussian noise (std.) and CEST-pool fraction.

The NN used to retrieve the B_0 shift, B_1 and T_1 parameters from the simulated or scanned WASABITI spectra was developed after the deepCEST approach (5) as a prototype for this proof-of-principle investigation. From the 31 offsets of the WASABITI spectra as input, it predicts the parameters B_0, B_1 and T_1 each as the mean of their assumed underlying Gaussian distributions, using a Gaussian negative log-likelihood loss function. As an additional output, the standard deviation for each parameter is given as an uncertainty estimate.

The training data was simulated with parameters drawn from uniform distributions in a broad range of parameters (B_0 shifts: –1 to 1 ppm, relative B_1: 20 to 200 %, T_1: 0.01 to 7 s and T_2: 0.005 to 5 s). Adding different random noise intensities resulted in a dataset of more than 20 million spectra (examples in Fig. 2). To compare the influence of training data, a NN with the same architecture was trained on a dataset simulated with parameters drawn from continuous distributions shaped to subjectively represent brain-scan-like probabilities of occurrence.

As a comparative approach, the full analytical fit for the phantom was solved using the lmfit package (13). For one, initialization parameters were draw from within arbitrarily chosen boundaries to reflect expected values. Secondly, the initialization values were set close to the simulation parameters to achieve results close to the best possible solution.

The applicability of the maps of the NN was investigated by running a complete CEST correction pipeline on a virtual experiment with a large arbitrary APT-like CEST pool. Different exchange-weighted contrasts were compared: The MTR_{Rex} contrast with and without correction of B_0 and B_1 and the AREX contrast, which accounts for the T_1 effects (1).

Results and Discussion

In CEST-MRI, the influence of field inhomogeneities and T_1 times need to be corrected for to allow the determination of the isolated CEST-contrast. In this thesis, the new WASABITI sequence was designed to enable a simultaneous mapping of all three parameters and the subsequent analysis by a simple NN was investigated for proof-of-principle.

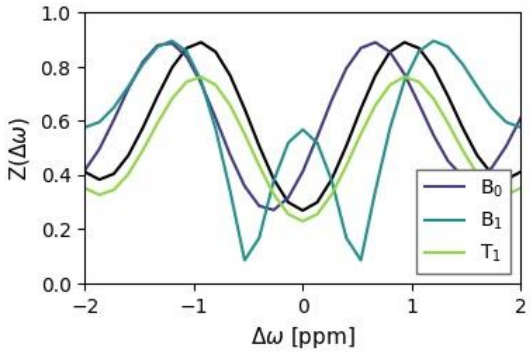

Fig. 2: Influence of the target parameters on WASABITI spectra. Black: WASABITI spectrum simulated with $\Delta B_0 = 0$ ppm, relative $B_1 = 100$ %, and $T_1 = 0.8$ s. Colored: single parameters changed. $\Delta B_0 = 0.3$ ppm (green), $B_1 = 80$ % (blue), $T_1 = 1.3$ s (yellow), 3 % Gaussian noise (grey).

As a main indicator for the performance of the NN, the output maps of a virtual brain-scan-like experiment were compared to the ground truth (Fig. 3). The differences show a good performance for all parameters, even for high B_1. The B_1 estimation has the least errors, followed by B_0 shift and then T_1. These findings were also reflected in statistical evaluations, with a mean B_0 error of 0.003 ppm, a B_1 error of 0.011 µT (0.3 % of the nominal B_1) and a T_1 error of 0.054 s (2.8 % of the mean T_1).

Generally, the B_1 field has the strongest impact on all parameter maps and, as expected, the performance decreases with very high noise. However, the uncertainty maps match the errors very well, especially for regions with high noise and high B_1, making the use of the maps more reliable.

The coefficients of determination R^2 (1.0 for B_0, 0.999 for B_1 and 0.985 for T_1) show a strong linear correlation of the target values and the prediction, indicating good predictions over the parameter ranges in the phantom. However, a decreasing performance occurs for relative B_1 below about 80 %. This is probably caused by an increasing occurrence of high amplitudes, which result in a non-differentiable flip at the zero axis in the absolute WASABITI spectrum (s. Fig. 2). The lowest T_1 of 0.8 s also shows a higher deviation in performance, which is probably due to its closeness to the parameter range edges.

Analyzing the same virtual experiment with the analytical fit, the NN maps could be shown to be advantageous. Even using initialization values for the analytical fit close to the ground truth, it performed worse than the NN for B_1 and for T_1, especially for noisier spectra and for high B_1 inhomogeneities.

A preliminary scanner experiment on a phantom with different T_1 times proved the applicability of the new WASABITI sequence, which is easily reproducible due to the use of the Pulseq format. As can be seen in Fig. 4, it showed realistical results for the B_0 and B_1 field maps of the NN, even representing high uncertainties on the vial edges. The T_1 maps are also promising. With a mean difference of 0.042 s (6 % of the mean T_1), the mean results of regions of interests in the vials match the T_1 values obtained by a saturation recovery sequence well. However, the NN predicted negative values for T_1 times below 0.55 s, which were not represented in the uncertainty maps. These negative values were probably caused by the choice of suboptimal activation functions in the employed NN.

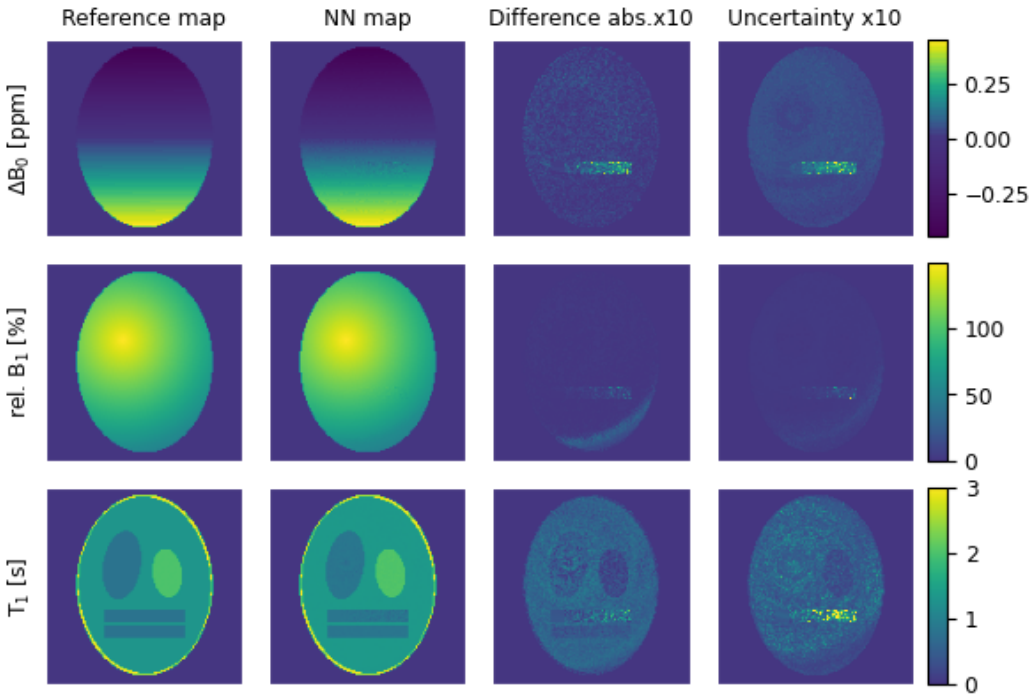

Fig. 3: Parameter maps for the virtual phantom (Top to bottom: B_0 shift, relative B_1 and T_1). Left to right: Simulation parameters as a reference, NN output maps, the difference between the reference (as absolute values, x 10) and the NN maps, and the uncertainty output of the NN (x 10).

These findings indicate several possible improvements as next steps after this thesis. Apart from optimizing the NN architecture, different activation functions should be explored. Additionally, the analytical function could be included in the loss function, which has recently shown promising results in similar projects. Alternative results in the comparison of the network trained on different dataset showed the importance to optimize the dataset, while keeping in mind a potential bias. With that, the improvement of T_1 parameter mapping should also be investigated. Furthermore, the uncertainties currently represent the aleatoric uncertainties, which can lead to some undetected errors like the negative T_1 values for the scanner experiment. Methods to include epistemic uncertainties should be incorporated. After optimization, further scanner experiments, including *in vivo* CEST-MRI at higher field strengths, should be conducted to further prove the applicability of this new method.

Nevertheless, the virtual CEST experiment with corrections using the NN maps could show that the method leads to the desired results, even in the current prototypical state. Fig. 5 shows that the MTR_{Rex} contrast becomes much clearer after the application of the B_0 shift and B_1 inhomogeneity correction using the parameter maps obtained with the proposed method. The AREX contrast eliminates the underlying T_1 contrast and allows to determine the isolated CEST contrast of the different fractions in the bar at the bottom.

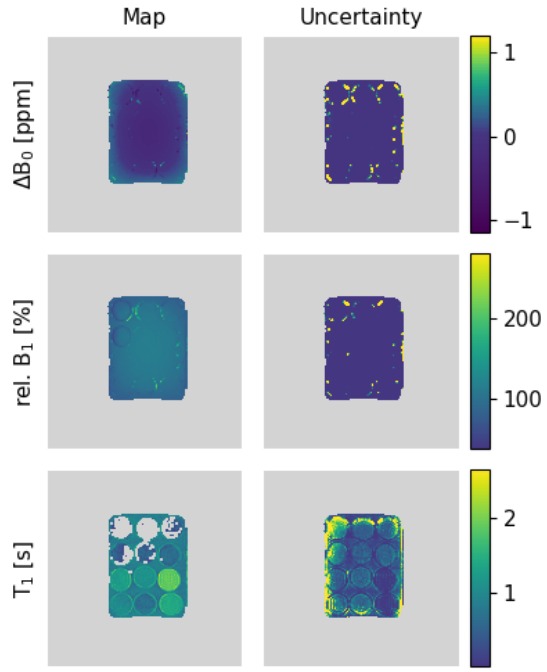

Fig. 4: Parameter and uncertainty maps as predicted by the NN for a scanned phantom with different T_1 times in each vial. Negative values are masked.

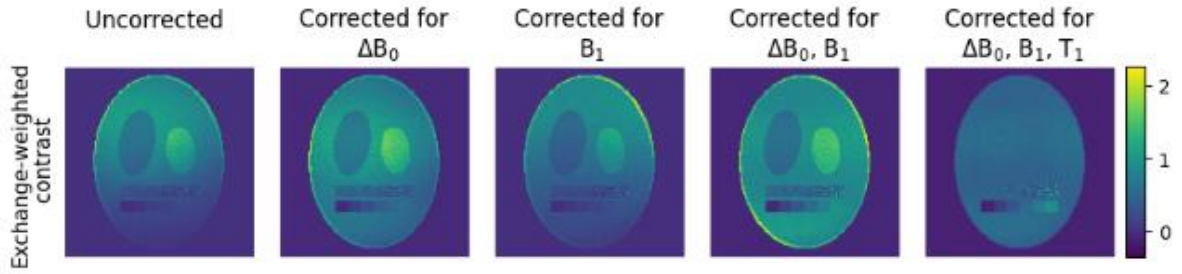

Fig. 5: Exchange-weighted contrasts of a virtual CEST-MRI experiment. Left to right: The MTR_{Rex} contrast of the uncorrected data, after ΔB_0 correction, after B_1 correction and with both field inhomogeneity corrections. Right: AREX contrast to weigh in T_1 effects (ΔB_0 and B_1 corrected).

Conclusion

This thesis proves the feasibility of a new method for simultaneous mapping of B_0, B_1 and T_1, using the newly developed WASABITI sequence and a neural network-based analysis. The applicability and adaptability of this method is ensured by the WANTED framework for CEST-correction, including a simulation tool, the NN, analytical fit functionalities, correction algorithms and data post-processing pipelines. Using this framework, a complete proof-of principle investigation was conducted, showing very promising results and indicating the way for the pending optimization of the NN. It became apparent that the WANTED framework for the correction of CEST-MRI provides a useful tool for the development and analysis of CEST and other MRI experiments.

Author's note

Most of the optimizations are currently being investigated and further scanner experiments are conducted. The NN has evolved, the negative output issues were resolved, and the results improved. It is planned to make the framework available as open source software to share this new mapping method and simplify the design of CEST and other MRI experiments.

References

1. Zaiss M, Xu J, Goerke S, et al. Inverse Z-spectrum analysis for spillover-, MT-, and T1 -corrected steady-state pulsed CEST-MRI--application to pH-weighted MRI of acute stroke. NMR Biomed. 2014;27:240–52 doi: 10.1002/nbm.3054.

2. Kim M, Gillen J, Landman B a, Zhou J, van Zijl PCM. Water saturation shift referencing (WASSR) for chemical exchange saturation transfer (CEST) experiments. Magn. Reson. Med. 2009;61:1441–50 doi: 10.1002/mrm.21873.

3. Sacolick LI, Wiesinger F, Hancu I, Vogel MW. B1 mapping by Bloch-Siegert shift. Magn. Reson. Med. 2010;63:1315–22 doi: 10.1002/mrm.22357.

4. Schuenke P, Windschuh J, Roeloffs V, Ladd ME, Bachert P, Zaiss M. Simultaneous mapping of water shift and B1 (WASABI)-Application to field-Inhomogeneity correction of CEST MRI data. Magn. Reson. Med. 2017;77:571–580 doi: 10.1002/mrm.26133.

5. Glang F, Deshmane A, Prokudin S, et al. DeepCEST 3T: Robust MRI parameter determination and uncertainty quantification with neural networks-application to CEST imaging of the human brain at 3T. Magn. Reson. Med. 2019:1–17 doi: 10.1002/mrm.28117.

6. Layton KJ, Kroboth S, Jia F, et al. Pulseq : A Rapid and Hardware-Independent Pulse Sequence Prototyping Framework. Magn. Reson. Med. 2017;1552:1544–1552 doi: 10.1002/mrm.26235.

7. Ravi K, Geethanath S, Vaughan J. PyPulseq: A Python Package for MRI Pulse Sequence Design. J. Open Source Softw. 2019;4:1725 doi: 10.21105/joss.01725.

8. Heinecke K, Schuenke P. pypulseq-cest. https://github.com/KerstinHut/pypulseq-cest. Published 2021. Accessed July 03, 2021.

9. Herz K, Zaiss M. pulseq-cest. https://github.com/kherz/pulseq-cest. Published 2021. Accessed July 03, 2021.

10. Schuenke P, Heinecke K. BMCTool. https://github.com/schuenke/BMCTool. Published 2021. Accessed July 03, 2021.

11. Herz K, Mueller S, Zaitsev M, et al. Pulseq-CEST: Towards multi-site multi-vendor compatibility and reproducibility of CEST experiments using an open source sequence standard. Magn. Reson. Med. 2021:1–14 doi: 10.1002/mrm.28825.

12. Ben-Kiki O, Evans C, döt Net I. YAML. https://yaml.org/. Published 2001. Accessed January 10, 2021.

13. Newville M, Stensitzki T, Allen DB, Ingargiola A. LMFIT: Non-Linear Least-Square Minimization and Curve-Fitting for Python. 2014 doi: 10.5281/ZENODO.11813.

Merging T1w and QSM provides a unique Tissue Contrast

Rakshit Dadarwal,[1,2] and Susann Boretius[1,2]

[1] Functional Imaging Laboratory, German Primate Center, Göttingen, Germany.
[2] Georg August Universität Göttingen, Göttingen, Germany
* rdadarwal@dpz.eu.

Synopsis: We propose a unique image contrast by linearly combining T1-weighted images and maps of the magnetic susceptibility. The approach works equally well in healthy humans and non-human primates. The achieved delineation of white matter (WM), cortical, and subcortical structures significantly improved the performance of automatic brain tissue segmentation. A measurement time of only 13 min may enable its use in human diagnostics. A pilot study on a patient with multiple sclerosis revealed WM-alterations that were not detectable on single-contrast images.

Zusammenfassung: Durch die lineare Kombination von T1-gewichteten Bildern und Karten der magnetischen Suszeptibilität konnte ein Bildkontrast erzeugt werden, der die Darstellung von weißer Substanz, kortikalen und subkortikalen Strukturen signifikant verbessert. Die Methode funktioniert gleichermaßen in Menschen und nicht-humanen Primaten und verbesserte das Ergebnis automatischer Gehirn-Segmentierungen deutlich. Die kurze Messzeit von 13 min ermöglicht den Einsatz in der humanmedizinischen Diagnostik. Eine Pilotstudie an einem Patienten mit Multipler Sklerose deckte Veränderungen der weißen Substanz auf, die auf den Einzelbildern so nicht erkennbar waren.

Motivation

Most algorithms of automatic brain tissue segmentation rely on T1-weighted (T1w) datasets, which provide excellent contrast between gray matter (GM) and white matter (WM). However, with the exception of the caudate and putamen, T1w images barely show any contrast between subcortical structures and their surroundings (Fig. 1). By this, automated brain tissue segmentation largely misclassifies the majority of subcortical GM structures as part of WM.

The correct delineation of subcortical structures is, however, key to many questions in neurosciences and neurology. These structures are vital for motor integration and complex brain functions such as memory, emotions, and hormone production (1). Structural and functional abnormalities of subcortical structures have been associated with healthy aging and various neurological disorders, including Parkinson's disease, ADHD, and depression (2–6).

Quantitative Susceptibility Mapping (QSM), a recently rapidly evolving method, provides a unique contrast of subcortical structures (Fig. 1 & 2). Improved algorithms for phase unwrapping, background field removal, and solving the phase to susceptibility inverse problem have recently made QSM reconstruction more robust and reliable (7,8). However, this method goes along with limited GM-to-WM contrast.

Accurate brain tissue segmentation of subcortical structures but likewise of WM and GM is essential for a variety of therapeutic interventions. However, most of the currently available segmentation tools fail, particularly in non-human primates, a precious animal model for studying the anatomical and functional organization of the human brain and diseases of the nervous system.

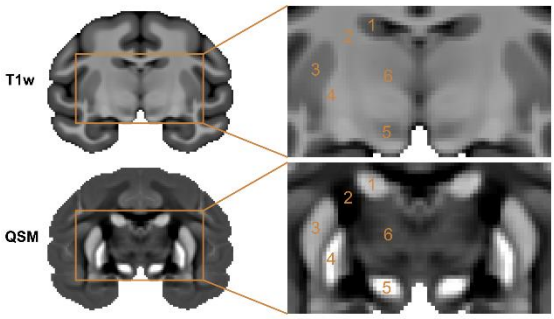

Fig. 1: T1w images and QSM maps of a monkey brain (coronal plane). T1w provides excellent WM-GM contrast, while QSM is superior in delineating subcortical structures (magnification on the right: 1 - caudate, 2 - internal capsule, 3 - putamen, 4 - globus pallidus, 5 - substantia nigra, and 6 - thalamus).

In order to improve automatic brain tissue segmentation, we aimed to combine the benefits of T1w and QSM. We introduce a unique brain tissue contrast that provides a superior delineation of brain structures in healthy non-human primates and humans but may also yield valuable additional information on the diseased brain.

Materials and Methods

Four healthy, adult, female long-tailed macaque monkeys (mean age: 8 years) and three healthy humans (mean age: 27 years, male) were included in the study. In addition, the proposed method was exemplarily applied to a patient diagnosed with multiple sclerosis (MS).

All MR data were acquired at a magnetic field strength of 3 T (MAGNETOM Prisma, Siemens) using a 7 cm single loop coil (monkey) and 20-channel head coil (human) for signal detection. T1-weighted and T2*-weighted images were obtained using the MR parameters given below.

Monkey: T1w: 3D MPRAGE, TE/TR = 2.7/2700 ms, spatial resolution = 0.5 mm isotropic, FA = 8˚, and TA = 14.3 minutes. T2*w: ME-GRE sequence, TE1/ spacing/ TE9/ TE10 of 3.7/ 4.9/ 48 ms, TR = 57 ms, spatial resolution = 0.31 mm isotropic, FA = 20˚, and TA = 24 minutes.

Human: T1w: 3D MPRAGE, echo time/ repetition time (TE/TR) = 2.2/2400 ms, spatial resolution = 0.8 mm isotropic, flip angle (FA) = 8˚, and total acquisition time (TA) of 6.3 minutes. T2*w: 3D multi-echo gradient echo (ME-GRE) sequence, TE1/ spacing/ TE8 of 4.5/ 4.5/ 36 ms, TR = 41 ms, spatial resolution = 0.75 mm isotropic, FA = 20˚, and TA = 7 minutes.

The T1w images were denoised and corrected for the bias field using ANTs (9). Monkey and human brain masks were manually generated on T1w using the ITK-SNAP tool (10). The mean of the ME-GRE images across echo times (mGRE) was linearly registered to the T1w of each subject using ANTs registration. QSM maps were reconstructed using the coil combined ME-GRE phase data. QSM reconstruction included the multi-scale dipole inversion approach, phase unwrapping was done with the best-path algorithm, and background field removal was performed using the Laplacian boundary value and variable spherical mean value filtering algorithms (11–13). T1w and QSM symmetric brain templates were constructed by aligning the duplicated and mirrored original maps to the hemispheric planes. Preprocessed T1w image and QSM map of the single subjects were fused by a weighted linear combination. The weights (W) for the T1w and QSM contrasts were generated at random between 0 and 1, and -1 and 0, respectively. The T1w signal intensities and QSM values (X_c) were normalized to a range of 0 and 1 before feeding into the fusion generation equation $\mathrm{Yi} = \sum_{c=0}^{c} Wic\ \mathrm{Xc}$ (c = 0;1).

The resulting fused images were evaluated to only select the desired contrast by discarding images with poor contrast-to-noise ratio (CNR) between all tissue classes (cortical GM + WM + deep GM (dGM) + CSF) and linear discriminant analysis (LDA) accuracy score. Selected four tissue classes served as labels for training the LDA model, and the accuracy of the model was used to select the desired weights.

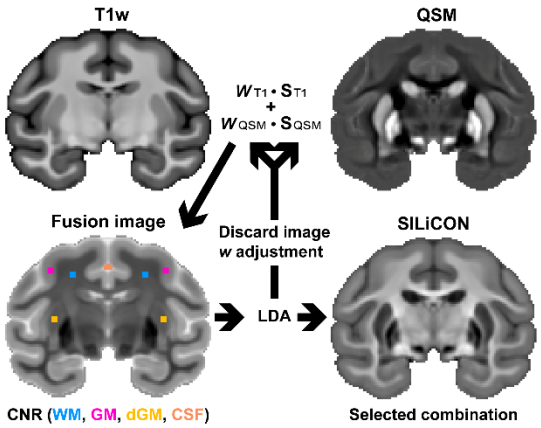

Fig. 2: Workflow for TQ-TQ-SILiCON data analysis. T1w and QSM images were merged to create a fusion image, which was then analyzed using CNR and LDA accuracy score for the volume to be accepted or discarded.

To evaluate the result, three-class tissue segmentation (inside the brain mask) was performed on T1w and the selected combination of T1w and QSM using ANTs Atropos, resulting in cerebrospinal fluid (CSF), GM, and WM segmentation masks together with their probabilistic maps.

Results

The finally selected TQ-SILiCON image was created using 0.318 and -0.790 as weights for T1w and QSM, respectively. Compared to a single contrast, the combination provided both an excellent GM-WM contrast and a clear delineation of the subcortical structures (Fig. 3).

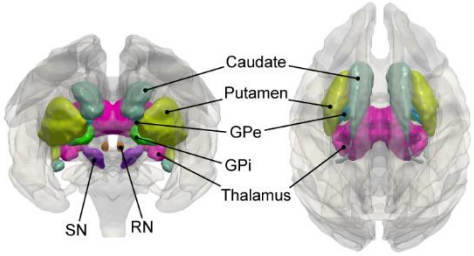

Fig. 3: Transparent white matter surface of the macaque monkey brain, along with the color segmented subcortical structures extracted from the TQ-SILiCON group average. Subcortical structures include the caudate, putamen, globus pallidus externus (GPe), globus pallidus internus (GPi), thalamus, substantia nigra (SN), and red nucleus (RN).

The results of the group-averaged automatic brain tissue segmentation of the monkey brain are shown in Fig. 4. In comparison to T1w, TQ-SILiCON allowed for a better separation of WM and brain nuclei such as the globus pallidus. This led to a slightly larger GM volume when using TQ-SILiCON compared to T1w (Table 1). Respectively, the T1w-based segmentation overestimated the WM volume by 0.70%.

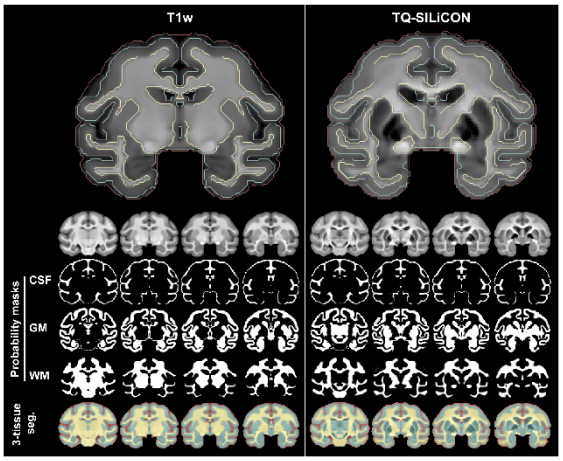

Fig. 4: Comparison of monkey brain tissue segmentation using T1w and TQ-TQ-SILiCON images, respectively (coronal view). The three-class tissue segmentation derived CSF, GM, and WM probability masks and segmentation images.

	T1w	TQ-SILiCON
Total (mm^3)	68,339	
CSF (mm^3)	16,428	
GM (mm^3)	30,826	31,302
WM (mm^3)	21,085	20,608

Table 1: Estimated volumes of different brain tissues in macaque monkeys when using T1w or TQ-SILiCON (group averaged) for automatic segmentation.

Similar findings could be observed in healthy human volunteers. The results of single-subject automatic brain tissue segmentation in humans are shown in **Figure 5**. The received tissue volumes are summarized in Table 2. As in monkeys, the segmentation based on T1w only overestimated the volume of WM (by 1.93%).

	T1w	TQ-SILiCON
Total (mm^3)	354,935	
CSF (mm^3)	63,723	
GM (mm^3)	168,370	175,228
WM (mm^3)	122,843	115,984

Table 2: Estimated volumes of different brain tissues in humans when using T1w or TQ-SILiCON (group averaged) for automatic segmentation.

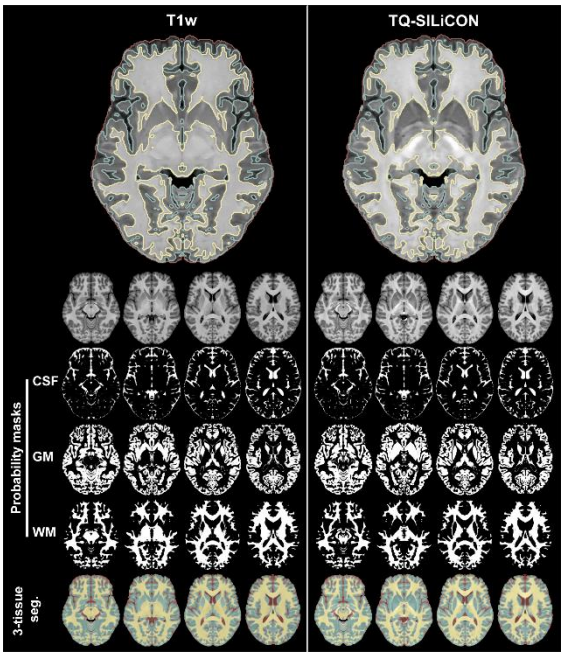

Fig. 5: Axial view of human brain tissue segmentation using T1w and TQ-TQ-SILiCON images. The three-class tissue segmentation derived CSF, GM, and WM probability masks and segmentation images for T1w and TQ-TQ-SILiCON images.

In order to evaluate the potential of TQ-SILiCON for the analysis of the diseased brain, we obtained T1w and QSM data sets from a patient with multiple sclerosis. In this pilot study, we could limit the measurement time to about 13 min, which makes the approach suitable for clinical use. The resulting TQ-SILiCON revealed alterations, particularly in the white matter, which were hardly visible on T1w and QSM alone (Fig. 6). How these findings relate to the underlining pathology needs to be further clarified and requires additional systemic investigations. As the TQ-SILiOCN approach works equally well for human and non-human primates, respective studies in non-human primates of MS will be of particular value in this context.

Discussion

Image synthesis based on multi-contrast MRI has become an emerging field of research. However, due to constraints in measurement time, the collected data sets need to be carefully chosen. Here we used a linear combination of T1w and QSM that significantly improved the visualization of brain structures and the quality of automatic brain segmentation. The method worked likewise successfully in humans and non-human primates, in the latter case even with a single loop receiver coil and its steep sensitivity profile.

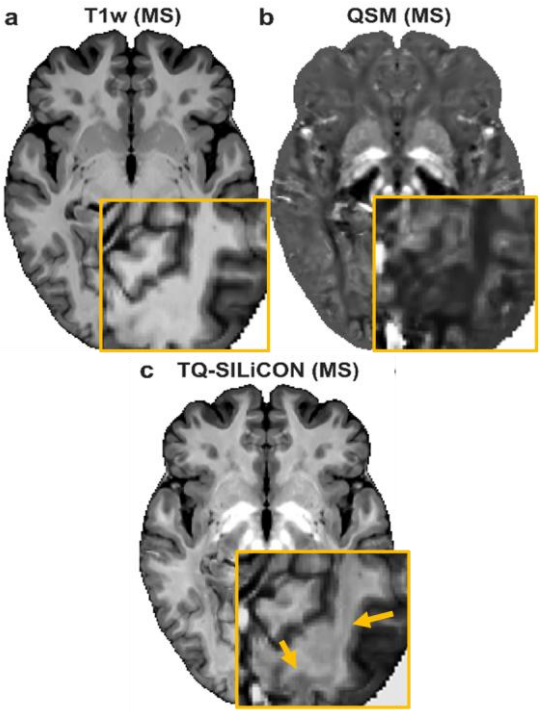

Fig. 6: T1w and QSM from a human subject with MS (a, b). The reconstructed TQ-TQ-SILiCON (c) reveals alterations particular in the white matter (arrows), which are hardly visible on the single-contrast images.

The proposed linear combination of T1w and QSM facilitates an excellent delineation of the cerebral cortex, WM structures, and deep GM nuclei. This may be of particular importance for the diagnostics of neurodegenerative diseases and age-related changes of the brain where the atrophy of specific brain structures has emerged as a valuable biomarker. Automatic brain segmentation based on T1w only may provide misleading results here since volume changes in white matter, and deep nuclei may not be correctly disentangled.

Another potential application is the guidance of neurosurgical interventions, for instance, to treat Parkinson's disease and depression by deep brain stimulation. As in basic neuroscience research on non-human primates, the correct delineation of the respective nuclei by maintaining anatomical information of the whole brain is essential for precise targeting.

Noteworthy, TQ-SILiCON images from an MS patient provided structural details of the lesioned WM, which were not visible on any of the single contrast images. The interpretation of these findings, however, requires further research. Here, the respective non-human primate models of human diseases might be of particular value.

The focus of the study was on automatic brain tissue segmentation, but the approach can be easily adapted and may even be extended by including additional contrasts. Depending on the research question and pathological alteration, the weighting of the single contrasts may require an adaptation to meet the requirements of the particular case.

Conclusion

The TQ-SILiOCN approach offered a unique brain tissue contrast and worked equally well for human and non-human primates. This may facilitate further comparative and translational neuroimaging studies.

References

1. Koshiyama D, Fukunaga M, Okada N, et al. Role of subcortical structures on cognitive and social function in schizophrenia. Sci Rep 2018;8:1183 doi: 10.1038/s41598-017-18950-2.

2. van Erp TGM, Hibar DP, Rasmussen JM, et al. Subcortical brain volume abnormalities in 2028 individuals with schizophrenia and 2540 healthy controls via the ENIGMA consortium. Mol Psychiatry 2016;21:547–553 doi: 10.1038/mp.2015.63.

3. Nakao T, Radua J, Rubia K, Mataix-Cols D. Gray Matter Volume Abnormalities in ADHD: Voxel-Based Meta-Analysis Exploring the Effects of Age and Stimulant Medication. AJP 2011;168:1154–1163 doi: 10.1176/appi.ajp.2011.11020281.

4. Zhang Y, Zhang X, Zhang J, et al. Gray matter volume abnormalities in type 2 diabetes mellitus with and without mild cognitive impairment. Neuroscience Letters 2014;562:1–6 doi: 10.1016/j.neulet.2014.01.006.

5. Ladouceur CD, Almeida JRC, Birmaher B, et al. Subcortical Gray Matter Volume Abnormalities in Healthy Bipolar Offspring: Potential Neuroanatomical Risk Marker for Bipolar Disorder? Journal of the American Academy of Child & Adolescent Psychiatry 2008;47:532–539 doi: 10.1097/CHI.0b013e318167656e.

6. Yang X, Ma X, Huang B, et al. Gray matter volume abnormalities were associated with sustained attention in unmedicated major depression. Comprehensive Psychiatry 2015;63:71–79 doi: 10.1016/j.comppsych.2015.09.003.

7. Milovic C, Tejos C, Acosta-Cabronero J, et al. The 2016 QSM Challenge: Lessons learned and considerations for a future challenge design. Magnetic Resonance in Medicine 2020;84:1624–1637 doi: 10.1002/mrm.28185.

8. Bilgic B, Langkammer C, Marques JP, Meineke J, Milovic C, Schweser F. QSM reconstruction challenge 2.0: Design and report of results. Magnetic Resonance in Medicine 2021;86:1241–1255 doi: 10.1002/mrm.28754.

9. Avants BB, Tustison NJ, Song G, Cook PA, Klein A, Gee JC. A reproducible evaluation of ANTs similarity metric performance in brain image registration. Neuroimage 2011;54:2033–2044 doi: 10.1016/j.neuroimage.2010.09.025.

10. Yushkevich PA, Piven J, Hazlett HC, et al. User-guided 3D active contour segmentation of anatomical structures: significantly improved efficiency and reliability. Neuroimage 2006;31:1116–1128 doi: 10.1016/j.neuroimage.2006.01.015.

11. Acosta-Cabronero J, Milovic C, Mattern H, Tejos C, Speck O, Callaghan MF. A robust multi-scale approach to quantitative susceptibility mapping. Neuroimage 2018;183:7–24 doi: 10.1016/j.neuroimage.2018.07.065.

12. Abdul-Rahman HS, Gdeisat MA, Burton DR, Lalor MJ, Lilley F, Moore CJ. Fast and robust three-dimensional best path phase unwrapping algorithm. Appl. Opt., AO 2007;46:6623–6635 doi: 10.1364/AO.46.006623.

13. Zhou D, Liu T, Spincemaille P, Wang Y. Background field removal by solving the Laplacian boundary value problem. NMR in Biomedicine 2014;27:312–319 doi: 10.1002/nbm.3064.

Teilnehmerliste / List of Participants

Vorname	Nachname	Institut	Email
Emily Louise	Baadsvik	Institute for Biomedical Engineering, ETH Zurich and University of Zurich	baadsvik@biomed.ee.ethz.ch
Ina	Barnekow	Deutsches Primatenzentrum, Leibniz-Institut für Primatenforschung, Funktionelle Bildgebung, Göttingen	ibarnekow@dpz.eu
Tamara	Bäuchle	Radiologisches Institut, Universitätsklinikum Erlangen, Friedrich-Alexander-Universität Erlangen-Nürnberg (FAU), Erlangen, Germany	Tamara.Baeuchle@extern.uk-erlangen.de
Melanie	Bauer	Institute of forensic medicine in Basel	melanie.bauer@unibas.ch
Celine	Berger	Institut für Rechtsmedizin der Universität Basel	celine.berger@unibas.ch
Samuel	Bianchi	IBT, ETHZ	bianchi@biomed.ee.ethz.ch
Florian	Birk	Max Planck Institute for Biological Cybernetics	florian.birk@tuebingen.mpg.de
Andreas	Bitz	FH Aachen, University of Applied Sciences	bitz@fh-aachen.de
Xuming	Chen	The Max Planck Institute for Biological Cybernetics	xu-ming.chen@tuebingen.mpg.de
Ying	Chu	Institut für Systemische Neurowissenschaften, Universitätsklinikum Hamburg-Eppendorf	y.chu@uke.de
Rakshit	Dadarwal	Deutsches Primatenzentrum, 37077 Göttingen	rdadarwal@dpz.eu
Hoai Nam	Dang	Universitätsklinikum Erlangen	HoaiNam.Dang@uk-erlangen.de
Marco	Deckers	Deutsches Primatenzentrum	mdeckers@dpz.eu
Hannes	Dillinger	IBT, D-ITET, University and ETH Zurich	dillinger@biomed.ee.ethz.ch
Nico	Egger	Friedrich-Alexander Universität Erlangen-Nürnberg, Universitätsklinikum Erlangen, Radiologisches Institut	nico.egger@uk-erlangen.de

Christian	Eisen	Radiologisches Institut, Friedrich-Alexander-Universität Erlangen-Nürnberg (FAU), Erlangen, Deutschland	christian.eisen@uk-erlangen.de
Jürgen	Finsterbusch	University Medical Center Hamburg-Eppendorf, Department of Systems Neuroscience	j.finsterbusch@uke.uni-hamburg.de
Carola	Fischer	TU Berlin	carola.fischer@siemens-healthineers.com
Lena	Gast	University Hospital Erlangen	lenav.gast@gmail.com
Alexander	German	Radiologisches Institut, Universitätsklink Erlangen	alex.german@fau.de
Mirjam	Gerwing	Clinic of Radiology, Medical Faculty - University of Muenster - and University Hospital Muenster	Mirjam.Gerwing@ukmuenster.de
Daniel	Giese	Siemens Healthcare & FAU Erlangen	giese.daniel@siemens-healthineers.com
Felix	Gloger		felix.gl@gmx.de
Christian	Günthner	University and ETH Zurich	guenthner@biomed.ee.ethz.ch
Jannis	Hanspach	Universitätsklinikum Erlangen, Radiologisches Institut, Friedrich-Alexander-Universität Erlangen-Nürnberg	jannishanspach@gmail.com
Kerstin	Heinecke	Physikalisch-Technische Bundesanstalt Braunschweig und Berlin	kerstin.heinecke@ptb.de
Franciszek	Hennel	Institute for Biomedical Engineering, University of Zurich and ETH	hennel@biomed.ee.ethz.ch
Jürgen	Herrler	Universitätsklinikum Erlangen	juergen.herrler@uk-erlangen.de
Verena	Hörr	University Hospital Münster	vhoerr@uni-muenster.de
Thomas	Kampf	Würzburg	thomas.kampf@physik.uni-wuerzburg.de
Tobias	Krähling	Clinic of Radiology, Medical Faculty - University of Muenster - and University Hospital Muenster	tobias.kraehling@uni-muenster.de
Fabian	Kratzer	German Cancer Research Center (DKFZ)	f.kratzer@dkfz.de

Marie-Luise	Kromrey	Department of Diagnostic Radiology and Neuroradiology, University Medicine Greifswald, Greifswald, Germany	marie-luise.kromrey@uni-greifswald.de
Frederik	Laun	Radiologisches Institut, Universitätsklinikum Erlangen, Maximiliansplatz 1, 91054 Erlangen, Deutschland	frederik.laun@uk-erlangen.de
Martin	Loh	Friedrich-Alexander-Universität Erlangen-Nürnberg	martin.loh@extern.uk-erlangen.de
Roger	Lüchinger	IBT	rluchin@ethz.ch
Marta Brigid	Maggioni	Universitätsklinikum Jena, Medical Physics Group	marta.maggioni@uni-jena.de
Tor Rasmus	Memhave	Deutsches Primatenzentrum GmbH, Kellnerweg 4, 37077 Göttingen	TMemhave@dpz.eu
Eric	Michael	Institute for Biomedical Engineering, ETH Zurich and University of Zurich	michael@biomed.ee.ethz.ch
Nikolaos	Molochidis		nikolaos.molochidis@uniklinik-freiburg.de
Amir	Moussavi	Deutsches Primatenzentrum	amoussavi@dpz.eu
Astrid	Müller	Radiologisches Institut, Universitätsklinikum Erlangen, Friedrich-Alexander-Universität Erlangen-Nürnberg (FAU), Erlangen, Deutschland	astrid.mueller@uk-erlangen.de
Lena	Nohava	Medical University of Vienna, Vienna, Austria	lena.nohava@meduniwien.ac.at
Arnd	Obert	Hannover Medical School	obert.arnd@mh-hannover.de
Franz	Patzig	IBT, ETHZ	patzig@biomed.ee.ethz.ch
Eva	Peschke	Section Biomedical Imaging, UKSH, Kiel	eva.peschke@rad.uni-kiel.de
Mona	Pistel	Universitätsklinikum Erlangen & Siemens Healthineers	mona.pistel@extern.uk-erlangen.de
Daniel	Polak	Siemens Healthcare GmbH	daniel.polak@siemens-healthineers.com
Julian	Rauch	Medizinische Physik in der Radiologie, Deutsches Krebsforschungszentrum, Heidelberg	j.rauch@dkfz-heidelberg.de

Laurent	Ruck	institute of radiology, university hospital Erlangen	Laurent.Ruck@uk-erlangen.de
Céline	Steger	University of Zurich/ University Children's Hospital Zürich	celine.steger@kispi.uzh.ch
Jonathan	Stelter	Technical University of Munich (TUM)	jonathan.stelter@tum.de
Christoph	Stuprich	Radiologisches Institut, Universitätsklinikum Erlangen, Friedrich-Alexander Universität Erlangen-Nürnberg (FAU)	christoph.stuprich@uk-erlangen.de
Rui	Tian	Max Planck Institute for Biological Cybernetics, Tuebingen	rui.tian@tuebingen.mpg.de
Julia	Trächtler	ETH Zürich	traechtler@biomed.ee.ethz.ch
Ruth	Tuura	University Children's Hospital Zürich	ruth.tuura@kispi.uzh.ch
Patricia	Ulloa	Dept. Radiology and Neuroradiology, University Hospital Schleswig-Holstein (UKSH)	patricia.ulloaalmendras@uksh.de
Thomas	Ulrich	Institute for Biomedical Engineering, ETH Zürich und Universität Zürich	ulrich@biomed.ee.ethz.ch
Isil	Unal	Universitätsklinikum Schleswig-Holstein, Klinik für Radiologie und Neuroradiologie, Kiel	isil.unal@uksh.de
Patrick	Winter	University Clinics Wuerzburg, Medical Clinic and Policlinic I, 97080 Wuerzburg Universiy of Wuerzburg, Experimental Physics 5, 97074 Wuerzburg	patrick.winter@physik.uni-wuerzburg.de